Spectroscopic studies of neutron-rich ^{129}Sn and ^{80}Ge nuclei using the GRIFFIN spectrometer

by

Fatima H. Garcia

M.Sc., Simon Fraser University, 2017
B.Sc., University of Calgary, 2013

Thesis Submitted in Partial Fulfillment of the
Requirements for the Degree of
Doctor of Philosophy

in the
Department of Chemistry
Faculty of Science

SIMON FRASER UNIVERSITY
Summer 2021

Declaration of Committee

Name:	**Fatima H. Garcia**
Degree:	**Doctor of Philosophy**
Thesis title:	**Spectroscopic studies of neutron-rich ^{129}Sn and ^{80}Ge nuclei using the GRIFFIN spectrometer**
Committee:	**Chair:** Hua-Zhong Yu Professor, Chemistry
	Corina Andreoiu Supervisor Associate Professor, Chemistry
	Daniel B. Leznoff Committee Member Professor, Chemistry
	Greg Hackman Committee Member Research Scientist, TRIUMF
	Caterina Ramogida Examiner Assistant Professor, Chemistry
	Alfredo Galindo-Uribarri External Examiner Senior Scientist Physics Division Oak Ridge National Laboratory

Abstract

Spectroscopic studies provide information about the structure of nuclei. Information that, in turn, serves to inform theoretical models and astrophysical studies. Recent work using the GRIFFIN spectrometer at TRIUMF has uncovered novel information in two isotopes, ^{129}Sn and ^{80}Ge, which lie close to the two magic nuclei: ^{132}Sn and ^{78}Ni, respectively.

The work on ^{129}Sn observed 31 transitions and 9 excited states for the first time, populated through the β-decay of ^{129}In. Most notably, this experiment was the first to observe the β-decay of the $(29/2^+)$ 1911-keV isomer of ^{129}In.

The work on ^{80}Ge searched for a previously observed 0^+ state at 639-keV, just below the 2^+ 659-keV excited state, through the β-decay of ^{80}Ga. The presence of the former was proposed as evidence for low-energy shape coexistence in ^{80}Ge, in the region around doubly-magic ^{78}Ni, though further signatures for the presence of this state were missing. The GRIFFIN experiment was unable to observe this state, despite using a superior detector system and observing higher statistics . The nonobservation, coupled with theoretical calculations performed, led to the conclusion that this 0^+ 639-keV does not exist. Furthermore, the analysis observed, for the first time, 66 excited states and 157 γ-ray transitions, which were added to the known ^{80}Ge level scheme.

The data here presented will serve to improve upon existing nuclear structure theories and will inform future applications of nuclear science to fields such as astrophysics.

Keywords: decay spectroscopy; neutron-rich species; nuclear structure; β-decay

Dedication

A mis padres. Gracias por enseñarme a perseverar.

A mi hermana. Gracias por escucharme cuando más lo necesito.

A Daniel. Gracias por compartir tu alegría y amor en cada instante.

Acknowledgements

The work that follows would not have come to be, but for the presence of some very crucial individuals. I take this opportunity to thank them and acknowledge their invaluable contributions. Without their support, the document before you would not have come to exist.

To my supervisor, Dr. Corina Andreoiu, thank you. Not only for the opportunity to work with you on studying fundamental nuclear structure, but also for your unwavering support, advice, lessons — both academic and life — and your encouragement and fostering of my abilities. Your ingenuity, strength and alacrity will continue to be a source of inspiration throughout my scientific endeavours and beyond.

To my committee members, Dr. Greg Hackman and Dr. Daniel Leznoff, thank you for your insight throughout the course of my doctoral program. The support and counsel I have received from you both has been integral to this work.

To current and past members of the SFU Nuclear Chemistry Groups. Drs. Jenn Pore, Jonathan Williams, Kenneth Whitmore, Pietro Spagnoletti; Kevin Ortner, Kurtis Raymond, Isaiah Djianto, Melanie Gascoine and Frank Wu. For sharing your wisdom, time and laughter; for answering my sometimes ridiculous questions and for supporting me through the roller coaster that is grad school, thank you. I am very grateful to have been able to share a literal and metaphorical office with such a talented group of people.

To members of the GRSI Collaboration at TRIUMF, specially Dr. Gordon Ball. Thank you for your assistance in conducting the experiments herein contained, your aid in the analysis of the datasets and your help with the scientific articles that resulted from these investigations. Your input was critical to this work, and your lessons will continue to guide me in the future.

To my friends in Vancouver, and at home, specially, Nas Yousefi, Luiza Gomez, and Allison Whitworth. Thank you. Your constant presence throughout the course of this degree has been instrumental to its successful completion, and your strength has been a source of comfort and encouragement when I have needed it most. For the support during tough times, for the celebrations during successful moments and for your unrivaled positivity, thank you. I am incredibly thankful for your friendship.

To my parents, Vilma and Roberto Garcia, and to my sister Lourdes Garcia. Thank you. For everything. For your love and support; for your tireless encouragement and confidence in me; for your sacrifices and example. This would not have been possible without your presence and your words. Thank you. You are the rock on which can I stand tall. Los quiero mucho.

Finally, to Daniel Nuñez. For your tireless support. For your infinite patience. For your unconditional love. Thank you. Your presence during my studies, and especially during what turned out to be an extraordinarily strange year, has been vital. Thank you for sharing your life with me. Te amo.

Contents

List of Tables

List of Figures

List of Abbreviations

ADC	Analog-to-Digital Converter
ALTO	Accélérateur Linéaire et Tandem à Orsay.
ARIEL	Advanced Rare IsotopE Laboratory.
ARIES	Ancillary Detector for Rare-Isotope Event Selection.
ASCII	American Standard Code for Information Interchange.
BR	Branching Ratio.
BGO	Bismuth Germanate.
CERN	European Organization for Nuclear Research.
DAEMON	Detector Array for Energy Measurements of Neutrons.
DESCANT	DEuterated Scintillator Array for Neutron Tagging.
EC	Electron Capture.
EMMA	ElectroMagnetic Mass Analyzer.
ENSDF	Evaluated Nuclear Structure Data File.
FRIB	Facility for Rare Isotope Beams.
FRS	Fragment Separator at GSI.
FWHM	Full Width Half Maximum.
GEANT4	Geometry and Tracking 4.
Ge(Li)	Lithium-drifted Germanium.
GRIFFIN	Gamma-Ray Infrastructure For Fundamental Investigations of Nuclei.
HPGe	High Purity Germanium.
IGLIS	Ion-Guide Laser Ion Source.
ILL	Institut Laue Langevin.
IOI	Island of Inversion.
ISAC	Isotope Separator and ACcelerator.

ISOL	Isotope Separation On-Line.
LEBT	Low Energy Beam Transport.
LN2	Liquid Nitrogen.
NIST	National Institute of Standards and Technology.
NNDC	National Nuclear Data Centre.
OSIRIS	On-line Separation of Isotopes at a Reactor in Studsvik.
PACES	Pentagonal Array of Conversion Electron Spectrometers.
RCMP	Regina Cube for Multiple Particles.
RFQ	Radio Frequency Quadrupole.
RIB	Radioactive Isotope Beam.
RIKEN	Institute of Physical and Chemical Research
SCEPTAR	SCintiallation Electron-Positron Tagging ARray.
Si(Li)	Lithium-drifted Silicon.
TIGRESS	TRIUMF-ISAC Gamma Ray Suppressed Spectrometer.
TITAN	TRIUMF's Ion Trap for Atomic and Nuclear science.
TRINAT	TRIUMF Neutral Atom Trap.
W.u	Weisskopf units.
ZDS	Zero Degree Scintillator.

The following are proper names:

GSI	GSI Helmholtz Center for Heavy Ion Research.
ISOLDE	Isotope Mass Separator On-line facility at CERN.
ISOLTRAP	Mass Spectrometer at ISOLDE.
LNPS	Valence space based on a $^{48}_{20}\mathrm{Ca}^{28}$ core + the $0f^{7/2}$, $0g^{9/2}$ and $1d^{5/2}$ neutron orbitals.
LOGFT	logft calculator provided by NNDC.
LOHENGRIN	Recoil Mass Spectrometer at the Institut Laue-Langevin.
PF-SDG	Valence space using the full pf proton shell and the sdg neutron shells
ROOT	Particle physics data analysis software.
TRIUMF	Canada's Particle Accelerator Centre.

Chapter 1

Introduction

The atom. The quintessential building block of matter takes its name from the Greek philosopher Democritus, who asserted that matter was composed of *atomos*, indivisible, imperishable and unchanging particles [1].

The discovery of the nucleus by Rutherford [2] and the neutron by Chadwick [3] revealed that the atom had a more complex structure than previously thought: the electrons orbited a central nucleus and that the nucleus itself was composed of smaller particles, protons and neutrons. Following these discoveries, a plethora of particles were further observed, collected into the so-called "particle zoo" we know today. The protons (Z) and the neutrons (N) were found to be composed of quarks, even smaller subatomic particles that come in different "flavours". But at the core of these observations, lay the question: what force governs the behaviour of the nucleus?

The fundamental force was called the "strong force", alluding to its strength compared to the well understood electromagnetic and gravitational forces. Observation revealed that it was a residual force; particles were subject to it in a small range, and it had the power to bind neutral and positively charged particles together to form the nucleus of an atom.

Like the elements in the periodic table, nuclei can be arranged in accordance to their contents, specifically based on the number of protons and neutrons they contain. This arrangement is called the chart of nuclides, shown in Figure 1.1.

The chart exhibits some interesting features. The valley of stability at the centre of the chart contains the most stable nuclei; isotopes further away from this area of stability are, as implied, increasingly unstable. This valley does not follow the $N = Z$ line above mass number $\sim$10, but rather curves to the neutron-rich side; the deviation due to the increasingly strong Coulomb force that the protons are subject to, requiring more and more neutrons to achieve a bound system. The magic numbers, occurring at 2, 8, 20, 28, 50, 82 (and 126 for N) are nucleon numbers that exhibit added stability, in a manner akin to the noble gases in the atomic shell model. The proton and neutron drip lines, at the left and right sides of the charts, respectively, represent the edges of the nuclear landscape; effectively the point at which no more nucleons (of the appropriate type) can be added and still result in a bound

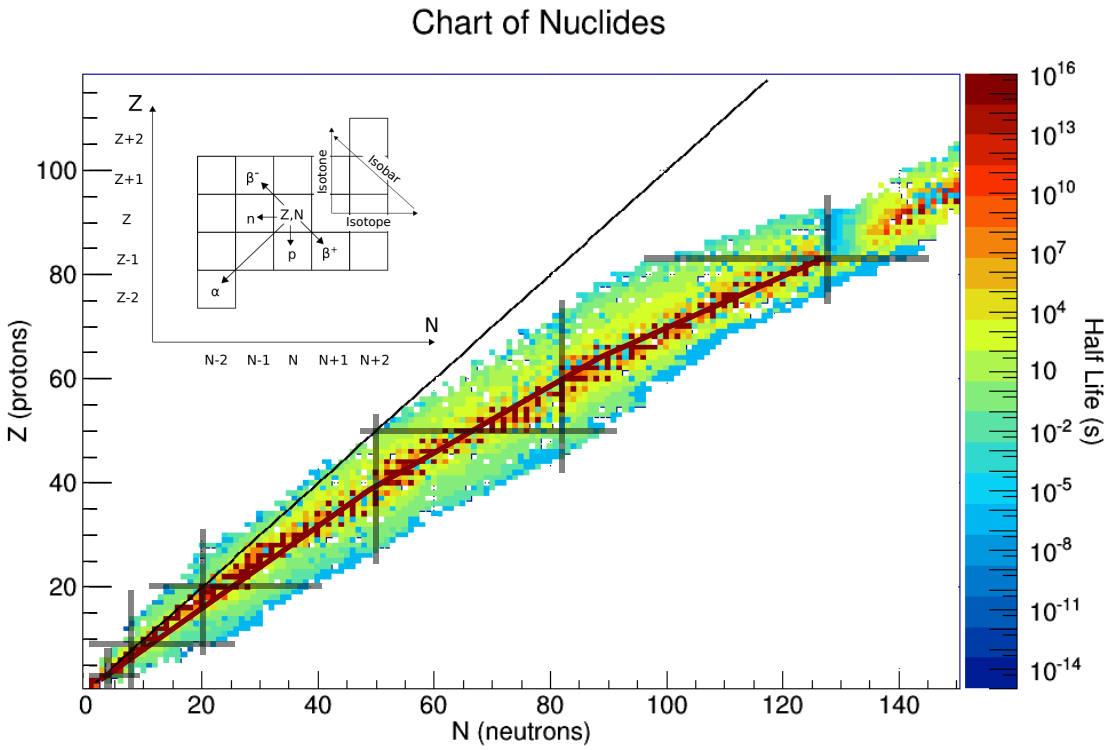

Figure 1.1: The Chart of Nuclides, with neutron number N on the x-axis, proton number Z on the y-axis and the colour contour representing the half-lives of each isotope. The $N = Z$ line is shown in black, while the valley of stability is delineated in burgundy. The opaque lines delineate the magic number, nucleon values which conferred stability, akin to the noble gases. The inset shows the various decay modes, such as α and β decay, neutron and proton evaporation, and their paths along the chart. Adapted from Ref [4].

nucleus. The edges shown in Figure 1.1 are by no means established, work is still ongoing to determine the number of bound nuclei, with some predictions counting up to 7000 bound nuclei between mass number $A = 2$ and $A = 120$ [5].

The features of the chart of nuclides gave rise to the questions driving nuclear theory, questions regarding the nature of the strong force, the evolution of the magic numbers and shell structure and the underlying behaviour of the nucleons inside the nucleus. So far, a full theoretical description of the nucleus has eluded scientists, but efforts have been made to tackle different regions of interest.

Experimental results have done a great deal to advance nuclear theory, while at the same time providing information for applications such as nuclear medicine and materials science, demonstrating the versatility of the field as well as justifying further study of radioactive isotopes.

The present work will focus on two isotopes that are relevant to the study of nuclear structure, and therefore the development of a cohesive nuclear theory. The following Introduction will detail the background information necessary to the study of radioactive

isotopes through β- and γ-decay, the two main processes that were observed during this work. Chapter 2 will outline the GRIFFIN experimental station, which was the apparatus used to observe nuclear decay. Chapter 3 will discuss the results of the β-decay study of ^{129}In into excited states of ^{129}Sn, a nucleus in the vicinity of doubly magic ^{132}Sn. Chapter 4 will highlight findings on the structure and the shape coexistence phenomenon in the region of doubly magic ^{78}Ni, obtained through the β-decay study of ^{80}Ga into excited states of ^{80}Ge. Chapter 5 will conclude by summarizing the efforts herein contained and will make assertions and suggestions as to future directions.

1.1 The Shell Model

A complete working theoretical description of the nucleus has yet to be realized. Currently, some theories are able to describe the properties of the lightest elements, while others can reasonably predict energy levels of heavier nuclei. A cohesive theory has eluded scientists so far, but advances have been made throughout the decades to come to these working theories.

In an effort to better understand the nucleus, nuclear scientists looked to the atom first, a well-established model that could shine some light into nuclear structure.

1.1.1 The Atomic Case

The experiments of Johannes Rydberg led to the observation of atomic spectra [6, 7]. These discrete lines, observed in an emission or absorption spectrum, were what lead Niels Bohr to surmise that electrons occupied specific, defined shells [8]. The quantized orbitals, Bohr proposed, prevented the negatively charged electrons from spiraling into or exiting out of the vicinity of positively charged nucleus; the movement between these orbitals was proposed to be the cause of the lines in Rydberg's spectra.

Each orbital could only contain a certain number of electrons, and no two electrons could have the same quantum numbers, according to the Pauli exclusion principle, which governs fermions [9]. Evidence for the shell structure of atoms was also observed in the atomic radii and ionization energies for the elements, as seen in Figure 1.2. Here, sharp increases were observed in radius with the addition of one electron above a closed shell, while a sharp decrease in ionization energy was noted in these same elements, when compared to those with a closed shell of electrons.

The electrons present in these closed shell elements, termed the noble gases, conferred stability, preventing the easy addition or removal of electrons, thereby making them inert. The outer, or valence, shell of electrons was later determined to be critical in the chemical reactions that are seen in the laboratory.

The success of the atomic shell model in describing elemental properties was an attractive option to the nuclear scientists, when the time came to describe properties of nuclei.

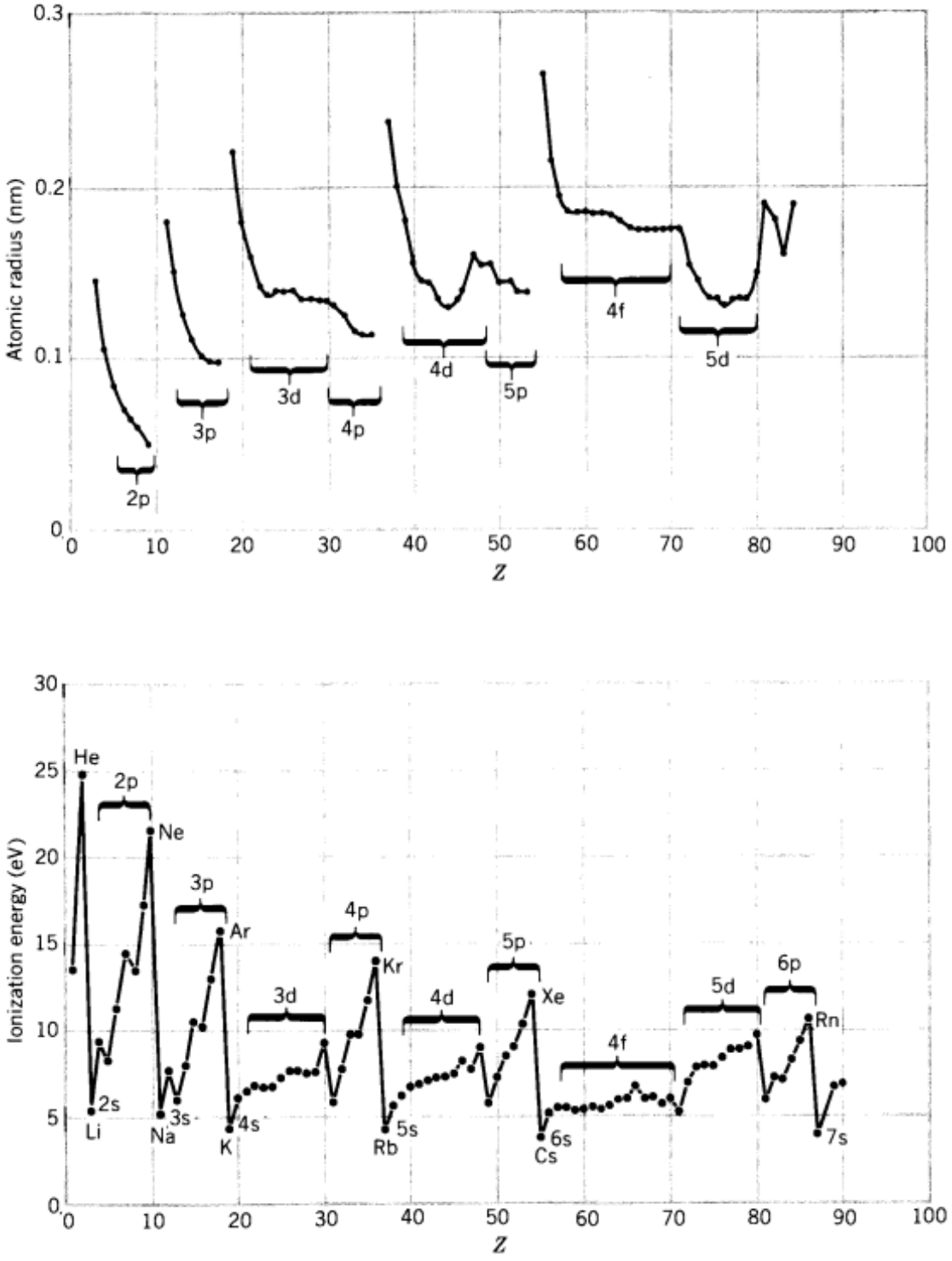

Figure 1.2: Atomic radii and ionization energy of the elements in the periodic table. Evidence for shell structure in the atom is seen in the sudden jumps between the radii, as different shells are occupied (top) and a corresponding decrease in ionization energy for the same elements (bottom). Reprinted with permission from [10].

1.1.2 The Nuclear Case

The atomic shell model is a cohesive theory with which to describe the behaviour of electrons, and is supported by the extensive array of experimental data, such as the atomic radii and the ionization energies of various elements, as previously discussed. In the nuclear case, similar phenomena were observed, leading to the development of an analogous shell model for the nucleus.

Evidence of shell structure came from experimental observation of the nucleon separation energies, where nuclei with either proton, Z, or neutron, N, numbers 2, 8, 28, 50 and 82 (as well as $N = 126$) required more energy to have one nucleon removed than that of their neighbours [10], with Figure 1.3 showing this phenomenon for neutrons. Clear jumps in the energy required to remove one neutron are seen at these specific neutron numbers, just as was the case for the ionization energies of the atoms, hinting at the fact that these configurations were closed shells. Similar jumps were also observed at the same proton numbers. This behaviour is also indicative of increased stability to these particular nuclei; the numbers at which this occurred came to be called the "magic" numbers, analogous to the electronic configurations of the noble gases.

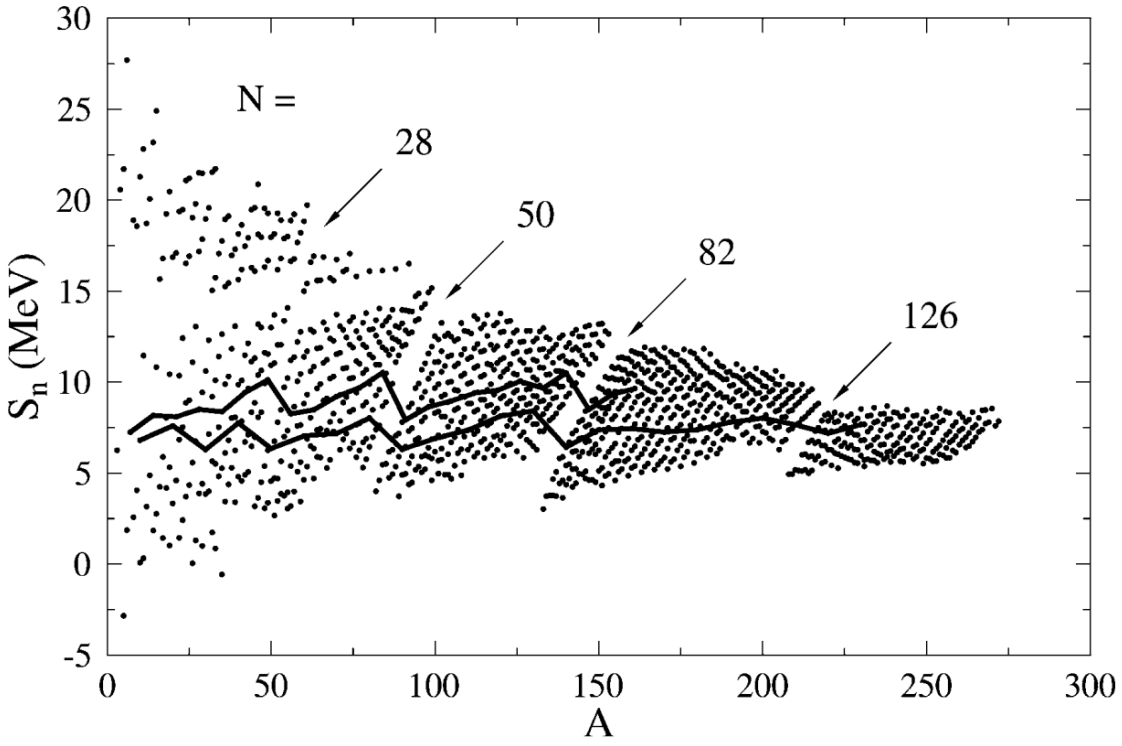

Figure 1.3: Experimentally observed neutron separation energies, key evidence for the nuclear shell model. Thin lines track nuclei with a constant N/Z ratio. Reprinted from Ref. [11], reprinted under CC BY 3.0.

Any complete nuclear theory would then need to be able to at least reproduce these magic numbers, and the push to use the analogous atomic shell model meant describing a suitable potential. In the atomic case, the electrons are said to occupy orbitals and move in the Coloumb potential created by the nucleus, with the Pauli exclusion principle dictating the orbits that can be occupied. The questions then, in the nuclear case, were how the fermonic nucleons behaved in the nucleus and if the Pauli principle held true.

Assume, for a moment, that the nucleons do occupy an orbital structure. If two nucleons at the bottom of the potential well were to collide with one another, a transfer of energy would occur, and one of the nucleons would be promoted up the energy level structure. However, if the levels above were fully occupied, the nucleon would have to be promoted all the way into the valence band. This, in and of itself, would require more energy than that available to the colliding nucleons, giving credence to the concept that nucleons orbit as if they were transparent to one another, and are subject to the Pauli exclusion principle [10]. Having reconciled the shell structure of the nucleons, a nuclear potential had to be established. Though the Coulomb potential would have contributed in the case of the charged protons, no such potential could be used for the neutrons. The assumption was made that the potential governing the nucleus was self-generated by the motion of the nucleons in the system.

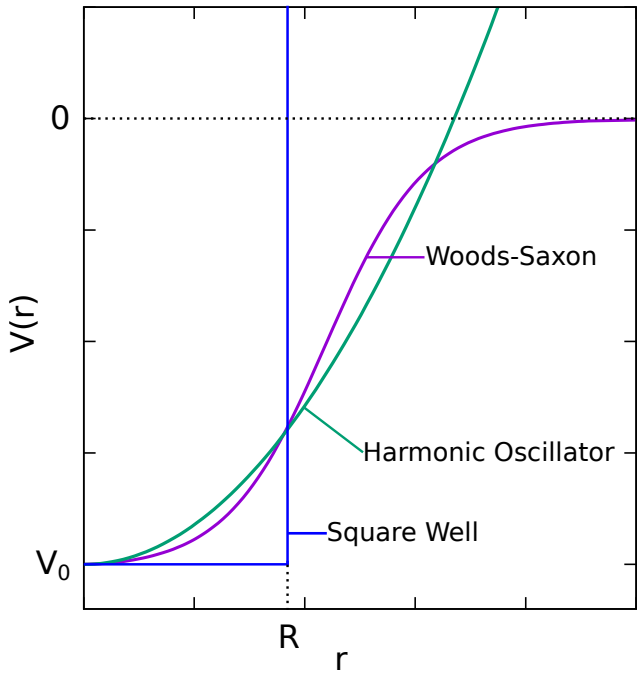

Figure 1.4: Schematic of candidate potentials for describing the nucleus.

The shape of the potential was described through successive iterations of known potential functions. The square well [12] and harmonic oscillator potentials [13] were successful

in reproducing the lowest magic numbers, but failed at reproducing the experimentally observed higher shell closures. Additionally, their infinite boundaries would have required an infinite amount of energy to remove nucleons, a fact that was refuted by the nucleon separation energies that were observed. This lead to the development of a more realistic description, in the shape of the Woods-Saxon potential [14], described in Equation 1.1,

$$V(r) = \frac{-V_0}{1 + \exp\left[(r - R)/a\right]}, \tag{1.1}$$

where V_0 is the depth of the potential well, typically taken as $\sim$50 MeV to reproduce observed the separation energies, R is the nuclear radius, $R = 1.25A^{1/3}$ fm, A is the nuclear mass number $(Z+N)$ and a is the skin thickness of the nucleus, 0.524 fm [10]. This potential presented a key feature that made it a more realistic potential: it has an edge that smoothly vanishes beyond the average nuclear radius, allowing for bound and unbound states. A comparison between the square well, harmonic oscillator and Woods-Saxon potential is shown in Figure 1.4.

Using the Woods-Saxon potential, the wavefunctions describing the nucleus can be accessed through the time-independent Schrödinger wave equation:

$$\left[-\frac{\hbar^2}{2m}\nabla^2 + V(r)\right]\psi(\vec{r}) = E\psi(\vec{r}), \tag{1.2}$$

where ψ may be separated into radial and angular components, with the solutions of the form:

$$\psi(\vec{r}) = \psi_{n\ell m_\ell}(\vec{r}) = \varphi_{n\ell}(r)Y_{\ell m_\ell}(\theta, \phi), \tag{1.3}$$

where n, ℓ and m_ℓ are the principal quantum number, the orbital angular momentum quantum number and the projection of the orbital angular momentum along the z-axis, respectively. The orbital angular momentum takes the same "naming" convention as the atomic case, with shells being labeled: $s(\ell = 0)$, $p(\ell = 1)$, $d(\ell = 2)$, $f(\ell = 3)$ and so on, while m_ℓ can take values from $-\ell$ to ℓ. Each orbital carries a degeneracy of $2(2\ell+1)$, with the former factor due to the two possible values of the spin quantum number, $s = 1/2$, being $m_s = \pm 1/2$, while the latter is due to the possible m_ℓ values available for a given ℓ.

The form of the Woods-Saxon potential allowed for the lifting of the ℓ degeneracies inherent in the harmonic oscillator potential, but it could still only replicate the first three magic numbers: 2, 8 and 20. It was only after the introduction of the spin-orbit coupling by Goeppert-Mayer [15, 16] and Haxel, Jensen and Suess [17] in 1949, that the shell model could reproduce the higher shell gaps that had been observed. This spin-orbit coupling term was inspired by the same term that plays a role in the atomic shell model. In the atomic shell model, this coupling arises from the magnetic moment of the electron interacting with the magnetic field generated by the motion of the same electron around the nucleus, but this contribution is generally very small. In the nuclear case, the strength of the spin-

orbit coupling would be much more significant, due to the strong force, which binds quarks together to form subatomic particles, and nucleon-nucleon interactions, which occur between the protons and the neutrons inside the nucleus.

The addition of the spin-orbit force would modify the nuclear potential, with the crucial factor in the form of $\vec{\ell} \cdot \vec{s}$. As in the atomic case, the orbitals are labeled with a total angular momentum $\vec{j}$, where

$$\vec{j} = \vec{\ell} + \vec{s}. \tag{1.4}$$

This s can only take the value of $\pm 1/2$ for the nucleons (they are fermions), the possible values of j are $\ell + 1/2$ and $\ell - 1/2$, save for the case where $\ell = 0$ in which only $j = 1/2$ is allowed.

The energy splitting can be obtained through the expectation values of the angular momenta:

$$\langle j^2 \rangle = j(j+1)\hbar^2, \tag{1.5}$$
$$\langle \ell^2 \rangle = \ell(\ell+1)\hbar^2, \tag{1.6}$$
$$\langle s^2 \rangle = s(s+1)\hbar^2. \tag{1.7}$$

Given that

$$\vec{j}^2 = (\vec{\ell} + \vec{s})^2 = \ell^2 + s^2 + 2(\vec{\ell} \cdot \vec{s}), \tag{1.8}$$

the expectation values in Eqs. 1.5, 1.6 and 1.7 can be used to calculate the strength of the coupling:

$$\vec{\ell} \cdot \vec{s} = \frac{1}{2}(j^2 - \ell^2 - s^2) \tag{1.9}$$
$$\langle \vec{\ell} \cdot \vec{s} \rangle = \frac{1}{2}[j(j+1) - \ell(\ell+1) - s(s+1)]\hbar^2. \tag{1.10}$$

Finally, the difference between the two levels, given that $s = 1/2$, can be written as:

$$\langle \vec{\ell} \cdot \vec{s} \rangle_{\ell+1/2} - \langle \vec{\ell} \cdot \vec{s} \rangle_{\ell-1/2} = \frac{1}{2}(2\ell+1)\hbar^2. \tag{1.11}$$

In this formalism, the m_ℓ and m_s values are no longer adequate quantum numbers, instead m_j is used, and the degeneracy is described by $(2j+1)$. By convention, the spin-orbit potential is chosen to be negative, meaning that the $j + 1/2$ component is pushed down. The effect of this spin-orbit term in shown in Figure 1.5; the level with the higher j becomes more attractive, with a flatter bottom, while the state with the lower j is slightly less attractive.

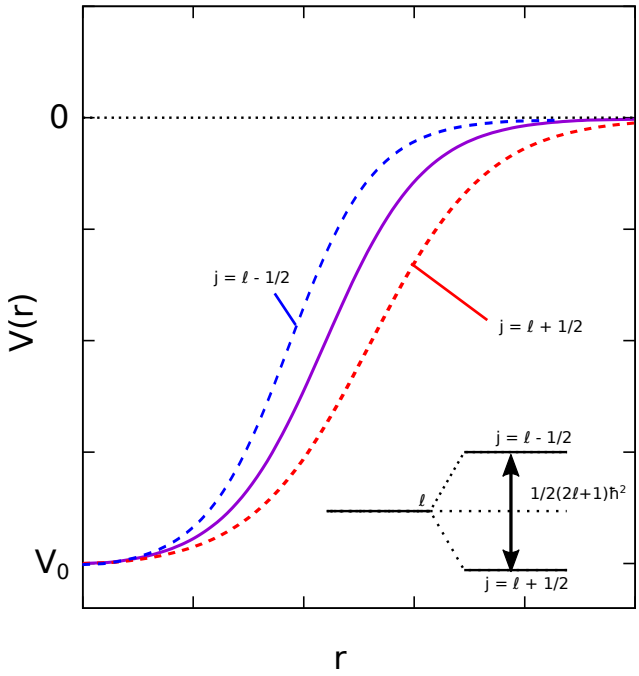

Figure 1.5: The effect of spin-orbit coupling on the nuclear potential. The state with the higher total angular momentum j is pushed down in energy, making that state slightly more bound than the lower j component.

Figure 1.6 shows the impact of this coupling on the nuclear potential, in the form of the reproduction of the higher lying magic numbers. The $1f_{7/2}$ orbital is lowered to the region between the second and third gaps, and with its capacity for 8 nucleons, gives rise to the magic number 28. Similarly, the $1g_{9/2}$ orbital is pushed to the lower shell, adding 10 nucleons to the previous 40, therefore establishing the magic number 50. The case is the same for 82 and 126 with the lowering of the $1h_{11/2}$ and $1i_{13/2}$ orbitals, respectively, thereby reproducing all the experimentally observed magic numbers, as well as predicting an additional one at 184, which has yet to be observed. These aforementioned orbitals are often referred to as intruder orbitals, since they have opposite parity to the others in the group.

1.2 Decay Theory

Nuclear decay provides an insight into the structure of matter. Spectroscopy sets out to observe the products of this decay in order to make inferences about the decaying species. The necessary underlying theory of β- and γ-decay will be outlined. The theory of α-decay will not be presented, as it is outside the scope of this project, but the author refers the reader to Refs. [8, 10, 18, 19] for further discussion of this decay mode.

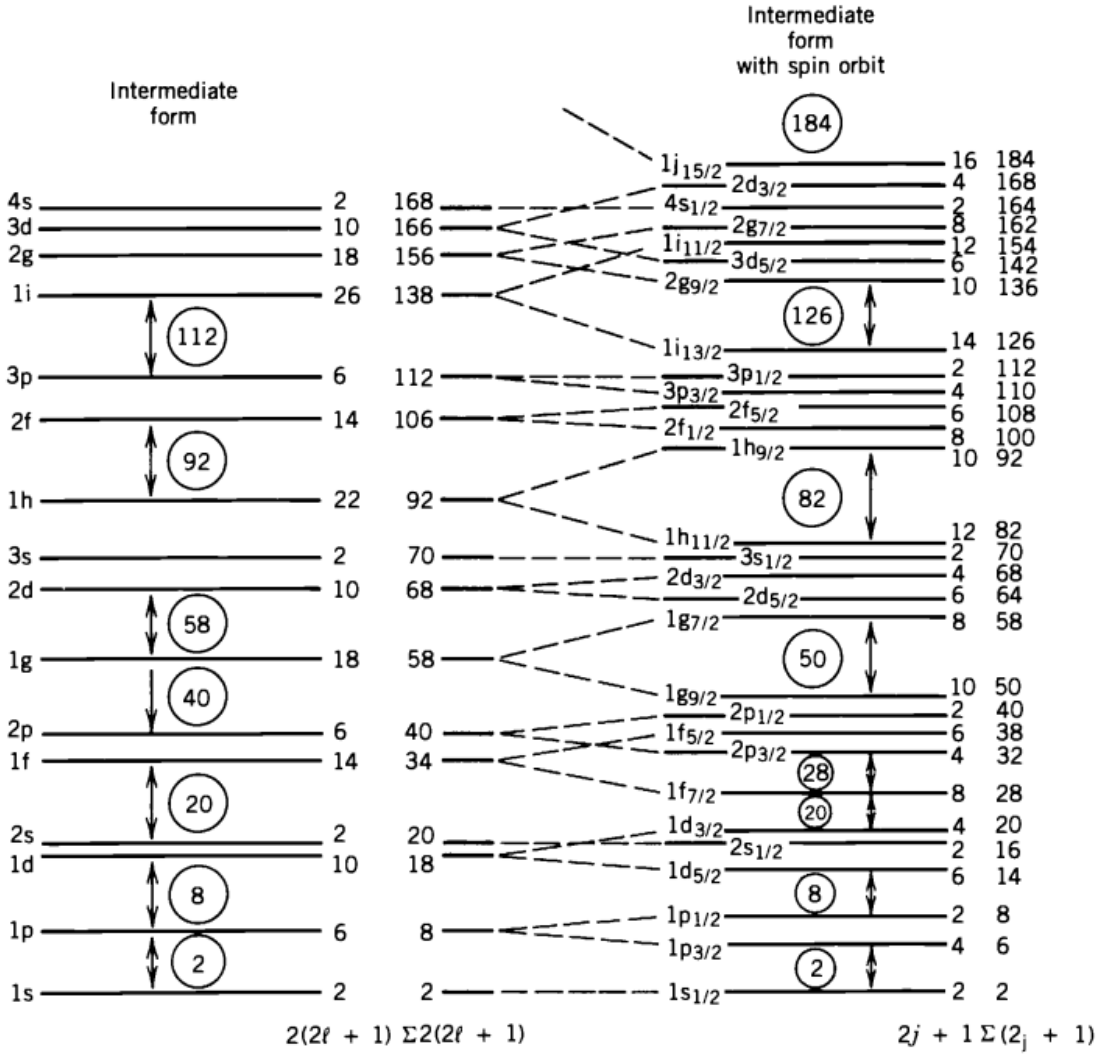

Figure 1.6: The effect of the spin-orbit interaction on the nuclear potential, leading to the experimentally observed magic numbers and nuclear orbitals. Reprinted from Ref. [10], with permission.

1.2.1 β-decay theory

Beta-decay is the most prevalent type of radioactive isotope decay in the nuclide chart. Radioactive isotopes will undergo β-decay towards the so-called valley of stability, shedding excess energy through conversion of a nucleon from one type to another (proton to neutron or neutron to proton) and the resulting emission of a β-particle and associated (anti)neutrino. The decay process is mediated by the W boson, and will change the flavour of one quark inside a nucleon, changing the nucleon type.

Mathematical Formalism

The β-decay process occurs in three different forms: β^-, β^+ and electron capture (EC). In β^- decay, a neutron will be transformed into a proton, described by Equation 1.12, where A is the mass number (total number of nucleons), N is the number of neutrons and Z is the number of protons. The β-particle is an electron, and the final piece is an electron antineutrino, $\bar{\nu}_e$. The Q-value refers to the amount of energy available for the process, shown in Equation 1.13 for β^- decay, where M_P is the atomic mass of the parent and M_D is the atomic mass of the daughter. During the decay process, the energy of the parent nucleus will be distributed to the decay products, which can leave the daughter nucleus in an excited state. This excited daughter can then undergo further decay, typically in the form of γ-decay. If Q is greater than 0, the nucleus will undergo decay spontaneously,

$$\begin{aligned} {}^{A}_{Z}X_N &\rightarrow {}^{A}_{Z+1}Y_{N-1} + \beta^- + \bar{\nu}_e & (1.12)\\ Q_{\beta^-} &= (M_P - M_D)c^2. & (1.13) \end{aligned}$$

The β^+ decay process will transform a proton into a neutron, emitting a positron and an electron neutrino, ν_e, as shown in Equation 1.14, with a Q-value shown in 1.15, where m_e is the rest mass of the electron,

$$\begin{aligned} {}^{A}_{Z}X_N &\rightarrow {}^{A}_{Z-1}Y_{N+1} + \beta^+ + \nu_e & (1.14)\\ Q_{\beta^+} &= (M_P - M_D)c^2 - 2m_e c^2. & (1.15) \end{aligned}$$

The electron capture (EC) process will occur when the nucleus captures an atomic electron, enters an atomic excited state and undergoes decay, Equation 1.16. In this instance, the process will create a vacancy in the atomic orbital, that will then be filled by the higher electrons cascading down. This will emit one or several X-rays, with the total energy emitted being equal to the binding energy of the captured electron. This binding energy is reflected in the Q-value equation, with the presence of the binding energy, B_n,

$$\begin{aligned} {}^{A}_{Z}X_N + e^- &\rightarrow {}^{A}_{Z-1}Y_{N+1} + \nu_e & (1.16)\\ Q_{EC} &= (M_P - M_D)c^2 - B_n. & (1.17) \end{aligned}$$

The electron capture process directly competes with the β^+ process.

Fermi's Golden rule, Equation 1.18, can be used to describe the transition rate between an initial state i in the parent nucleus and a final state f in the daughter nucleus;

$$\lambda = \frac{2\pi}{\hbar}|M_{fi}|^2 \frac{dn}{de}, \tag{1.18}$$

where M_{fi}, the nuclear matrix element, is given by:

$$M_{fi} = \int \psi_d^* H \psi_p d^3\vec{r}, \tag{1.19}$$

and $\frac{dn}{de}$ in Equation 1.18 is the density of final states. A higher density of final states implies the increased likelihood of a particular transition. The probability will also increase with the overlap between the initial and final state wavefunctions.

Consider a nucleus with its A nucleons, described by their coordinates $(\vec{r_1}, \vec{r_2}, \vec{r_3}, ...\vec{r_A})$. The β^- decay process can then be taken as a point interaction, whereby one of the neutrons, n is turned into a proton, p, at coordinate $\vec{r_n}$, emitting an electron and an antineutrino. The Hamiltonian for such an interaction would then take the form of:

$$H = g\delta(\vec{r}_n - \vec{r_p})\delta(\vec{r}_n - \vec{r}_{e^-})\delta(\vec{r}_n - \vec{r}_{\bar{\nu}_e})(\hat{O}(n \to p)) \tag{1.20}$$

with $\hat{O}(n \to p)$ representing the transformation of the nucleon, and g is the β^- decay strength constant [18]. Taking the neutron at $r_{n,1}$ as the one transformed into a proton, $r_{p,Z+1}$, the parent and daughter wavefunctions can be written as

$$\psi_P(\vec{r}_{p,1}, \vec{r}_{p,2}, ...\vec{r}_{p,Z}; \vec{r}_{n,1}, ..., \vec{r}_{n,N}), \tag{1.21}$$

$$\psi_D(\vec{r}_{p,1}, \vec{r}_{p,2}, ...\vec{r}_{p,Z}, \vec{r}_{p,Z+1}; \vec{r}_{n,2}, ..., \vec{r}_{n,N}), \tag{1.22}$$

respectively. The matrix element in Equation 1.19 can then be written as:

$$\begin{aligned} M_{fi} = \int \psi_D^*(\vec{r}_{p,1}, ..., \vec{r}_{p,Z+1}; \vec{r}_{n,2}, ..., \vec{r}_{n,N})\psi_{e^-}^*(\vec{r}_{e^-})\psi_{\bar{\nu}_e}^*(\vec{r}_{\bar{n}_e}) \cdot H \\ \times \psi_P(\vec{r}_{p,1}, ..., \vec{r}_{p,Z}; \vec{r}_{n,1}, ..., \vec{r}_{n,N}) d\vec{r}_{e^-} d\vec{r}_{\bar{\nu}_e} d\vec{r}_i, \end{aligned} \tag{1.23}$$

where ψ_{e^-} and $\psi_{\bar{\nu}_e}$ are the wavefunctions of the electron and antineutrino, respectively. The wavefunctions describing the parent and daughter nuclei, Equations 1.21 and 1.22 can also be further simplified, provided the coordinates of all other nucleons $(A-1)$ have not changed. Their simplified form is written as,

$$\psi_P(\vec{r}_i) = \prod_{i=1}^{Z} \varphi_P(\vec{r_{p,i}}) \cdot \prod_{j=1}^{N} \varphi_P(\vec{r}_{n,j}), \tag{1.24}$$

$$\psi_D(\vec{r}_i) = \prod_{i=1}^{Z+1} \varphi_D(\vec{r_{p,i}}) \cdot \prod_{j=2}^{N} \varphi_D(\vec{r}_{n,j}). \tag{1.25}$$

With these modifications, the matrix element becomes,

$$M_{fi} = g \int \varphi_D^*(\vec{r})_p \psi_{e^-}^*(\vec{r}) \psi_{\bar{\nu}_e}^*(\vec{r}) \hat{O}(n \to p) \varphi_P(\vec{r})_n d\vec{r}, \tag{1.26}$$

The electron and antineutrino wavefunctions can be described as plane waves and expanded via the Taylor expansion, considering $\vec{k} = \vec{p}/h$,

$$\psi_{e^-}(\vec{r}) \psi_{\bar{\nu}_e}(\vec{r}) = e^{i(\vec{k}_{e^-} + \vec{k}_{\bar{\nu}_e}) \cdot \vec{r}} = 1 + i(\vec{k}_e + \vec{k}_{\bar{\nu}_e})\vec{r} - \frac{1}{2}(\vec{k}_e + \vec{k}_{\bar{\nu}_e})\vec{r}^2 + ... \tag{1.27}$$

Since their wavelengths are much longer, compared to the nuclear radius R ($R/\lambda_{e^-} << 1$ and $R/\lambda_{\bar{\nu}_e} << 1$), all other components beyond the first two need not be considered. Then the matrix element can be further reduced to,

$$\begin{aligned} M_{fi} = g \Big[& \int \varphi_D^*(\vec{r})_p \hat{O}(n \to p) \varphi_P(\vec{r})_n d\vec{r} \\ & + i(\vec{k}_{e^-} + \vec{k}_{\bar{\nu}_e}) \int \varphi_D^*(\vec{r})_p \vec{r} \hat{O}(n \to p) \varphi_P(\vec{r})_n d\vec{r} \Big]. \end{aligned} \tag{1.28}$$

The first term in Equation 1.28 contains the information of the transformation of a neutron into a proton, with the integral evaluating the overlap of the two single particle wavefunctions. For this term to be nonzero, the parities of the parent and daughter wavefunctions must be the same. The second term requires the wavefunctions to have opposite parity, due to the $\vec{r}$ factor, otherwise it will vanish. These conditions thus give rise to the parity selection rule in the β-decay process. In this context, parity refers to the reflection of all coordinates through the origin: if $\psi(-\vec{r}) = \psi(\vec{r})$, the wavefunction is said to have even parity; if $\psi(-\vec{r}) = -\psi(\vec{r})$, the wavefunction is said to have odd parity.

Performing an expansion in spherical harmonics of the electron and antineutrino wavefunctions, $\psi_{e^-}(\vec{r})$ and $\psi_{\bar{\nu}_e}(\vec{r})$, respectively, uncovers the angular momentum selection rules:

$$e^{i(\vec{k}_{e^-} + \vec{k}_{\bar{\nu}_e}) \cdot \vec{r}} = \sum_{L,M} (4\pi) i^L j_L(kr) Y_L^M(\widehat{\vec{k}_{e^-} + \vec{k}_{\bar{\nu}_e}}) \cdot Y_L^{M^*}(\hat{r}), \tag{1.29}$$

where $k \equiv |\vec{k}_{e^-} + \vec{k_{\bar{\nu}_e}}|$ and $\hat{r} \equiv (\theta_r, \phi_r)$ contains the angular variables. Using these expansions, the matrix element in Equation 1.28 can be written as,

$$M_{fi} \propto g \int \varphi_D^*(\vec{r})_p \hat{O}(n \to p) Y_L^{M^*}(\vec{r}) \varphi_P(\vec{r})_n j_L(kr) d\vec{r} \tag{1.30}$$

The wavefunctions in Equation 1.30 can be further separated into radial and angular components, with the spin component being ignored for the time being. The equations then take the form,

$$\varphi_P(\vec{r}) = R_P(r) Y_{L_P}^{M_P}(\hat{r}) \qquad \varphi_D(\vec{r}) = R_D(r) Y_{L_D}^{M_D}(\hat{r}). \tag{1.31}$$

Using this formalism, the matrix element can subsequently be split into radial and spherical parts,

$$\int Y_{L_D^*}^{M_D}(\hat{r}) Y_L^{M^*}(\hat{r}) Y_{L_P}^{M_P}(\hat{r}) d\Omega \cdot \int R_D(r) j_L(kr) R_P(r) r^2 dr. \tag{1.32}$$

Conservation of angular momentum implies that $\vec{L}_P = \vec{L}_D + \vec{L}$ and thus places constraints on the angular momentum $\vec{L}$ of the outgoing electron and antineutrino: this is the angular momentum selection rule.

The formalism here presented follows that of Ref. [18]; further discussion and formalism are found in Refs. [13, 20].

Since parity is dependent on the angular momentum, given as $\pi = (-1)^L$, the parity selection rule must be of the form [18],

$$\pi_P = (-1)^L \pi_D, \tag{1.33}$$

where π_P is the parity of the parent wavefunction, π_D is the parity of the daughter wavefunction.

In the framework of β-decay, allowed transitions can only have a change of zero or one unit of angular momentum, and also show no change in parity. Forbidden transitions, those less likely to occur, have increasing maximal change in angular momentum and alternating change in parity. Table 1.1 shows the changes in angular momentum units and parity for each degree of forbiddenness.

Like the fermionic nucleons, the electron and antineutrino have intrinsic spin that cannot be ignored, leading to a further classification of decays. Two different situations arise: the case where the spins of the electron and the antrineutrino are anti-aligned, the sum of the spins will add to zero, such that their intrinsic spins do not contribute to the total angular momentum of the state, this is called a Fermi transition, often referred to as "superallowed". The opposite case, referred to as a Gamow-Teller transition, will have the spins aligned, adding one unit of angular momentum — each lepton partner contributing spin of 1/2.

The half-life of a particular state is dependent on the decay probability of that state, and is indicative of its forbiddenness. This relationship is described by the comparative half-life, given as,

$$ft = ln(2) \frac{2\pi^3 \hbar^7}{g^2 |M_{fi}|^2 m_e^5 c^4}, \tag{1.34}$$

where g is the strength parameter, a value used to compare β-decay probabilities, and m_e is the rest mass of the electron. The factor f is known as the Fermi integral, representing a phase space factor, and encapsulates important information about the decay, including the Z of the daughter, the Q_β of the decay and the maximum momentum of the electron [13, 22].

Table 1.1: Selection rules governing β-decay, describing the allowed total angular momentum change, ΔJ, the allowed change in parity, $\Delta\pi$ and the $\log ft$ value range. Table adapted from Refs. [10, 21].

Forbiddenness	ΔJ	$\Delta\pi$	$\log ft$
Superallowed	$0^+ \rightarrow 0^+$	No	2.9-3.7
Allowed	0, 1	No	4.4-6.0
1*st* Forbidden	0, 1, 2	Yes	6-10
2*nd* Forbidden	1, 2, 3	No	10-13
3*rd* Forbidden	2, 3, 4	Yes	>15
nth Forbidden	$\pm$1, $\pm$(n+1)	(-1)^n(1 = yes; -1 = no)	

Though the calculation of these values is incredibly complex, they have been tabulated for numerous β-decays and can be found in Refs. [23, 24], among others.

Given the massive range of half-lives of β-decays in the chart of nuclides, this comparative half-life is reported as $\log ft$, rather than ft. Ranges of $\log ft$ values for each of the degrees of forbiddenness are shown alongside the associated change in angular momentum and parity in Table 1.1.

1.2.2 γ-decay theory

Gamma-decay is present in nearly all regions of the chart and involves the de-excitation of a nucleus by emission of a high-energy photon. The excited nucleus sheds excess energy through this process, to come to a more stable state by reordering of its constituent nucleons; as a result, in contrast to β-decay, γ-decay involves the same nucleus, rather than the transmutation into another element.

Consider a nucleus, X, and one of its excited states, denoted by X^*. The energy balance of the γ-ray emission process will take the form,

$$E_{X^*} = E_X + E_\gamma + T_{recoil}, \tag{1.35}$$

where E_{X^*} represents the energy of the initial excited state, E_X the energy of the final state, E_γ the energy of the emitted γ-ray and T_{recoil} the kinetic energy of the recoiling nucleus. Conservation of momentum implies that,

$$p_{recoil} + p_\gamma = 0. \tag{1.36}$$

Equation 1.35 can then be rearranged to describe the difference between the initial and final states:

$$\Delta E = E_{X^*} - E_X = E_\gamma + T_{recoil}, \tag{1.37}$$

with $T_{recoil} = \frac{E_\gamma^2}{2Mc^2}$ (M is the mass of the nucleus) [10]. This recoil energy is, on average, very small since the energies of the emitted γ-rays, E_γ, are much smaller than the rest masses of the nuclei, between 50 keV and 10 MeV to compared to 10^3 MeV, respectively. This implies that,

$$\Delta E = E_\gamma. \tag{1.38}$$

Conservation of angular momentum constrains the transitions that can occur between the initial and final states, each of which has its own spin J and parity π (J^π). Due to angular momentum coupling, there are many possible values that can be imparted onto the photon, also known as its multipolarity, L. Given the spin of the initial states, I_i, and the final state, I_f, the multipolarity of the photon is given by,

$$|I_i - I_f| \leq L \leq I_i + I_f. \tag{1.39}$$

The multipolarity can take on any value within this range, save for $L = 0$. This is due to the fact that the photon has an intrinsic spin of 1 angular momentum unit, meaning that the decay must result in a change of at least $L = 1$, precluding a transition of the type $0^+ \rightarrow 0^+$ via a single photon. Two photon decay between 0^+ states, however, is possible [25].

The parity in γ-decay arises from the apparent rearrangement of the nucleons in a system that undergoes this decay. Since the initial and final states in the nucleus are said to have specific distributions of mass and charge, the change of either of these through γ-decay and subsequent reorganization of nucleons will determine the parity of the outgoing photon. If a proton changes from one orbital to another, the motion will induce an electric field, while a shift in the distribution of current will induce a magnetic field. The parity of the photon will in turn depend on the angular momentum difference between the initial and final states and the type of the shift or transition [22]. The parity of the photons can be calculated by [26]:

$$\pi(EL) = (-1)^L \tag{1.40}$$
$$\pi(ML) = (-1)^{L+1} \tag{1.41}$$

where L is the multipole order, E denotes a transition with electric character and M denotes transition with magnetic character. Table 1.2 summarizes the γ-decay selection rules.

As in the case of β-decay, the transition rate, or the transition probability $\lambda(\sigma L)$ can be calculated for each type of radiation; the transition probability will be higher if the overlap between the initial and final state wavefunctions is large. However, given that the more nucleons present in the system, the more intractable the nuclear wavefunction becomes, it

Table 1.2: Selection rules for γ-decay along with transition multipolarity. Table adapted from [26].

Multipolarity	Name	L	$\Delta\pi$
E1	Electric Dipole	1	Yes
M1	Magnetic Dipole	1	No
E2	Electric Quadrupole	2	No
M2	Magnetic Quadrupole	2	Yes
E3	Electric Octupole	3	Yes
M3	Magnetic Octupole	3	No
E4	Electric Hexapole	4	No
M4	Magnetic Hexapole	4	Yes

is prohibitively difficult to calculate the transition probabilities. Weisskopf [27, 28] proposed the use of single particle estimates, where the transition is due to a single proton, going from a higher excited state to a lower one, and though the estimates may vary several order of magnitudes from the actual values, they still prove useful when comparing different transition rates.

The estimates assume that the radial components of the separable wavefunctions of the initial and final states are constant within the radius of the nucleus, R, and vanish outside this region [27]. Given a γ-ray E_γ, with angular momentum L, transition probabilities for electric-type transitions are given by,

$$\lambda(EL) \approx \frac{8\alpha\pi(L+1)}{L[(2L+1)!!]^2}\left(\frac{E_\gamma}{\hbar c}\right)^{2L+1}\left(\frac{3}{L+3}\right)^2 cR^{2L}, \tag{1.42}$$

while for magnetic-type transitions they are given by,

$$\lambda(ML) \approx \frac{8\alpha\pi(L+1)}{L[(2L+1)!!]^2}\left(\mu_p - \frac{1}{L+1}\right)^2\left(\frac{\hbar}{m_p c}\right)^2\left(\frac{E_\gamma}{\hbar c}\right)^{2L+1}\left(\frac{3}{L+2}\right)^2 cR^{2L-2}, \tag{1.43}$$

where $\alpha = \frac{e^2}{4\pi\epsilon_0\hbar c} \approx \frac{1}{137}$ is the fine structure constant, m_p and μ_p are the mass and the magnetic moment of the proton, respectively, and $R = R_0 A^{1/3}$ is the nuclear radius ($R_0 \approx$ 1.2 fm) [10]. Evaluating Equation 1.42 for multipole L and comparing the transition probability to the next higher multipole, $L+1$, yields information about the dominant type of radiation and the preferred energy of that radiation. Consider the transition probability for the electric dipole, $L = 1$, and the electric quadrupole, $L = 2$, the ratio between these probabilities, given Equation 1.42 is then,

$$\frac{\lambda(E2)}{\lambda(E1)} \approx 10^{-7} E_\gamma^2, \tag{1.44}$$

showing that higher energy γ-rays and lower multipolarities are favoured. Additionally the transition probabilities depend upon the size of the nucleus, with the inclusion of the nuclear radius term R. Comparing the same multipole electric and magnetic transition probabilities,

$$\frac{\lambda(E1)}{\lambda(M1)} \approx 1.8A^{2/3}, \tag{1.45}$$

indicating that electric transitions are preferred over magnetic transitions of the same multipolarity.

These estimates, when compared to observed values, can also provide information about the underlying nuclear structure. An observed value that is higher than the Weisskopf estimate is indicative that more than one nucleon is responsible for the transitions; an observed value lower than the estimate hints at a minimal overlap between the initial and final state wavefunctions, which may hinder the transition [10, 21]. The Weisskopf estimates for the first four multipoles are found in Table 1.3.

Table 1.3: The Weisskopf estimates for (σL) transition rates, for a given γ-ray of energy E_γ. E denotes a transition with an electric character and M a magnetic character transition. Table adapted from Ref. [22].

L	$\lambda(EL)$ (s^{-1})	$\lambda(ML)$ (s^{-1})
1	$1.03 \times 10^{14} A^{2/3} E_\gamma^3$	$3.15 \times 10^{13} E_\gamma^3$
2	$7.28 \times 10^{7} A^{4/3} E_\gamma^5$	$2.24 \times 10^{7} A^{4/3} E_\gamma^5$
3	$3.39 \times 10^{1} A^{2} E_\gamma^7$	$1.04 \times 10^{1} A^{4/3} E_\gamma^7$
4	$1.07 \times 10^{-5} A^{8/3} E_\gamma^9$	$3.27 \times 10^{-6} A^{2} E_\gamma^9$

There is no guarantee that a transition will have a purely electric or magnetic character, mixtures can sometimes occur and, due to the nature of the γ-decay selection rules, an $E(L+1)$ transition is likely to mix with an ML transition [27]. The mixing ratio is used to compare the electric transition matrix element and the magnetic transition matrix element,

$$\delta = \frac{\langle \psi_f | \, E(L+1) \, | \psi_i \rangle}{\langle \psi_f | \, M(L) \, | \psi_i \rangle}. \tag{1.46}$$

Most often, it is the electric quadrupole transition that is in competition with the magnetic dipole transition, but this does not preclude the possible mixing of the electric dipole with the magnetic quadrupole. However, based on the Weisskopf estimates in Table 1.3, the ratio of transition rates between $E1$ and $M2$ transitions is on the order of

$$\frac{\lambda(E1)}{\lambda(M2)} \sim 10^{-7} E_\gamma^2, \tag{1.47}$$

making this mixing very unlikely.

Internal Conversion

There is another process that nuclei can undergo in order to shed excess excitation energy. In this process, the nucleus transfers the energy to a bound electron, which, depending on the amount of energy exchanged, may cause the electron to become unbound and be ejected from the nucleus. The energetics depend upon the electron binding energy, B_n,

$$T_{e^-} = (E_i - E_f) - B_n, \tag{1.48}$$

where T_{e^-} is the kinetic energy of the electron in question, and $E_i - E_f$ is the excitation of the nucleus, with no real photons taking part in the process. The electrons in the inner K shell have the largest probability of being ejected, as their wavefunction overlaps with that of the nucleus.

The transition matrix element of this process, when a K shell electron in the $1s$ atomic orbital is converted, can be written as [18],

$$M_{if} \propto \sum_i \int e^{-i\vec{k}_e \cdot \vec{r}_e} \psi_f^*(\vec{r}_i) \frac{e^2}{4\pi\epsilon_0 |\vec{r}_e - \vec{r}_i|} b_0^{-3/2} e^{\frac{-r_e}{b_0}} \psi_i(\vec{r}_i) d\vec{r}_i d\vec{r}_e. \tag{1.49}$$

In Equation 1.49, the sum is done over all protons in the nucleus, while $\vec{k}_{e^-}$ describes the wavevector of the electron in question. The $\psi_i(\vec{r}_i)$ and $\psi_f(\vec{r}_i)$ wavefunctions describe the initial and final nuclear wavefunctions, respectively; b_0 is the Bohr radius for the pertinent electron.

In the case of the K shell electron,

$$b_0 = \hbar^2 4\pi\epsilon_0 / me^2, \tag{1.50}$$

if $Z = 1$. The transition probability will drop as the electron distance from the nucleus increases. Expanding the relevant $|\vec{r}_e - \vec{r}_i|$ factor in Equation 1.49 for the case of $r_e > r_i$,

$$\sum_i \frac{1}{|\vec{r}_e - \vec{r}_i|} = \frac{1}{r_e} \sum_i \sum_l (\frac{r_i}{r_e})^l P_l(\cos\theta). \tag{1.51}$$

with the product $\vec{r}_i \cdot \vec{r}_e = r_i r_e \cos\theta$ and $P_l(\cos\theta)$ being the Legendre polynomials. With this expansion, Equation 1.49 can be separated into constituent nuclear and electron components, when expanded using the expression,

$$P_l(\cos\theta) = \sum_m \frac{4\pi}{2l+1} Y_l^{m*}(\hat{r}_e) Y_l^m(\hat{r}_i). \tag{1.52}$$

Using Equation 1.52, the matrix element can be written as

$$M_{if} \propto \sum_{l,m} \frac{e^2 k_e^{l-2}}{b_0^{3/2}} \frac{4\pi}{2l+1} \int e^{-i\vec{k}_e \cdot \vec{r}_e} \left(\frac{1}{k_e r_e}\right)^{l+1} Y_e^{m*}(\hat{r}_e) \times e^{-\frac{r_e}{b_0}} d(k\vec{r}_e) \cdot M_{fi}^N(l,m) \qquad (1.53)$$

where M_{if}^N refers to the nuclear component [18]. The shorthand of this nuclear matrix element is given as,

$$M_{if}^N(l,m) \equiv \sum_i \int \psi_f^*(\vec{r}_i) r_i^l Y_l^m(\hat{r}_i) \psi_i(\vec{r}_i) d\vec{r}_i. \qquad (1.54)$$

It should be noted that, though photon emission requires a minimal change of one unit of angular momentum that is carried away by the photon, electron conversion, as can be seen from Equation 1.54, is not constrained by this requirement. This implies then that electron conversion can mediate processes such as $0^+ \rightarrow 0^+$ transitions.

The electron conversion coefficient [18, 21],

$$\alpha_K = \frac{\lambda_{if}(e)}{\lambda_{if}(\gamma)}, \qquad (1.55)$$

compares the transition probabilities in the case where both the internal conversion process and the photon emission process are in competition. The processes where these two compete will be lowest order, dipole type processes, typically from a $1s$ bound electron to an outgoing electron. The formalism here presented for the conversion electron process is that found in Ref. [18]; additional comments on this process can be found in Refs. [19, 22, 27].

Angular Correlations

Gamma-ray cascades can provide information about the spins of states, through the use of angular correlation measurements, which require a large number of detectors are well-characterized angles and a large number of statistics. This experimental technique was employed for the work herein contained, though no new information was obtained for ^{129}Sn due to low statistics. The angular correlations in ^{80}Ge are still under analysis and will be published in a forthcoming article [29]. The author refers the reader to Appendix C for a description of the angular correlation methodology.

Interactions with Matter

There are three major ways in which a γ-ray photon will interact with matter, in the energy range between 80 keV and 10 MeV; photoelectric absorption, Compton scattering and pair production.

Photoelectric Absorption

Photoelectric absorption occurs when a photon interacts with an atom, and completely imparts that energy to the atom [30]. Depending on its energy, the γ-ray may induce the ejection of a photoelectron from one of the bound atomic shells, as shown in Figure 1.7. In this process, the energy of the photoelectron is described as,

$$E_{e^-} = h\nu - E_b, \tag{1.56}$$

where E_b is the binding energy of the ejected electron. Since the photoelectron is ejected in the process, the atom with which the γ-ray interacted will be left in an ionized state, a vacancy in its bound shells. The vacancy is then filled, either through other bound electrons cascading down to fill an inner vacancy or through capture of an electron from the surrounding environment. In the case where electron rearrangement occurs, the process of filling inner shells may release further energy, enough that it may kick out another, less bound electrons. An electron ejected through this mechanism is called an Auger electron.

This process may then create an X-ray photon of characteristic energy. These X-rays may be reabsorbed close to where they were generated or they may escape from the detection medium, causing a signature or otherwise altering the final results measured.

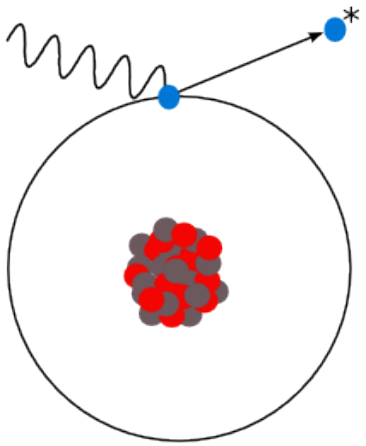

Figure 1.7: Photoelectric absorption. In this process the γ-ray interacts with a bound electron of a nucleus, possibly ejecting it, depending on the energy of the incoming γ-ray

This process is the primary mode of interaction of lower energy γ-rays, and is dependent on the atomic number of the absorber. Higher Z materials will undergo a higher incidence of this effect.

Compton Scattering

This inelastic process occurs between an incident γ-ray and an electron in the material

absorbing the γ-ray. This process has the impinging γ-ray photon striking an electron, and being deflected at an angle θ from its original path, while imparting some of its incoming energy to the electron. The resulting electron is referred to as a recoil electron [31].

Due to the large possibility of scattering angles, the γ-ray can impart anywhere from a small amount to nearly all of its energy onto the electron, resulting in a wide range of energies of the outgoing γ-ray, which in turn produces a continuum.

The interaction can be described by,

$$h\nu' = \frac{h\nu}{1 + \frac{h\nu}{m_0c^2}(1 - \cos\theta)}, \tag{1.57}$$

where m_0c^2 is the rest-mass of the electron, 511 keV. As can be seen by the form of the equation, small scattering angles result in little energy being transferred, while larger angles will result in larger fractions of the γ-ray energy being imparted to the electron. The extreme of this interaction would be $\theta = \pi$. Figure 1.8 shows a schematic of Compton scattering. This process is the most common interaction of matter with γ-rays emitted from radiation sources [32].

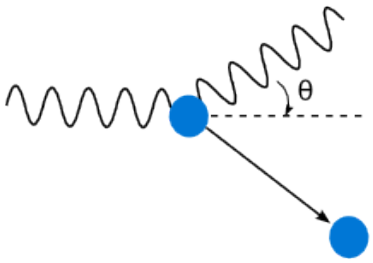

Figure 1.8: Compton scattering. In this process an incident γ-ray will impart some of its enegry onto an electron, and be scattered at a angle θ. The large range of possible angles means that a range of enegies can be imparted to the electron.

Pair production

In the extreme case where a high energy γ-ray photon is found in the vicinity of a nucleus, pair production can take place.

In this process, an incoming photon with at least an energy of twice the rest-mass of an electron, 1.02 MeV, will interact with the Coulomb field of a nearby nucleus and be converted into an electron-positron pair [20]. Any remaining energy the photon carried, apart from that required to produce the pair, will be imparted to the electron and positron as kinetic energy as they leave the interaction point.

Upon leaving, the positron is likely to annihilate with an electron in the surrounding environment, an interaction which will emit two annihilation photons, each with 511 keV.

This particular feature of the interaction has implications in the detection of this γ-ray interaction with matter. A pictorial description of the pair production process is shown in Figure 1.9.

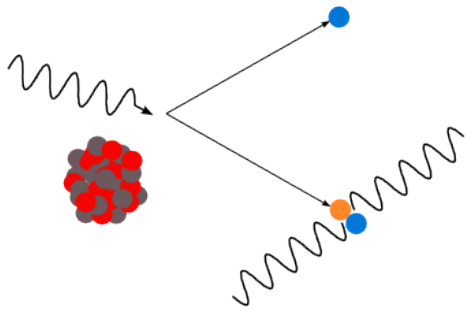

Figure 1.9: Pair production.

Figure 1.10 shows the dominant interaction, given an absorber with Z, as a function of γ-ray energy.

The prevalence of each interaction will depend upon the Z of the absorber and the energy of γ-ray, as shown in Figure 1.10. The photoelectric effect will dominate in the region up to 100 keV; Compton scattering will take over between 100 keV and 5 MeV, while pair production, which is possible starting at 1.022 MeV (twice the electron rest mass) will dominate in the region beyond 10 MeV.

Detection signatures

Each of the γ-ray interactions with matter will produce different key signatures in a resulting spectrum. These characteristic peaks, are found in Figure 1.11.

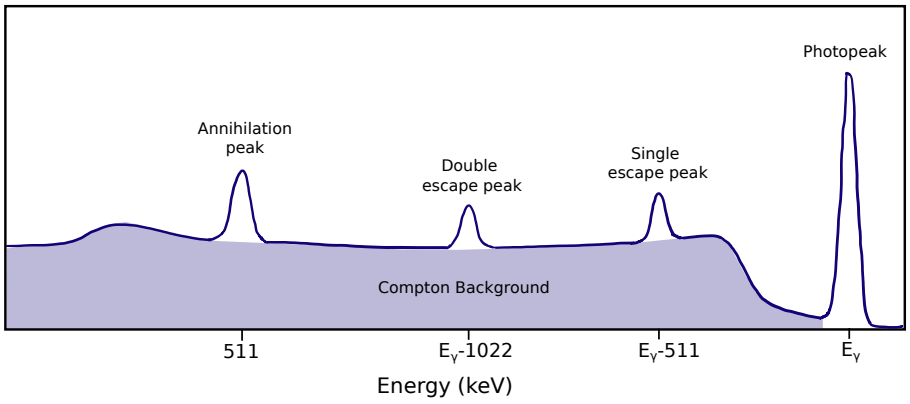

Figure 1.11: Example γ-ray spectrum, showing the different signatures of the interaction of γ-rays with matter. Adapted from Ref. [34].

The photopeak contains the relevant information about the energy and intensity of the γ-ray. The Compton continuum forms the background, the annihilation peak appears at 511

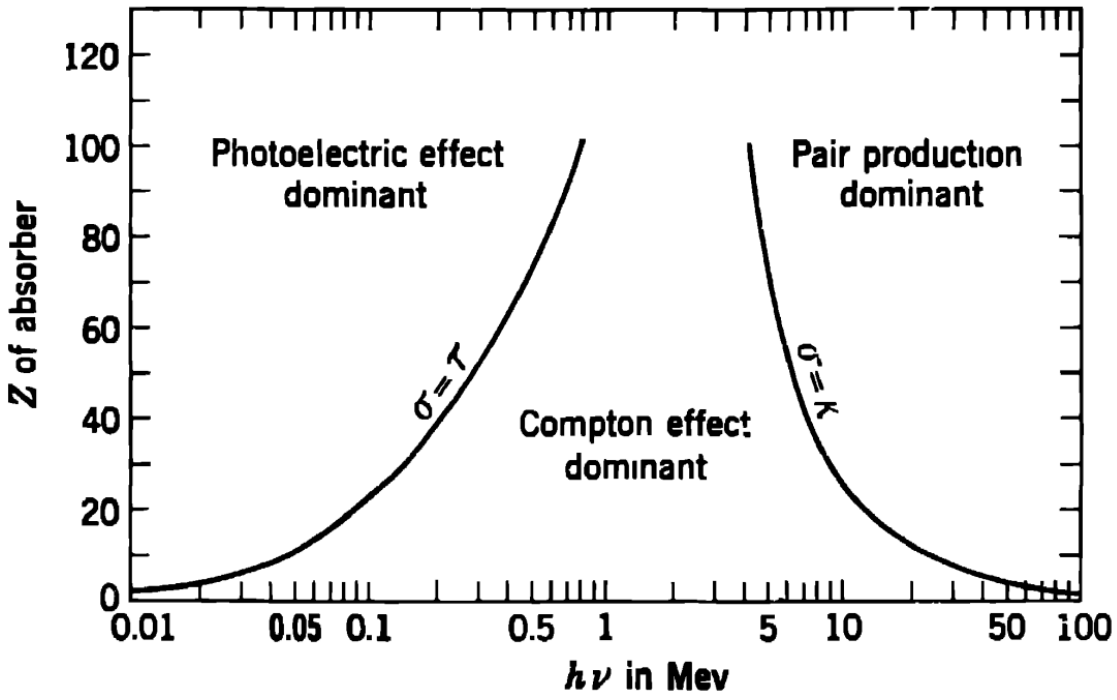

Figure 1.10: The dominating γ-ray interaction with matter, given the Z of the absorber as a function of energy. Reprinted with permission from Ref. [33].

keV — the rest mass of the electron — while the single- and double-escape peaks will appear at the γ-ray energy minus one and two times the rest mass of the electron, respectively.

Each recorded γ-ray will have their information appended to form the total γ-ray spectrum, containing a plethora of peaks, from which the real transitions must be distinguished from artifacts such as the single- and double-escape peaks, annihilation peaks and the Compton continuum.

Chapter 2

β-decay spectrometry

2.1 Production of Isotopes at TRIUMF-ISAC

The isotopes studied at the Isotope Separator and ACcelerator (ISAC) facility of TRIUMF [35], shown in Figure 2.1, are produced via the Isotope Separation On-Line (ISOL) technique. The ISOL technique involves the impingement of a high-energy light particle onto a heavy target in order to produce isotopes of interest [36].

TRIUMF utilizes its main cyclotron to provide a beam of accelerated protons, typically ∼9.8 μA at 480 MeV, and a uranium carbide target, which is required to produce neutron-rich species. Proton bombardment of this target induces fission, fragmentation and spallation reactions that can theoretically produce every isotope up to the production target mass.

The isotopes produced must then be extracted from the target via an ionization mechanism. Several different ionization methods are available at TRIUMF [37], and the appropriate method must be chosen to maximize production of the desired isotope, while suppressing isobaric contaminants. In order to suppress these unwanted and potentially harmful species, the Ion-Guide Laser Ion Source (IGLIS), shown in Figure 2.2, is used in order to greatly suppress isobaric contaminants [38], which are typically isotopes of the alkali metals in the mass region of the isotopes of interest. Without the use of IGLIS, the alkali and alkali earth metals would readily exit the target as a very intense beam, making detection of the species of interest nearly impossible.

For the purpose of this work the species of concern would be cesium and barium isobars for the indium study, and the rubidium and strontium isobars for the gallium study.

Once the species of interest are ionized and extracted from the target, they pass through a high-resolution mass separator, with a resolution of $M/\delta M$ ∼2000 [39], to generate an nearly isotopically pure beam. After separation, the radioactive isotope beam (RIB) is sent to the ISAC experimental hall where it may be used as a driver beam for other experiments, or studied for its fundamental nuclear structure properties at experimental stations such as the GRIFFIN array.

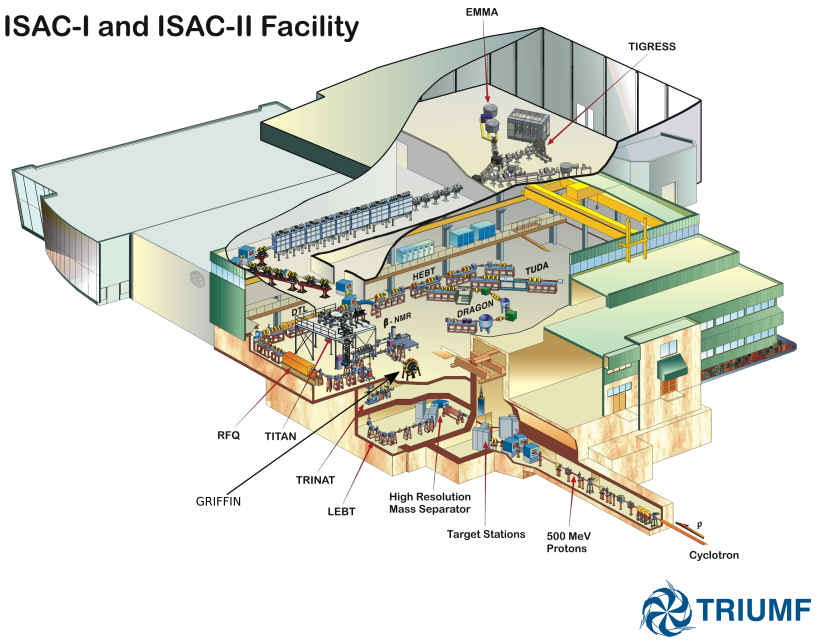

Figure 2.1: Floor plan of ISAC, showing both the experimetal halls. The lower energy experiments, housed in ISAC-I, include TITAN, TRINAT and GRIFFIN, while the accelerated beam experiments are housed in ISAC-II and include EMMA and TIGRESS. Adapted from Ref. [35].

2.2 GRIFFIN

The Gamma-Ray Infrastructure For Fundamental Investigations of Nuclei (GRIFFIN) is a state-of-the-art, high resolution decay station designed for the study of species through γ-ray spectrometry [40, 41, 42]. Comprised of up to 16 high-purity germanium (HPGe) detectors, and accommodating a range of different ancillary detectors, the GRIFFIN spectrometer is used to study rare and exotic species.

GRIFFIN is arranged in a rhombicuboctahedral geometry with 18 square faces and 8 triangular faces, such that it provides 4π coverage of the chamber. Two of the square faces are used for beam transport to the station and for the cycling Mylar tape used to remove unwanted activity out of the array; the remaining 16 square faces are used to mount the 16 HPGe detectors, while the eight triangular faces are used for the $LaBr_3$ fast timing array that can be coupled to study lifetimes of excited states. The GRIFFIN array is shown in Figure 2.3.

2.2.1 HPGe detectors

The HPGe clover detectors that make up the core of the GRIFFIN spectrometer are each made up of four individual highly pure n-type germanium crystals which are used to detect the γ-rays emitted from de-exciting nuclei [43]. The quoted average resolution of the GRIFFIN HPGe detectors is 1.89(6) keV at 1332 keV [43], while the absolute efficiency in clover

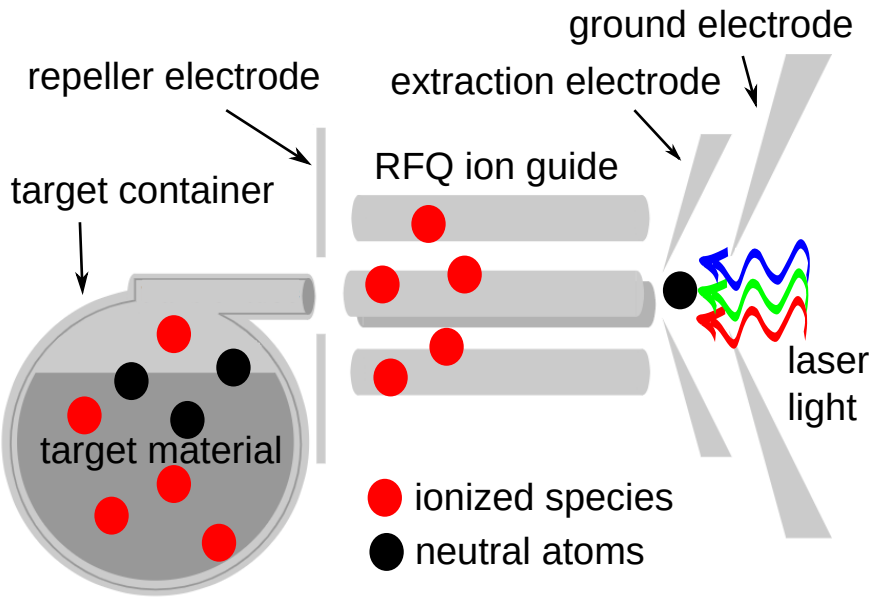

Figure 2.2: Schematic of IGLIS, showing its mechanism of action. The radioactive isotopes are produced in the target in both ionized and neutral states, and move to the repeller electrode. The Radio Frequency Quadrupole (RFQ) ion guide traps the ionized species, while the neutral species are allowed to drift towards the extraction electrode, at which point they are laser ionized using specific ionization schemes for the elements of interest. Adapted from Ref. [38].

addback mode is given as 14.20(16)% [42]. A depiction of a GRIFFIN Clover detector is shown in Figure 2.4.

These germanium crystals are semiconductor detectors, specifically chosen for their capabilities in detecting γ-rays. Since the early 1960s, these types of detectors systems have been used for this purpose, as they provided advantages over the previous scintillation detectors, considered at the time the industry standard.

One of the many advantages of semiconductor detectors is the increase of information carriers, which in turn improved the energy resolution of the detector, making the observation of weaker γ-rays possible, when compared to the scintillation detectors. In these detectors, the electron-hole pairs generated by an incident particle serve as the information carriers, and their movements in an applied electric field are what constitute the electrical signal from the detector [32].

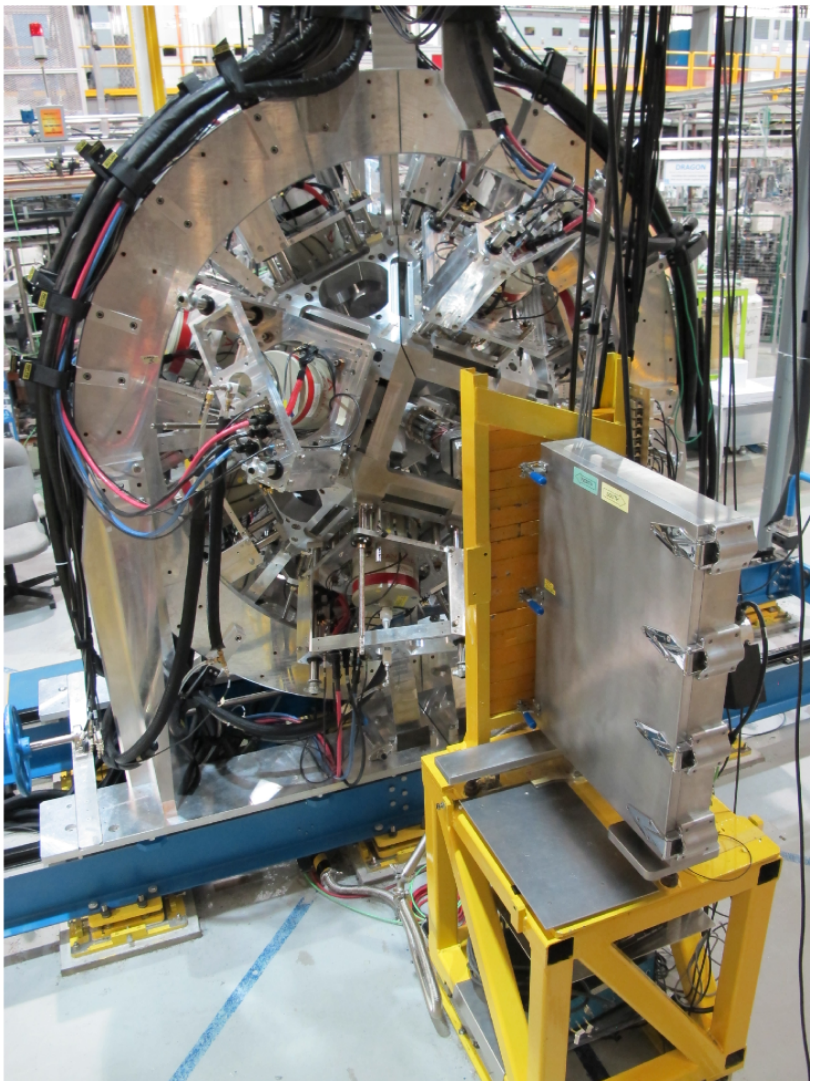

Figure 2.3: The GRIFFIN array, fully populated with the 16 HPGe detectors. The lead box (foreground) serves to house the used Mylar type that is cycled through the array in order to provide a clean implantation spot.

Semiconductor detectors posses unique structures in their valence and conductions bands, particularly when it comes to the bandgap between the two, and it is this small gap that allows for the detection of exceedingly weak γ-ray transitions [32].

GRIFFIN is currently outfitted with a set of Compton suppression shields, which allow for vetoing of Compton scattering events, reducing this background, and improving the peak-to-total ratio. An image of fully-suppressed GRIFFIN is shown in Figure 2.5. The shields are made of four front shields, a single side catcher and two back catchers, with a set of these seven shields being fit to each of the HPGe detectors populated in the GRIFFIN array. The shields themselves are made of bismuth germanate (BGO), a scintillator with high Z-density and high detector efficiency, but with poor energy resolution.

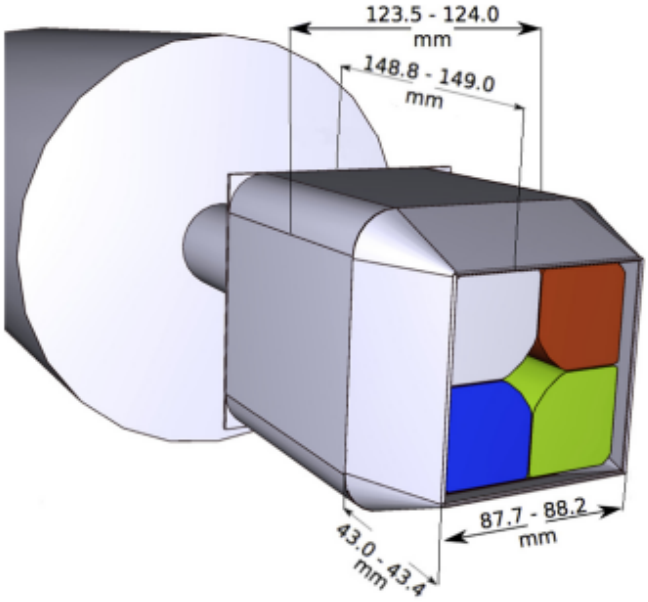

Figure 2.4: A technical drawing of a GRIFFIN clover. The colours represent the four different Ge crystals that comprise one clover detector. Reprinted from Ref. [43], with permission from Elsevier.

GRIFFIN can run in two different modes: maximum efficiency and peak-to-total mode. In maximum efficiency mode, the front BGO shields are retracted, so as to push the HPGe detectors as close to the vacuum chamber as possible at a nominal distance of 11 cm from the centre of the array. In peak-to-total mode, the front shields are in position around each of the detectors, with a distance of 14.5 cm to the centre of the array [42]. The BGO shields installed at GRIFFIN were tested and characterized for detection properties such as efficiency during the course of this work.

The high resolution data of GRIFFIN can be sorted into two different types: crystal singles data and clover addback data. The crystal singles refers to the data obtained by all individual germanium crystals in the 16 HPGe clovers. Clover addback refers to the collection of data where some events have been "added back" to retrieve partially lost events. This is done due to the fact that when a γ-ray interacts with a germanium crystal, there is a chance that it will be Compton scattered out of the crystal, depositing only a portion of its energy, or none at all, causing its information to be lost. If the γ-ray is scattered out of one crystal, into a neighbouring crystal in the same clover, it can deposit a portion of its energy in the first and the rest into the second. This event can be reconstructed, by "adding back" the partial energies and thus recovering the true event energy. This improves the overall efficiency of the detector array, where the addback efficiency is higher than that of crystal singles mode.

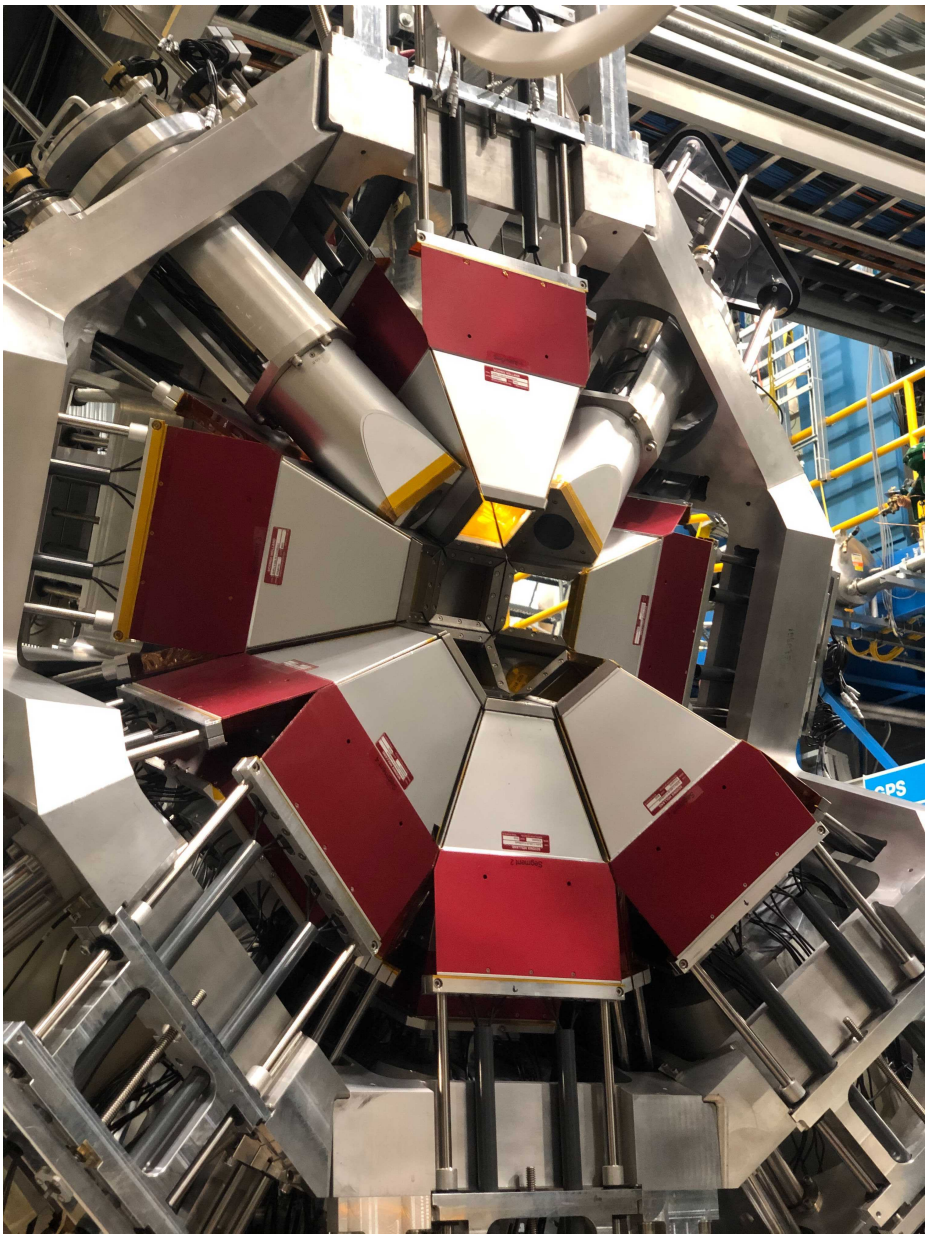

Figure 2.5: An image showing the Compton Suppression BGO shields installed onto the GRIFFIN clover detectors [44]. The shields are the red and silver components, encasing the HPGe clover detectors, while the tapered cylindrical shields at the top show the BGO shields surrounding the $LaBr_3$ detectors.

2.2.2 SCEPTAR

The SCintillating Electron-Positron Tagging ARray is a series of 10+10 BC404 plastic scintillator detectors that are used to detect β particles emitted in the β-decay process. This detector is made up of an upstream and downstream group of ten detectors, making a set of twenty, with an 80% coverage of the solid angle and a quoted absolute efficiency

of 80% [42]. The β-tag provided by SCEPTAR serves to reduce signal-to-background ratio, since it can serve as an added condition for detection to isolate only the pertinent γ-rays from the de-exciting nuclei [45].

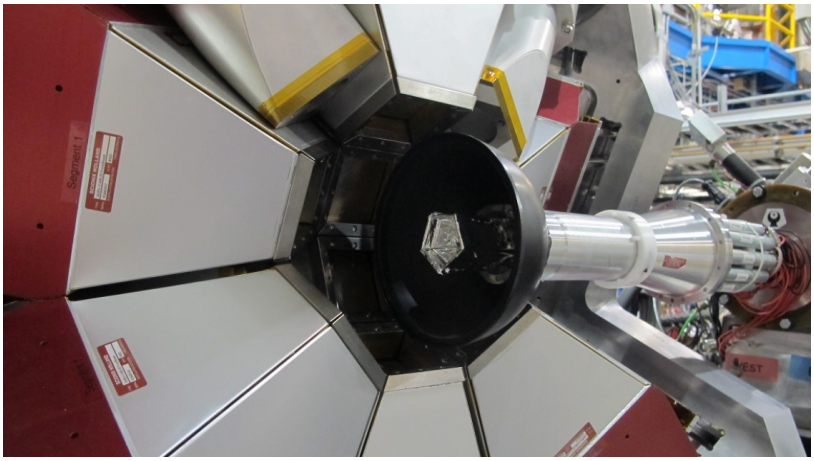

Figure 2.6: The upstream half of the SCEPTAR array, composed of ten plastic scintillators, shown covered in foil. This half can be coupled with the other, downstream half, to make a 10+10 scintillator geometry, sitting at the center of the chamber, surrounded by the GRIFFIN HPGe detectors. Reprinted from Ref. [42].

2.2.3 PACES

The Pentagonal Array of Conversion Electron Spectrometers (PACES) detector is used to detect the electrons emitted during the conversion electron process. This array is a set of five lithium drifted silicon detectors, Si(Li), cooled with liquid nitrogen (LN_2) in order to improve their resolution. The detector system is shown in Figure 2.7, and has a simulated efficiency of $\sim$2% [46].

When used within the GRIFFIN chamber, the system is placed in the upstream position, and the cooling requires the displacement of GRIFFIN clover number 13 to allow space for the LN_2 dewer that accompanies the array, meaning that only 15 of the 16 HPGe detectors are used when PACES is installed [42].

2.2.4 Other ancillary detectors

Apart from the SCEPTAR and PACES detectors, GRIFFIN can host a series of different detector systems in order to study various other mechanisms of decay. The DEuterated SCintillator Array for Neutron Tagging (DESCANT) [47] is composed of up to 70 individual liquid scintillators that serve to tag neutron events. When in use, the detector replaces the four HPGe clover detectors that comprise the forward "lampshade" of GRIFFIN. DESCANT is able to provide a neutron coincidence, such that it is capable of discriminating between, for example, β-decay and β-delayed neutron emission, in order to study nuclei.

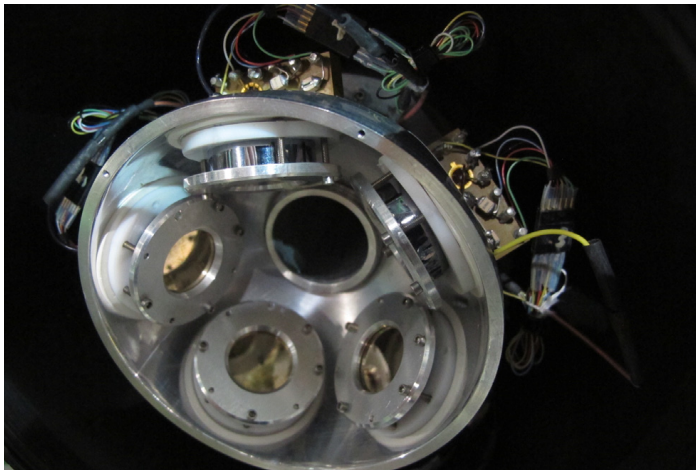

Figure 2.7: The PACES array, comprised of five LN_2 cooled lithium-drifted silicon detectors and is used for conversion electron spectroscopy. Reprinted from Ref. [42].

The Zero-Degree-Scintillator (ZDS) is a plastic scintillator detector which is placed at 0° to the beam axis, directly behind the implantation spot. It is used to record β decays, and has a quoted detection efficiency of ∼40% [42].

To study state lifetimes, the triangular faces of GRIFFIN can be populated with the 8 detectors of the Cerium doped $LaBr_3$ array — $LaBr_3$(Ce). These detectors are used for fast-coincidence-timing measurements of γ-rays.

2.3 Calibrations and Corrections

The GRIFFIN spectrometer and its ancillary detectors require calibrations specific to each experiment, owing to the possibility of changes in detector set-up and response. Several factors must be taken into account when obtaining γ-ray transition data. General details as to the calibrations and corrections that must be completed in order to obtain accurate and precise data from the GRIFFIN spectrometer are contained in the following sections. Cases of additional corrections, specific to each nucleus, are found in Chapter 3 for the β-decay of ^{129}In and Chapter 4 for the β-decay of ^{80}Ge.

2.3.1 Energy Calibrations

An energy calibration is required in order to correlate the detector response to known energies. This is done by using a set of standard calibration sources, with precisely known γ-ray energies. Known sources of ^{56,60}Co, ^{133}Ba and ^{152}Eu were used in order to calibrate the detector up to an energy of 3.6 MeV.

Gain matching was performed on a per-crystal and per-clover basis, to correlate a bin number to an energy value corresponding to ∼1 keV per bin, and consisted of a linear energy calibration. Additionally, a non-linear component was added due to the non-linearities

introduced by the Analog-to-Digital Converter (ADC) modules required by each detector. These corrections were unique to each crystal, and thus the non-linearity correction had to be applied on a crystal-to-crystal basis. This was completed by checking the deviation of each of the measured transitions used when compared to the literature values of the calibration sources.

Once the energy calibration was successfully applied, all crystal or clover spectra could be appropriately summed in order to generate a single γ-ray spectrum.

2.3.2 Efficiency Calibrations

The same calibration sources also served to determine the efficiency of the detector system. The HPGe detectors of the type used in GRIFFIN are known to have decreased efficiency at higher energies since higher energy γ-rays are more likely to scatter, resulting in events that must be accounted for.

The relative efficiency of the GRIFFIN array was calculated, first by determining the number of decays expected from the ^{60}Co standard source, given its activity, the length of time it was measured and its half-life. The photopeaks at 1173 and 1332 keV were then fit, and the values scaled by the total number of decays expected. These two points were subsequently used to scale the other calibration sources. The source data were then fit, in the form of the natural logarithm of the efficiency as a function of the natural logarithm of the energy, with a sixth-order polynomial function, and a reduced-χ^2 obtained in order to verify the accuracy of the fit. Like the energy calibration, the efficiency was determined up to 3.6 MeV.

2.3.3 Corrections

There are several corrections that are needed in order to properly establish the intensity of a transition. The cross-talk and sum-out corrections are required for every transition, while the sum-in correction is only required if certain conditions are met.

Cross-talk Corrections

The cross-talk effect is endemic to closely packaged detector systems. An incoming γ-ray that is detected in one crystal will induce an electric signal in a neighbouring crystal. Should another γ-ray then interact with the affected crystal, the measured energy will be modified, due to the signal induced by the first γ-ray. The effect is a broadening of the measured peak, with the spread centered around the true energy, making for a poor peak fit, increasing the error of the measurement, and effectively lowering the resolution of the detectors. This effect is pronounced when the addback method is used, since this method relies on energy detection in two crystals within the same clover. Thus, a correction is necessary to ensure

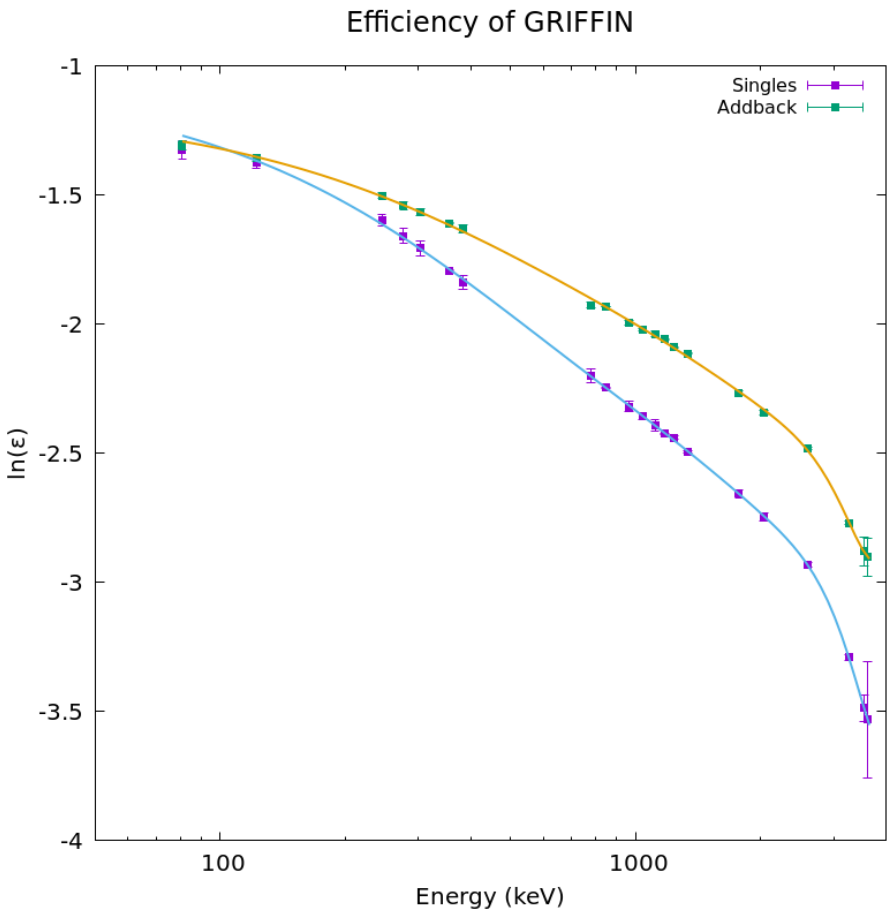

Figure 2.8: Efficiency of the GRIFFIN array for the ^{129}In dataset. The energy values are taken from well known sources: ^{56,60}Co, ^{133}Ba and ^{152}Eu. The data are fit with a sixth order polynomial. The efficiency in addback mode is higher since in this mode otherwise lost Compton scattering events are added back and their real energy recorded.

proper resolution and must be applied to each clover [42]. Details on this correction can be found in [48].

This correction is extracted from the well-known ^{60}Co source data, and is then applied to the experimental data.

Summing Corrections

Summing corrections occur when two cascading γ-rays are detected simultaneously in the same detector, and require the production of a γ-γ matrix. This matrix is a 2D graph built to observe coincidences, with the condition that events are recorded within a short time window. This is done by plotting the energy of one γ-ray on the x-axis and the energy of another γ-ray on the y-axis. A projection of this 2D matrix centered around a γ-ray energy generates a 1D spectrum, known as a gate, that shows all coincident γ-rays. Using these gates, the sequence of the γ-rays and states in a nucleus can be determined.

Consider the γ-ray cascade shown in Figure 2.9. There are two different types of effects that can manifest when simultaneous detection occurs, and must be corrected in order to properly account for γ-ray intensities. Figure 2.10 shows a schematic representation of both summing effects.

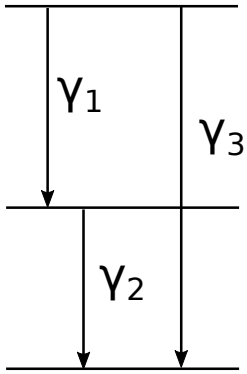

Figure 2.9: A simple level scheme with two coincident transitions, γ_1 and γ_2, in parallel to another transition, γ_3.

The sum-in peak correction refers to the possibility of two transitions adding up to a third energy that also happens to be a transition in the nucleus of interest. If two coincident γ-rays, γ_1 and γ_2, are detected in the same detector, they will be indistinguishable from a single, higher energy photon: the apparent energy observed will be $E_{\gamma,\text{observed}} = E_{\gamma 1} + E_{\gamma 2}$. If this γ_{observed} happens to be a real transition, γ_3, the intensity of γ_3 will be artificially enhanced. A schematic of this effect is shown in Figure 2.10(a). A classic experimental example is the transitions in the decay ^{60}Co. The two benchmark transitions are the 1172- and 1332-keV transitions. These two transitions add up to 2505-keV, which happens to be a real transition in the ^{60}Ni daughter. These transitions are quite strong, and will falsely contribute intensity to that of the 2505-keV transition. In order to obtain the true intensity, the detected counts must be modified, by subtracting off the intensity of 1172-keV peak in the 1332-keV gated spectrum and vice versa, in order to produce an average correction. This type of correction is not required by all peaks, only those whose energy totals the sum of two other transitions in cascade.

The sum-out correction must be applied to all peaks in the spectrum. In this case, two γ-rays, γ_1 and γ_2, are detected simultaneously in the same detector, with a scattering event occurring soon after. The apparent measured energy will not reflect either γ-ray energy, but rather a sum of the energies, $E_{\gamma_1} + E_{\gamma_2}$ minus the energy of the scattered $\gamma\prime$ ($E_{\gamma_{\text{observed}}} = E_{\gamma_1} + E_{\gamma_2} - E_{\gamma\prime}$), contributing to the Compton continuum and thereby decreasing the apparent intensity of both γ_1 and γ_2. A schematic of the effect is shown in Figure 2.10(b).

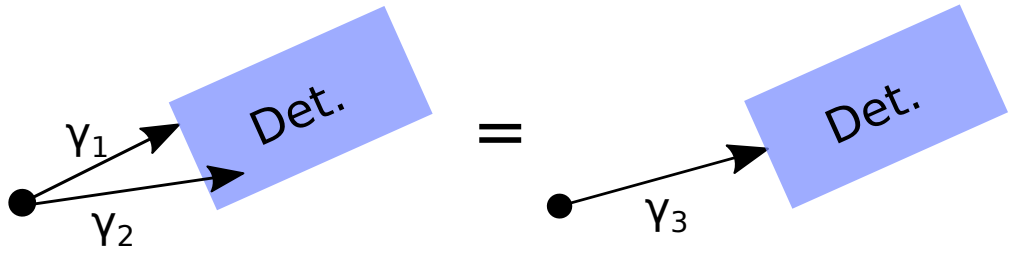

(a) The sum-in event occurs when both γ-ray energies are fully deposited in the detector as shown on the left, but since they cannot be distinguished, the observed energy is the sum of the two $\gamma_3 = \gamma_1 + \gamma_2$, as shown on the right. This results in an artifical increase in the intensity of γ_3.

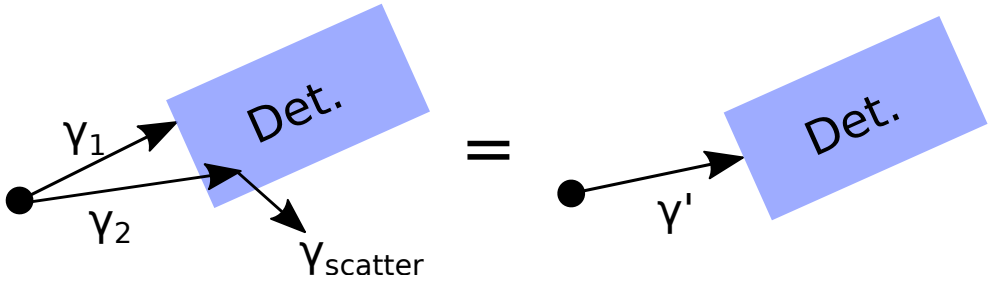

(b) The sum-out case occurs when the simultaneous detection is followed by a scatter event, shown on the left. This results in the observed energy being modified by the scattered energy, resulting in an apparent detection of $\gamma\prime$, thereby decreasing the intensity of γ_1 and γ_2.

Figure 2.10: Summing effects observed in HPGe clover detectors when two coincident γ-rays are detected simultanesouly. Adapted from Ref. [48].

To correct both for sum-in and sum-out, a γ-γ matrix can be constructed, with a requirement that coincident events be measured in detectors at 180° from each other. Described in Appendix C, Equation C.4, the angular correlation, $W(\theta)$, between two coincident γ-rays is a function of the even Legendre polynomials $P_k(\cos\theta)$. This implies that emission of both γ-rays in the same direction ($\theta = 0$, Figure 2.11, Scenario A) is equally probable to back-to-back emission ($\theta = 180°$, Figure 2.11, Scenario B). This coincidence at 180° can thus be used to account for both the sum-in and sum-out cases. The sum-out corrections are obtained from all coincidences with a gated γ-ray, while the sum-in counts require fitting the summing partner transition in the gate, ie. if γ_1 and γ_2 sum-in, then the fit must be done for γ_2 in the γ_1 gate, and vice versa, and then subtracted from the observed intensity of γ_3.

Summing corrections optimized for the GRIFFIN spectrometer are further described in Ref. [48, 49].

2.3.4 Gamma-ray intensities

The corrections described previously must be applied in order to obtain the correct intensity for each of the observed γ-rays.

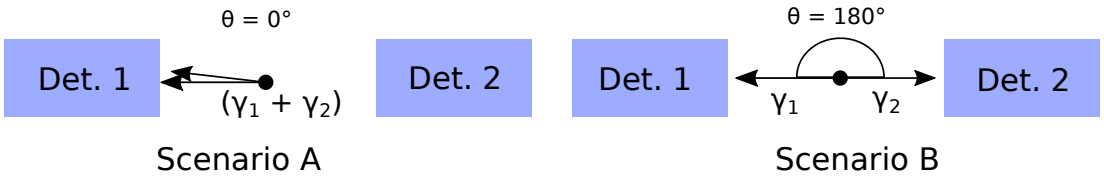

Figure 2.11: Summing correction schematic. Statistically, due to angular correlations, Scenario A occurs just as often as Scenario B, allowing for the recovery of an otherwise lost event. In Scenario A, the energy of the γ-rays would be lost, since it would be recorded as the total energy of $\gamma_1 + \gamma_2$, but by construction of a matrix with detectors at 180°, a fair estimate on how many events were lost can be made and then be added back to the photopeaks of γ_1 and γ_2.

Gamma-singles data

In many cases, the transitions are discernible above the Compton background, and their intensities can be measured from this spectrum and corrected for efficiency and summing, in the form shown in Equation 2.1:

$$I_\gamma = \frac{A_{peak} - N_{\text{sum in}} + N_{\text{sum out}}}{\epsilon_\gamma}, \tag{2.1}$$

where A_{peak} is the area of the peak, $N_{\text{sum in}}$ and $N_{\text{sum out}}$ are the contribution due to summing in and summing out, respectively and ϵ_γ is the detection efficiency of the γ-ray.

Gamma-gamma coincidence data

The coincidence method dictates that if two transitions are measured within a short time window, they are emitted nearly simultaneously and are in sequence — referred to as a $\gamma - ray$ cascade — with one another, as shown in Figure 2.12.

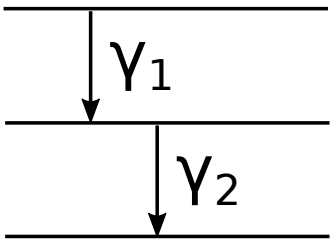

Figure 2.12: A diagram of a γ-cascade, with two γ-rays shown to be emitted one after the other. If they are detected within a small time window, they are said to be in cascade.

The coincidence window is determined from the $\gamma-\gamma$ time difference, as shown in Figure 2.13. The prompt events are those that occur within a short time, constituting a coincidence, while the events beyond this window are time-random background events, which could come from other decays, not associated with the nucleus of interest.

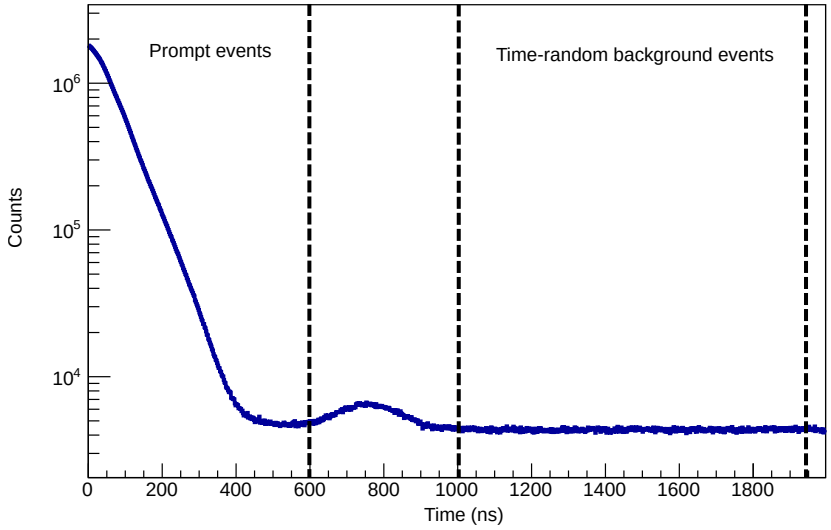

Figure 2.13: The $\gamma - \gamma$ coincidence time window for the ^{129}In dataset. The prompt events are those events that are close enough in time to be considered to be coming from the same nucleus. The time random events are those uncorrelated events that cannot be said to come from the same nucleus. The time-random correction involves the subtraction of these background events from the prompt events, to then generate a time-random background corrected coincidence matrix.

In some cases, transitions are observed that are either so weak that they are buried in the background or on the shoulders of much more intense transitions. These are often only observed by gating on other, more intense transitions. The gates in which they appear suggest their placement in the level scheme, but can also provide their intensity. Since this intensity requires information about the gated γ-ray, Equation 2.1 is modified to become;

$$I_{\gamma_1} = \frac{N_{\gamma 1}}{\epsilon_{\gamma 1}\epsilon_{\gamma 2} BR_{\gamma 2} N}, \tag{2.2}$$

where $N_{\gamma 1}$ is the number of counts in the peak, as observed in the γ_2 gate, $\epsilon_{\gamma 1,\gamma 2}$ are the efficiencies of the γ-rays, N is a scaling factor associated with the events observed in the spectrum and $BR_{\gamma 2}$ is the branching ratio of the gated transition. The branching ratios are specific to each transition depopulating a state, and are calculated by determining the strongest transition depopulating the state, and calculating the ratio of the others based on this transition.

This scaling value must be obtained by using the same mechanism of gating from below, but doing so with a transition that has an already corrected intensity and is in coincidence with another corrected transition. This requires rearranging Equation 2.2, as follows:

$$N = \frac{N_{\gamma 1}}{\epsilon_{\gamma 1}\epsilon_{\gamma 2} BR_{\gamma 2} I_{\gamma 1}}. \tag{2.3}$$

The $\gamma - \gamma$ coincidence matrix that is used to obtain the intensities through gating from below, should first be corrected for so called "time-random" events.

The gating from below method has been previously used for data acquired using the GRIFFIN spectrometer, and details can be found in Refs. [50, 51].

Chapter 3

β-decay of ^{129}In

The tin isotopes occupy a unique place in the chart of nuclides, since they have a magic proton number, $Z = 50$. This closed proton shell helps to explain the large number of tin isotopes, ranging from ^{99}Sn through to ^{139}Sn, spanning the region of two full neutron shell closures, and ten stable isotopes, the highest number of stable isotopes in the chart.

This span of isotopes between the classical $N = 50$ and $N = 82$ neutron shell closures makes the tin isotopes an ideal testing ground for the nuclear shell model, since studies can be performed on isotopes approaching the magic neutron numbers from either side. Additionally, the doubly magic nuclei ^{100}Sn and ^{132}Sn are themselves isotopes of interest.

The ^{129}Sn isotope is three neutrons away from the doubly-magic ^{132}Sn and is thus in a key position to explore behaviour close to the $N = 82$ neutron shell closure, particularly when it comes to single neutron excitations across the shell gap.

The isotopes ^{129}In and ^{129}Sn were studied at the GRIFFIN facility of TRIUMF, described in Chapter 2. The analysis methodology, intensity assignment and γ-ray corrections were applied to this dataset as described in that chapter. The work presented here has been published in Physical Review C[1]. The full article can be found in Appendix A.

3.1 Previous studies

Previous studies of the neutron-rich ^{129}In and ^{129}Sn observed a plethora of transitions and excited states. In the majority of the studies, excited states in ^{129}Sn were populated through the β-decay of the ^{129}In parent, in turn produced by the thermal neutron induced fission [52, 53, 54, 55], by the thermal neutron induced fission of ^{239,241}Pu [56], and by the fragmentation of ^{136}Xe and the relativistic projectile fission of ^{238}U [57].

[1]**Garcia, F. H.** and Andreoiu, C. and Ball, G. C. and Bernier, N. and Bidaman, H. and Bildstein, V. and Bowry, M. and Cross, D. S. and Dunlop, M. R. and Dunlop, R. and Garnsworthy, A. B. and Garrett, P. E. and Henderson, J. and Measures, J. and Olaizola, B. and Ortner, K. and Park, J. and Petrache, C. M. and Pore, J. L. and Raymond, K. and Smith, J. K. and Southall, D. and Svensson, C. E. and Ticu, M. and Turko, J. and Whitmore, K. and Zidar, T., *Spectroscopic studies of neutron-rich ^{129}In and its β-decay daughter, ^{129}Sn, using the GRIFFIN Spectrometer*, *Physical Review C*, 103, 2, 024310 (2021).

Spanier *et al.* [52] were able to study the ^{129}In nucleus using the OSIRIS facility at the Studsvik Neutron Research Laboratory, which relied on the radioactive decay of neutron rich ^{235}U fission products . There, they were able to establish the Q_β value of 7.655(32) MeV for what they termed the high-spin isomer — the $(9/2^+)$ ground state — using an array of HPGe detectors and a planar detector for the β particles. They were also able to observe several transitions in the β-decay ^{129}Sn daughter.

The work by Aleklett *et al.* [53] used the OSIRIS facility for the production of isotopes, but used a pair of NaI(Tl) scintillation detectors coupled with a lithium-drifted silicon Si(Li) and a lithium-drifted germanium Ge(Li) detector to obtain β-γ coincidences. By arranging their detectors in three different configurations they were able to observe some additional transitions for the first time. With their experimental set-up they separated the half-lives of the $(9/2^+)$ ground state and the $(1/2^+)$ isomer in ^{129}In. From their analysis, they corroborated the previous Q_β value of 7.60(12) MeV of ^{129}In.

Once again, exploiting the capabilities of the OSIRIS facility, De Geer and Holm [54] undertook the study of these two nuclei. For their experiment, they used three HPGe detectors to obtain γ-γ coincidence data. They expanded the level scheme, by adding newly observed γ-rays and were able to distinguish between the decay of the ground state and first isomeric state of ^{129}In, into excited states ^{129}Sn, in a similar way that Aleklett *et al.* were able to do so. Additionally, they were able to tentatively assign spins and parities to the states, based on $\log ft$ values.

Experiments carried out by Genevey *et al.* [56] using the LOHENGRIN spectrometer [58] at ILL in Grenoble, were able to decouple high spin isomers in ^{129}Sn. The experiment used two large volume germanium detectors and a Si(Li) detector for γ-ray and β particles, respectively. Two low energy transitions at 19 and 41 keV were observed depopulating the 1761- and the 1802-keV states, respectively, and establishing these as two μs isomers.

The largest and most comprehensive study of the level scheme of ^{129}Sn arguably came in 2004, when Gausemel *et al.* [55] completed their study, again at OSIRIS. They utilized γ-γ coincidence data, obtained through the use of three HPGe detectors. They were able to observe the β-decay of not only the ground state and the $(1/2^+)$ isomer (^{129m1}In) in ^{129}In, but also the $(23/2^-)$ (^{129m2}In) isomer. The dataset they obtained was quite extensive and included γ-ray intensities, β-branching ratios and $\log ft$ values. They were able to observe 18 excited states for the first time and add 78 newly observed transitions to the level scheme of ^{129}Sn.

The recent work by Lozeva *et al.* [57] at the Fragment Separator (FRS) at GSI [59], studied a newly observed μs isomer in ^{129}Sn. For this work, they used eight HPGe cluster detectors and populated excited states in ^{129}Sn through projectile induced fission of ^{238}U and the fragmentation of ^{136}Xe. Using this experimental set-up, two transitions, at 145 and 605 keV were observed, and attributed to a cascade from a newly observed $(27/2^-)$ isomeric state at 2552 keV in ^{129}Sn.

The summary of the information available for ^{129}In and ^{129}Sn is found in the Nuclear Data Sheets, compiled by Timar, Elekes and Singh [60].

The number of previous studies on ^{129}In and ^{129}Sn is indicative of the importance of these nuclei in the chart. These studies were each able to observe a series of transitions and excited states for the first time, in their respective instance, expanding the information available for these nuclei.

The power afforded by the GRIFFIN spectrometer meant that a verification of the level scheme was possible, and also ensured a more comprehensive study of the β-decay of ^{129}In into excited states in ^{129}Sn.

3.2 Experimental Details

The ^{129}In parent isotope was produced using the ISOL technique at the ISAC facility as described in Chapter 2. For this experiment, the Uranium Carbide (UC_x) target was bombarded with a 9.8 μA beam of 480 MeV protons, and the use of IGLIS ensured a reduction in the isobaric contamination expected from cesium and barium. GRIFFIN was fully populated, in its high efficiency configuration, with its 16 HPGe detectors for γ-ray detection with the full SCEPTAR array in place for the detection of β-particles. A 20 mm Delrin shield was installed around SCEPTAR, to minimize Bremsstrahlung radiation from potentially high energy β particles.

The ^{129}In beam was delivered to GRIFFIN as a mix of ground state and isomeric states and implanted at a rate of ∼5000 particles per second. Information on the spin, energy and half-life of the β-decaying ground state and isomers is found in Tab. 3.1. The Mylar tape was run in cycle mode, meaning that it would be moved out of the chamber to provide a clean implant spot after a preset amount of time. The 21.5 s cycles were set as follows: a 1.5 s tape move, 5 s background collection, 10 s isotope implant, 5 s isotope decay. The ^{129}In cycles were run for 460 cycles, amounting to 2.75 hrs of experimental time, and recorded 6×10^7 clover addback singles events and 4×10^7 coincidence events. This coincidence window was set to 500 ns for both the $\gamma-\gamma$ and $\beta-\gamma$ events, in order to correlate decays from ^{129}In.

Table 3.1: Ground state and isomer information for β-decay branches of ^{129}In. Literature data from Ref. [60]

State	Energy (keV)	Spin	$t_{1/2}$ (s)
^{129gs}In	0	$(9/2^+)$	0.611(5)
^{129m1}In	459	$(1/2^-)$	1.23(3)
^{129m2}In	1630	$(23/2^-)$	0.67(10)

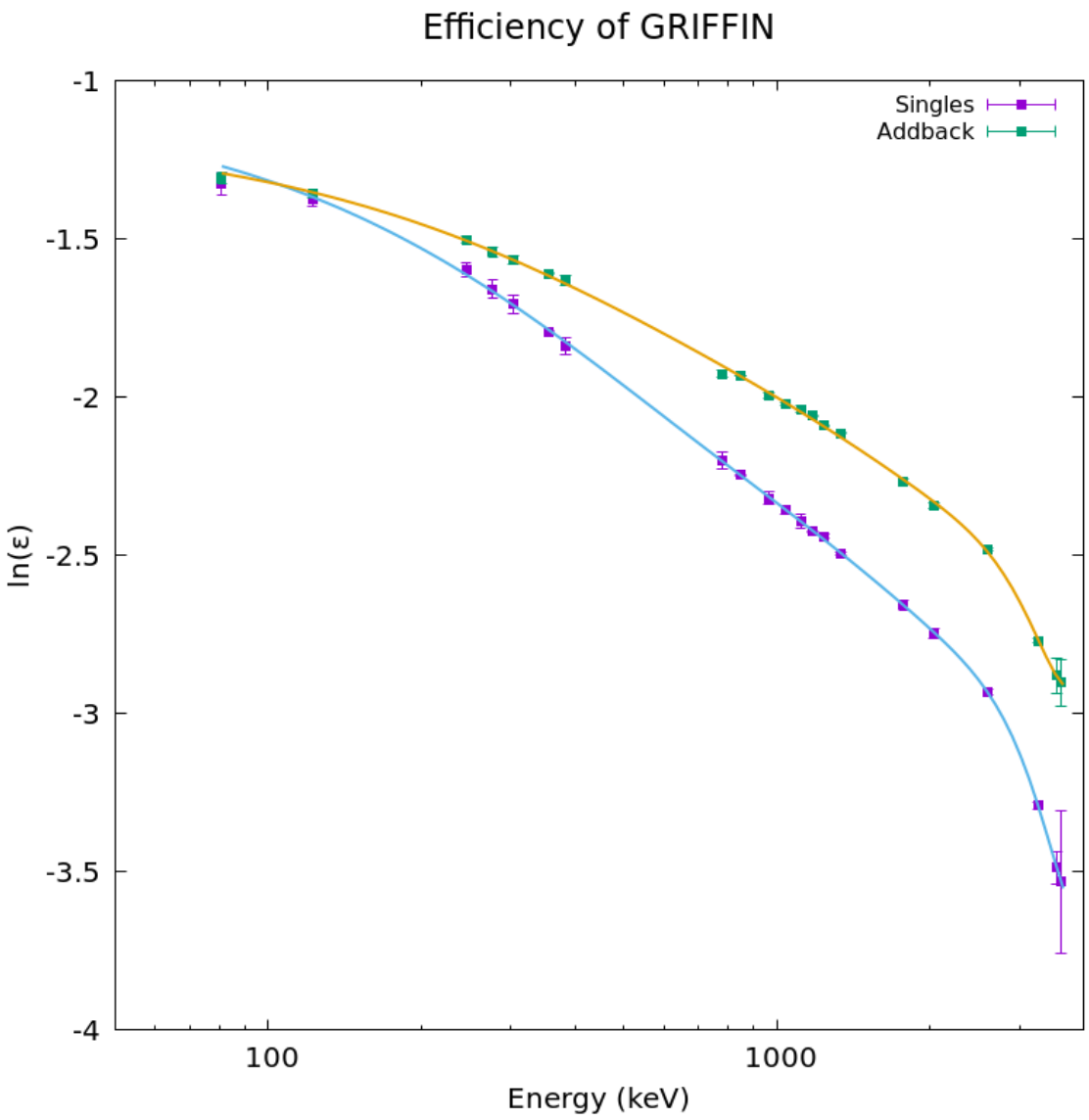

Figure 3.1: The relative crystal singles and clover addback efficiency — presented in the natural logarithm form — as a function of energy, obtained for the β-decay study of ^{129}Sn. The curve was obtained using standard sources of ^{56,60}Co, ^{133}Ba and ^{152}Eu.The χ^2 returned for the fit of the crystal singles efficiency is 2.59 and that for clover addback is 1.55.

The energy and efficiency calibrations were performed using the standard sources, as described in Chapter 2 Section 2.3.2. The clover addback efficiency of GRIFFIN during this experiment was calculated to be 12% at 1332 keV; the efficiency curve is shown in Figure 3.1. The energy calibration was done using the same sources, encompassing the energy range between 81 keV and 3.6 MeV.

The uncertainty in the energy values was obtained by applying the energy residuals (due to the nonlinearities observed in the Analogy-to-Digital converters) associated with the ^{129}Sn data to the energy calibration data. This provided a systematic uncertainty of

0.24 keV. The measured energy column of Table 3.2 contains the energy values obtained from the calibration data once the energy residuals for ^{129}Sn were applied to the data.

Table 3.2: Transitions used to build energy and efficiency calibration for experiment S1519, to study the β-decay of ^{129}In. The transitions are taken from the IAEA Gamma-Ray Decay Data standards [61], while those labelled with † are taken from Ref. [62].

Source	Transition (Lit. Value) (keV) [61]	Measured Energy (keV)
^{60}Co	1173.228	1173.219
	1332.492	1332.435
^{133}Ba	80.9979	81.029
	276.3989	276.388
	302.8508	302.841
	356.0129	356.009
	384.8485	383.846
^{152}Eu	121.7817	121.770
	244.6974	244.656
	778.9045	778.11
	964.072	963.961
	1085.837	1085.761
	1112.076	1111.946
^{56}Co	1238.2736	1238.274
	1771.327	1771.327
	2034.752	2037.719
	2598.438	2598.457
	3253.402	3253.053
	3548.05†	3547.555
	3611.53†	3611.188

3.3 γ-ray analysis

Spectroscopic analysis of the β-decay of ^{129}In was able to uncover thirty-one newly observed γ-ray transitions and nine excited states in the ^{129}Sn β-decay daughter. Transitions in this experiment were investigated using clover addback mode up to $\sim$5 MeV, since the neutron separation energy of ^{129}Sn is quoted as 5.316(26) MeV [60]. This range in shown in Figure 3.2.

Figure 3.3 shows a portion of the γ-ray spectrum, obtained in clover addback mode. Several transitions belonging to ^{129}Sn are identified, alongside transitions from ^{128}Sn and

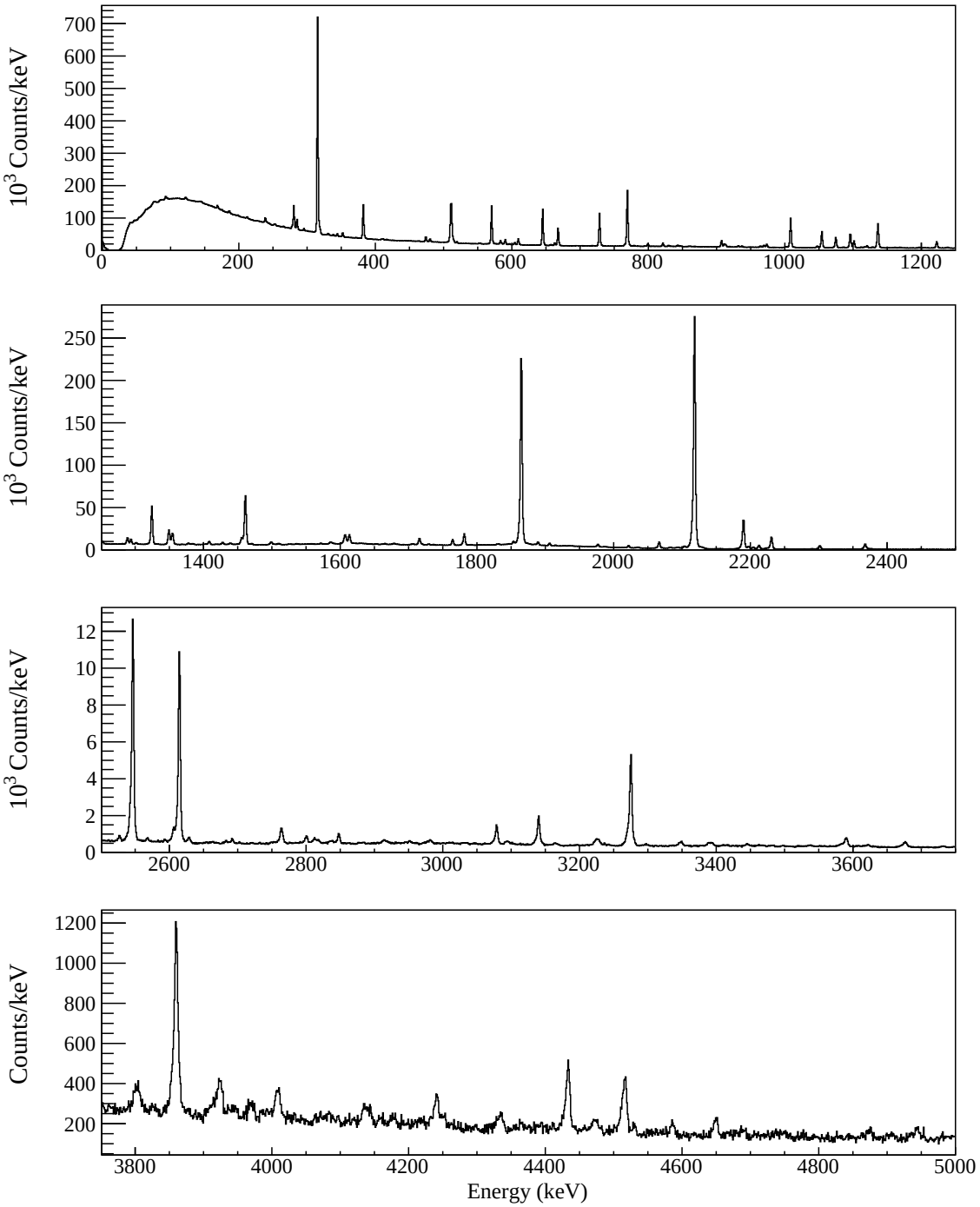

Figure 3.2: Full clover addback γ-singles energy spectrum. The transitions from 81 keV through to 5 MeV were investigated, up to the neutron separation energy of ^{129}Sn.

^{129}Sb; the latter two are expected since ^{129}In does have a β-delayed neutron branch, and ^{129}Sb is the daughter of the ^{129}Sn β-decay.

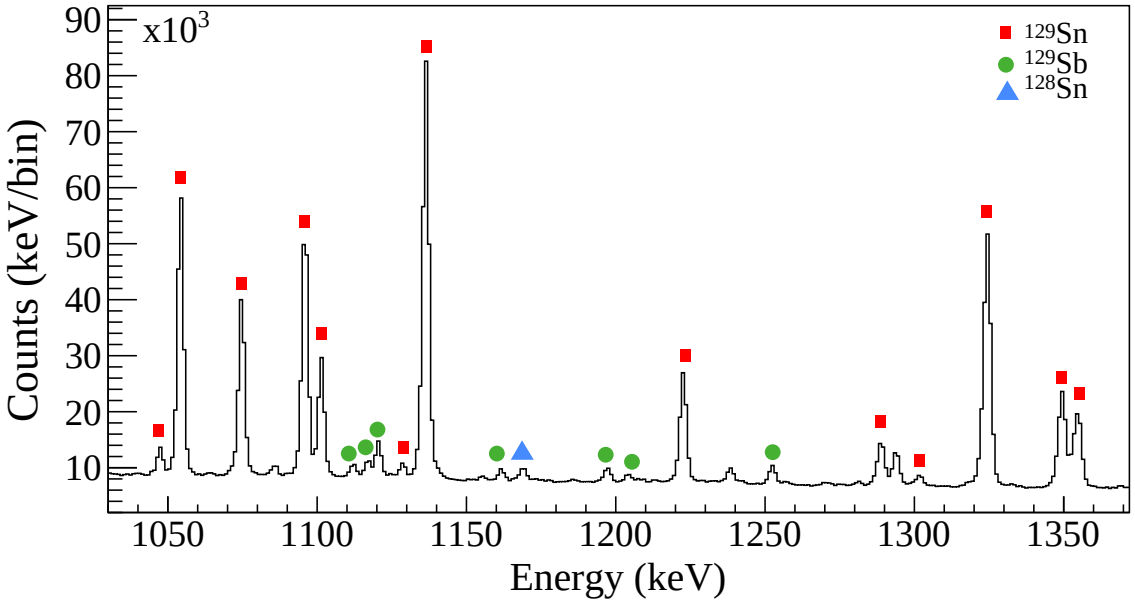

Figure 3.3: A portion of the clover addback γ-ray spectrum. The (red) squares identify transitions associated with ^{129}Sn, the (green) circles identify transitions from ^{128}Sn and the (blue) triangles, identify transitions from ^{129}Sb. Reprinted figure with permission from Ref. [63]. Copyright (2021) by the American Physical Society.

Only two of the known transitions in the ^{129}Sn nucleus were not observed, at 19 and 41 keV, due to the high background present in the region between 0 keV and 50 keV. The transitions observed during the course of the analysis are shown in Table 3.3, which includes information about the initial and final states of the transition, its relative intensity and the branching ratio. The transition intensities are calculated as described in Chapter 2 Section 2.3.4.

All but seven transitions intensities were obtained from the clover addback spectrum. The transitions at 146, 278, 280, 1071, 1096, 1586 and 2371 keV required gating from below in order to establish their intensity, as described in Section 2.3.4. Figure 3.4 shows the $\gamma-\gamma$ matrix, in clover addback mode, used to obtain these gated intensities.

The states in ^{129}Sn can be split into different level schemes, since their feeding from ^{129}In is governed by the β-decay selection rules as presented in Chapter 1. The spins of each of the ground and isomeric states in ^{129}In are distinct enough that their contributions can be clearly disentangled.

Given that particular transitions can be attributed to the decay of the ground state or either of the two isomeric states, their timing information can be used to determine their half-life. This is done using the γ-ray energy as a function of cycle time matrix, shown in Figure 3.6.

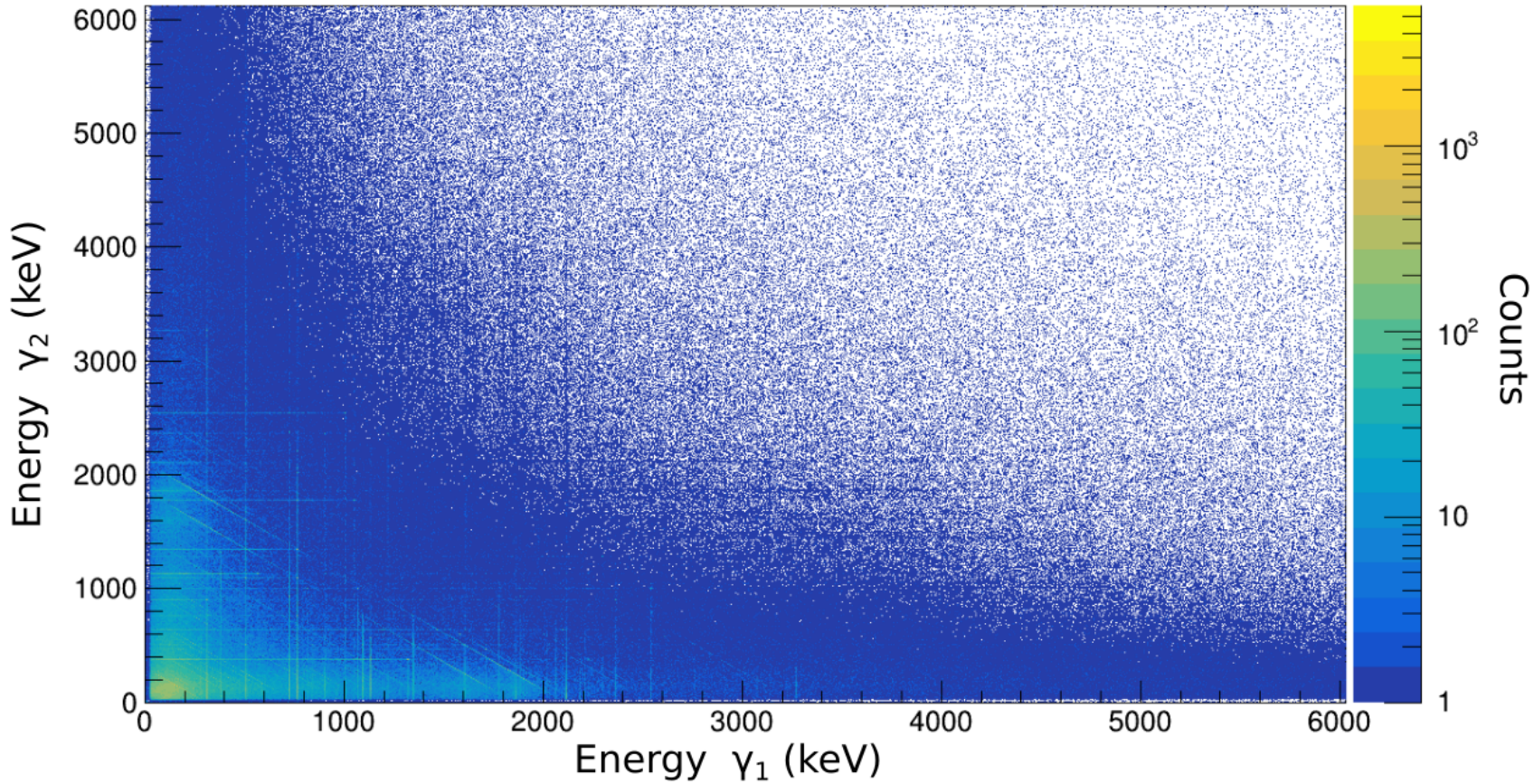

Figure 3.4: The $\gamma - \gamma$ matrix, in clover addback mode, constructed with a 600 ns coincidence window. The x- and y-axes represent the energies of two coincident γ-rays, while the colour contour on the z-axis shows the coincidence frequency at those energies.

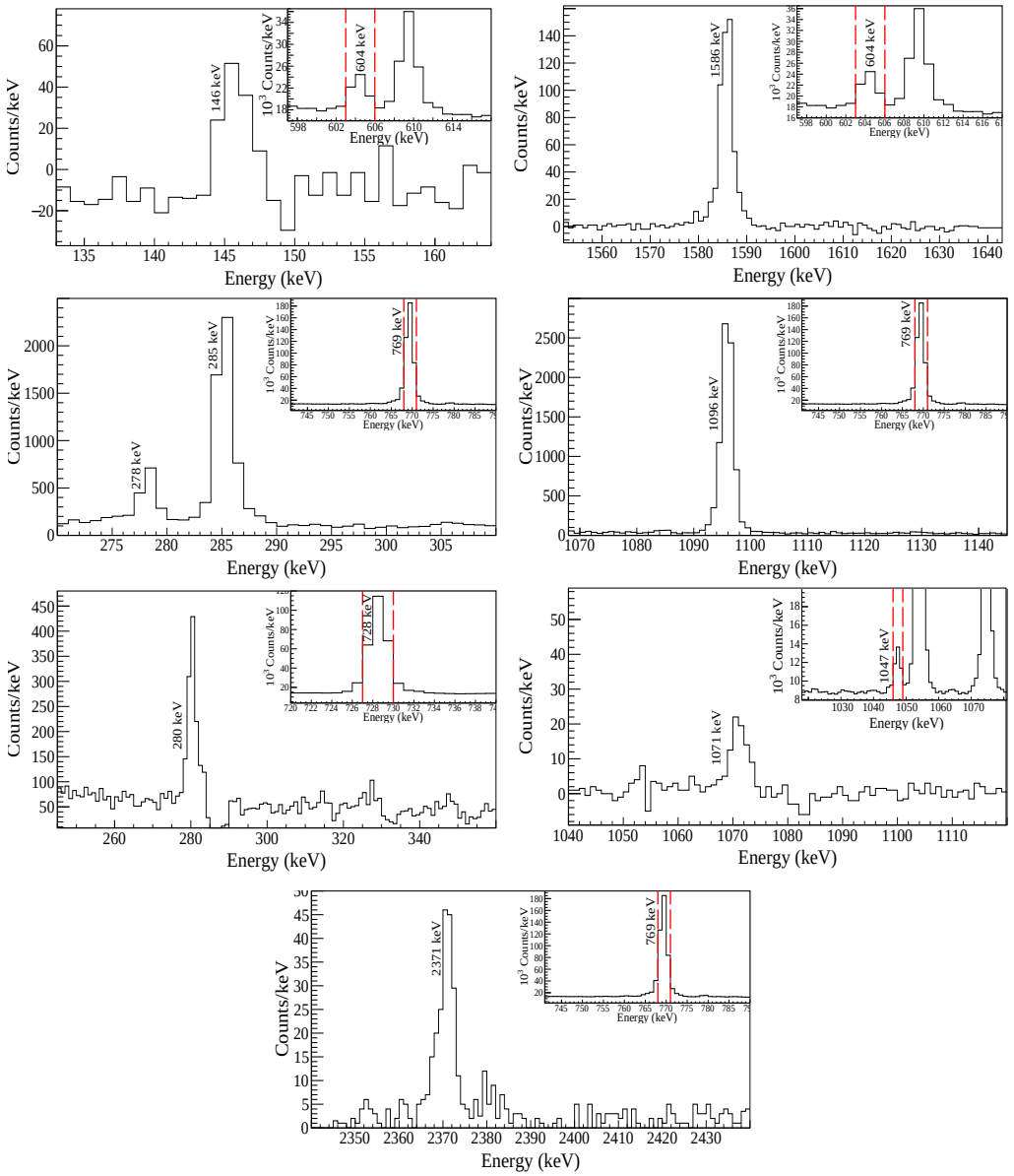

Figure 3.5: Prompt coincidence gates showing the seven transitions that require gating from below. The insets show the transitions which are gated on in order to produce the spectra shown. The (red) lines indicate the placement of the gates.

By gating on γ-ray transitions of interest, with the appropriate background subtraction, a half-life plot is obtained and then fit using a standard decay exponential, shown in Equation 3.1,

$$N(t) = a + e^{\lambda(t-b)}, \tag{3.1}$$

where a and b are free parameters, and λ is the decay constant.

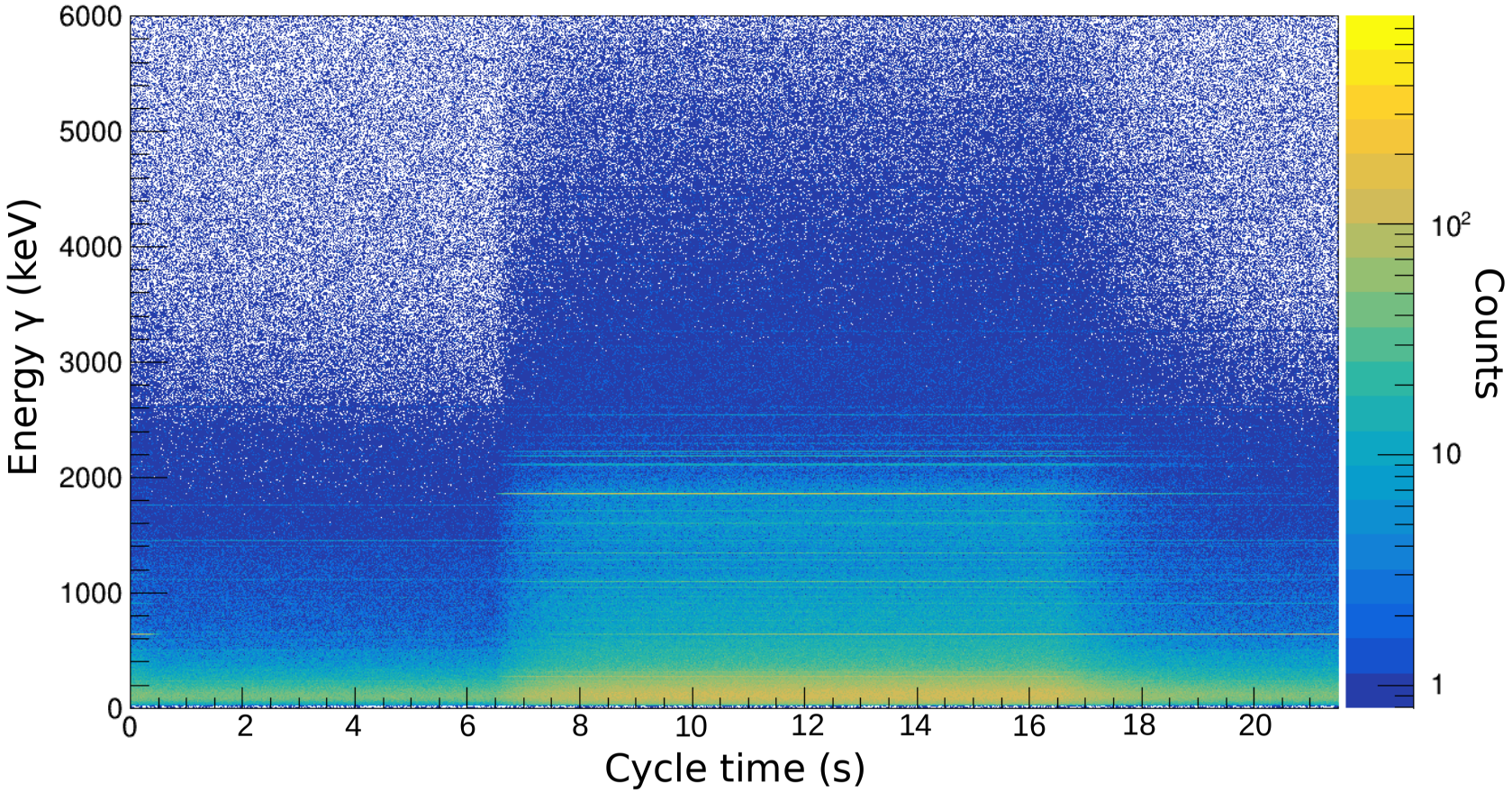

Figure 3.6: Energy as a function of cycle time matrix, in clover addback mode. The cycle time (in s) is on the x-axis, while the γ-ray energy is on the y-axis.

Gating on the matrix shown in Figure 3.6, produces a plot of the type shown in Figure 3.7, which can then be fit using Equation 3.1.

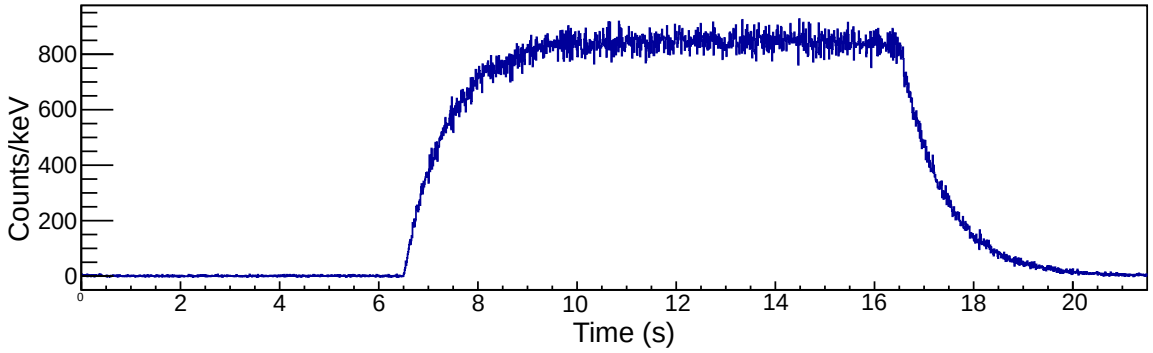

Figure 3.7: A resulting gate placed on the matrix in Figure 3.6, centered around 2118 keV. This plot can then be fit with Equation 3.1 and the half-life of the parent isotope extracted.

Additionally to the measurement of the half-life of each of the isomers and the ground state of ^{129}In, the β-feeding of these states to excited states in ^{129}Sn was calculated. The β-feeding for each state is obtained by performing an intensity balance calculation, where the γ-ray intensity populating a specific state is subtracted from the intensity depopulating the state. Note that a γ-ray with a energy $< \sim 400$ keV will require a correction for internal conversion, which is achieved using the BrIcc Conversion Coefficient Calculator [64]. An excess in intensity indicates level feeding from the β-decay of the parent isotope. This β-feeding value can then be used to calculate the $\log ft$ value for each state, which in turns provides information about the type of β-decay and thus can be used to tentatively assign a spin to said state. This β-feeding analysis was done for each of the β-decaying ^{129}In states, into associated states in ^{129}Sn, where the association is made through decay systematics and previously established spin assignments.

Apart from the presentation of the entire γ-ray intensity table (Tab. 3.3), the results from the analysis of this dataset are split into four distinct parts, one for the ground state and one each for the three β-decaying isomers in ^{129}In, the last of which is observed to β-decay for the first time in this work.

Table 3.3: Energy levels and transitions observed in ^{129}Sn, observed from the β^- decay of ^{129}In. All intensities are normalized to the most intense transition, at 2118 keV, from the $(7/2^+)$ 2118-keV state to the $3/2^+$ ground state. The level spins and parities are adopted from Ref. [60], unless otherwise stated. Table adapted from Ref. [63].

E_i (keV)	E_γ (keV)	J_i^π	J_f^π	E_f (keV)	Relative I_γ	BR_γ
0		$3/2^+$				
35.2(2)		$11/2^-$				
315.1(2)	315.4(2)	$(1/2^+)$	$3/2^+$	0	0.611(5)	100
763.7(1)	728.5(2)	$(9/2^-)$	$11/2^-$	35.2(2)	0.163(2)	100
769.1(1)	769.3(2)	$(5/2^+)$	$3/2^+$	0	0.297(3)	100
1043.9(1)	280.4(2)†	$(7/2^-)$	$(9/2^-)$	763.7(1)	0.0068(8)	3.6(5)
	1008.5(2)	$(7/2^-)$	$11/2^-$	35.2(2)	0.186(2)	100(1)
1047.0(2)	278.0(2)†	$(7/2^+)$	$(5/2^+)$	769.1(1)	0.0081(10)	95(7)
	1047.4(2)	$(7/2^+)$	$3/2^+$	0	0.0086(4)	100(5)
1054.3(2)	285.2(2)	$(7/2^+)$	$(5/2^+)$	769.1(1)	0.036(2)	34(1)
	1054.4(2)	$(7/2^+)$	$3/2^+$	0	0.1050(10)	100.0(5)
1171.5(3)	1136.4(2)	$(15/2^-)$	$11/2^-$	35.2(2)	0.1698(14)	100
1222.4(2)	175.5(4)	$(3/2^+)$	$(7/2^+)$	1047.0(2)	0.0025(6)	5(1)
	907.3(2)	$(3/2^+)$	$(1/2^+)$	315.1(2)	0.0394(7)	86(1)
	1222.6(2)	$(3/2^+)$	$3/2^+$	0	0.0461(5)	100.0(9)
1288.6(2)	519.5(7)	$(3/2^+)$	$(5/2^+)$	769.1(1)	0.007(3)	32(14)
	973.6(2)	$(3/2^+)$	$(1/2^+)$	315.1(2)	0.0193(9)	88(4)
	1288.8(2)	$(3/2^+)$	$3/2^+$	0	0.0220(4)	100(2)
1359.5(3)	1324.4(2)	$(13/2^-)$	$11/2^-$	35.2(2)	0.1306(13)	100
1455.2(2)	1455.0(2)	$(5/2^+)$	$3/2^+$	0	0.0306(9)	100
1534.4(2)	480.2(2)	$(7/2^-, 9/2^+)$	$(7/2^+)$	1054.3(2)	0.0137(11)	100(8)
	765.0(3)	$(7/2^-, 9/2^+)$	$(5/2^+)$	769.1(1)	0.0037(11)	27(8)
	1499.1(2)	$(7/2^-, 9/2^+)$	$11/2^-$	35.2(2)	0.0114(7)	84(5)
1607.3(3)	553.1(3)	$(7/2 - 11/2)^*$	$(7/2^+)$	1054.3(2)	0.0037(6)	58(9)
	843.4(3)	$(7/2 - 11/2)^*$	$(7/2^+)$	763.7(1)	0.0064(5)	100(7)

Table 3.3: *Continued from previous page.*

E_i (keV)	E_γ (keV)	J_i^π	J_f^π	E_f (keV)	Relative I_γ	BR_γ
1613.6(3)	1613.4(2)	$(7/2^+)^\ddagger$	$3/2^+$	0	0.0359(5)	100
1688.3(3)	919.0(3)	$(7/2^-, 9/2^+)$	$(5/2^+)$	769.1(1)	0.0027(2)	100(9)
	1653.0(3)	$(7/2^-, 9/2^+)$	$11/2^-$	35.2(2)	0.0025(3)	92(12)
1701.0(2)	657.3(2)	$(7/2^-)$	$(7/2^-)$	1043.9(1)	0.0043(3)	45(4)
	932.0(2)	$(7/2^-)$	$(5/2^+)$	769.1(1)	0.0094(4)	100(4)
	937.4(2)	$(7/2^-)$	$(9/2^-)$	763.7(1)	0.0075(5)	79(6)
	1665.6(3)	$(7/2^-)$	$11/2^-$	35.2(2)	0.0027(7)	28(8)
1741.9(3)	382.4(2)	$(15/2^+)$	$(13/2^-)$	1359.5(3)	0.1235(12)	77.2(6)
	570.4(2)	$(15/2^+)$	$(15/2^-)$	1171.5(3)	0.160(2)	100.0(7)
1853.3(2)	318.0(6)	(7/2, 9/2)	$(7/2^-, 9/2^+)$	1534.4(2)	0.0073(3)	48(2)
	799.4(2)	(7/2, 9/2)	$(7/2^+)$	1054.3(2)	0.0153(9)	100(6)
	806.3(4)	(7/2, 9/2)	$(7/2^+)$	1047.0(2)	0.0016(4)	11(3)
	1085.7(6)	(7/2, 9/2)	$(5/2^+)$	769.1(1)	0.0046(3)	30(2)
1865.1(1)	330.9(3)	$(7/2^+)$	$(7/2^-, 9/2^+)$	1534.4(2)	0.0060(14)	0.7(2)
	411.2(6)	$(7/2^+)$	$(5/2^+)$	1455.2(2)	0.0083(5)	1.03(6)
	576.1(3)	$(7/2^+)$	$(3/2^+)$	1288.6(2)	0.0009(2)	0.11(3)
	821.4(2)	$(7/2^+)$	$(7/2^-)$	1043.9(1)	0.0173(5)	2.14(5)
	$1095.9(2)^\dagger$	$(7/2^+)$	$(5/2^+)$	769.1(1)	0.081(5)	9.9(6)
	1101.4(2)	$(7/2^+)$	$(9/2^-)$	763.7(1)	0.0435(7)	5.36(7)
	1830.6(3)	$(7/2^+)$	$11/2^-$	35.2(2)	0.0039(5)	0.48(6)
	1864.8(2)	$(7/2^+)$	$3/2^+$	0	0.812(7)	100.0(6)
1906.2(2)	1906.2(2)	(7/2)	$3/2^+$	0	0.0093(4)	100
2023.6(4)	969.2(3)	$(7/2 - 11/2)^*$	$(7/2^+)$	1054.3(2)	0.0123(7)	100
2118.3(1)	212.2(3)	$(7/2^+)$	(7/2)	1906.2(2)	0.0045(6)	0.45(6)
	253.1(3)	$(7/2^+)$	$(7/2^+)$	1865.1(1)	0.0057(4)	0.57(4)
	265.5(3)	$(7/2^+)$	(7/2, 9/2)	1853.3(2)	0.0036(4)	0.36(4)
	583.6(2)	$(7/2^+)$	$(7/2^-, 9/2^+)$	1534.4(2)	0.0144(7)	1.44(7)
	662.9(2)	$(7/2^+)$	$(5/2^+)$	1455.2(2)	0.0125(3)	1.25(3)

Table 3.3: *Continued from previous page.*

E_i (keV)	E_γ (keV)	J_i^π	J_f^π	E_f (keV)	Relative I_γ	BR_γ
	829.9(2)	$(7/2^+)$	$(3/2^+)$	1288.6(2)	0.0048(3)	0.48(3)
	1071.0(2)†	$(7/2^+)$	$(7/2^+)$	1047.0(2)	0.0006(1)	0.06(1)
	1074.7(2)	$(7/2^+)$	$(7/2^-)$	1043.9(1)	0.0666(7)	6.66(7)
	1349.5(2)	$(7/2^+)$	$(5/2^+)$	769.1(1)	0.0511(8)	5.11(8)
	1354.7(2)	$(7/2^+)$	$(9/2^-)$	763.7(1)	0.0417(11)	4.2(1)
	2083.0(3)	$(7/2^+)$	$11/2^-$	35.2(2)	0.0033(4)	0.33(4)
	2118.3(2)	$(7/2^+)$	$3/2^+$	0	1	100.0(6)
2277(1)	474.0(2)	(21/2)	$(23/2)^+$	1803(1)	0.0220(5)	100(2)
	514.8(3)	(21/2)	$(19/2)^+$	1762(1)	0.0081(6)	37(6)
2326.1(4)	1270.5(6)	(7/2, $9/2^+$)*	$(7/2^+)$	1054.3(2)	0.0012(3)	82(21)
	1558.1(4)	(7/2, $9/2^+$)*	$(5/2^+)$	769.1(1)	0.0015(3)	100(18)
2406(1)	604.4(5)	$(23/2^-)$	$(23/2^+)$	1803(1)	0.0090(4)	100
2552(1)	145.5(3)†	$(27/2^-)$	$(23/2^-)$	2406(1)	0.0011(2)	100
2568.0(3)	2252.9(3)	(1/2, 3/2)*	$(1/2)^+$	315.1(2)	0.0009(3)	93(30)
	2568.0(3)	(1/2, 3/2)*	$3/2^+$	0	0.0010(6)	100(56)
2606.2(2)	1150.9(3)	(1/2, 3/2)*	$(5/2^+)$	1455.2(2)	0.0002(2)	6(4)
	1384.2(3)	(1/2, 3/2)*	$(3/2^+)$	1222.4(2)	0.0035(4)	90(11)
	2290.5(3)	(1/2, 3/2)*	$(1/2)^+$	315.1(2)	0.0013(2)	33(6)
	2606.9(4)	(1/2, 3/2)*	$3/2^+$	0	0.0039(4)	100(9)
2791.0(3)	1736.6(3)	(7/2, $9/2^+$)	$(7/2^+)$	1054.3(2)	0.0018(3)	22(3)
	2021.9(2)	(7/2, $9/2^+$)	$(5/2^+)$	769.1(1)	0.0082(3)	100(3)
2836.0(2)	718.0(3)	($7/2^+$, $9/2^+$)	$(7/2^+)$	2118.3(1)	0.0026(5)	5(1)
	1301.8(2)	($7/2^+$, $9/2^+$)	($7/2^-$, $9/2^+$)	1534.4(2)	0.0058(8)	12(2)
	1781.4(2)	($7/2^+$, $9/2^+$)	$(7/2^+)$	1054.3(2)	0.0490(6)	100(1)
	1791.4(3)	($7/2^+$, $9/2^+$)	$(7/2^-)$	1043.9(1)	0.0031(4)	6.3(7)
	2066.5(2)	($7/2^+$, $9/2^+$)	$(5/2^+)$	769.1(1)	0.0299(6)	61(1)
	2072.9(3)	($7/2^+$, $9/2^+$)	$(9/2^-)$	763.7(1)	0.0003(1)	0.6(2)
2981.9(2)	863.8(4)	$(7/2^+)$	$(7/2^+)$	2118.3(1)	0.0007(3)	3(1)

Table 3.3: *Continued from previous page.*

E_i (keV)	E_γ (keV)	J_i^π	J_f^π	E_f (keV)	Relative I_γ	BR_γ
	1128.7(2)	$(7/2^+)$	(7/2, 9/2)	1853.3(2)	0.0036(8)	18(4)
	1927.6(3)	$(7/2^+)$	$(7/2^-)$	1054.3(2)	0.0015(3)	8(1)
	2212.6(2)	$(7/2^+)$	$(5/2^+)$	769.1(1)	0.0201(5)	100(2)
	2980.7(7)	$(7/2^+)$	$3/2^+$	0	0.0009(2)	4.5(8)
3079.3(3)	2035.6(3)	$(3/2^-)$	$(7/2^-)$	1043.9(1)	0.0045(7)	79(11)
	2764.0(2)	$(3/2^-)$	$(1/2)^+$	315.1(2)	0.0057(3)	100(5)
3140.3(2)	1526.1(3)	$(7/2^+)$	$(7/2^+)$	1613.6(3)	0.0020(5)	17(4)
	2094.0(3)	$(7/2^+)$	$(7/2^+)$	1047.0(2)	0.0041(4)	34(3)
	2371.1(3)†	$(7/2^+)$	$(5/2^+)$	769.1(1)	0.0045(3)	37(3)
	2376.4(3)	$(7/2^+)$	$(9/2^-)$	763.7(1)	0.0025(6)	20(5)
	3140.1(2)	$(7/2^+)$	$3/2^+$	0	0.0123(3)	100(2)
3393.9(4)	3078.7(3)	(1/2, 3/2)	$(1/2)^+$	315.1(2)	0.0077(3)	100
3446.7(4)	2683.0(3)	(7/2 – 11/2)*	$(9/2^-)$	763.7(1)	0.0005(2)	100
3581.8(3)	1257.0(6)	(7/2, $9/2^+$)*	(7/2, 9/2)	2326.1(4)	0.0013(2)	90(17)
	2527.1(3)	(7/2, $9/2^+$)*	$(7/2^+)$	1054.3(2)	0.0013(3)	93(23)
	2812.7(8)	(7/2, $9/2^+$)*	$(5/2^+)$	769.1(1)	0.0014(4)	100(25)
	2818.4(5)	(7/2, $9/2^+$)*	$(9/2^-)$	763.7(1)	0.0010(4)	69(27)
3590.4(1)	1889.5(2)	$(3/2^-)$	$(7/2^-)$	1701.0(2)	0.0106(5)	23(1)
	1977.0(2)	$(3/2^-)$	$(7/2^+)$	1613.6(3)	0.0113(5)	24(1)
	2301.7(2)	$(3/2^-)$	$(3/2^+)$	1288.6(2)	0.0178(3)	38.0(5)
	2367.9(2)	$(3/2^-)$	$(3/2^+)$	1222.4(2)	0.0292(4)	62.3(7)
	2546.2(2)	$(3/2^-)$	$(7/2^-)$	1043.9(1)	0.0469(5)	100(1)
	3276.0(2)	$(3/2^-)$	$(1/2)^+$	315.1(2)	0.0440(6)	94(1)
	3589.7(3)	$(3/2^-)$	$3/2^+$	0	0.0058(5)	12(1)
3993(1)	1586.3(3)†	$(21/2^-)$	$(23/2^-)$	2406(1)	0.011(6)	7.2(1)
	1715.9(2)	$(21/2^-)$	(21/2)	2277(1)	0.0286(7)	17.6(4)
	2189.8(2)	$(21/2^-)$	$(23/2^+)$	1803(1)	0.162(2)	100.0(7)
	2230.8(2)	$(21/2^-)$	$(19/2^+)$	1762(1)	0.0577(9)	35.5(5)

Table 3.3: *Continued from previous page.*

E_i (keV)	E_γ (keV)	J_i^π	J_f^π	E_f (keV)	Relative I_γ	BR_γ
4136.6(3)	2847.8(2)	(1/2, 3/2)*	($3/2^+$)	1288.6(2)	0.0026(1)	100(3)
	2915.5(5)	(1/2, 3/2)*	($3/2^+$)	1222.4(2)	0.0019(3)	73(12)

* Spin assignment for new levels, based on β and γ decay systematics.

† Revised spin assignment for known levels, based on β and γ decay systematics.

‡ Intensity calculated from coincidences.

3.4 ^{129}In ground state decay

The $9/2^+$ ground state decay of ^{129}In populates excited states in ^{129}Sn according to the β-decay selection rules, with allowed and first forbidden transitions being the most common, meaning states with spins between 5/2 and 13/2 are likely to be populated. From this analysis, six excited states and twenty two transitions are observed for the first time. Spins are assigned to the newly observed levels based on systematics and the spin of one previously observed state is constrained considerably from previous measurements.

3.4.1 Half-life of ^{129}In

A plot of the γ-ray intensity as a function of time produces the time curve of the decaying isotope, thus the half-life of the isotope can be extracted using this mechanism. However, the limited statistics of the γ-rays observed following the ground state decay of ^{129}In, made it difficult to fit individual transitions. To overcome this obstacle, the addition of several transitions associated uniquely with this decay was done, and the resulting plot fit for the half-life value.

Thirty nine transitions, shown in Table 3.4 associated, in literature, with the ground state decay of the indium parent were added in order to obtain enough statistics to fit the intensity as a function of time plot, seen in Figure 3.8.

The fit, in red, returns a half-life value of $t_{1/2} = 0.60(1)$ s — with a reduced-χ^2 of 1.3 — in complete agreement with the literature value of $t_{1/2} = 0.611(5)$ s [65], and thus attributable to the ground state decay of ^{129}In.

To ensure that no systematic effects were present in the fit, effects that could produce an inaccurate value, a chop analysis was carried out [48]. This involved varying the size of the fit window; by choosing different start and end points of the fit the systematic effects were removed.

Table 3.4: Transitions used to build the half-life plot shown in Figure 3.8. These were identified as transitions from states populated by the ground state decay of ^{129}In.

Transitions (keV)			
212.2(3)	662.9(2)	1349.5(2)	2021.9(2)
253.1(3)	765.0(3)	1354.7(2)	2066.5(2)
265.5(3)	799.4(2)	1499.1(2)	2072.9(3)
278.0(2)	821.4(2)	1613.4(2)	2083.0(3)
285.2(2)	829.9(2)	1736.6(3)	2118.3(2)
318.0(6)	1054.4(2)	1781.4(2)	2212.6(2)
330.9(3)	1074.7(2)	1791.4(3)	2376.4(3)
411.2(6)	1095.9(2)	1830.6(3)	2980.7(7)
480.2(2)	1101.4(2)	1864.8(2)	3140.1(2)
576.1(3)	1301.8(2)	1906.2(2)	

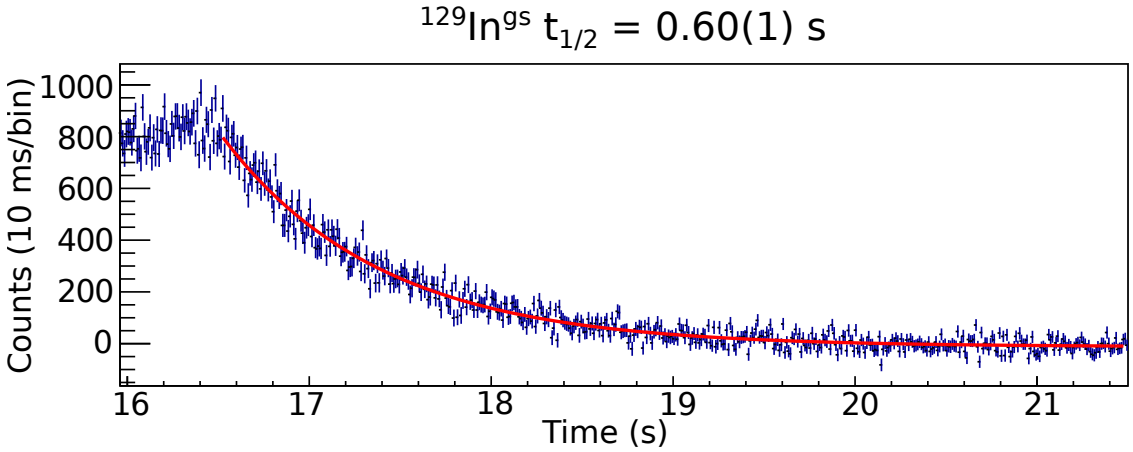

Figure 3.8: A spectrum of total counts as a function of cycle time, representing 39 transitions associated with the ^{129}In ground state decay into states in ^{129}Sn. The fit, seen in red, returned a value of $t_{1/2}$ = 0.60(1) s, with a reduced χ^2 of 1.3. Reprinted figure with permission from Ref. [63]. Copyright (2021) by the American Physical Society.

3.4.2 γ-ray transitions and β-feeding

The ^{129}Sn level scheme, associated with the decay of the ground state in ^{129}In is shown in Figure 3.9. The newly observed states are also assigned spin values, based on the γ-ray systematics and logft calculations. The logft values are calculated using the NNDC LOGFT calculator [66], which intakes information about the parent half-life, β-decaying state, the daughter state and the observed β-feeding.

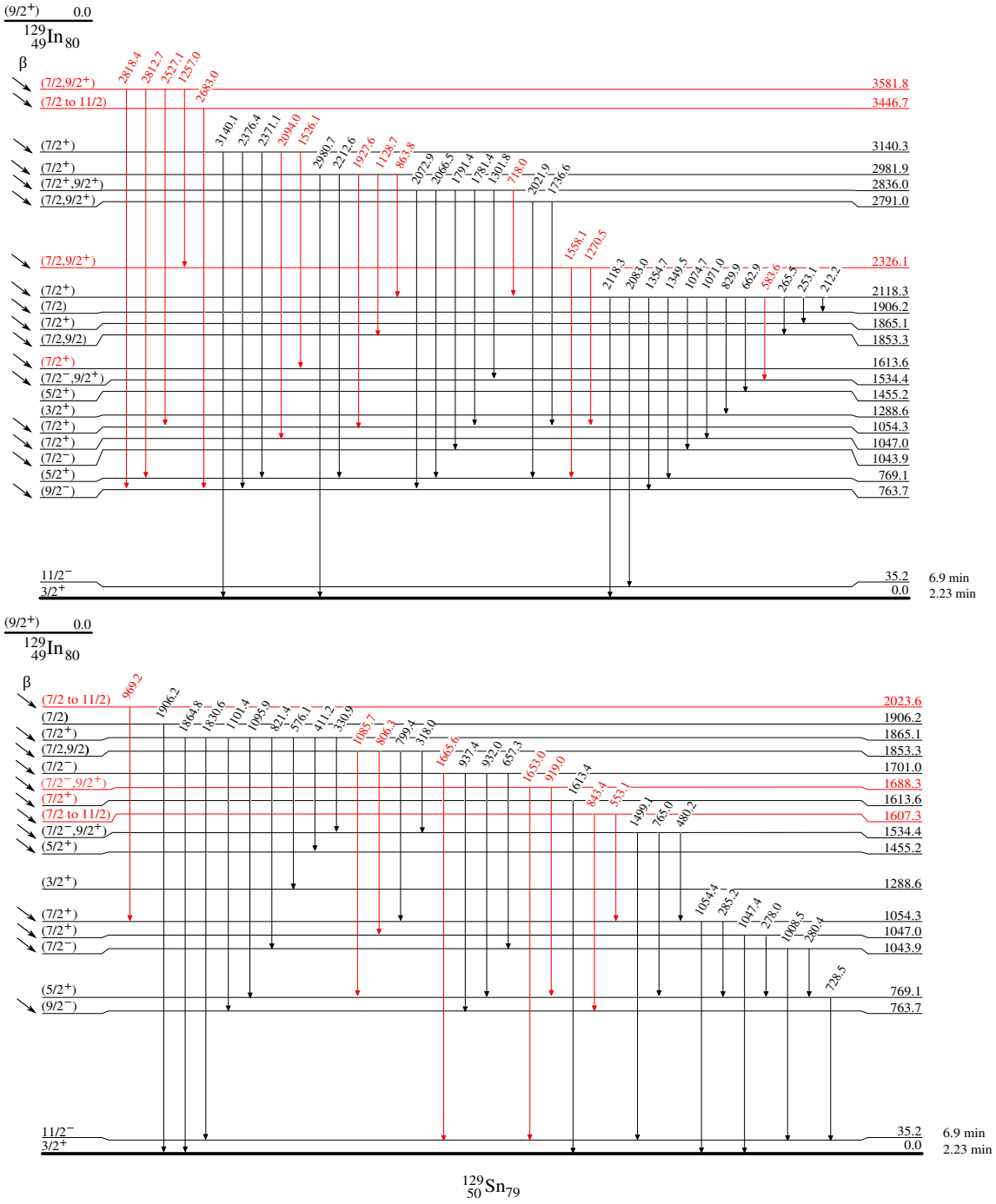

Figure 3.9: The level scheme of ^{129}Sn, populated through the β-decay of the ground state of ^{129}In. The colour (red) represents new transitions and levels found in this work. For the case of the 1614-keV state, the coloured $(7/2^+)$ spin indicates a spin assignment to a previously observed level. The half-lives of the ground state and the ^{129m1}Sn 35-keV isomer are 2.23(4) min and 6.9(1) min, respectively, as given by Timar, Elekes and Singh [60]. Information about γ-ray intensities and their uncertainties can be found in Table 3.3. Reprinted figure with permission from Ref. [63]. Copyright (2021) by the American Physical Society.

The β-feeding intensities, along with the logft values are shown in Table 3.5. Recall that the β-feeding values are calculated from the intensity balance calculation, attributing any excess intensity to β-feeding.

This work was not sensitive to the direct feeding of the 35-keV $(11/2^-)$ isomer of ^{129}Sn, and since the $(9/2^+)$ ground state of ^{129}In is able to populate this state, a normalization is required. Gausemel *et al.* [55] observed a $< 10\%$ direct feeding to this $(11/2^-)$ state, this analysis is normalized to reflect 95(5)% feeding to excited state in ^{129}Sn.

Table 3.5: The β-feeding intensities and logft values calculated for states in ^{129}Sn, observed through the β-decay of the $(9/2^+)$ ^{129g}In state. Columns denoted by Ref. [55] contain values established in the work of Gausemel *et al.* Reprinted table with permission from Ref. [63]. Copyright (2021) by the American Physical Society.

E_x (keV)	I_β (%)		logft	
	This work	Ref. [55]	This work	Ref. [55]
763.7(1)	2.03(8)	2.1(4)	6.42(2)	6.4(1)
1043.9(1)	1.95(8)	2.0(4)	6.36(2)	6.4(1)
1047.0(2)	0.30(4)	0.35(6)	7.17(6)	7.1(1)
1054.3(2)	1.62(10)	2.1(3)	6.43(3)	6.33(7)
1534.4(2)	0.60(9)	0.46(6)	6.72(7)	6.85(6)
1607.3(3)	0.14(2)		7.32(7)	
1613.6(3)	0.88(3)		6.53(2)	
1688.2(3)	0.20(2)		7.15(4)	
1701.0(2)	0.52(5)	0.24(2)	6.73(5)	7.08(4)
1853.3(2)	0.85(5)	0.76(6)	6.47(3)	6.53(4)
1865.1(1)	37.6(3)	36(2)	4.82(1)	4.85(3)
1906.2(2)	0.18(3)	0.13(3)	7.12(8)	7.3(1)
2023.6(4)	0.48(3)		6.66(3)	
2118.3(1)	46.9(3)	49(3)	4.64(1)	4.63(3)
2326.1(4)	0.06(2)		7.48(14)	
2791.0(3)	0.39(15)	0.47(9)	6.47(2)	6.4(1)
2836.0(2)	3.53(5)	3.36(15)	5.50(1)	5.54(2)
2981.9(2)	1.01(4)	0.74(5)	5.99(2)	6.14(3)
3140.3(2)	0.99(4)	0.67(4)	5.93(2)	6.11(3)
3446.7(4)	0.020(9)		7.5(2)	
3581.8(3)	0.19(3)		6.46(7)	

The spins of the newly observed levels, at 1607, 1688, 2023, 2326, 3446 and 3581 keV are assigned based on the β- and γ-decay selection rules outlined in Chapter 1. The states

at 1607, 2024 and 3446 keV are all shown to decay to states with spins between 7/2 and 9/2, and have logft values 7.34(8), 6.68(3) and 7.5(2), respectively, consistent with either allowed or first forbidden transitions and thus are tentatively assigned spins between (7/2) and (11/2). The newly observed 1688-keV state is shown to decay via a 919-keV transition to the $(5/2^+)$ 769-keV state and also via a 1653-keV transition to the $11/2^-$ 35-keV isomeric state, which means that its spin can be constrained to either $(7/2^-)$ or $(9/2^+)$, supported by the logft value of 7.15(4), indicative of a first forbidden transition. The aforementioned states are not observed to decay to lower-spin states, further supporting the tentative spin assignments.

The new states at 2326 and 3581 keV are observed to decay to the $(5/2^+)$ 769-keV state, among other transitions. This further constrains their tentative spin assignments to be either (7/2) or $(9/2^+)$. The logft values for these states are given as 7.48(14) and 6.46(7), respectively, consistent with the tentative assignments.

The 1614-keV state, though previously observed, was assigned a spin value between (1/2) and $(7/2^+)$ in the literature [65], where there was no observed evidence of β-feeding from the $(1/2^-)$ ^{129}In^{m1} parent. The work done by Gausemel et al. [55] observed a transition of 1977 keV from a state at 3591 keV, a state assigned as having a spin of $(3/2^-)$; this transition was verified in this work, as seen in Table 3.3 and Figure 3.9. A 1526-keV transition between the 3140-keV state and the 1614-keV state, was newly observed in this experiment, linking a state with a spin of $(7/2^+)$ to the 1614-keV state. This would rule out the lowest 1/2 spin assignment for the 1614-keV state. Finally, β-feeding was observed to this state, amounting to double the intensity of the 1977-keV transition from the 3590-keV state, unattributable to any other decay into this state. Thus the spin for the 1614-keV state is revised to be $(7/2^+)$ and is observed to be fed by the $(9/2^+)$ ^{129}In ground state. The 6.53(2) logft value supports this spin assignment.

3.5 ^{129m1}In decay

The half-life of the $(1/2^-)$ isomer, ^{129m1}In, was determined in the same manner described in Section 3.4.1. In this case, twelve transitions, found in Table 3.6, associated with this isomer, were added in order to produce a summed half-life curve. The resulting plot, seen in Figure 3.10 was fit, and returned a value of $t_{1/2}$ =1.16(1) s, which is reasonable agreement with the literature half-life of $t_{1/2}$ =1.23(3) s [60]. A chop analysis was also conducted and found no systematic effects.

Table 3.6: The transitions "added" to build the half-life graph shown in Figure 3.10. These were identified as transitions from states in ^{129}Sn populated by the ^{129m1}In isomer.

Transitions (keV)		
175.5(4)	1889.5(2)	2764.0(2)
315.4(2)	2035.6(3)	3078.7(3)
907.3(2)	2367.9(2)	3276.0(2)
1222.6(2)	2546.2(2)	3589.7(3)

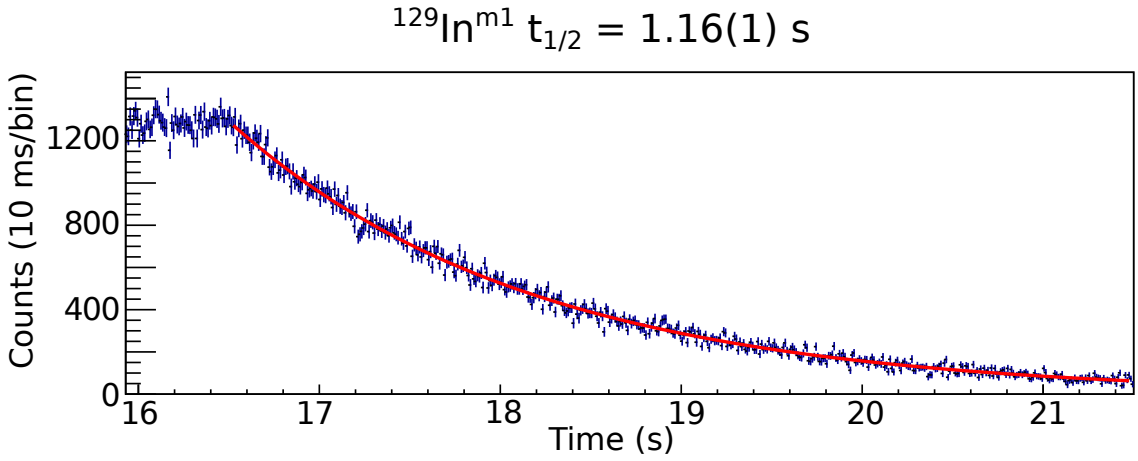

Figure 3.10: A spectrum of total counts as a function of cycle time, representing twelve transitions associated with the decay of ^{129m1}In into states in ^{129}Sn. The fit, seen in red (reduced-$\chi^2 = 1.5$), represents a value of $t_{1/2} = 1.16(1)$ s. Reprinted figure with permission from Ref. [63]. Copyright (2021) by the American Physical Society.

3.5.1 γ-ray transitions and β-feeding

Using the coincidence method, eight newly observed transitions and three excited states in ^{129}Sn were placed in the level scheme, populated by the decay of the 459-keV ^{129m1}In isomer and placed in the ^{129}Sn level scheme. Figure 3.11 shows the placement of the previously observed states and transitions, alongside those that were newly observed in this dataset.

As before, the β-feeding and logft values were calculated. With this information, tentative spins were assigned to the newly observed states, summarized in Table 3.7. Since the half-life value in literature and that measured in this experiment were not within error, a weighted average of $t_{1/2}$ =1.17(2) s was used to compute the logft values.

The previous work on this nucleus, by Gausemel *et al.* [55], observed a β-feeding to the $(3/2^+)$ ground state in ^{129}Sn of 77(15)%. Since this experiment was not sensitive to this direct feeding, the state feeding for this data subset, found in Table 3.7, is scaled to represent a 23% β-feeding to excited states in the ^{129}Sn nucleus.

The intensity balance calculated for the states at 769 and 1455 keV, both with spin $(5/2^+)$, indicated some β-feeding. This excess has been attributed not to unobserved γ-ray transitions to these states from higher levels, but rather solely to direct β-feeding from the ^{129m1}In isomer. The logft values, given in Table 3.7 as 9.27(9) and 9.52(6), respectively, support the previously assigned $(5/2^+)$ spin.

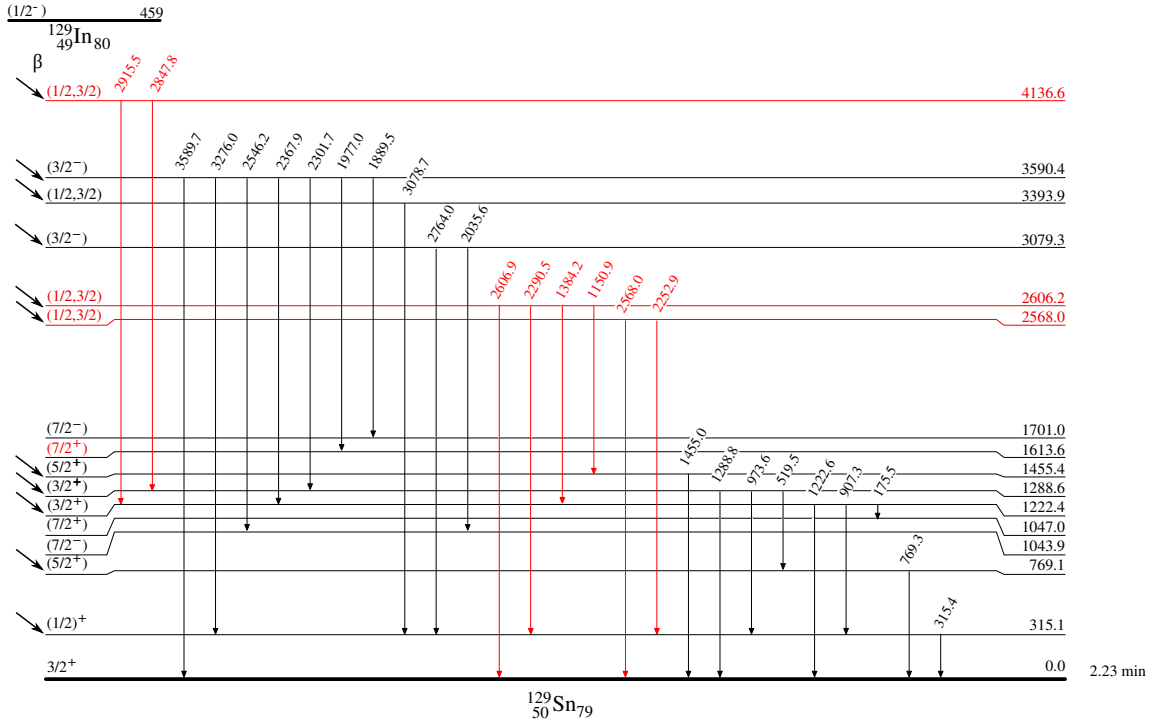

Figure 3.11: The level scheme of ^{129}Sn, populated through the β-decay of the $(1/2^-)$ 459-keV isomer of ^{129}In. The colour (red) represents new transitions and levels found in this work. The half-life of the ^{129}Sn ground state is 2.23(4) min, as given by Timar, Elekes and Singh [60]. Information about γ-ray intensity and their uncertainties can be found in Table 3.3. Reprinted figure with permission from Ref. [63]. Copyright (2021) by the American Physical Society.

Transitions observed between the newly observed 2568- and 2606-keV states, respectively, and the $(3/2^+)$ ^{129}Sn ground state indicate the spin of each of these states must be either 1/2 or 3/2, and must be fed by the $(1/2^+)$ 459-keV ^{129m1}In isomer. The logft values, 7.83(15) for the 2568-keV state and 7.16(5) for the 2606-keV state, shown in Table 3.7, support these spin assignments.

The state at 4137 keV is shown to decay via two transitions: a 2878-keV transition to the 1288-keV state and a 2916-keV transition to the 1222-keV state. Both of the states populated have a tentative spin assignment of $(3/2^+)$, indicating that the spin of this 4137-keV state should be either 1/2 or 3/2. Once more, the logft values are in line with either the allowed

Table 3.7: The β-feeding intensities and logft values calculated for states in ^{129}Sn, observed through the β-decay of the $(1/2^-)$ ^{129m1}In isomer. The values calculated in this work are compared to the values calculated by Gausemel *et al.* [55]. Reprinted table with permission from Ref. [63]. Copyright (2021) by the American Physical Society

E_x (keV)	I_β (%)		logft	
	This work	Ref. [55]	This work	Ref. [55]
315.1(2)	14.3(2)	15.1(13)	6.07(4)	6.10(4)
769.1(1) †	0.9(2)		9.27(9)	
1222.4(2)	1.52(4)	1.56(14)	6.80(4)	6.85(4)
1288.6(2)	0.63(9)	0.58(7)	7.17(7)	7.26(6)
1455.2(2) †	0.28(3)		9.52(6)	
2568.0(3)	0.06(2)		7.83(15)	
2606.2(2)	0.25(2)		7.16(5)	
3079.3(3)	0.29(2)	0.42(3)	6.93(5)	6.82(4)
3393.9(4)	0.22(1)	0.22(2)	6.93(4)	6.98(5)
3590.4(1)	4.70(6)	5.10(17)	5.52(4)	5.54(2)
4136.6(3)	0.127(9)		6.85(5)	

† Unique 1^{st} forbidden

or first-forbidden nature of the transitions expected from the $(1/2^-)$ first isomer of ^{129}In to these newly observed excited states in ^{129}Sn.

This work adds information about the β-feeding of the first isomer, ^{129m1}In to excited state in the ^{129}Sn daughter, as is shown in Table 3.7. Several newly observed β-feeding and logft values are assigned to previously observed states.

3.6 ^{129m2}In decay

The half-life for the $(23/2^-)$ ^{129m2}In isomer was obtained in the same manner as for the previously discussed isomer and ground state. In this case only four γ-rays were available with enough statistics to produce a meaningful fit, they are found in Table 3.8. The fit, shown in Figure 3.12, returned a value of 0.65(2) s (with $\chi^2 = 2.2$), which is in agreement with the literature value, quoted at 0.67(10) s [60], while greatly improving upon its uncertainty.

Table 3.8: Transitions used to build the half-life plot shown in Figure 3.12. These were identified as transitions from states populated by the ^{129}In^{m2} isomer.

Transitions (keV)			
382.4(2)	514.8(3)	2189.8(2)	2230.8(3)

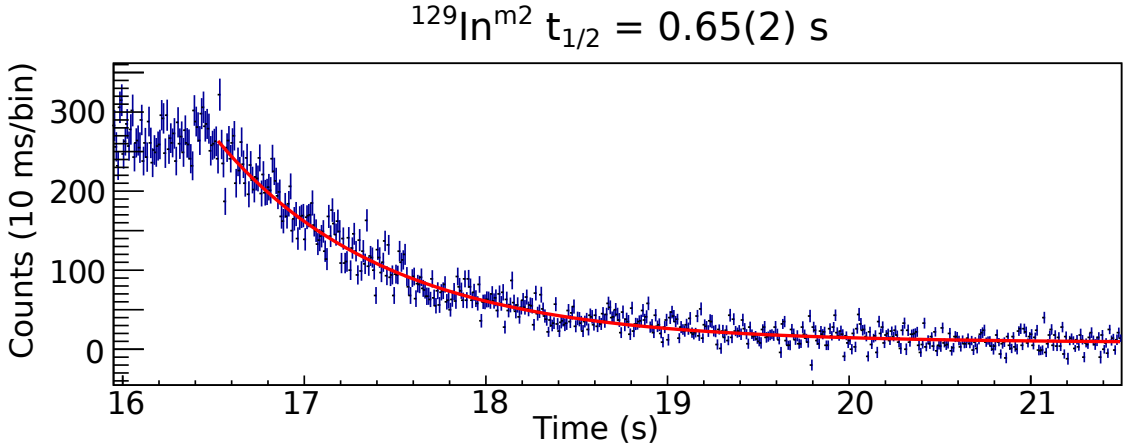

Figure 3.12: A spectrum of total counts as a function of cycle time, representing four transitions associated with ^{129m2}In decay into states in ^{129}Sn. The fit, seen in red, returned a value of $t_{1/2} = 0.65(1)$ s (with reduced-$\chi^2 = 2.2$). Reprinted figure with permission from Ref. [63]. Copyright (2021) by the American Physical Society.

3.6.1 γ-ray transitions and β-feeding

One transition was newly observed from a previously observed state in ^{129}Sn, as fed by the 1630-keV $(23/2^-)$ ^{129m3}In. Two of the states populated by this ^{129}In isomer, at 1762 and 1803 keV, were observed indirectly, in that transitions feeding into the states were observed, but the two transitions known to depopulate these states, at 19.7(10) and 41.0(2) keV [60], were not observed due to high background present in the energy range below 50 keV.

Shown in Table 3.3, the branching ratios of γ-rays depopulating the the 3993- and 2275-keV states and populating the 1803- and 1762-keV states agree with those of the evaluated data set in Ref. [60]. However, the β-feeding value for the 2275-keV state is a factor of ten times smaller than the value reported in the evaluation.

Though direct calculation of the β-feeding of the 1803-keV state was unfeasible, an estimation was done based on the γ-ray intensities populating this state from above and those depopulating the states below. This method estimated an 11(4)% direct β-feeding component, which is consistent with the literature value of 14.4(4)%.

3.7 ^{129m3}In decay - new β-branch

While two ^{129}In isomers and the ground state have previously been shown to β-decay, there was no evidence that the higher lying $(29/2^+)$ isomer, ^{129m3}In at 1191 keV would undergo β-decay. Instead, this state was known to decay via an internal transition of 281-keV to the 1630 keV ^{129m2}In.

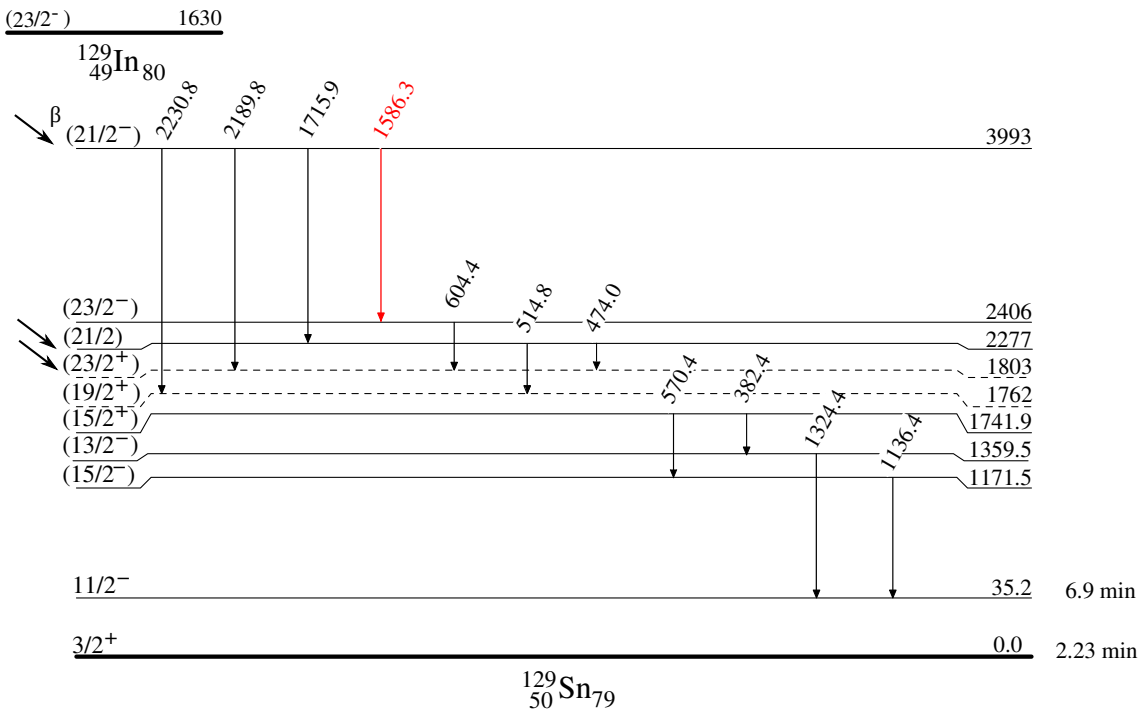

Figure 3.13: The level scheme of ^{129}Sn, populated through the β-decay of the $(23/2^-)$ ^{129}In. The colour (red) represents the newly observed transition found in this work. The half-life of the ^{129}Sn ground state is 2.23(4) min, as given by Timar, Elekes and Singh [60]. Information about γ-ray intensity and their uncertainties can be found in Table 3.3. The dashed lines are two known states, at 1761 keV and 1802 keV, whose energies are adapted from literature values [60]. Reprinted figure with permission from Ref. [63]. Copyright (2021) by the American Physical Society.

Table 3.9: The β-feeding intensities and logft values calculated for states in ^{129}Sn, observed through the β-decay of the $(23/2^-)$ ^{129m2}In isomer. The values are calculated in this work are compared to those calculated by Gausemel *et al.* [55].Reprinted table with permission from Ref. [63]. Copyright (2021) by the American Physical Society

E_x (keV)	I_β (%)		logft	
	This work	Ref. [55]	This work	Ref. [55]
1803(1)	10(4)	14(4)	5.88(18)	5.8(2)
2277(1)	0.5(3)	8.0(12)	7.1(3)	5.9(1)
3993(1)	89(4)	75(4)	4.27(5)	4.4(1)

This transition, if present in the clover addback spectrum in this dataset, would lie right on top of the two known transitions at 278 keV and 280 keV, depopulating the 1074- and 1044-keV states in ^{129}Sn, respectively.

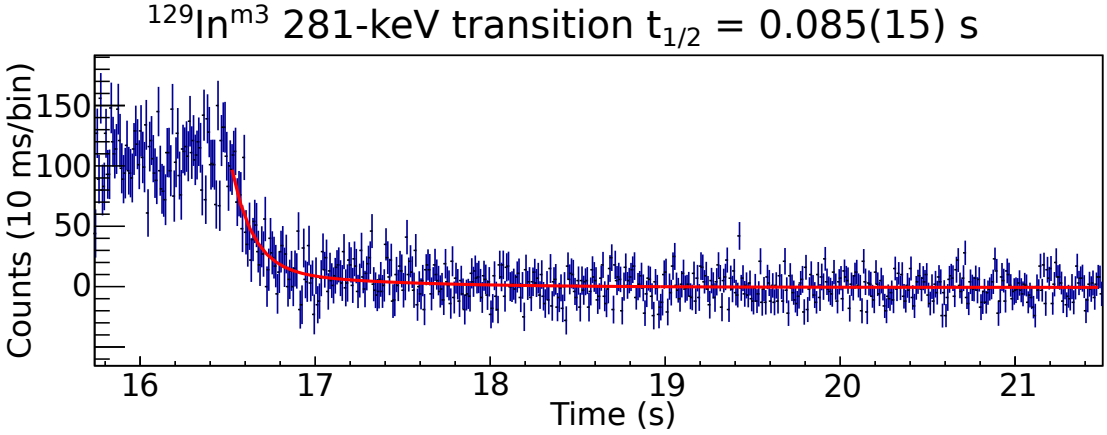

Figure 3.14: A spectrum of total counts as a function of cycle time for the 280-keV transition. The fit, in red and including a contribution related to ^{129gs}In, returned a value of $t_{1/2}$ = 0.085(15) s, which consistent with the half-life of the 1911-keV ^{129m3}In, quoted as 0.110(15) s [65]. The ^{129gs}In decay must be accounted for, since contributions from the 278- and 280-keV γ-rays in ^{129}Sn will be also be present in this energy range. The reduced χ^2 for this fit is 1.1. Reprinted figure with permission from Ref. [63]. Copyright (2021) by the American Physical Society.

There was, in fact, a discrepancy between the previously measured intensities of the 278- and 280-keV γ-ray transitions, observed by Gausemel *et al.* [55] and those measured in this work, centered around 280 keV. The relative intensity value in this energy range was calculated to be 0.0805(4), much higher than expected. To determine the true intensities of the 278- and 280-keV γ-ray transitions, the gating from below method described in Chapter 2 Section 2.3.4 was used. For the intensity of the 278-keV transition, the gate was placed at 769 keV, which is the γ-ray transition that depopulates the 769-keV state. A gated relative intensity of 0.0081(10) was obtained. For the 280-keV transition, the 728-keV transition from the 764-keV state was used, returning a relative intensity of 0.0068(8). This left a discrepant relative intensity of 0.0657(11) at the energy centered on 280 keV.

Producing an energy vs time plot, like those produced for the half-lives of the other isomers and the ground state, confirmed that this was the internal transition of ^{129m3}In. Figure 3.14 shows the resulting plot, with the fit returning a half-life value of this transition as 0.085(15) s, consistent with the 0.110(15) s half-life previously measured. The fit contained a contribution associated with the ^{129}In ground state decay, since the 278- and 280-keV transitions are expected to contribute counts to this energy gate. This was done by modifying Equation 3.1, to contain another exponential term associated with the ground state half-life.

The spin of this 1911-keV ^{129m3}In isomer is assigned as $(29/2^+)$, meaning that, based on the β-decay selection rules, it can only populate very high spin states. A $(27/2^-)$ state at 2552 keV was previously observed in ^{129}Sn; Lozeva *et al.* [57] observed this state, in the

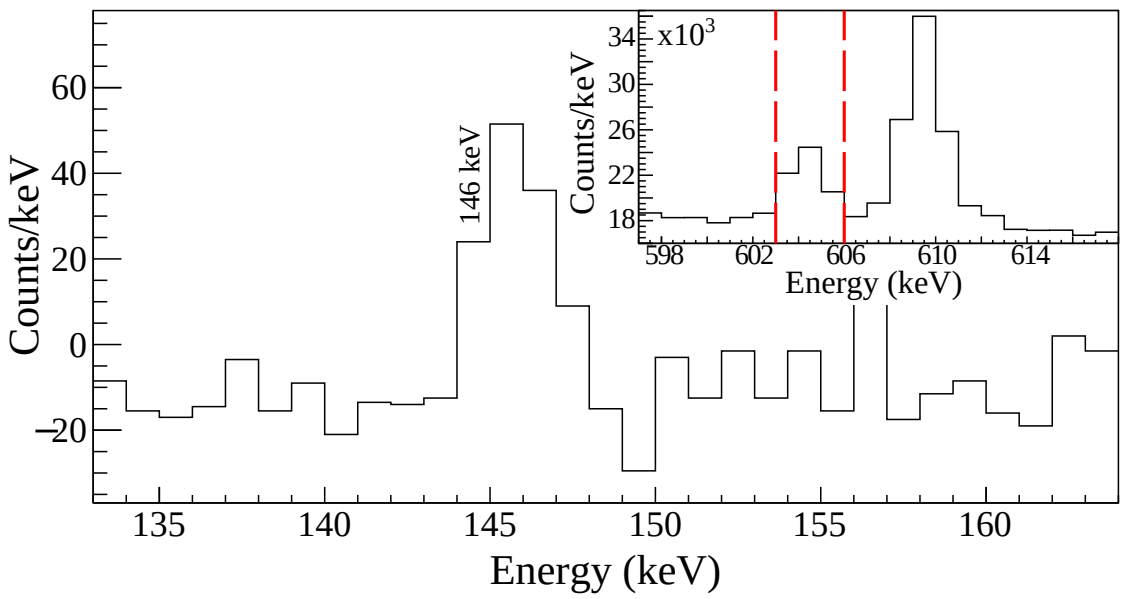

Figure 3.15: Spectrum showing the coincidence of the γ-ray transition at 146 keV with the 604-keV transition. The inset shows the gate, with the dashed lines showing the placement of the gate. The main graph shows a clear peak at 146 keV. Reprinted figure with permission from Ref. [63]. Copyright (2021) by the American Physical Society.

population of ^{129}Sn states via ^{136}Xe fragmentation and ^{238}U fission. This state was shown to decay through a 146-keV γ-ray transition, down to the $(23/2^-)$ state at 2406-keV. Through gating on the 604-keV transition from the 2406-keV state, the 146-keV was observed, as shown in Figure 3.15.

Performing an intensity balance of the 2552-keV state indicates some β-feeding, since there is excess intensity between the transitions populating and depopulating the state. No higher lying state observed in ^{129}Sn thus far can populate the 2552-keV, due to its high spin, $(27/2^+)$, and the β-decay selection rules. This then means that the β-feeding is equivalent to the intensity of the 146-keV transition, since nothing else can cause this excess intensity.

The feeding of this state would then be the intensity of the 146-keV with respect to the sum of intensity between the 281-keV internal transition and 146-keV γ-ray — which would both require correction for internal conversion. The comparison between the β-feeding of the 2552-keV state and the intensity of the 281-keV internal transition yields a β-branching ratio of 2.0(5)%. The logft value calculated for the decay from the $(29/2^+)$ ^{129m3}In at 1911 keV to the $(27/2^-)$ state at 2552 keV in ^{129}Sn is calculated to be 5.68(12), characteristic of a first forbidden transition and in line with the spin change required. This logft value is also similar to the 5.88(18) value observed in this work, between the 1630-keV ^{129m2}In and 1803-keV state in ^{129}Sn. This value is expected, since the β-decay transition would be of a $\pi(g_{9/2})^{-1} \rightarrow \nu(h_{11/2})^{-1}$ character. The logft of this transition is also consistent with that 5.8 value reported by Gausemel *et al.* for the same state [55].

The proposed level scheme for the ^{129m3}In decay is shown in Figure 3.16.

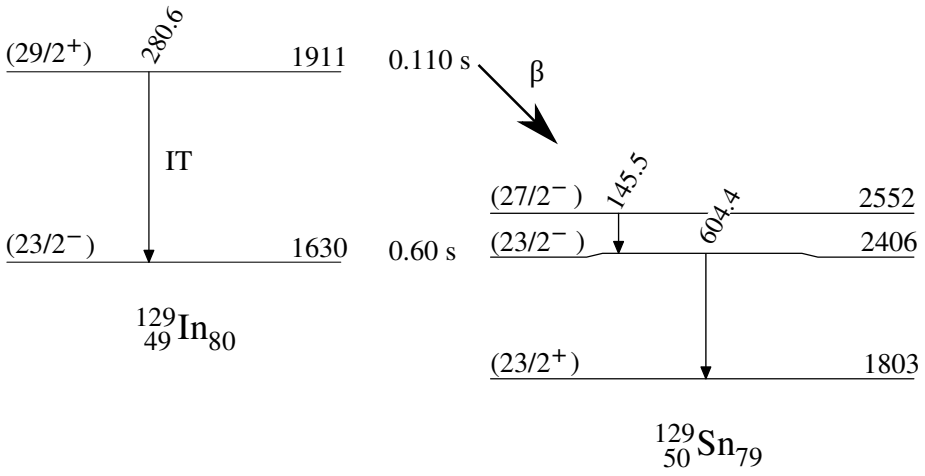

Figure 3.16: Partial level scheme showing the decay of the $(29/2^+)$ 1911-keV ^{129m3}In isomer into the $(27/2^-)$ 2551-keV state in ^{129}Sn. The intensity of the 146-keV transition was obtained in coincidence with the 604-keV transition. Reprinted figure with permission from Ref. [63]. Copyright (2021) by the American Physical Society.

This represents the first observation of the ^{129m3}In isomer undergoing β-decay to excited state in ^{129}Sn.

3.8 Isomeric Ratio

The ratio of ground and isomeric states in the beam can be inferred by the β-feeding observed in states fed only by each of the components. The β-decay selection rules can be used to determine which states are populated by the components, for example, the $9/2^+$ ^{129gs}In can only reasonably feed states with spins 7/2 and 11/2, while the $(1/2^-)$ ^{129m1}In isomer can only reasonably feed states with spins between 1/2 and 5/2. Using this methodology, four states with distinct spins can be isolated in order to establish the isomeric ratio.

The 2118-keV state in ^{129}Sn has a tentative spin of $(7/2^-)$, and thus is mostly likely populated solely by the $(9/2^+)$ ^{129}In ground state; the 315-keV state has a tentative spin of $(1/2^+)$ and is most likely populated by the $(1/2^-)$ ^{129m1}In isomer; the $(21/2^-)$ 3992-keV state can only be populated by the $(23/2^-)$ ^{129m2}In; the $(29/2^+)$ ^{129m3}In isomer was observed to populate the $(27/2^-)$ 2552-keV state.

By taking the balance of γ-ray intensities populating and depopulating a particular state, and then factoring in the observed β-feeding intensities, the fraction of the component in the beam can be determined. This can be done for the 2118- and 315-keV state, but the 2552- and 3992-keV states require that the internal conversion of the 281-keV internal transition be taken into account.

Based on this intensity balance, the beam contained approximately 41% $9/2^+$ ground state, 54% $(1/2^-)$ ^{129m1}In, 3% $(23/2^-)$ ^{129m2}In and 1% $(29/2^+)$ ^{129m3}In.

3.9 Conclusion & Future work

The ^{129}In and ^{129}Sn isotopes are of special importance to the development of the nuclear shell model, since they lie very close to doubly-magic ^{132}Sn.

Through the above described spectroscopy experiment, new information was uncovered. A comprehensive study observed 31 γ-ray transitions and 9 excited states for the first time. The β-feeding analysis allowed for the tentative spin assignments of newly observed levels, with the study further constraining the spin of a previously observed level considerably. Most notably, a new β-decay branch in ^{129}In, from the 1911-keV state was observed for the first time in this study, further expanding the knowledge of the species in this region. Future work in this region must include the firm spins assignments through techniques such as angular correlations, as well as the push to observe new states and transitions in heavier indium and tin isotopes. Pushing towards the neutron-drip line, the ^{134,135}In isotopes can be used to study ^{133,134}Sn, through the β-delayed neutron emission process, with ^{135}In being a good candidate for β-delayed 2 neutron emission, a very rare process, that may ultimately prove to be more common within the region close to the neutron drip line.

The information added through this study will help to round out the region, particularly where it pertains to this new β-decaying branch. Given that this is a region of magicity, lying very close to ^{132}Sn, any cohesive nuclear theory must be able to accurately reproduce the energy states of the isotopes in this region.

This study will also aid in the study of nuclear astrophysics, since ^{129}Sn lies very close to the $A \sim 130$ solar system abundance peak, associated with neutron magic number $N = 82$. This abundance peak is key to understanding the rapid neutron capture (r-process) which is responsible for the formation of heavy isotopes in stellar environments [67]. Beta-decay properties are important inputs provided to astrophysical models in order to track nucleosynthesis in environments we cannot directly replicate here on Earth. The more available data, the better the models that can be developed in order to understand the formation and disintegration of not only the small buildings block of the universe, but also the largest structures in our cosmos.

Chapter 4

Spectroscopy of ^{80}Ga

The regions around the magic numbers are rich in interesting phenomena, such as shape coexistence and shell evolution. The study of these regions is key since a cohesive theory of nuclear structure must, at the very least, be able to describe the properties and energy levels of these important nuclei. In order to benchmark nuclear theories, experimental data on these key nuclei must be gathered and understood.

The area around the doubly magic ^{78}Ni, $Z = 28$ and $N = 50$, nucleus is one such region, which also lies close to the neutron drip line. The ^{80}Ge nucleus lies in this region, with $Z = 32$ and $N = 48$, and as a result it is of interest to experimental and theoretical nuclear science.

Excited states of ^{80}Ge were populated via the β-decay of ^{80}Ga, and their decay radiation studied at the GRIFFIN facility. The analysis techniques and methodology used to analyze this dataset are those described in Chapter 2, and follow the same prescription as the ^{129}In and ^{129}Sn analysis in Chapter 3. The spectroscopy dataset was quite rich and uncovered numerous previously unobserved transitions and excites states. The spectroscopy work will be submitted to Physical Review C in the coming months.

Alongside the γ-ray spectroscopy data, conversion electron data was gathered to investigate low-energy shape coexistence in this nucleus. Motivation and results from this study are found in Section 4.8. The findings on low-energy shape coexistence in ^{80}Ge have been published in Physical Review Letters[2]. The full article is found in Appendix B.

---

[2] **Garcia, F. H.** and Andreoiu, C. and Ball, G. C. and Bell, A. and Garnsworthy, A. B. and Nowacki, F. and Petrache, C. M. and Poves, A. and Whitmore, K. and Ali, F. A. and Bernier, N. and Bhattacharjee, S. S. and Bowry, M. and Coleman, R. J. and Dillmann, I. and Djianto, I. and Forney, A. M. and Gascoine, M. and Hackman, G. and Leach, K. G. and Murphy, A. N. and Natzke, C. R. and Olaizola, B. and Ortner, K. and Peters, E. E. and Rajabali, M. M. and Raymond, K. and Svensson, C. E. and Umashankar, R. and Williams, J. and Yates, D., *Absence of Low-Energy Shape Coexistence in ^{80}Ge: The Nonobservation of Proposed 0_2^+ at 639 keV*, *Physical Review Letters*, 125, 17, 172501 (2020).

4.1 Previous studies

Due to its vicinity to doubly-magic ^{78}Ni, the ^{80}Ge nucleus has been extensively studied. Hoff [68] undertook the study of this isotope through the β-delayed neutron emission of ^{81}Ga, at the OSIRIS facility. By examining the decay curves of each γ-ray, he was able to identify them as belonging to ^{80}Ge. However, the experiment suffered from a lack of statistics and consequently only a small number of transitions and excited states could be identified.

Soon after this study, Hoff and Fogelberg [69] were able to establish higher lying states, from the β-decay of the ^{80}Ga parent. With a set of lithium drifted germanium, Ge(Li), detectors, they observed states at 1573 and 1743 keV, tentatively assigning spins as 2^+ and either 0^+ or 4^+, respectively. They subsequently discounted the 0^+ assignment for the latter, since no strong transitions through the $0^+ \rightarrow 2^+ \rightarrow 0^+$ cascade were observed, as would have been expected if the spin and parity of the 1743-keV state were 0^+. The spins of the ground state and the previously observed 659-keV state were assigned 0^+ and 2^+, respectively. They noted that based on the isotopic systematics, a low lying 0^+ was expected but not observed, likely due to the high spin ground state in ^{80}Ga, which they ascribed as 3 or higher. They noted that they did not observe an expected isomer, having searched for it by comparing the β-decay of ^{80}Ga into ^{80}Ge to the β-decay chain of ^{80}Zn$\rightarrow$ ^{80}Ga $\rightarrow$ ^{80}Ge — the ground state of ^{80}Zn is given as 0^+, such that any population of the subsequent ^{80}Ga and ^{80}Ge is exclusive to low spin states. At this stage, the ground state spin of the ^{80}Ga parent was still undetermined, though the prevailing thought was that it must be high.

A study by Winger *et al.* [70], using a set of HPGe detectors, observed various transitions, adding to the level scheme. Based on logft values, they assigned a spin of 3^+ to the ^{80}Ga ground state, in apparent agreement to the work of Hoff and Fogelberg.

Through deep inelastic scattering, Makishima *et al.* [71] were able to identify the 8^+ and 6^+ states in ^{80}Ge, at 3445 and 2978 keV, respectively, expanding the information on the yrast band – the band composed of the energy states with lowest energy for a given angular momentum. This 8^+ state was found to be isomeric in nature, as expected by systematics of isotones in this region (^{84}Kr to ^{94}Pd), and was described as the two neutron hole state, $\nu(g_{9/2}^{-2})$. Given the population of this 8^+ state, it was implied that there must be a high-spin isomer in the ^{80}Ga β-parent. This was in contravention of the study by Hoff and Fogelberg, who explicitly noted the nonobservation of the expected isomeric state in ^{80}Ga.

Using heavy-ion scattering Iwasaki *et al.* [72] were able to gain further information on the transition probably between the 1573-keV 2_2^+ state and the 0^+ ground state. Their work indicated that the $2_2^+ \rightarrow 0_{gs}^+$ transition is dominated by proton excitation. Padilla-Rodal *et al.* [73] were able to investigate the transition probability between the ground state and the 659-keV 2_1^+ excited state through Coulomb excitation. In their work, they observed reduced transition probabilities in ^{78,80}Ge that were lower than those expected from shell model

calculations, highlighting the importance of an accurate description and model of the *pn* interaction.

Some years later, Cheal *et al.* [74], through collinear laser spectroscopy uncovered the presence of a low-lying isomer in ^{80}Ga, along side the ground state, with a half-life larger than 200 ms. Based on their observations, the preferred spin for this state was 3^-, but they could not firmly establish whether this was the ground state or the isomer. Coupling their laser spectroscopy set-up to ISOLTRAP (for mass measurements), they concluded that the isomer had to be within 50 keV of the ground state. They also performed shell model calculations, using a ^{56}Ni core which reproduced 3^- and 6^- states, though the stacking of ground state and isomer appeared dependent upon the proton model space used. Based on their shell model calculations, they tentatively assigned the 6^- state as the ground state and the 3^- as the isomer.

The most recent comprehensive spectroscopy of ^{80}Ge was performed by Verney *et al.* [75] at the ALTO facility [76]. They produced the ^{80}Ga β-decay parent through electron bombardment of a uranium carbide target and had a series of HPGe detectors for γ-ray detection. They concluded that the level schemes populated by the parent ground state and isomer of ^{80}Ga were fragmented and very interlinked, making their separation difficult. Setting out several assumptions, including the presence of only two β-decaying states in ^{80}Ga, that they were both negative parity states, and the observation of direct feeding and indirect feeding, they were able to assign excited states in ^{80}Ge as being uniquely populated by either the ground state or the isomer in ^{80}Ga.

The importance not only of the region surrounding ^{78}Ni, but the ^{80}Ge isotope itself is shown by the large number and methods of study. A recent study by Gottardo *et al.* [77], also carried out at the ALTO facility, observed the presence of a 0^+ excited state at 639 keV, much lower than that expected by the systematics of this region, and heralded the presence of shape coexistence in this nucleus. However, they were unable to locate a transition between this state and the 2_2^+ state at 1573-keV, nor were they able to observe further states in this "deformed" band, despite locating a coincidence between a 628-keV conversion electron peak and a 1764-keV γ-ray, depopulating a proposed 2^+ state at 2403-keV.

In her doctoral work, A. M. Forney [78] studied this nucleus, alongside ^{78,82}Ge, through deep inelastic scattering, in context of the structure of ^{76}Ge, and confirmed and constrained spins proposed in the work by Hoff and Fogelberg [69]; shell model calculations accompanied the experimental data, concluding that the effective interactions used were suitable in describing the observed levels in ^{80}Ge, save for the 0_2^+ at 639-keV observed by Gottardo *et al.* [77], which was not within the model space used. However, the experimental data also did not reveal the presence of this state.

Efforts to corroborate the presence of this 0_2^+ 639-keV state as well as to find states built upon this band, and the transitions linking them, were required to gain more informa-

tion about this nucleus. The targeted results from the GRIFFIN study to search for these signatures of low-energy shape coexistence will be discussed later, in Section 4.8.

4.2 Experimental details

The ISOL technique as employed at TRIUMF was used to produce the ^{80}Ga parent isotope, as described in Chapter 2. A 480 MeV proton beam with a current of 9.8 μA bombarded a Uranium Carbide (UC_x) target to produce isotopes, while IGLIS was used in order to selectively ionize the ^{80}Ga isotope of interest. A strong contamination of ^{80}Rb was observed during this experiment, at 78% of the delivered beam content, leaving 22% of the beam in the ^{80}Ga parent, in both the ground state and isomer. The beam was delivered to the GRIFFIN spectrometer, which, for the purposes of this experiment was outfitted with 15 out of the possible 16 HPGe detectors, the PACES array for conversion electron spectroscopy, the ZDS detector for β-tagging and the $LaBr_3$(Ce) array for fast timing measurements. A 10 mm Delrin shield was placed around the central vacuum chamber to protect the HPGe detectors from high-energy β-particles and to reduce the detection of Bremsstrahlung radiation.

At the time of the experiment, GRIFFIN had been outfitted with the BGO shields for background suppression, and as such it was placed its optimal peak-to-total mode, with each of the HPGe detectors sitting at 14.5 cm from the implantation spot. The cycling mylar tape system was employed to remove background decays, as it moved into the lead shielded box after each cycle. The cycles for this isotope were set to the following sequence: 1.5 s of tape move, 1.0 s of background collection, 15 s of beam implantation and 10 s of beam decay, for a total of 27.5 s per cycle. Data was collected over 51 hrs at a rate of 2×10^4 particles per second. The coincidence window for this experiment was set to 400 ns for both $\gamma-\gamma$ events and $\beta-\gamma$ events.

4.3 Gamma-ray spectroscopy of ^{80}Ge

The γ-ray dataset collected for ^{80}Ge was quite extensive, allowing for a thorough spectroscopic study. This data was treated as described in Chapter 2, with some added modifications to the process, given that the dataset spans a larger set of γ-ray energies.

4.3.1 High-energy Calibration

The efficiency curve was obtained and the energy calibration was performed in a similar manner to that of the ^{129}In dataset, in Chapter 3, using standard sources of ^{56,60}Co, ^{152}Eu and ^{133}Ba, with a $\chi^2 = 1.52$. Based on this efficiency curve, the efficiency of the GRIFFIN array in crystal singles mode for this experiment was calculated to be 5% at 1332 keV. However, the dataset had the added complexity of having several known γ-rays above 3.6 MeV (the upper limit of the calibration).

To obtain the systematic error at high-energy, the ADC nonlinearities were first characterized by using the known literature values of transitions in ^{80}Ge and extracting the experimental data above 2.7 MeV. The systematic uncertainty was then computed by comparing the energy difference between the states depopulated and populated by the transition, respectively, and the energy of the transition as measured from the spectra; the energy of the states and their uncertainties are obtained from a fit of the entire level scheme. The transitions examined are found in Table 4.1. From this, a systematic uncertainty above 3.6 MeV of 0.44 keV was established, and added, in quadrature, to the uncertainty in fitting the photopeak.

Table 4.1: High energy systematic uncertainty, determined from known transitions in ^{80}Ge. The γ-ray enegy values are obtained from this experimental dataset.

E_γ (keV)	E_i (keV)	E_f (keV)	Difference
2764.430	3423.6	659.213	-0.03
3664.445	4323.8	659.213	0.16
4678.912	5338.1	659.213	-0.02
5387.977	6047.6	659.213	0.44

In order to account for the detector efficiency at high energies, the GRIFFIN Efficiency Calculator [46] was used to extend the efficiency curve to 7.8 MeV. The Efficiency Calculator is based upon GEANT4 simulations and can be used to calculate simulated efficiencies using various detector set-ups. The calculation required information on the experimental configuration — 15 HPGe clover detectors, at 14.5 cm, with the full BGO shields in place and the 10 mm Delrin absorber surrounding the vacuum chamber. The crystal singles efficiency values obtained from the calculator are given in Table 4.2, with the uncertainty at high-energy taken from the last known calibration point at 3.6 MeV. These were then scaled to fit the experimentally observed efficiency calibration and the entire curve fit to produce a $\chi^2 = 0.83$, the fit is shown in Figure 4.1. This high-energy efficiency curve was then applied to the transitions above the 3.6 MeV calibration threshold.

4.4 γ-ray analysis

The γ-ray spectrum, in crystal singles, observed during this experiment is shown in Figure 4.2. Transitions were examined up to the neutron separation energy of ^{80}Ge (S_n = 8.08 MeV [79]).

Figure 4.3 shows the γ-γ coincidence matrix, constructed with a 400 ns window, used to verify transitions as well as to determine γ-ray intensities in coincidence.

Analysis of the observed transitions uncovered a large number of γ rays and excited states in ^{80}Ge. In total, 166 γ-ray transitions and 52 excited states were newly observed

Table 4.2: Simulated high-energy efficiency, obtained using the GRIFFIN Efficiency Calculator [46].

Energy (keV)	ϵ_{sim}	Scaled ϵ_{sim}
2600	0.0377	0.0346
3000	0.0333	0.0306
3400	0.0296	0.0272
3800	0.0265	0.0243
4200	0.0238	0.0219
4600	0.0215	0.0197
5000	0.0195	0.0179
5400	0.0177	0.0163
5800	0.0162	0.0149
6200	0.0148	0.0136
6600	0.0136	0.0125
7000	0.0125	0.0115
7400	0.0115	0.0106
7800	0.0106	0.0098

and placed in the level scheme. Additionally, 16 transitions that were previously observed but unplaced within the level scheme, have now been assigned to either known or newly observed states. Table 4.3 details the γ-ray information observed for ^{80}Ge, including excited states, proposed spins and parities and the branching ratios of each transition.

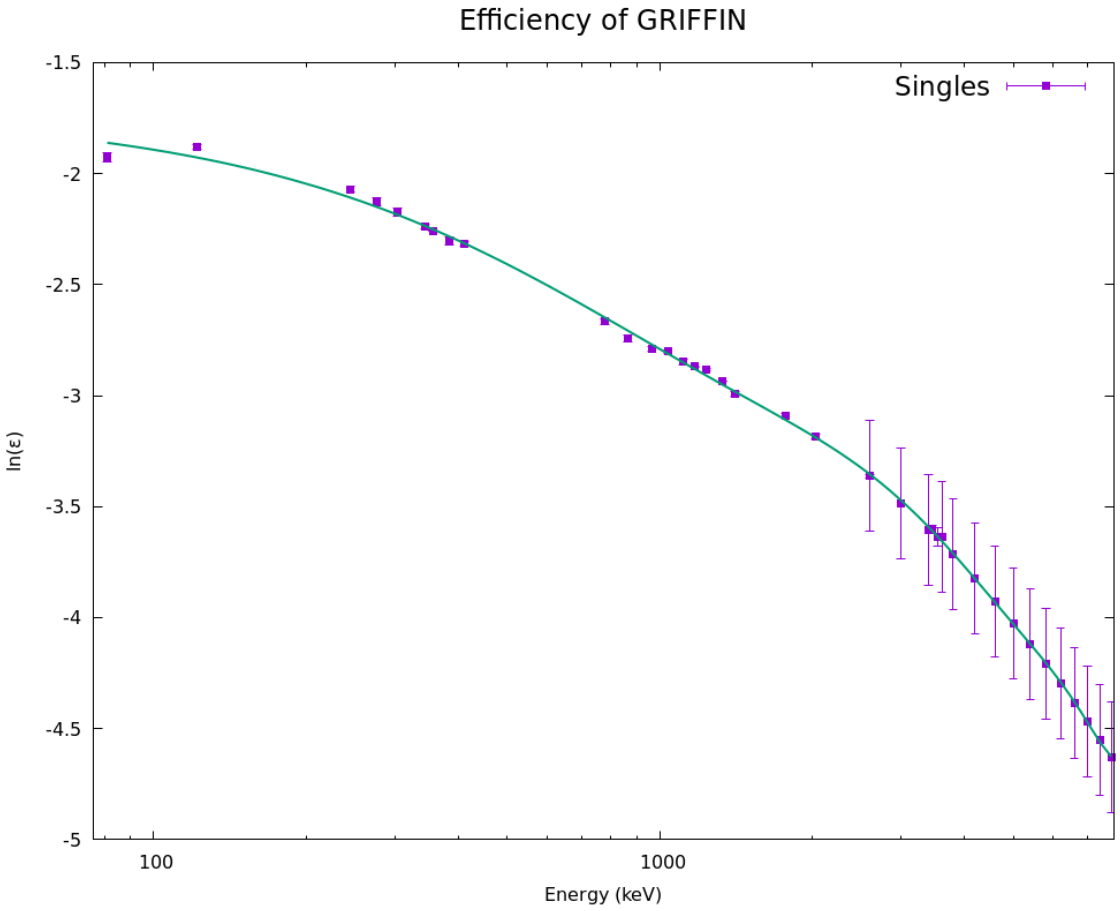

Figure 4.1: The relative efficiency, in crystal singles mode, obtained experimentally from 81 keV to 3.6 MeV and simulated between 2.6 MeV to 7.8 MeV. The simulated efficiency is calculated from the GRIFFIN Efficiency Calculator [46]. The fit returned a χ^2 value of 1.52.

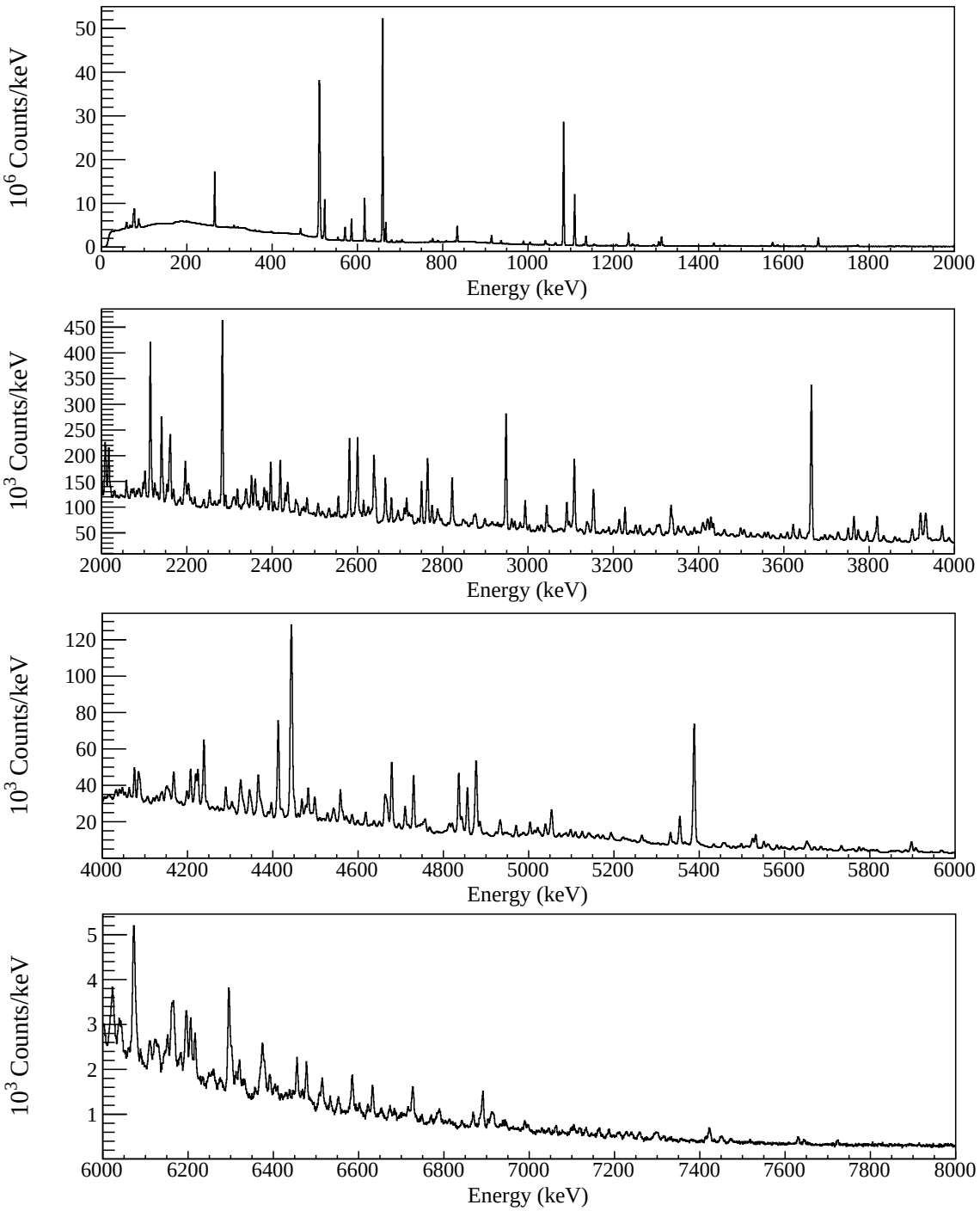

Figure 4.2: Full crystal singles γ-singles energy spectrum. The transitions from 81 keV through to 8 MeV were investigated, up to the neutron separation energy of ^{80}Ge.

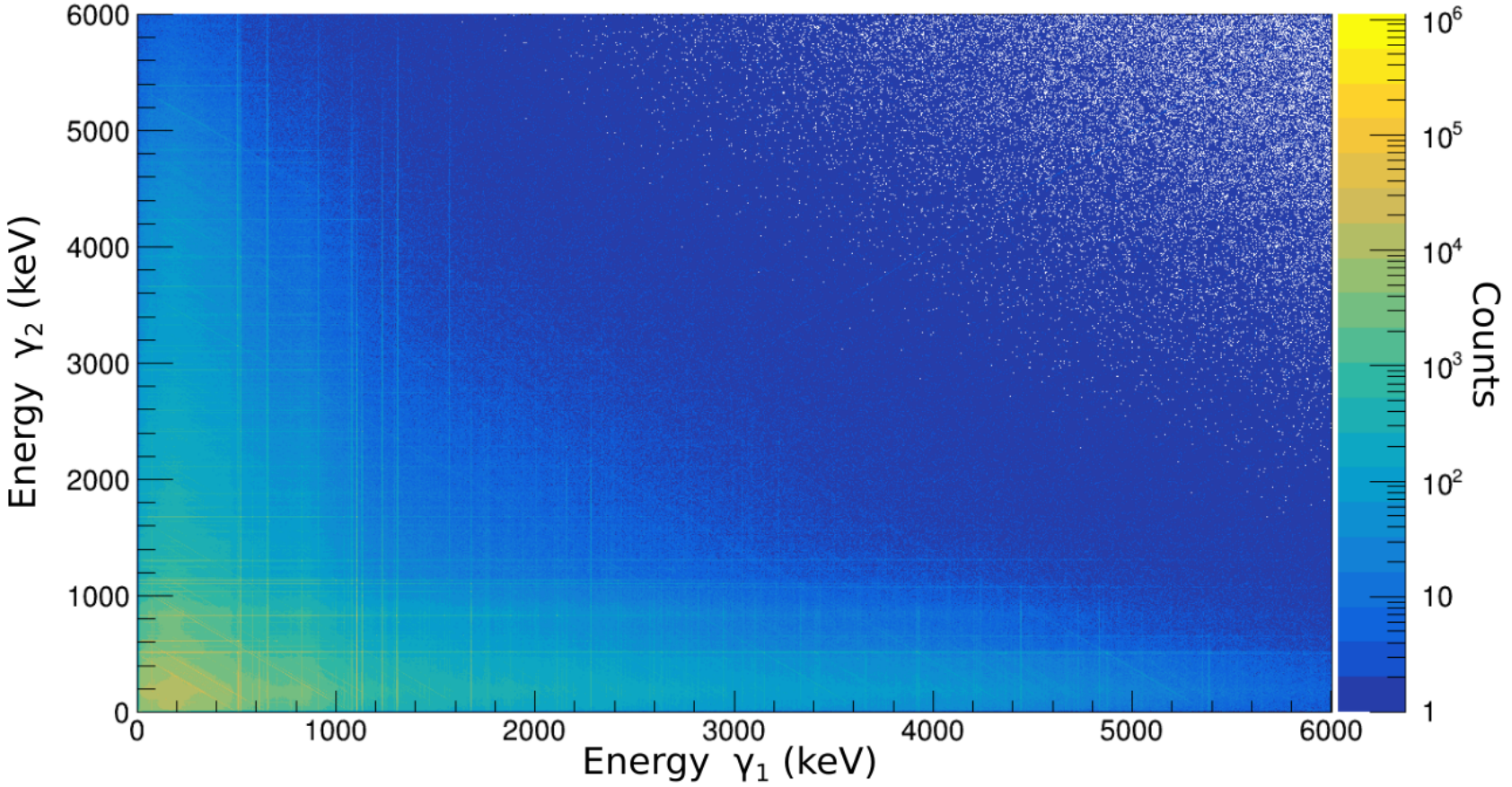

Figure 4.3: The γ—γ matrix, in crystal singles mode, constructed with a 400 ns window. The x- and the y-axes represent energies of coincident γ-rays, with the z-axis colour contour indicating the frequency of these coincidences.

Table 4.3: Intensity table for ^{80}Ge transitions observed in the β-decay ^{80}Ga experiment. All transitions have been normalized to the strongest transition, the 659-keV γ-ray, connecting the first excited 659-keV 2^+ state to the 0^+ ground state in ^{80}Ge. The level spins and parities are adopted from Ref. [69], unless otherwise stated.

E_i (keV)	E_γ (keV)	J_i^π	J_f^π	E_f (keV)	Rel. I_γ	BR_γ
0		0^+				
659.2(2)	659.2(2)	2^+	0^+	0	100.0(1.4)	100
1573.8(2)	914.5(2)	(2^+)	2^+	659.2(2)	3.94(6)	100(2)
	1573.7(2)	(2^+)	0^+	0	3.35(6)	85(2)
1742.5(2)	1083.6(2)	(4^+)	2^+	659.2(2)	75.7(12)	100
1972.1(2)	398.2(2)	$(3^+)^{\wr}$	(2^+)	1573.8(2)	0.448(7)	6.6(2)
	1313.1(2)	$(3^+)^{\wr}$	2^+	659.2(2)	6.76(12)	100(2)
2265.7(2)	293.8(2)	$(4^+)^{\wr}$	$(3^+)^\dagger$	1972.1(2)	0.192(4)	1.32(3)
	523.3(2)	$(4^+)^{\wr}$	(4^+)	1742.5(2)	14.6(2)	100.0(14)
	692.3(2)	$(4^+)^{\wr}$	(2^+)	1573.8(2)	0.655(10)	4.49(9)
2851.8(2)	586.2(2)	$(5^-)^{\wr}$	$(4^+)^{\wr}$	2265.7(2)	8.92(13)	28.1(6)
	1109.4(2)	$(5^-)^{\wr}$	(4^+)	1742.5(2)	31.7(5)	100(2)
2978.2(2)	1235.8(2)	(6^+)	(4^+)	1742.5(2)	9.05(2)	100
3036.7(2)	771.2(2)	$(5^+)^{\wr}$	$(4^+)^{\wr}$	2265.7(2)	0.571(9)	34.8(8)
	1064.4(2)	$(5^+)^{\wr}$	$(3^+)^{\wr}$	1972.1(2)	1.64(3)	100(2)
	1294.4(2)	$(5^+)^{\wr}$	(4^+)	1742.5(2)	0.90(2)	54.7(12)
3423.1(2)	571.0(2)	$(6^-)^{\wr}$	$(5^-)^{\wr}$	2851.8(2)	5.92(8)	100
3423.6(2)	1157.6(2)	$(3^-)^{\wr}$	$(4^+)^{\wr}$	2265.7(2)	0.807(15)	79(2)
	1451.8(2)†	$(3^-)^{\wr}$	$(3^+)^{\wr}$	1972.1(2)	0.38(5)	37(5)
	1849.5(2)	$(3^-)^{\wr}$	(2^+)	1573.8(2)	0.77(2)	75(2)
	2764.4(2)	$(3^-)^{\wr}$	2^+	659.2(2)	1.02(2)	100(2)
3445.3(2)	466.8(2)	(8^+)	(6^+)	2978.2(2)	2.10(3)	100
3472.0(4)	620.2(2)†	$(3^-, 4)^*$	$(5^-)^{\wr}$	2851.8(2)	0.089(10)	100
3498.3(2)	520.0(2)†	$(6^+)^{\wr}$	(6^+)	2978.2(2)	1.07(10)	100(9)
	1232.6(2)†	$(6^+)^{\wr}$	$(4^+)^{\wr}$	2265.7(2)	0.52(5)	49(7)

Table 4.3: *(Continued).*

E_i (keV)	E_γ (keV)	J_i^π	J_f^π	E_f (keV)	Rel. I_γ	BR_γ
3515.5(2)	1249.6(2)	$(4^-)^\wr$	$(4^+)^\wr$	2265.7(2)	0.369(7)	26.2(7)
	1772.9(2)	$(4^-)^\wr$	(4^+)	1742.5(2)	1.41(3)	100(2)
3685.8(2)	707.6(2)	$(7^-)^\wr$	(6^+)	2978.2(2)	0.301(6)	3.55(9)
	834.1(2)	$(7^-)^\wr$	$(5^-)^\wr$	2851.8(2)	8.48(13)	100(2)
3755.7(5)	3096.4(2)	$(2, 3, 4^+)^*$	2^+	659.2(2)	0.0066(2)	100
3882.8(3)	1030.9(2)†	$(3^-, 4)^*$	$(5^-)^\wr$	2851.8(2)	0.09(2)	74(14)
	1617.2(2)	$(3^-, 4)^*$	$(4^+)^\wr$	2265.7(2)	0.118(10)	100(9)
3913.3(3)	1941.7(3)	$(2, 3, 4^+)^*$	$(3^+)^\wr$	1972.1(2)	0.498(10)	100(2)
	2339.2(2)	$(2, 3, 4^+)^*$	(2^+)	1573.8(2)	0.252(6)	51(2)
3982.5(2)	559.1(2)	$(5)^*$	$(3^-)^\wr$	3423.6(2)	0.240(6)	21.0(6)
	1130.6(2)	$(5)^*$	$(5^-)^\wr$	2851.8(2)	1.14(2)	100(2)
	1716.8(2)	$(5)^*$	$(4^+)^\wr$	2265.7(2)	0.096(1)	8.4(3)
	2010.6(2)†	$(5)^*$	$(3^+)^\wr$	1972.1(2)	0.27(4)	24(3)
3987.7(2)	1136.0(2)	$(5, 6, 7^-)^*$	$(5^-)^\wr$	2851.8(2)	6.59(11)	100
4025.9(2)	1047.9(2)	$(5, 6^+)^*$	(6^+)	2978.2(2)	0.347(6)	19.0(5)
	2283.3(2)	$(5, 6^+)^*$	(4^+)	1742.5(2)	1.84(4)	100(2)
4138.7(2)	640.0(2)	$(5, 6^+)^*$	$(6^+)^\wr$	3498.3(2)	1.263(18)	100.0(14)
	1873.4(2)†	$(5, 6^+)^*$	$(4^+)^\wr$	2265.7(2)	0.123(12)	9.7(10)
	2396.6(2)‡	$(5, 6^+)^*$	(4^+)	1742.5(2)	0.563(12)	44.6(11)
4157.2(3)	1891.7(2)	$(2^+, 3, 4)^*$	$(4^+)^\wr$	2265.7(2)	0.099(4)	100(4)
	2184.7(2)	$(2^+, 3, 4)^*$	$(3^+)^\wr$	1972.1(2)	0.046(2)	46(3)
4173.2(3)	674.9(2)†	$(5 — 7)^*$	$(6^+)^\wr$	3498.3(2)	0.084(11)	30(4)
	1195.0(2)	$(5 — 7)^*$	(6^+)	2978.2(2)	0.276(5)	100(13)

Table 4.3: *(Continued).*

E_i (keV)	E_γ (keV)	J_i^π	J_f^π	E_f (keV)	Rel. I_γ	BR_γ
4323.8(2)	808.5(2)	$(3^-)^*$	$(4^-)^\wr$	3515.5(2)	0.613(10)	21(7)
	900.2(2)	$(3^-)^*$	$(3^-)^\wr$	3423.6(2)	0.400(7)	14(4)
	1471.9(2)†	$(3^-)^*$	$(5^-)^\wr$	2851.8(2)	0.46(3)	16(5)
	2058.1(2)	$(3^-)^*$	$(4^+)^\wr$	2265.7(2)	0.122(9)	4.2(14)
	2351.7(2)	$(3^-)^*$	$(3^+)^\wr$	1972.1(2)	0.367(9)	13(4)
	2581.2(2)	$(3^-)^*$	(4^+)	1742.5(2)	0.92(2)	32(10)
	2750.4(2)	$(3^-)^*$	(2^+)	1573.8(2)	0.495(11)	17(5)
	3664.4(4)	$(3^-)^*$	2^+	659.2(2)	2.9(9)	100(45)
4412.5(2)	989.5(2)	$(7^-)^\wr$	$(6^-)^\wr$	3423.1(2)	1.89(3)	100(2)
	1560.5(2)†‡	$(7^-)^\wr$	$(5^-)^\wr$	2851.8(2)	0.11(2)	5.9(10)
4422.5(3)	396.4(2)†	$(5 — 7)^*$	$(5, 6^+)^*$	4025.9(2)	0.113(12)	29(5)
	924.1(2)†	$(5 — 7)^*$	$(6^+)^\wr$	3498.3(2)	0.046(6)	12(2)
	999.4(2)†	$(5 — 7)^*$	$(6^-)^\wr$	3423.1(2)	0.39(5)	100(13)
	1444.6(2)	$(5 — 7)^*$	(6^+)	2978.2(2)	0.169(4)	44(6)
4518.7(3)	1002.6(2)†	$(5, 6^-)^*$	$(4^-)^\wr$	3515.5(2)	0.042(5)	18(2)
	1020.8(3)†	$(5, 6^-)^*$	$(6^+)^\wr$	3498.3(2)	0.020(3)	8.4(14)
	1481.9(2)	$(5, 6^-)^*$	$(5^+)^\wr$	3036.7(2)	0.240(6)	100(2)
4530.6(4)	1032.3(2)†	$(5 — 7)^*$	$(6^+)^\wr$	3498.3(2)	0.11(2)	100
4532.5(2)	1680.7(2)	$(5, 6, 7^-)^*$	$(5^-)^\wr$	2851.8(2)	7.86(14)	100
4615.2(2)	626.9(2)	$(5, 6^-)^*$	$(5, 6, 7^-)^*$	3987.7(2)	0.212(4)	68(7)
	632.9(2)	$(5, 6^-)^*$	$(5)^*$	3982.5(2)	0.249(5)	79(8)
	1099.9(2)†	$(5, 6^-)^*$	$(4^-)^\wr$	3515.5(2)	0.020(3)	6.2(11)
	1763.4(2)†	$(5, 6^-)^*$	$(5^-)^\wr$	2851.8(2)	0.31(3)	100(11)
	2872.6(2)	$(5, 6^-)^*$	(4^+)	1742.5(2)	0.0070(2)	2.2(2)
4732.5(3)	744.7(2)†	$(5 — 7)^*$	$(5, 6, 7^-)^*$	3987.7(2)	0.056(6)	19(3)
	1754.1(2)†	$(5 — 7)^*$	(6^+)	2978.2(2)	0.29(3)	100(9)

Table 4.3: *(Continued).*

E_i (keV)	E_γ (keV)	J_i^π	J_f^π	E_f (keV)	Rel. I_γ	BR_γ
4843.4(3)	817.4(2)	$(6^+, 7)^*$	$(5, 6^+)^*$	4025.9(2)	0.094(3)	44(2)
	1345.2(2)†	$(6^+, 7)^*$	$(6^+)^\wr$	3498.3(2)	0.054(7)	25(4)
	1398.9(2)	$(6^+, 7)^*$	(8^+)	3445.3(2)	0.143(5)	67(3)
	1864.8(2)	$(6^+, 7)^*$	(6^+)	2978.2(2)	0.214(8)	100(4)
4851.3(2)	1336.0(2)†	$(3^-, 4^-)^*$	$(4^-)^\wr$	3515.5(2)	0.061(7)	5.4(7)
	1999.4(2)	$(3^-, 4^-)^*$	$(5^-)^\wr$	2851.8(2)	0.365(7)	32.6(10)
	2879.1(2)†	$(3^-, 4^-)^*$	$(3^+)^\wr$	1972.1(2)	0.13(2)	11(2)
	3108.7(2)	$(3^-, 4^-)^*$	(4^+)	1742.5(2)	1.12(3)	100(2)
4943.4(3)	1257.2(2)	$(5^-, 6, 7)^*$	$(7^-)^\wr$	3685.8(2)	0.708(12)	100
4964.9(4)	1519.6(2)	$(6^+, 7^+)$	(8^+)	3445.3(2)	0.079(2)	100
4993.0(2)	1004.9(2)	$(7^-)^*$	$(5, 6, 7^-)^*$	3987.7(2)	1.56(3)	49.4(12)
	1306.8(2)	$(7^-)^*$	$(7^-)^\wr$	3685.8(2)	3.16(5)	100(2)
	1547.7(2)†‡	$(7^-)^*$	(8^+)	3445.3(2)	0.45(6)	14(2)
	1957.5(2)†	$(7^-)^*$	$(5^+)^\wr$	3036.7(2)	0.050(8)	1.6(3)
	2140.9(2)	$(7^-)^*$	$(5^-)^\wr$	2851.8(2)	0.88(3)	28.0(12)
5072.6(4)	3498.7(2)	$(2, 3, 4^+)^*$	(2^+)	1573.8(2)	0.196(6)	100
5103.4(3)	1658.4(2)†	$(6^+, 7)^*$	(8^+)	3445.3(2)	0.14(1)	100(13)
	2124.9(2)	$(6^+, 7)^*$	(6^+)	2978.2(2)	0.116(3)	82(11)
5218.3(4)	1773.0(2)†	$(6^+)^*$	(8^+)	3445.3(2)	0.063(8)	100
5232.6(2)	1244.9(2)	$(6^+, 7)^*$	$(5, 6, 7^-)^*$	3987.7(2)	1.35(2)	100(2)
	1547.5(2)†‡	$(6^+, 7)^*$	$(7^-)^\wr$	3685.8(2)	0.74(11)	55(8)
	1787.6(2)†	$(6^+, 7)^*$	(8^+)	3445.3(2)	0.066(9)	4.9(7)
	2253.5(2)	$(6^+, 7)^*$	(6^+)	2978.2(2)	0.213(5)	15.8(5)
	2381.6(2)	$(6^+, 7)^*$	$(5^-)^\wr$	2851.8(2)	0.260(10)	19.3(8)
5338.1(2)	3365.8(2)†	$(2, 3, 4^+)$	$(3^+)^\wr$	1972.1(2)	0.072(11)	13(5)
	3764.3(4)	$(2, 3, 4^+)$	(2^+)	1573.8(2)	0.46(15)	83(40)
	4678.9(4)	$(2, 3, 4^+)$	2^+	659.2(2)	0.6(2)	100(36)

Table 4.3: *(Continued).*

E_i (keV)	E_γ (keV)	J_i^π	J_f^π	E_f (keV)	Rel. I_γ	BR_γ
5345.4(3)	1659.5(2)†	$(6^+, 7^+)^*$	$(7^-)^\wr$	3685.8(2)	0.17(2)	100(14)
	1847.4(2)†	$(6^+, 7^+)^*$	$(6^+)^\wr$	3498.3(2)	0.060(8)	36(7)
	1899.9(2)	$(6^+, 7^+)^*$	(8^+)	3445.3(2)	0.130(6)	78(12)
	2308.3(2)†	$(6^+, 7^+)^*$	$(5^+)^\wr$	3036.7(2)	0.050(8)	30(6)
	2367.1(2)	$(6^+, 7^+)^*$	(6^+)	2978.2(2)	0.107(5)	64(10)
5408.3(3)	1722.8(2)	$(5^-, 6, 7)^*$	$(7^-)^\wr$	3685.8(2)	0.079(5)	100(6)
	2430.5(2)	$(5^-, 6, 7)^*$	(6^+)	2978.2(2)	0.0055(1)	6.9(5)
5452.4(2)	919.8(2)†	$(5^-, 6, 7^-)^*$	$(5, 6, 7^-)^*$	4532.5(2)	0.115(11)	11.8(12)
	1464.7(2)†	$(5^-, 6, 7^-)^*$	$(5, 6, 7^-)^*$	3987.7(2)	0.105(10)	10.8(11)
	1766.5(2)†	$(5^-, 6, 7^-)^*$	$(7^-)^\wr$	3685.8(2)	0.62(9)	64(9)
	2474.4(2)	$(5^-, 6, 7^-)^*$	(6^+)	2978.2(2)	0.0045(1)	0.47(2)
	2600.3(2)	$(5^-, 6, 7^-)^*$	$(5^-)^\wr$	2851.8(2)	0.97(2)	100(2)
5452.7(4)	1040.1(2)†	$(5^-, 6, 7)^*$	$(7^-)^\wr$	4412.5(2)	0.19(2)	100
5475.0(4)	3901.0(4)†	$(2, 3, 4^+)^*$	(2^+)	1573.8(2)	0.317(10)	100
5490.5(3)	957.9(2)†	$(5, 6, 7^-)^*$	$(5, 6, 7^-)^*$	4532.5(2)	0.041(5)	7.5(10)
	2638.5(2)‡	$(5, 6, 7^-)^*$	$(5^-)^\wr$	2851.8(2)	0.547(12)	100(2)
5517.9(3)	3252.6(2)	$(2^+, 3, 4^+)^*$	$(4^+)^\wr$	2265.7(2)	0.0059(2)	13(4)
	3943.3(5)	$(2^+, 3, 4^+)^*$	(2^+)	1573.8(2)	0.05(2)	100(34)
5545.1(4)	3971.2(4)‡	$(2, 3, 4^+)^*$	(2^+)	1573.8(2)	0.33(11)	100
5567.3(3)	1154.7(2)	$(5^-, 6, 7^-)^*$	$(7^-)^\wr$	4412.5(2)	0.755(13)	100(2)
	1881.2(2)	$(5^-, 6, 7^-)^*$	$(7^-)^\wr$	3685.8(2)	0.427(8)	57(2)
	2144.2(2)†	$(5^-, 6, 7^-)^*$	$(6^-)^\wr$	3423.1(2)	0.16(2)	20(3)
	2715.5(2)	$(5^-, 6, 7^-)^*$	$(5^-)^\wr$	2851.8(2)	0.0097(2)	1.28(4)
5573.3(2)	1040.7(2)	$(5^-, 6^-, 7^-)^*$	$(5, 6, 7^-)^*$	4532.5(2)	2.64(4)	100(2)
	1160.9(2)†	$(5^-, 6^-, 7^-)^*$	$(7^-)^\wr$	4412.5(2)	0.068(8)	2.6(3)
	1434.7(2)†	$(5^-, 6^-, 7^-)^*$	$(5, 6^+)^*$	4138.7(2)	0.021(3)	0.81(10)
	1585.5(2)	$(5^-, 6^-, 7^-)^*$	$(5, 6, 7^-)^*$	3987.7(2)	1.21(2)	45.6(11)

Table 4.3: *(Continued).*

E_i (keV)	E_γ (keV)	J_i^π	J_f^π	E_f (keV)	Rel. I_γ	BR_γ
5702.8(3)	1290.9(2)†	(6, 7$^+$)*	(7$^-$)$^\wr$	4412.5(2)	0.036(6)	13(2)
	2016.9(2)‡	(6, 7$^+$)*	(7$^-$)$^\wr$	3685.8(2)	0.237(7)	42(2)
	2665.6(2)‡	(6, 7$^+$)*	(5$^+$)$^\wr$	3036.7(2)	0.562(13)	100(2)
5800.2(2)	1185.1(2)	(5$^-$, 6$^-$, 7$^-$)*	(5, 6$^-$)*	4615.2(2)	0.175(4)	10.8(3)
	1267.6(2)†	(5$^-$, 6$^-$, 7$^-$)*	(5, 6, 7$^-$)*	4532.5(2)	0.026(3)	1.6(2)
	1661.7(2)†	(5$^-$, 6$^-$, 7$^-$)*	(5, 6$^+$)*	4138.7(2)	0.031(4)	1.9(2)
	1811.9(2)	(5$^-$, 6$^-$, 7$^-$)*	(5, 6, 7$^-$)*	3987.7(2)	0.117(5)	7.2(3)
	2114.5(2)	(5$^-$, 6$^-$, 7$^-$)*	(7$^-$)$^\wr$	3685.8(2)	1.56(3)	97(3)
	2822.2(2)	(5$^-$, 6$^-$, 7$^-$)*	(6$^+$)	2978.2(2)	0.66(2)	41.1(13)
	2948.4(2)	(5$^-$, 6$^-$, 7$^-$)*	(5$^-$)$^\wr$	2851.8(2)	1.62(4)	100(2)
5806.4(2)	1824.4(2)	(3$^+$,4)*	(5)*	3982.5(2)	0.075(2)	28.9(14)
	1893.3(2)†	(3$^+$,4)*	(2, 3, 4$^+$)*	3913.3(3)	0.058(8)	22(3)
	2291.1(2)†	(3$^+$,4)*	(4$^-$)$^\wr$	3515.5(2)	0.096(12)	37(5)
	2381.6(2)	(3$^+$,4)*	(3$^-$)$^\wr$	3423.6(2)	0.260(10)	100(4)
	3834.3(4)	(3$^+$,4)*	(3$^+$)$^\wr$	1972.1(2)	0.14(5)	55(18)
5812.0(4)	2775.2(2)	(5, 6, 7$^+$)*	(5$^+$)$^\wr$	3036.7(2)	0.0065(2)	100
5854.7(3)	1867.0(2)‡	(5$^-$, 6, 7)*	(5, 6, 7$^-$)*	3987.7(2)	0.603(12)	100(2)
	2168.8(2)†	(5$^-$, 6, 7)*	(7$^-$)$^\wr$	3685.8(2)	0.0037(1)	0.62(2)
5895.6(3)	1907.7(2)	(6$^+$, 7)*	(5, 6, 7$^-$)*	3987.7(2)	0.080(4)	100(5)
	2450.5(2)†	(6$^+$, 7)*	(8$^+$)	3445.3(2)	0.050(7)	62(9)
5903.4(4)	2458.1(2)†	(6$^+$, 7$^+$)*	(8$^+$)	3445.3(2)	0.043(6)	100
6033.9(3)	2008.9(2)‡	(5, 6)*	(5, 6$^+$)*	4025.9(2)	0.558(11)	100(2)
	2517.3(2)	(5, 6)*	(4$^-$)$^\wr$	3515.5(2)	0.0046(1)	0.82(3)
6045.1(4)	2599.8(2)†	(6$^+$, 7$^+$)*	(8$^+$)	3445.3(2)	0.059(8)	100
6047.8(3)	4075.7(4)	(2$^-$, 3$^-$)*	(3$^+$)$^\wr$	1972.1(2)	0.18(6)	14(7)
	4473.9(5)†	(2$^-$, 3$^-$)*	(2$^+$)	1573.8(2)	0.04(2)	3(2)
	5388.0(4)	(2$^-$, 3$^-$)*	2$^+$	659.2(2)	1.3(5)	100(39)

Table 4.3: *(Continued).*

E_i (keV)	E_γ (keV)	J_i^π	J_f^π	E_f (keV)	Rel. I_γ	BR_γ
6067.4(4)	4324.8(4)	$(2^+, 3, 4)^*$	(4^+)	1742.5(2)	0.34(12)	100
6079.5(10)	6079.2(7)	$(1^+, 2^+)^*$	0^+	0	0.015(7)	100
6141.3(3)	2153.6(2)	$(5^-, 6, 7^+)^*$	$(5, 6, 7^-)^*$	3987.7(2)	0.177(7)	100(16)
	2455.4(2)	$(5^-, 6, 7^+)^*$	$(7^-)^\wr$	3685.8(2)	0.0056(1)	3.2(2)
	3104.2(2)†	$(5^-, 6, 7^+)^*$	$(5^+)^\wr$	3036.7(2)	0.048(8)	27(4)
6155.3(4)	4412.7(4)	$(2^+, 3, 4)^*$	(4^+)	1742.5(2)	0.7(3)	100
6167.9(3)	1175.6(2)†	$(6^+, 7)^*$	$(7^-)^*$	4993.0(2)	0.037(4)	33(4)
	1224.9(2)	$(6^+, 7)^*$	$(5^-, 6, 7)^*$	4943.4(3)	0.115(5)	100(4)
	2180.4(2)	$(6^+, 7)^*$	$(5, 6, 7^-)^*$	3987.7(2)	0.034(3)	30(3)
	2481.8(2)	$(6^+, 7)^*$	$(7^-)^\wr$	3685.8(2)	0.0050(1)	4.3(2)
	2721.4(2)	$(6^+, 7)^*$	(8^+)	3445.3(2)	0.0054(1)	4.7(2)
6186.7(2)	1451.8(2)†	$(5^-)^*$	$(5 — 7)^*$	4732.5(3)	0.064(9)	3(1)
	1654.8(3)†	$(5^-)^*$	$(5, 6, 7^-)^*$	4532.5(2)	0.047(5)	1.2(4)
	1764.4(2)†	$(5^-)^*$	$(5 — 7)^*$	4422.5(3)	0.021(3)	3.5(13)
	1774.6(3)†	$(5^-)^*$	$(7^-)^\wr$	4412.5(2)	0.062(10)	3.6(14)
	2160.7(2)‡	$(5^-)^*$	$(5, 6^+)^*$	4025.9(2)	1.06(2)	59(21)
	2199.7(3)†	$(5^-)^*$	$(5, 6, 7^-)^*$	3987.7(2)	0.097(11)	5(2)
	2203.5(2)	$(5^-)^*$	$(5)^*$	3982.5(2)	0.409(9)	23(8)
	3335.4(2)‡	$(5^-)^*$	$(5^-)^\wr$	2851.8(2)	0.60(2)	33(12)
	3920.5(4)‡	$(5^-)^*$	$(4^+)^\wr$	2265.7(2)	0.7(2)	41(20)
	4443.4(4)	$(5^-)^*$	(4^+)	1742.5(2)	1.8(6)	100(35)
6203.9(4)	3352.0(2)†	$(5, 6, 7^-)^*$	$(5^-)^\wr$	2851.8(2)	0.056(6)	100
6211.0(3)	2787.8(2)	$(2, 3, 4^+)^*$	$(3^-)^\wr$	3423.6(2)	0.0063(2)	1.5(5)
	4238.5(4)‡	$(2, 3, 4^+)^*$	$(3^+)^\wr$	1972.1(2)	0.43(15)	100(34)
	4637.4(5)†	$(2, 3, 4^+)^*$	(2^+)	1573.8(2)	0.04(2)	10(6)
6301.2(2)	1977.3(2)†	$(5, 6)^*$	$(3^-)^*$	4323.8(2)	0.020(3)	10.5(14)
	2275.3(2)†	$(5, 6)^*$	$(5, 6^+)^*$	4025.9(2)	0.028(3)	15(2)
	2318.9(2)	$(5, 6)^*$	$(5)^*$	3982.5(2)	0.194(4)	100(2)

Table 4.3: *(Continued).*

E_i (keV)	E_γ (keV)	J_i^π	J_f^π	E_f (keV)	Rel. I_γ	BR_γ
	2785.8(2)†	(5, 6)*	$(4^-)^{\wr}$	3515.5(2)	0.022(3)	12(2)
	3264.2(3)†	(5, 6)*	$(5^+)^{\wr}$	3036.7(2)	0.026(6)	13(3)
6379.1(12)	6378.8(8)	$(1^+, 2^+)^*$	0^+	0	0.022(10)	100
6407.0(2)	1414.4(2)	$(6^+, 7)^*$	$(7^-)^*$	4993.0(2)	0.102(4)	17.8(8)
	1463.7(2)†	$(6^+, 7)^*$	$(5^-, 6, 7)^*$	4943.4(3)	0.065(6)	11.4(11)
	1874.6(2)†	$(6^+, 7)^*$	$(5 — 7)^*$	4530.6(4)	0.082(8)	14.3(14)
	2419.1(2)	$(6^+, 7)^*$	$(5, 6, 7^-)^*$	3987.7(2)	0.572(12)	100(2)
	2961.8(2)	$(6^+, 7)^*$	(8^+)	3445.3(2)	0.0080(2)	1.40(5)
	3554.7(2)	$(6^+, 7)^*$	$(5^-)^{\wr}$	2851.8(2)	0.093(4)	16.2(7)
6414.2(2)	1421.0(2)†	$(6^+, 7^-)^*$	$(7^-)^*$	4993.0(2)	0.009(3)	7.4(14)
	1471.9(2)†	$(6^+, 7^-)^*$	$(5^-, 6, 7)^*$	4943.4(3)	0.46(3)	46(5)
	2728.1(2)†	$(6^+, 7^-)^*$	$(7^-)^{\wr}$	3685.8(2)	0.10(2)	80(12)
	2916.0(2)†	$(6^+, 7^-)^*$	$(6^+)^{\wr}$	3498.3(2)	0.054(8)	43(7)
	2969.1(2)	$(6^+, 7^-)^*$	(8^+)	3445.3(2)	0.0075(2)	6.0(2)
	3562.9(2)	$(6^+, 7^-)^*$	$(5^-)^{\wr}$	2851.8(2)	0.126(4)	100(3)
6473.0(3)	3436.3(2)†	$(4^-)^*$	$(5^+)^{\wr}$	3036.7(2)	0.036(6)	9(3)
	4207.2(4)	$(4^-)^*$	$(4^+)^{\wr}$	2265.7(2)	0.23(8)	56(28)
	4730.2(4)‡	$(4^-)^*$	(4^+)	1742.5(2)	0.41(15)	100(36)
6557.1(5)	5897.6(4)	$(2, 3, 4^+)^*$	2^+	659.2(2)	0.13(5)	100
6599.1(4)	4856.4(4)	$(2^+, 3, 4)^*$	(4^+)	1742.5(2)	0.38(14)	100
6732.4(7)	6072.9(5)	$(2, 3, 4^+)^*$	2^+	659.2(2)	0.09(4)	100
6736.5(3)	1504.8(2)	$(5 — 7)^*$	$(6^+, 7)^*$	5232.6(2)	0.108(3)	100(3)
	1742.3(2)†	$(5 — 7)^*$	$(7^-)^*$	4993.0(2)	0.005(1)	4.8(12)
6855.4(7)	6195.9(4)	$(2, 3, 4^+)^*$	2^+	659.2(2)	0.034(14)	100

Table 4.3: *(Continued).*

E_i (keV)	E_γ (keV)	J_i^π	J_f^π	E_f (keV)	Rel. I_γ	BR_γ
6864.2(2)	1290.9(2)†	(5 — 7)*	(5^-, 6^-, 7^-)*	5573.3(2)	0.036(6)	27(4)
	1631.4(2)	(5 — 7)*	(6^+, 7)*	5232.6(2)	0.135(3)	100(2)
	1760.8(2)†	(5 — 7)*	(6^+, 7)*	5103.4(3)	0.038(6)	28(5)
	1920.5(2)†	(5 — 7)*	(5^-, 6, 7)*	4943.4(3)	0.033(4)	25(3)
	2131.4(2)†	(5 — 7)*	(5 — 7)*	4732.5(3)	0.027(3)	20(2)
	2877.3(2)	(5 — 7)*	(5, 6, 7^-)*	3987.7(2)	0.0070(2)	5.2(2)
6869.9(7)	6869.6(5)	(1^+, 2^+)*	0^+	0	0.006(3)	100
6928.4(4)	5354.4(4)‡	(2, 3, 4^+)*	(2^+)	1573.8(2)	0.27(11)	100
6955.2(7)	6295.7(5)	(2, 3, 4^+)*	2^+	659.2(2)	0.05(2)	100
6961.3(9)	6301.8(5)	(2, 3, 4^+)*	2^+	659.2(2)	0.023(10)	100
7033.7(8)	6374.2(5)	(2, 3, 4^+)*	2^+	659.2(2)	0.018(10)	100
7053.7(3)	3608.0(2)	(6^+, 7)*	(8^+)	3445.3(2)	0.144(7)	78(4)
	4075.7(4)	(6^+, 7)*	(6^+)	2978.2(2)	0.18(6)	100(3)
7067.2(2)	1494.0(2)	(6^+, 7)*	(5^-, 6^-, 7^-)*	5573.3(2)	0.068(2)	24.7(10)
	1834.5(2)†	(6^+, 7)*	(6^+, 7)*	5232.6(2)	0.029(4)	10(2)
	2534.7(2)†	(6^+, 7)*	(5, 6, 7^-)*	4532.5(2)	0.075(9)	26(3)
	3079.5(2)†	(6^+, 7)*	(5, 6, 7^-)*	3987.7(2)	0.029(3)	10.7(13)
	3381.3(2)	(6^+, 7)*	(7^-)$^\wr$	3685.8(2)	0.049(3)	17.9(11)
	3621.8(4)	(6^+, 7)*	(8^+)	3445.3(2)	0.275(7)	100(3)
7115.0(8)	6455.5(5)	(2, 3, 4^+)*	2^+	659.2(2)	0.018(8)	100
7137.5(7)	6478.0(5)	(2, 3, 4^+)*	2^+	659.2(2)	0.018(7)	100
7174.0(8)	6514.5(5)	(2, 3, 4^+)*	2^+	659.2(2)	0.020(8)	100
7244.4(8)	6584.9(5)	(2, 3, 4^+)*	2^+	659.2(2)	0.025(11)	100
7292.3(8)	6632.8(5)	(2, 3, 4^+)*	2^+	659.2(2)	0.018(8)	100
7386.4(7)	6726.9(5)	(2, 3, 4^+)*	2^+	659.2(2)	0.022(10)	100
7504.8(5)	1692.8(2)†	(5 — 7)*	(5, 6, 7^+)*	5812.0(4)	0.005(3)	100

Table 4.3: *(Continued).*

E_i (keV)	E_γ (keV)	J_i^π	J_f^π	E_f (keV)	Rel. I_γ	BR_γ
7550.9(8)	6891.3(5)	(2, 3, 4^+)*	2^+	659.2(2)	0.019(8)	100
8082.3(9)	7422.8(5)	(2, 3, 4^+)*	2^+	659.2(2)	0.013(6)	100

† Intensity calculated from coincidences.

‡ Previously observed but unplaced transitions

≀ Spin assigned assigned by Ref. [78]

§ Spin assigned by Ref. [75]

* Spin assigned based on systematics.

4.4.1 Isomeric beam composition

The ISOL technique is known to produce rare isotope beams (RIBs) in their ground and isomeric states. The ^{80}Ga isotope is known to have one 3($^-$) isomer at 22.45(10) keV, above the 6($^-$) ground state with half-lives of $t_{1/2} = 1.9(1)$ s and $t_{1/2} = 1.3(2)$ s, respectively [79]. These two levels are known to undergo β-decay into excited states in ^{80}Ge. Since they are reasonably separated in their spins, they will populate different states in ^{80}Ge, a fact that can be exploited to find the in-beam isomeric ratio.

In a similar way to that established in Section 3.8, the isomeric ratio can be established by comparing the intensity populating a level and the intensity depopulating the level. For the case of ^{80}Ga, there are two candidate states in ^{80}Ge that can be used: a (2^+) at 1574 keV and a (8^+) at 3445 keV. These two states can only be populated by the 3($^-$) isomer and the 6($^-$) ground state in ^{80}Ga, respectively.

To extract the isomeric ratio, a comparison was done between this dataset and the data observed by Hoff and Fogelberg [69] in their thermal fission experiment. When comparing the β-feeding intensity of these two states between this experiment and the thermal fission, an increase of 1.55(6) was noted in the intensity of 3445-keV and a decrease of 0.66(3) was noted for the 1574-keV state, indicating that there was a difference in the population of each of the states.

Given that in the thermal fission experiment, they observed 62(4)% of the 3($^-$) isomer, and a decrease was observed in the GRIFFIN experiment, the ratio of this component of the beam must be 41(3)%.

This comparison can be extended to the literature excited states, determining whether feeding was increased or decreased to each state, and thereby assigning them as being fed by either the ground state or the isomer. Thirteen states were identified as being populated by the 3($^-$) isomer, since they all showed a decrease of ∼0.66 in the β-feeding intensity.

This grouping of states, represents 46(2)% of the total β-feeding, which is in line with that observed by using only the 1574- and 3445-keV states and the data previously available.

4.5 ^{80}Ga ground state decay

Previous work was unable to separate the excited states in ^{80}Ge populated from either the $6(^-)$ ground state or the $3(^-)$ isomer of ^{80}Ga. Based on comparison to ENSDF and the work of Hoff [69], a preliminary separation could be done, and a subsequent calculation of $\log ft$ values would corroborate or discount population from either the ground state or isomeric state in ^{80}Ga.

There were a total of 35 newly observed states in ^{80}Ge, populated by the β-decay of the $6(^-)$ ground state of ^{80}Ga. Amongst the known and newly observed excited states, 111 new transitions were observed, and 12 previously observed but unplaced transitions were placed. The details of the transitions are found in Table 4.3, while the detailed level scheme, showing the known transitions in black, the previously unplaced transitions in blue, and the newly observed transitions in red, is found in Figures 4.4 — 4.8.

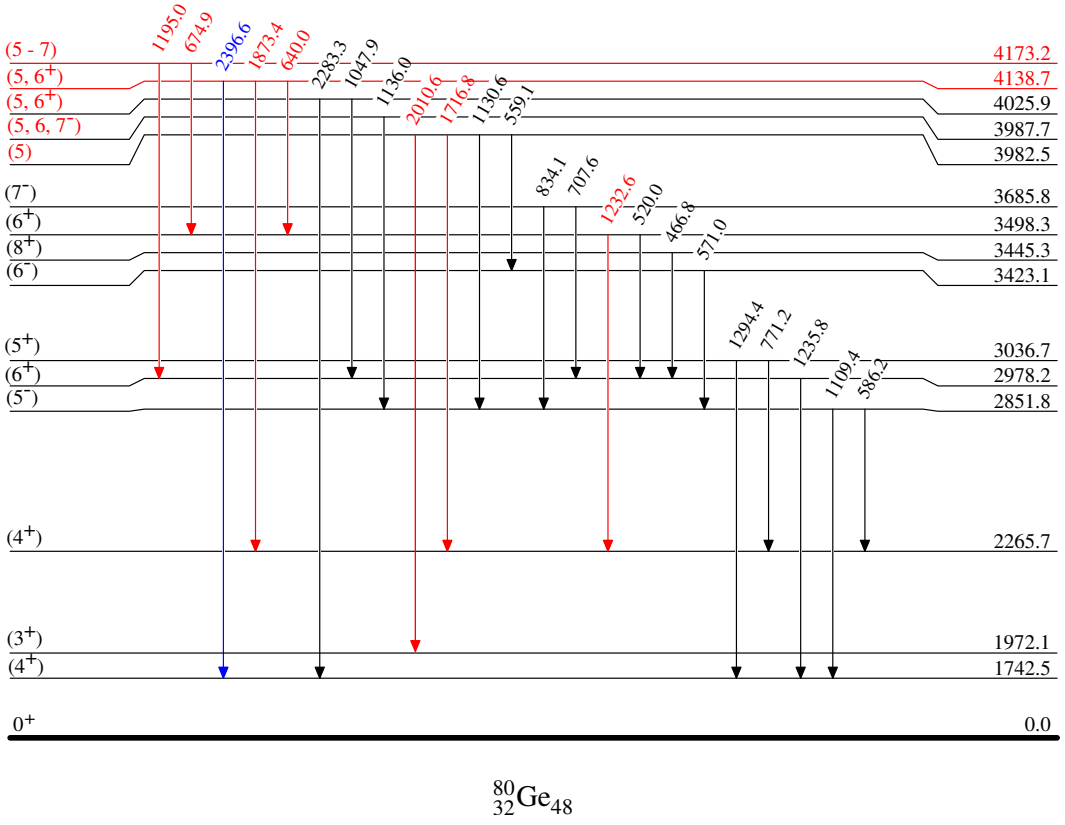

Figure 4.4: The ^{80}Ge level scheme, as populated by the ground state decay of ^{80}Ga. Red indicates newly observed transitions and states, blue indicates previously observed but unplaced transitions, and black indicates known transitions and states.

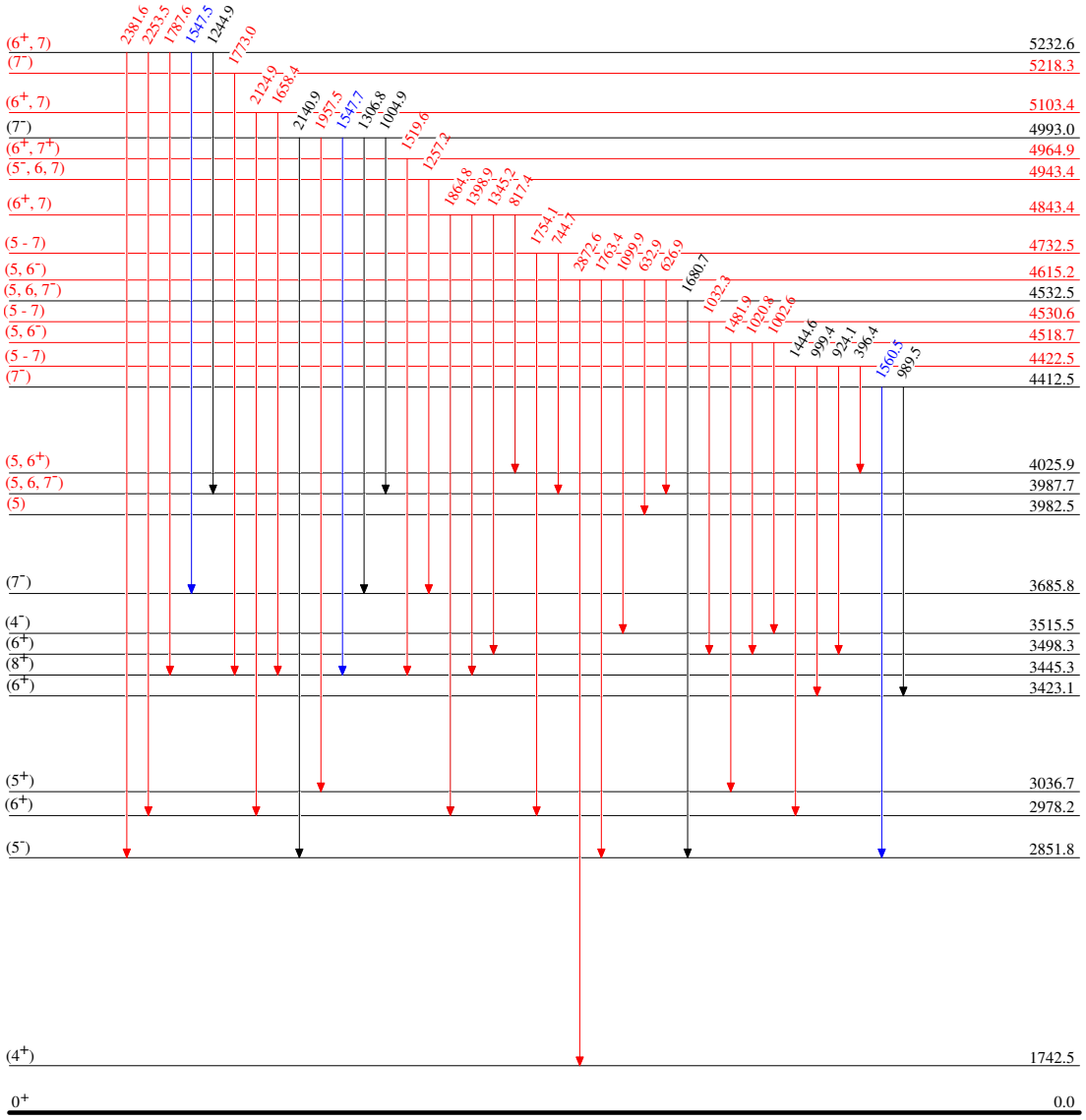

Figure 4.5: The ^{80}Ge level scheme, as populated by the ground state decay of ^{80}Ga (continued). Red indicates newly observed transitions and states, blue indicates previously observed but unplaced transitions, and black indicates known transitions and states.

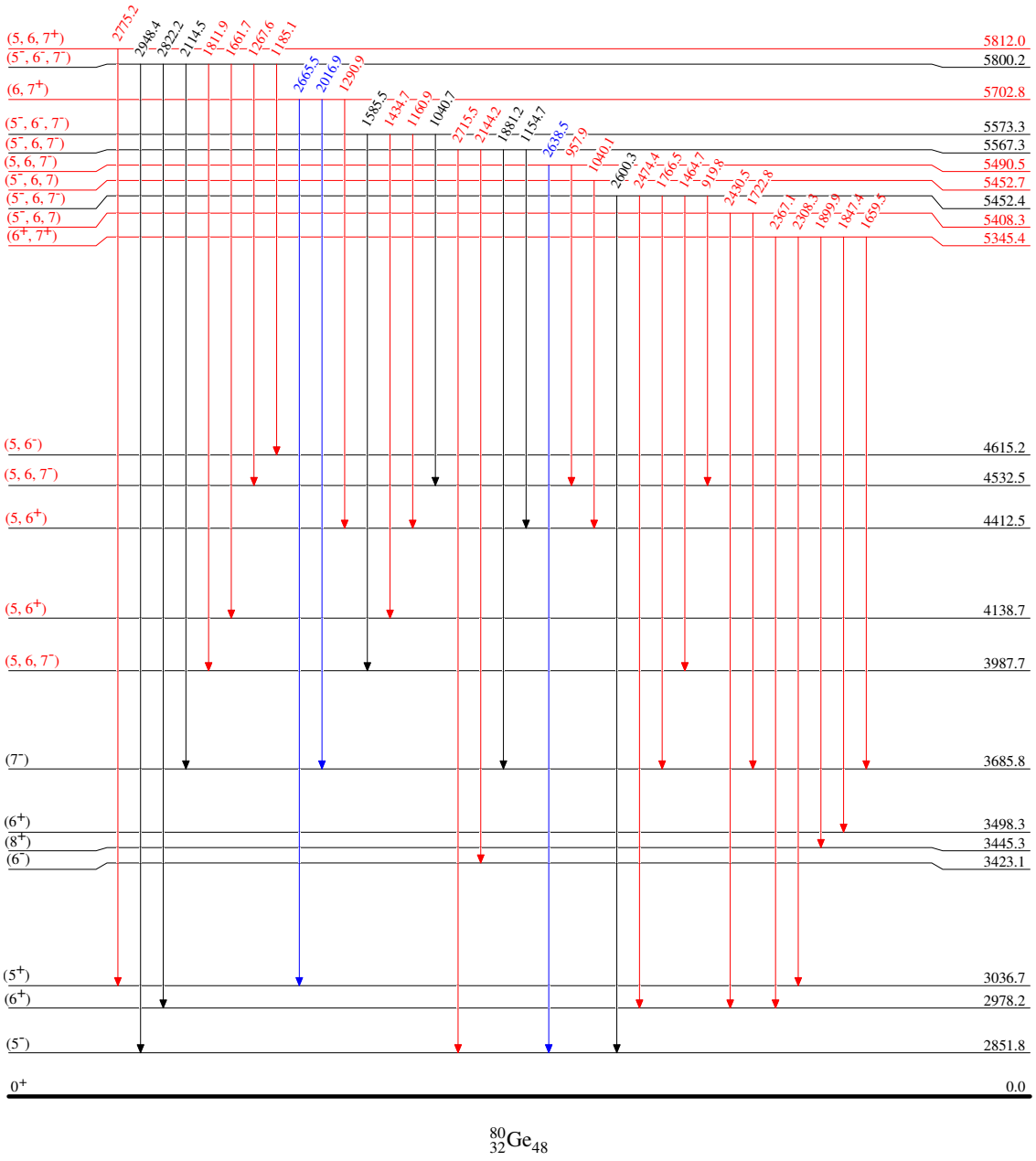

Figure 4.6: The ^{80}Ge level scheme, as populated by the ground state decay of ^{80}Ga (continued). Red indicates newly observed transitions and states, blue indicates previously observed but unplaced transitions, and black indicates known transitions and states.

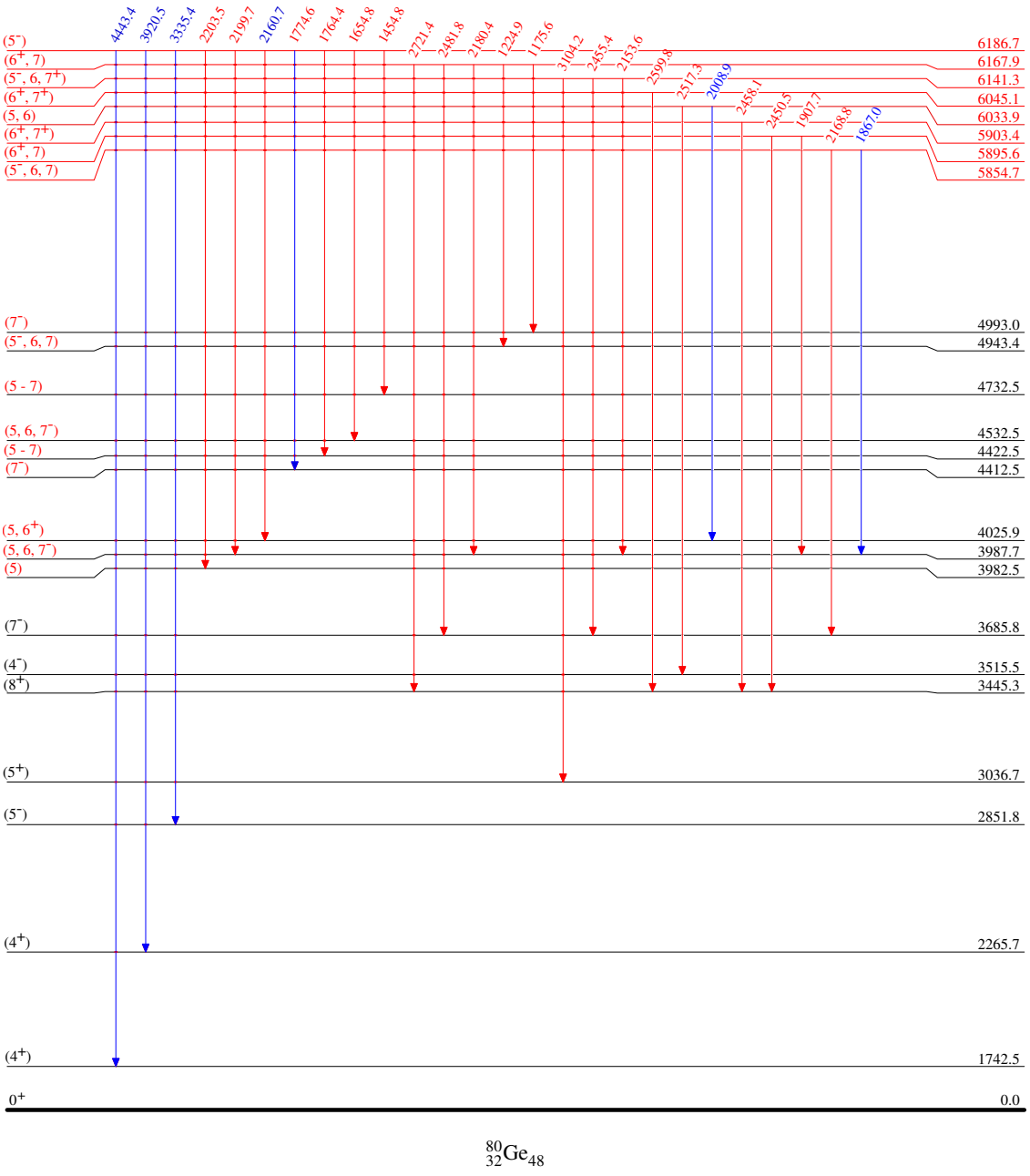

Figure 4.7: The ^{80}Ge level scheme, as populated by the ground state decay of ^{80}Ga (continued). Red indicates newly observed transitions and states, blue indicates previously observed but unplaced transitions, and black indicates known transitions and states.

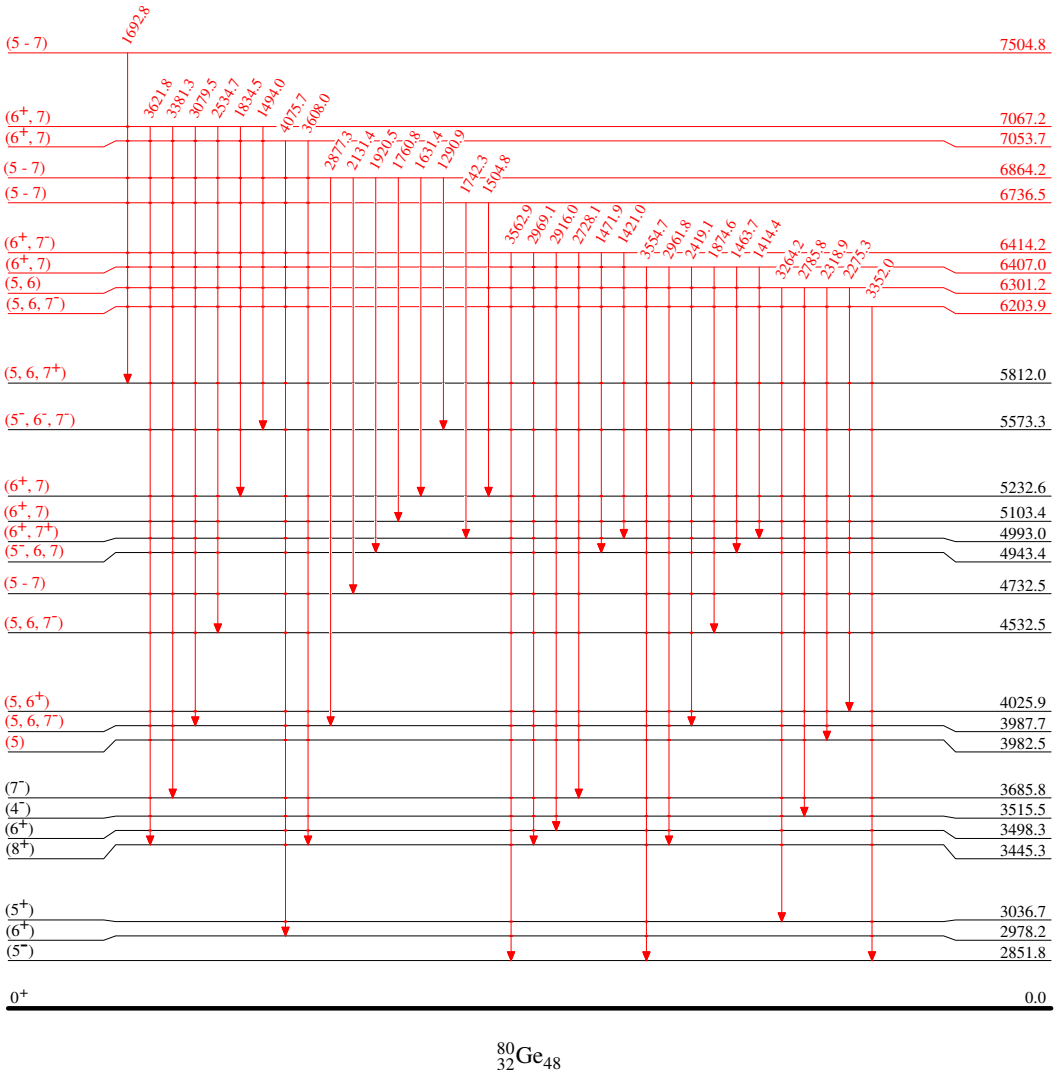

Figure 4.8: The ^{80}Ge level scheme, as populated by the ground state decay of ^{80}Ga (continued). Red indicates newly observed transitions and states, blue indicates previously observed but unplaced transitions, and black indicates known transitions and states.

4.5.1 β-feeding and logft values

As discussed in Chapter 1, the logft values can be calculated in order to tentatively assign spins and parities to states. This is done by computing the β-feeding intensity: if there is excess intensity after computing the balance between γ-ray transitions populating and depopulating a particular state, that excess intensity is attributed to the β-decay of the parent isotope. Table 4.4 summarizes the β-feeding intensity for those states populated by the decay of the $6(^-)$ ^{80}Ge ground state. The logft values are calculated using the NNDC LOGFT calculator [66], which intakes information about the parent half-life, β-decaying state, the daughter state and the β-feeding. The spin assignments infer unique population

from the ground state, and that the transitions are either allowed or first forbidden in nature, with the exception of the 3445-keV state — with a logft value of 9.14 — which has been previously identified as the (8^+) member of the yrast band. This makes the β-decay from the $6(^-)$ ^{80}Ge ground state to the 3445-keV state a unique first forbidden transition.

Table 4.4: The β-feeding intensities and logft values for states in ^{80}Ge, observed through the β-decay of the $6(^-)$ground state of ^{80}Ga.

E_x (keV)	I_β (%)	logft
2851.8(2)	6.9(10)	6.28(7)
2978.2(2)	5.0(4)	6.38(5)
3036.7(2)	4.48(10)	6.42(3)
3423.1(2)	5.9(2)	6.19(3)
3445.3(2)	0.75(13)[a]	9.14(8)
3498.3(2)	< 0.22[b]	
3685.8(2)	2.0(4)	6.58(9)
3982.5(2)	1.39(8)	6.65(4)
3987.7(2)	0.7(3)	6.9(2)
4025.9(2)	0.57(8)	7.03(7)
4138.7(2)	3.20(7)	6.24(3)
4173.2(3)	0.61(2)	6.94(3)
4412.5(2)	1.43(8)	6.50(4)
4422.5(3)	1.10(9)	6.51(5)
4518.7(3)	0.51(2)	6.91(3)
4530.6(4)	0.05(3)	7.9(3)
4532.5(2)	8.2(3)	5.70(3)
4615.2(2)	1.06(6)	6.56(4)
4732.5(3)	0.45(5)	6.89(6)
4843.4(3)	0.85(3)	6.57(3)
4943.4(3)	1.04(12)	6.45(6)
4964.9(4)	0.133(5)	7.33(3)
4993.0(2)	10.1(2)	5.44(3)

Table 4.4: *(Continued).*

E_x (keV)	I_β (%)	logft
5103.4(3)	0.37(3)	6.84(5)
5218.3(4)	0.11(2)	7.34(7)
5232.6(2)	4.2(2)	5.74(3)
5345.4(3)	0.87(5)	6.37(4)
5408.3(3)	0.143(9)	7.14(4)
5452.4(2)	3.1(2)	5.78(4)
5452.7(4)	0.33(4)	6.25(6)
5490.5(3)	0.99(3)	6.26(3)
5567.3(3)	2.28(6)	5.87(3)
5573.3(2)	6.60(14)	5.40(3)
5702.8(3)	1.47(4)	6.00(3)
5800.2(2)	7.1(2)	5.27(3)
5812.0(4)	$< 0.013^b$	
5854.7(3)	1.03(3)	6.09(3)
5895.6(3)	0.218(14)	6.75(4)
5903.4(4)	0.074(11)	7.22(7)
6033.9(3)	0.95(3)	6.04(3)
6045.1(4)	0.100(14)	7.02(7)
6141.3(3)	0.39(2)	6.38(4)
6167.9(3)	0.333(14)	6.44(3)
6186.7(2)	8.3(11)	5.03(7)
6203.9(4)	0.095(10)	6.97(6)
6301.2(2)	0.49(2)	6.21(3)
6407.0(2)	1.56(4)	5.65(3)
6414.2(2)	0.60(3)	6.06(4)
6736.5(3)	0.191(6)	6.40(3)
6864.2(2)	0.47(2)	5.94(3)
7053.7(3)	0.55(11)	5.76(9)

Table 4.4: *(Continued).*

E_x (keV)	I_β (%)	logft
7067.2(2)	0.89(3)	5.54(3)
7504.8(5)	0.009(5)	7.3(3)

[a] Unique first forbidden decay

[b] 2σ limit

The logft values calculated for each of the states are in agreement with the proposed spins and parities. Though the NNDC suggests that the lower limit of the logft value for an allowed transition is 5.9, a more conservative value, 5.5, is used as the limit in this work. This consideration is due to the nature of the transition to the 1742-keV state (populated by ^{80m}Ga), which was previously assigned as being the (4^+) member of the yrast band, and has a calculated logft value in this work of 5.91.

Some commentary must be made regarding a number of states, populated by the ^{80}Ga ground state. The states at 3498 and 5812 keV do not exhibit β-feeding. The intensity balance of these states is calculated to be -0.01(12) and 0.0013(32), respectively. Thus the 2σ limit of β-feeding is provided, at $< 0.22\%$ for 3498 keV and $< 0.013\%$ for 5812 keV.

The case of the 3498-keV state is interesting as it is fed by eight different transitions from states with spins ranging between 5 and 7, corroborating its spins assignment of (6^+).

The states at 4173, 4422, 4530, 4732, 6864 and 7504 keV are all given spins between 5 and 7, with logft values ranging from 5.94 and 7.9. Given the systematics, this is the most appropriate spin range, though from the same systematics and the logft values, further constraints on the spins cannot be made.

The remaining states, including newly observed and previously known levels, are tentatively assigned spins and parities through γ-ray systematics, inferring only transitions of either E1, M1 and E2 character. The calculated logft values served to further constrain these assignments to those present in Table 4.3.

4.6 ^{80m}Ga decay

As in the case of the ground state decay, states can be identified as being populated by the $3(^-)$ 22.4-keV isomer in ^{80}Ga. Figures 4.9 and 4.10 show the level schemes of those states populated by ^{80m}Ga. This work identified 31 newly observed excited states and 46 newly observed transitions, and placed four new transitions among newly observed or known excited states. Information about the γ-ray transitions can be found on Table 4.3.

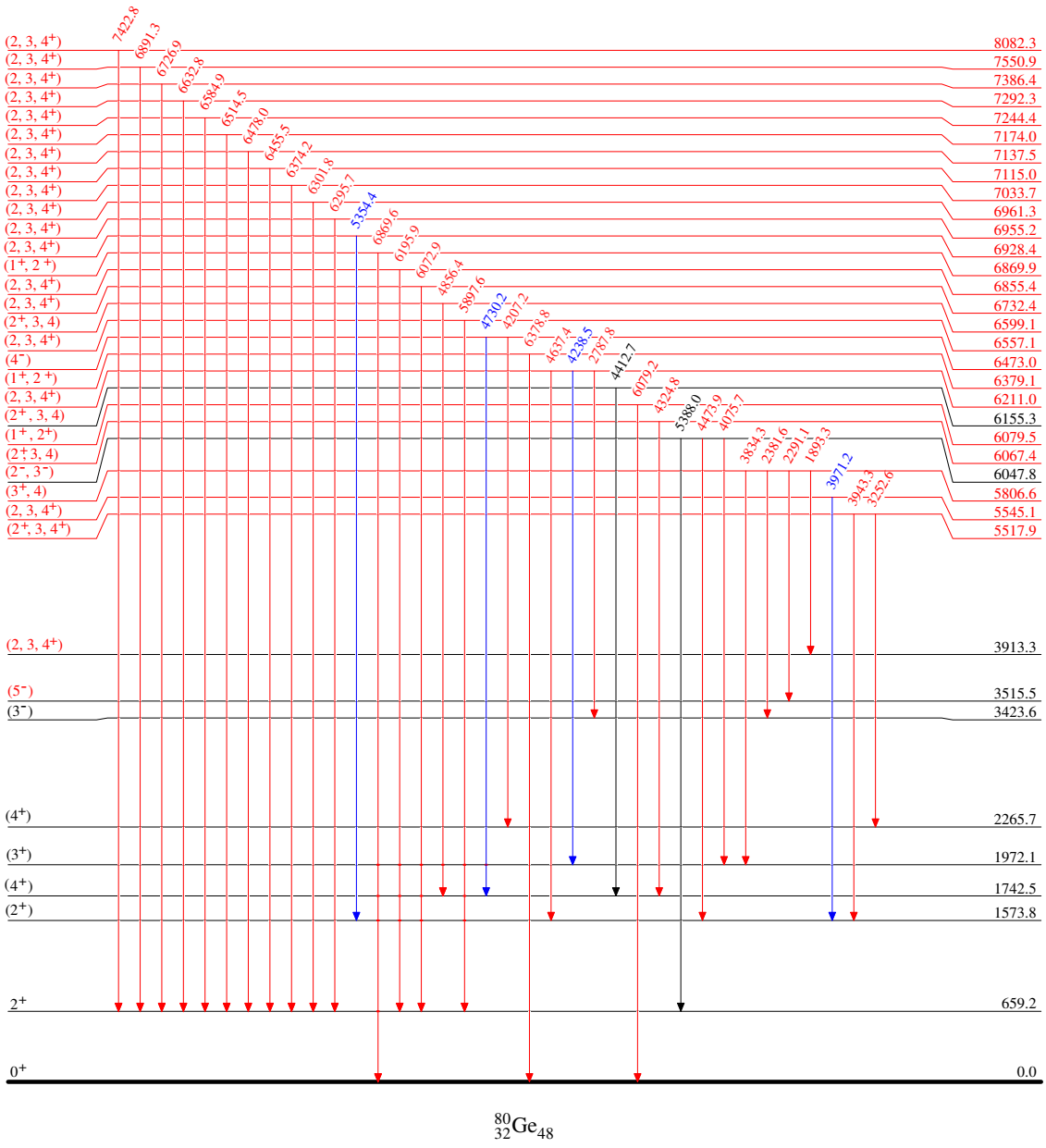

Figure 4.9: Excited states in ^{80}Ge, populated by the 3(−) 22.4-keV isomer in ^{80}Ga. Red indicates newly observed transitions and excited states, blue indicates previously observed by unplaced transitions and black indicated previously observed transitions.

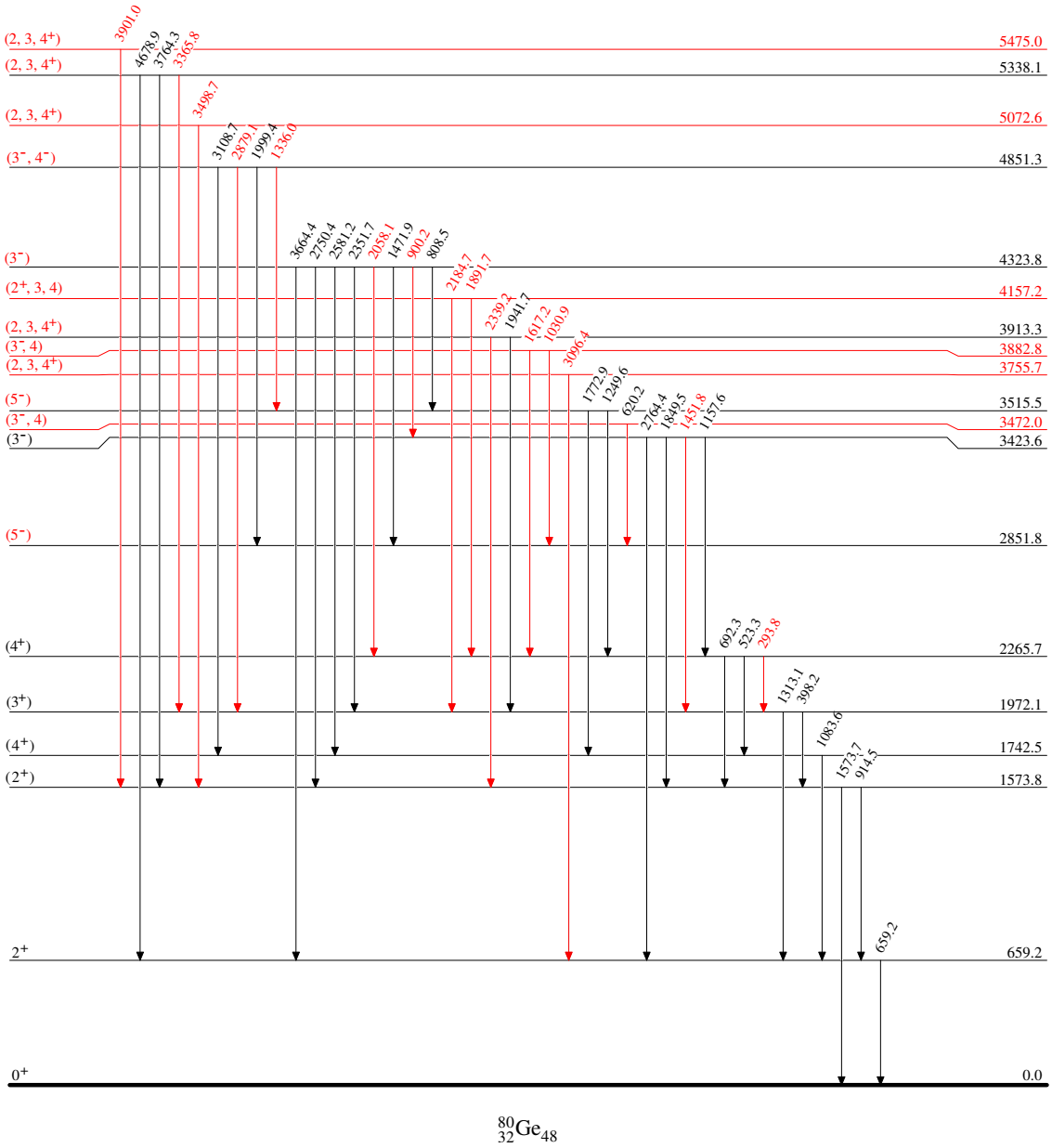

Figure 4.10: Excited states in ^{80}Ge, populated by the 3(−) 22.4-keV isomer in ^{80}Ga (continued). Red indicates newly observed transitions and excited states, blue indicates previously observed by unplaced transitions and black indicated previously observed transitions

4.6.1 β-feeding and logft values

As was the case with the states populated through the ground state decay, the intensity balance of those states populated by the β-decay of ^{80m}Ga can be calculated, and the excess attributed to feeding from this parent isotope. Table 4.5 summarizes the β-feeding as well as the logft values obtained using this feeding.

Table 4.5: The β-feeding intensities and logft values for states in ^{80}Ge, observed through the β-decay of the 3($^-$) 22.4 keV isomeric state.

E_x (keV)	I_β (%)	logft
659.2(2)	16(5)	6.3(2)
1573.8(2)	6.4(7)	6.47(9)
1742.5(2)	21(4)	5.91(11)
1972.1(2)	6.7(6)	6.36(8)
2265.7(2)	7.6(7)	6.23(8)
3423.6(2)	4.4(3)	6.16(8)
3472.0(4)	0.19(3)	7.51(10)
3515.5(2)	2.0(2)	6.48(8)
3755.7(5)	0.0142(10)	8.55(8)
3882.8(3)	0.44(5)	7.02(9)
3913.3(3)	1.49(10)	6.48(8)
4157.2(3)	0.31(2)	7.08(8)
4323.8(2)	14(2)	5.39(10)
4851.3(2)	3.6(2)	5.79(8)
5072.6(4)	0.42(3)	6.64(8)
5338.1(2)	2.3(6)	5.80(14)
5475.0(4)	0.7(2)	6.3(2)
5517.9(3)	0.11(4)	7.1(2)
5545.1(4)	0.7(3)	6.2(2)
5806.4(2)	1.36(14)	5.83(7)
6047.8(3)	3(1)	5.3(2)
6067.4(4)	0.7(3)	6.0(2)
6079.5(10)	0.03(2)	7.4(2)
6155.3(4)	1.6(6)	5.6(2)
6211.0(3)	1.0(3)	5.8(2)
6379.1(12)	0.05(2)	7.0(2)
6473.0(3)	1.5(4)	5.48(14)

Table 4.5: *(Continued).*

E_x (keV)	I_β (%)	logft
6557.1(5)	0.29(12)	6.2(2)
6599.1(4)	0.8(3)	5.7(2)
6732.4(7)	0.20(8)	6.2(2)
6855.4(7)	0.07(3)	6.6(2)
6869.9(7)	0.013(6)	7.3(2)
6928.4(4)	0.6(2)	5.7(2)
6955.2(7)	0.11(5)	6.34(2)
6961.3(9)	0.05(2)	6.7(2)
7033.7(8)	0.04(2)	6.8(3)
7115.0(8)	0.04(2)	6.7(2)
7137.5(7)	0.04(2)	6.7(2)
7174.0(8)	0.04(2)	6.7(2)
7244.4(8)	0.05(2)	6.5(2)
7292.3(8)	0.04(2)	6.6(2)
7386.4(7)	0.05(2)	6.3(8)
7550.9(8)	0.04(2)	6.4(2)
8082.3(9)	0.027(13)	6.2(2)

There were a total of 15 states that were observed to decay solely to the 2^+ 659-keV state. Their placement in the level scheme was corroborated by coincidence with the 659-keV γ-ray depopulating the 659-keV state, and also by β-coincidence. Given the $3(^-)$ spin of the ^{80m}Ga parent, these states are assigned tentative spins as either 2, 3 or 4^+. The logft values calculated from the β-feeding of these states are in the range between 5.3 and 8.55, corroborating these assignments.

Transitions were observed at 6079, 6379 and 6869 keV but where not observed in coincidence with other transitions in this nucleus. They were identified in coincidence with a β-particle, within the coincidence window, giving credence to the transition originating from the β-decay of the ^{80m}Ga parent. Given this observation, they were assigned as depopulating states at 6079, 6379 and 6869 keV, respectively. These states were assigned spins of either 1^+ or 2^+, given the β-decay selection rules, with the logft values, 7.4(2) for the 6079

keV state, 7.0(2) for the 6379 keV state and 7.3(2) for the 6869 keV state corroborate these spins assignments.

All newly observed and previously known states have been tentatively assigned spins and parities, according to the γ-ray systematics and the logft values calculated from the NNDC LOGFT calculator [66].

4.6.2 Unplaced γ-rays

There was one γ-ray that was observed in this dataset, but could not be convincingly placed within the newly observed or known states in ^{80}Ge. A 1528-keV γ-ray was observed in coincidence with γ-rays at 659, 1083, 1235, 1811 keV, which are known (newly observed in the case of the 1811-keV transition) transitions in the ^{80}Ge. However, it was also observed in coincidence with apparent transitions at 1900, 2547 and 2560, all of which were not identified as decaying from this nucleus.

There were also several unplaced transitions observed by Hoff [69] that, though observed in this work, were likely attributed to other nuclei or appeared due to scatter. The 2554-keV transition observed by Hoff is indeed in coincidence with the 659-keV, 1083-, 1235- and 2124-keV transitions in ^{80}Ge, but it is also in apparent coincidence with scatter peaks and furthermore, if it were due to a level at 7656-keV — as suggested by the coincidence with the 2124-keV γ-ray depopulating the 5102-keV excited state — it would require a coincidence with the 466-keV γ-ray, from the 3445-keV state to the 2978-keV state. No such coincidence was found, nor is this γ-ray transition found in any of the gates mentioned above.

The apparent 3044-keV transition appears to be in coincidence with a number of transitions, none of which belong to ^{80}Ge. Nor was this apparent γ-ray observed in coincidence with known transitions in the nucleus of interest.

The case of the 3090-keV γ-ray observed by Hoff is similar, in that no firm link could be established between this apparent transition and transitions in ^{80}Ge. Here, the transition appears to be in coincidence with a transition at 430-keV which in turn is in coincidence with a transition at 608-keV, which happens to be a transition in ^{79}Ge. Though small, ^{80}Ga does have a β-delayed neutron branch to ^{79}Ge, at 0.86% [79].

Finally, the 3818-keV apparent γ-ray was observed in coincidence with the 1083- and 1313-keV γ-rays, which run in parallel, and have no linking transition between their 1742- and 1972-keV states, respectively. Therefore, this transition is not placed as part of the decay scheme of ^{80}Ge.

4.7 Shape coexistence

Shape coexistence is now known to be ubiquitous in the chart of nuclides. In chemistry, the presence of isomers is an instance of shape coexistence, where different configurations of the same molecule can lead to different properties. The case of the limonene molecule is a

perfect example, where its different shapes lead to the difference of smells between oranges and lemons [80].

In nuclei, shape coexistence, previously thought to be extremely rare in the chart of nuclides, manifests as the presence of two or more excited states, exhibiting distinct properties, which can only be described by differing intrinsic shapes [81]. These states occur very close in energy, often within a few hundred keV.

The classic example of observed shape coexistence is that of ^{186}Pb. Studied by Andreyev *et al.* [82] through the α-decay of ^{190}Po, it was observed to have three 0^+ states: its spherical ground state, and two, closely spaced, excited 0^+ states, as shown in Figure 4.11.

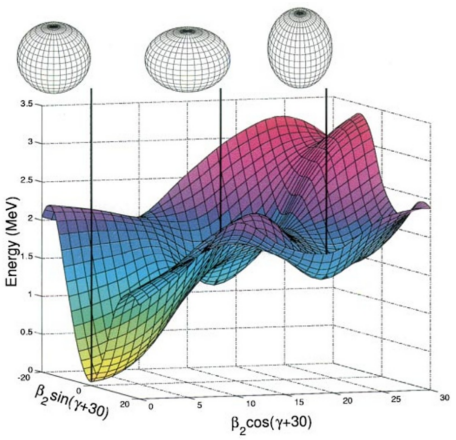

(a) Potential energy surface, showing two deformed 0^+ excited states, in the vicinity of the 0^+ ground state in ^{186}Pb.

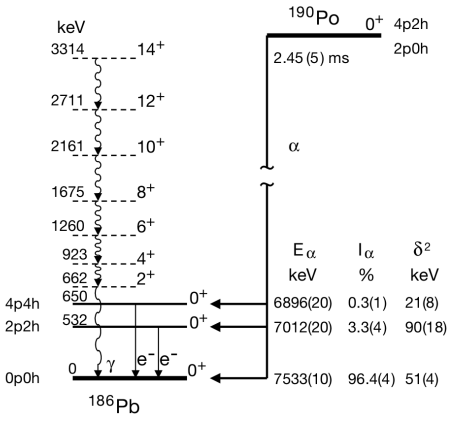

(b) The α-decay schematic of ^{190}Po into excited states in ^{186}Pb. Two excited 0^+ states were observed, above the 0^+ ground state. Their configurations are shown as 2 particle 2 hole (2p-2h) and 4 particle 4 hole (4p-4h) states.

Figure 4.11: A quintessential example of shape coexistence in the ^{186}Pb nucleus, observed by Andreyev *et al.* This experiment showed that there are two excited 0^+ states, each with different deformation, very close in energy to the 0^+ ground state. a) The potential energy surface showing the small energy range in which these three states exist. b) The configurations that allow for these excited states to appear are associated with two particle two hole (2p-2h) and four particle four hole (4p$-$4h) excitations, promoting the appropriate number of particles from the valence band to higher orbitals. Reprinted by permission from Nature [82].

The presence of these shapes was attributed to the excitation of proton pairs. Since pairing is favoured in nuclei, rather than breaking a pair and exciting one of the partners to the valence band, it is more energetically favourable to promote the pair, leaving proton holes in the lower band. The prolate, pancake-like, shape is attributed to a 2 proton$-$2 hole (2p-2h) configuration, where a proton pair has been promoted to the valence band. The oblate, cigar-like, shape is attributed to the promotion of two pairs of protons, leaving four

holes in the lower band (4p-4h). Shown in Figure 4.11, these states occur within a very small energy range, on the order of ∼600 keV in this case [82].

The change in the shape arises from the change in the attractive proton-neutron (p−n) interactions in the nucleus. Once proton pairs are promoted, the number of nearby p−n interactions in the nucleus is reduced, leading to a deformation in the shape of the nucleus. This deformation then leads to rotational bands in the level structure, alongside the vibrational bands expected of a spherical nucleus.

More and more nuclei have been observed to exhibit shape coexistence, but no single region has been deeply studied [80]. The ^{186}Pb nucleus lies at the $Z = 82$ proton shell closure, but contains neutrons in the midshell region, making it a good testing ground for this phenomenon. Other regions of this type may also prove to be good foundations with which to study this phenomenon.

4.8 Shape coexistence around the ^{78}Ni region

The ^{78}Ni nucleus is a doubly-magic nucleus. With its position on the nuclear chart so far away from stability, initial study of this nucleus was restricted to theoretical work [83] and to inferences from neighbouring nuclei [84, 85]. Taniuchi *et al.* [86], confirmed that its magicity, with $Z = 28$ and $N = 50$, is preserved, despite being so far from stability. Furthermore, it was observed to exhibit shape coexistence, in the form of an excited 2_2^+ at 2.91 MeV, very close in energy to the yrast 2_1^+ at 2.60 MeV. However, as noted by Taunichi *et al.*, isotopes in the neighbourhood, primarily ^{66}Cr and ^{70,72}Fe [87], show evidence of the weakening of shell closure at $Z = 28$, in the form of lowering of the 2_1^+ states . The vanishing of this shell gap may provide clues to the onset of deformation in this region, leading to shape coexistence and motivating the studies in this isotopic region.

Further motivation can be found in the recent work by Nowacki *et al.* [88]. In this work, the authors assert that shape coexistence is often found at the boundaries of areas called Islands of Inversion (IOI), areas of the chart of nuclides where sudden onset of deformation of the ground state is observed [89, 90]. This assertion is supported by observation of this phenomenon near lighter magic numbers, notably around $N = 20$, where evidence of shape coexistence has been corroborated through β-decay and $E0$ transition studies [91].

4.8.1 The case for ^{80}Ge

The ^{80}Ge nucleus is in the vicinity of the ^{78}Ni doubly magic nucleus, making it an excellent candidate for probing shape coexistence in the regions around shell closures.

The systematics of the region hint at the presence and expected energy value of the 0_2^+ state. The germanium isotopic chain and the $N = 48$ isotonic chain indicate a decrease in the energy of the 0_2^+ in ^{78}Ge, and an increased value of the same state in ^{84}Se. Connecting

these trends, as shown in Figure 4.12, to converge on the ^{80}Ge, indicates that the 0_2^+ state would appear at around 2 MeV.

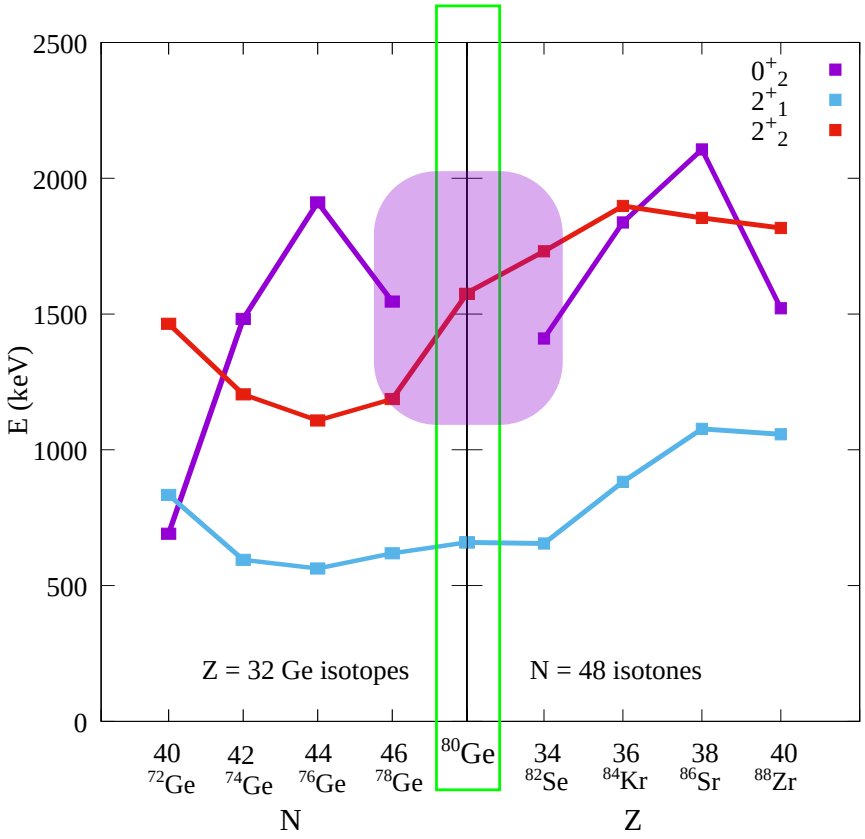

Figure 4.12: Select levels of the even germanium isotopes from $^{72-80}$Ge, alongside the levels of the N=50 isotones. These trends depict the excited 0_2^+ states (purple) in the region as well as the 2_1^+ (blue) and 2_2^+ (red) states in this region . Evidence of shape coexistence is observed in the isotopes surrounding ^{80}Ge (green), but, as suggested by the shaded region, there had been no observation of the 0_2^+ state in ^{80}Ge, until the work by Gottardo *et al* in 2016 [77]. Based on these systematics, the state is thought to be around 2 MeV. Data gathered from Ref. [92] .

A recent experiment by Gottardo *et al.* [77] at the ALTO facility observed the key signature of shape coexistence — an excited 0^+ very close in energy to the ground state. However, they did not observe it at the expected ∼2 MeV, but rather at 639 keV, just below the first excited 2_1^+ at 659-keV.

They observed it through electron-conversion spectroscopy, with the evidence manifesting as an electron peak at 628 keV — 639-keV minus the Ge K electron binding energy (11 keV) — as seen in Figure 4.13(a). Furthermore, they observed a coincidence between this electron peak and a γ-ray, and associated it with a transition de-exciting a 2403-keV state and populating the proposed 639-keV 0_2^+ state, as shown in Figure 4.13(b).

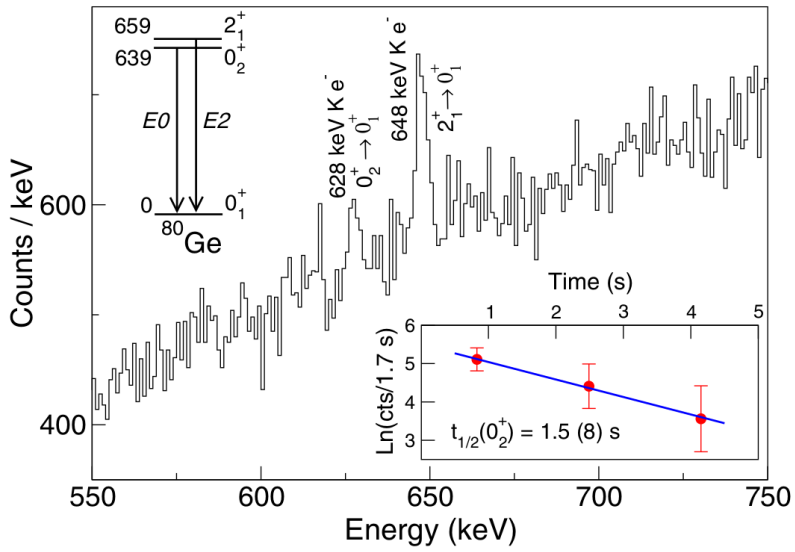

(a) The presence of a transition at 628-keV in the observed electron spectrum was presented as evidence for a 0^+ state at 639-keV, below the first 2^+ state at 659 keV.

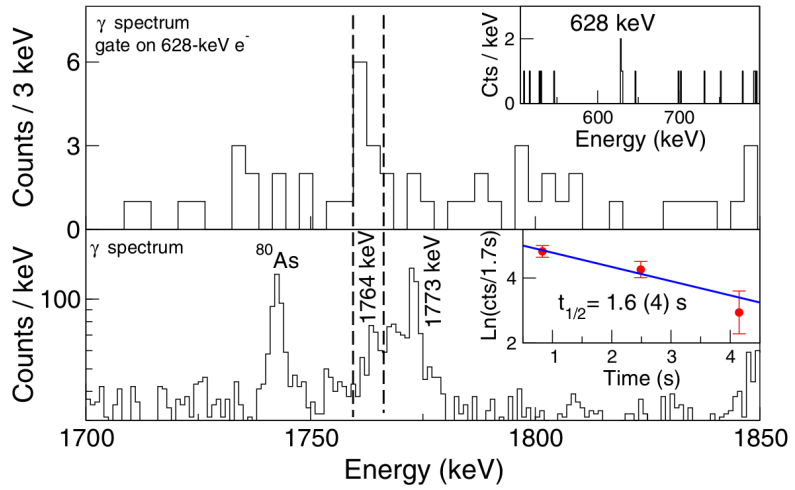

(b) Top: electron gated γ-ray spectrum, centered on the 628-keV electron peak, showing coincidence with the 628-keV transition. Bottom: β-gated γ-ray spectrum showing the location of the 1764-keV peak, and its half-life (inset), characteristic of the ^{80}Ga decay.

Figure 4.13: Evidence for the 639-keV 0^+ state in ^{80}Ge as observed by the ALTO collaboration. (a) The electron spectrum obtained in the ALTO experiment, showing a peak at 628-keV in their conversion electron spectrum, indicating a 0^+ excited state at 639-keV. (b) Gamma-ray spectra observed, showing coincidence between an observed 1764-keV γ-ray and the 628-keV electron peak, indicating the presence of a state at 2405-keV that would depopulate through a 1764-keV transition and populate the alleged 639-keV 0^+ state. Reprinted with permission from [77] by the American Physical Society.

Though this was strong evidence for shape coexistence in ^{80}Ge, they did not observe the deformed band that would be built upon this excited 0_2^+ state, nor did they observe a transition between the (2^+) state at 1573 keV expected due to the γ-ray selection rules. In an effort to search for these missing pieces of the puzzle, and to expand upon the level scheme of this nucleus, the β-decay of ^{80}Ga into excited states of ^{80}Ge was once again observed, this time using the GRIFFIN spectrometer.

4.9 Shape coexistence - the findings

Confirmation of the presence of the 639-keV 0_2^+ was expected during this experiment, and to that end, the detector set-up included the PACES array, in order to observe the conversion electrons that served as evidence for this state.

However, no such signature was found, despite multiple efforts to locate the 628-keV electron line and the 1764-keV γ-ray identified as populating the 639-keV state.

Figure 4.14 shows the electron spectrum obtained during the GRIFFIN experiment. The ^{80}Ge K-line (648-keV), expected from the 659-keV 2^+ state is observed, along with the L-line (658-keV). The ^{80}Kr K-line, at 602-keV, is also observed, as expected, since this is a prominent isobaric contaminant in the beam. No evidence for the 628-keV electron line is observed, despite Gottardo *et al.* observing it to be approximately one third as intense as the 648-keV electron peak. It is important to note than the L-line observed in Figure 4.14 is approximately one quarter the intensity of the K-line, by visual inspection alone.

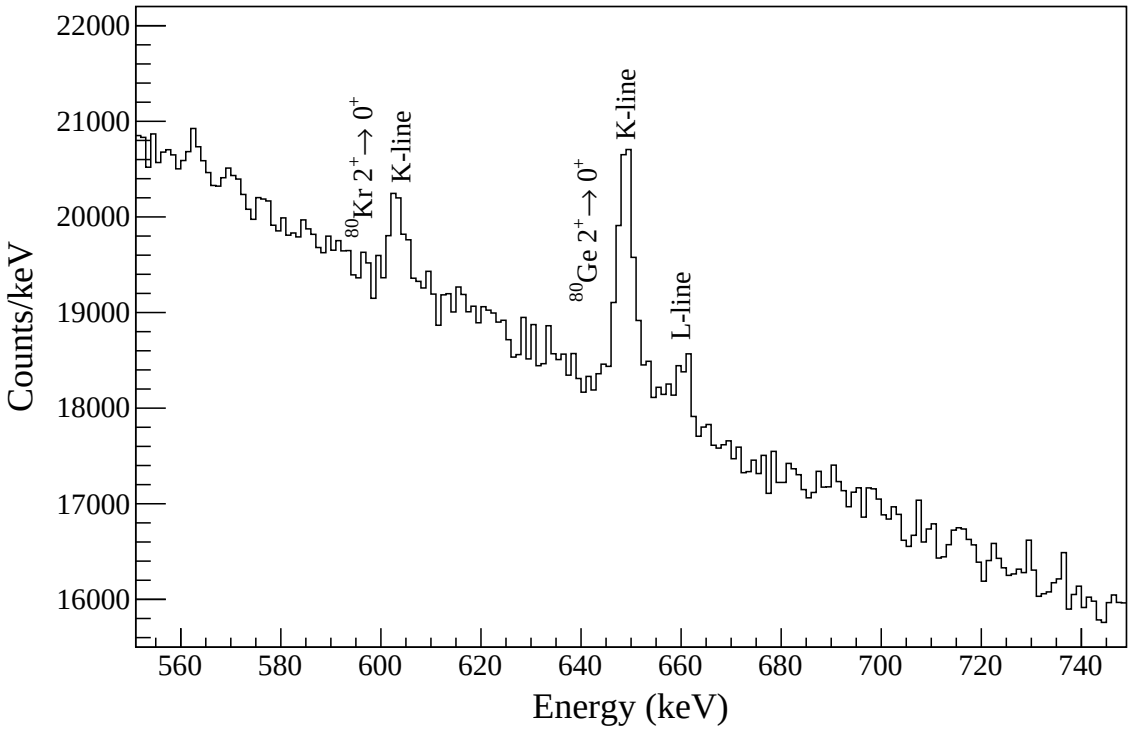

Figure 4.14: The conversion electron spectrum obtained from the PACES detector. Several transitions are observed, including the $2^+ \rightarrow 0^+$ transitions in both ^{80}Kr and ^{80}Ge, at 601 and 648 keV, respectively, with the former present as the daughter of the ^{80}Rb contaminant. Evidence for the L-line in ^{80}Ge is also observed. No transition is observed at 628 keV. Reprinted with permission from [93] by the American Physical Society.

Aside from the electron line at 628 keV, Gottardo *et al.* also observed a transition at 1764-keV in coincidence with the 628-keV line. In the present experiment, a broad feature was observed at 1764-keV, shown in the inset of Figure 4.15(b). Using an $e^- - \gamma$ coincidence matrix, a search was conducted for the 628-keV line. Though the 1764-keV peak was quite broad, providing a larger coincidence range, no electron peak was found at the expected 628 keV. The method is summarized in Figure 4.15. Figure 4.15(a) shows the efficacy of the $e^- - \gamma$ coincidence, where a clear coincidence is observed between the 1083-keV γ-ray and the 648-keV electron line; in Figure 4.15(b), the same method of coincidence between the 1764-keV γ-ray and the electron spectrum is shown, but no evidence is seen for the 628-keV electron line.

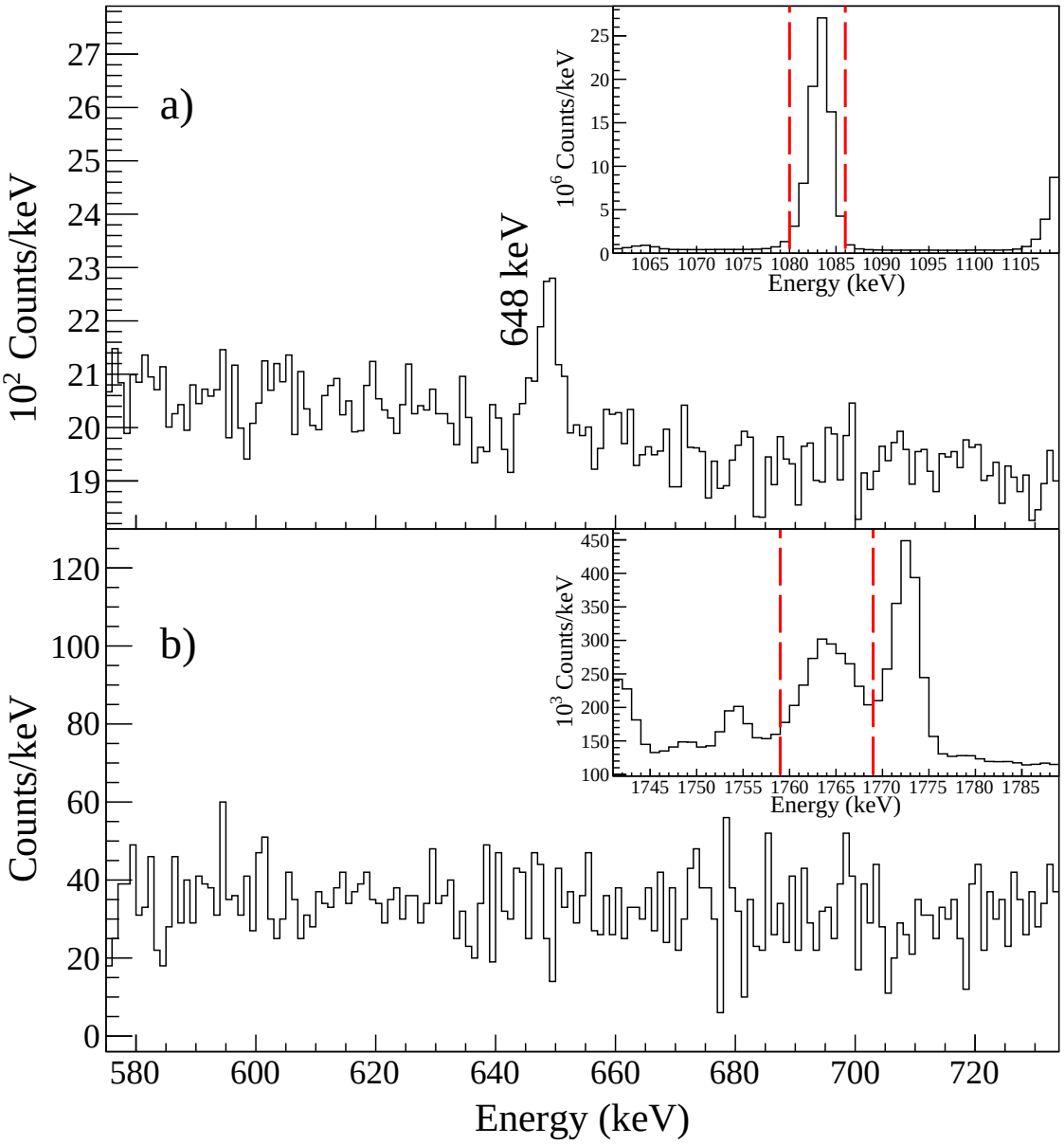

Figure 4.15: Gamma-gated electron spectra. (a) Electron spectrum in coincidence with the 1083-keV transition (inset), associated with the decay between the 4^+ 1743-keV and the 2^+ 659 keV states, clearly showing a coincidence with the 648-keV electron peak as expected. (b) Electron spectrum in coincidence with the broad 1764-keV transition (inset). There is no peak observed in the electron spectrum at the expected 628 keV. The (red) dashed lines indicated where the gate was placed in the γ-ray spectrum. Reprinted with permission from [93] by the American Physical Society.

The lack of an observed conversion electron peak at 628-keV and a coincidence between this electron peak and a γ-ray at 1764-keV were both strong indications that this 639-keV state was not in fact present in this nucleus.

4.9.1 Establishing detection limits

It is not uncommon for transitions to be buried in the background of a spectrum, or overwhelmed by stronger, more intense transitions. The nonobservation of the conversion electron peak and the coincident γ-ray could be due to high background or lack of statistics, which prompted the characterization of the detection limits of the GRIFFIN spectrometer set-up. This was done in two separate methods: using only the conversion-electron spectrum and using the $e^- - \gamma$ coincidence matrix.

The first case, using the conversion electron spectrum, established the detection limit for observing the 628-keV electron peak. Figure 4.16 shows the conversion electron spectrum, centered around the region of interest. The counts in the seven histogram bins centered around 628-keV were obtained, and then background counts were taken from either side of the region of interest, comprised of seven bins to the left of the region and seven bins to the right.

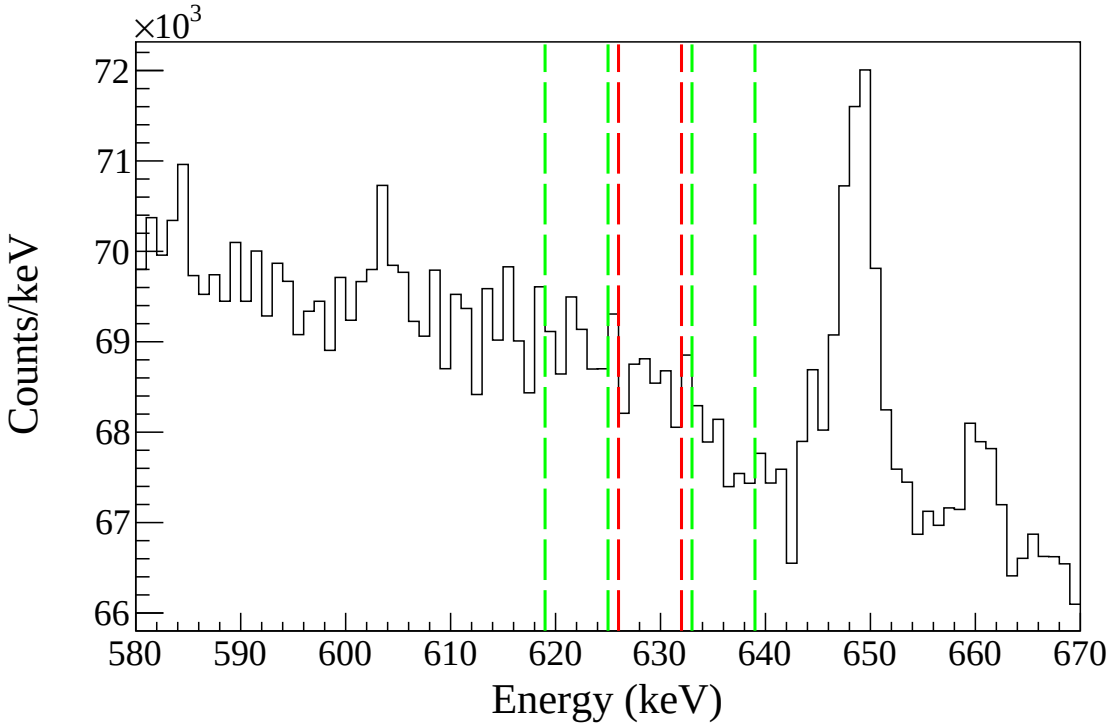

Figure 4.16: Ranges in the electron spectrum used to determine the 2σ detection limit for finding the 628-keV transition. The region (red-lined) centered around 628-keV is used as the detected counts, while an average of the two regions (green-lined) to either side of the peak region is taken as the background. The ^{80}Ge 648-keV K-line, the 658-keV L-line and the ^{80}Kr 602-keV K-line are all present in this spectrum.

The would-be-peak count number was determined by taking these values into account, as shown in Equation 4.1;

$$N_{counts}(628\text{ keV}) = N_{626-632} - \frac{N_{619-625} + N_{633-639}}{2} \tag{4.1}$$

where the subscripts refer to the histogram bins involved in the calculation. The uncertainty in this value was determined as per Equation 4.2;

$$\Delta N = \sqrt{N_{626-632} - \frac{N_{619-625} + N_{633-639}}{4}}. \tag{4.2}$$

The 2σ limit is then given by Equation 4.3,

$$2\sigma = \left| N_{counts}(628\text{ keV}) + 2\Delta N \right|. \tag{4.3}$$

Given this 2σ limit, an intensity limit for this transition can be calculated given the observed intensity of the 648-keV electron line associated with the 2^+ 659-keV state.

$$I_{628-keV} = \left| N_{counts}(628\text{ keV}) \frac{\alpha_{659\text{ keV}}}{N_{counts}(648\text{ keV})} \frac{100}{100 + 3.43} \right|, \tag{4.4}$$

where $\alpha_{659\text{keV}} = 9.276 \times 10^{-4}$ and is the internal conversion coefficient associated with the decay from the 659-keV state. Since these calculations were based upon the data available in ENSDF, and the data were not normalized to 100, the normalization factor used was 100+3.43, as per the feeding available in ENSDF.

Equation 4.4 yielded an intensity value of 0.02 per 100 decays. Based on the intensity of the 628-keV peak shown in the ALTO conversion electron spectrum, the intensity of that line is ∼0.08(2) per 100 decays. This value is four times higher than the 2σ limit for detection using the GRIFFIN spectrometer coupled to PACES, indicating that this transition is unlikely to exist. This also indicates that this experiment did not suffer from lack of statistics.

Further proof of this nonobservation is seen in the missing 628-keV conversion electron coincidence with the 1764-keV γ-ray observed by the ALTO collaboration, as shown in Figure 4.13(b). They stated that this 1764-keV γ-ray depopulated a newly observed (2^+) level at 2403-keV, and populated the 639-keV 0_2^+ state.

An $e^- - \gamma$ matrix was constructed, much like a $\gamma - \gamma$ matrix. Gating along this matrix will produce a γ-ray coincidence with a conversion electron peak and vice-versa. A successful use case of this $e^- - \gamma$ matrix can be seen in Figure 4.15(a), where a gate is placed on the 1083-keV γ-ray transition depopulating the 1743-keV state and populating the 659-keV, with which the 648-keV conversion electron peak is associated. This coincidence is evident in the conversion electron peak appearing at 648 keV as expected.

While the present experiment did observe an unusually broad peak at 1764 keV, a gate on the $e^- - \gamma$ matrix at this energy did not yield a peak at 628 keV in the conversion

electron spectrum. This is shown in Figure 4.15(b), and is contrary to the findings of the ALTO collaboration, which appear in Figure 4.13(b).

A similar calculation of the 2σ detection limit as for the conversion electron spectrum was computed to determine the lowest possible detection level in the $e^- - \gamma$ spectrum. The regions of interest appear in Figure 4.17, and are again seven bins centered about 628 keV for the placement of the peak and seven bins to the left and seven bins to the right to determine an average background. This 2σ limit was used to calculate the intensity of the 1764-keV associated with the 639-keV state, relative to a neighbouring known peak at 1772 keV, depopulating the 3513-keV state.

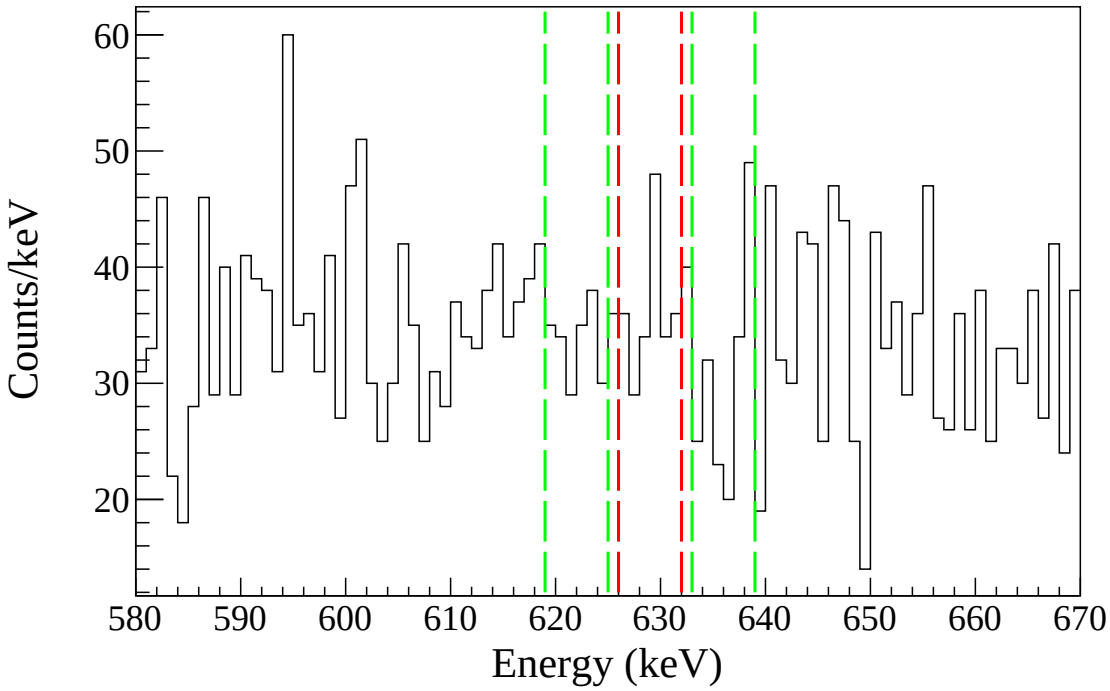

Figure 4.17: Gamma-gated electron spectrum used to calculate the 2σ limit for observation of the 628-keV peak in coincidence with the 1764-keV γ-ray transition. No peak is found to be in coincidence with the broad 1764-keV peak in the γ-ray spectrum. The low background observed in this spectrum is unlikely to impede observation of a possible transition.

Based on their findings, the ALTO collaboration asserted the intensity of the 1764-keV γ-ray transition to be 0.3 times that of the 1772-keV transition. However, the 2σ limit, calculated in the same manner as described in Equation 4.3, for the GRIFFIN experiment established that for this transition to not be observed given the GRIFFIN capabilities, it would have to be 0.003 times the intensity of the neighbouring 1772-keV transition. This limit is one hundred times lower than the intensity claimed by the ALTO collaboration, further proof that this 0_2^+ excited state at 639-keV was not in fact real.

Investigation of the broad 1764-keV γ-ray peak did reveal four new transitions, depopulating newly observed states in ^{80}Ge. This peak has a full width at half-maximum (FWHM) value of 5.4, compared to the FWHM of the nearby 1772-keV peak at 2.9, hinting at the possibility of a multiplet. These peaks and the associated cascades are shown in Figure 4.18, their intensity information is found in Table 4.3. However, none of these transitions were associated with the decay of the alleged 2403-keV state to the purported 0_2^+ 639-keV state.

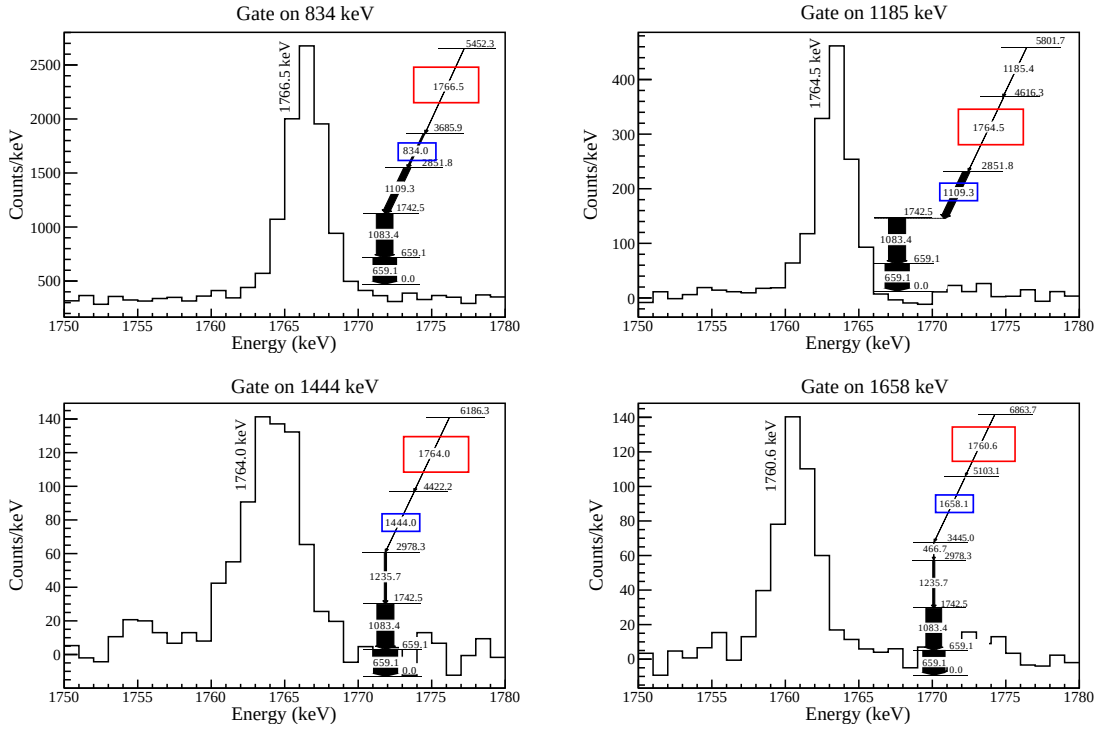

Figure 4.18: The broad peak centered around 1764-keV was found to be a convolution of several peaks, populating different states above 3.5 MeV. Note that none of these states is the supposed 2406-keV state that is depopulated by this 1764-keV transition, and populates the purported 639-keV 0_2^+ state. Reprinted with permission from [93] by the American Physical Society.

4.9.2 Theoretical interpretation

To compliment the experimental study, large scale shell model calculations were performed on the even isotopes ^{78,80,82}Ge, to better understand the capabilities of the models to reproduce experimental data and to gain information about the location of the 0_2^+ state. Two different large-scale shell model calculations, with two different cores and two different interactions were performed by theoretician collaborators.

The LNPS valence space is based on a $^{48}_{20}$Ca^{28} core, encompassing the full pf shell for the protons and neutrons and adding the $0f_{7/2}$, the $0g_{9/2}$ and $1d_{5/2}$ orbitals for the neutrons. The interactions used in this calculation were those described by Lenzi *et al.* [94], and are

composed of a hybrid interaction, encompassing different sets of two body matrix elements, which are realtistic in nature. The PF-SDG valence space is based on a $^{60}_{20}Ca^{40}$ core, and encompasses the $p = 3$ major oscillator shell — pf shell — for protons, and the $p = 4$ — sdf — major oscillator shell for neutrons. In this model, the effective interaction matrix elements are based on free nucleon-nucleon interactions, as described by Nowacki *et al.* [88]. It is important to note that the intricacies of these two large-scale shell models are described in detail in Ref. [88] and Ref. [94], respectively, and are beyond the scope of this work.

The levels produced by both models are shown in Figure 4.19. The large scale shell models are both reasonably good at predicting the experimentally observed levels for all involved isotopes. In particular, the presence of intruder states in ^{82}Ge is reproduced with remarkable accuracy in their energies, when compared to the experimental data.

A 0^+_2 state in ^{80}Ge is predicted by the theory, but this state occurs at 1.88 MeV, much closer to the energy expected from the systematics, as seen in Figure 4.12.

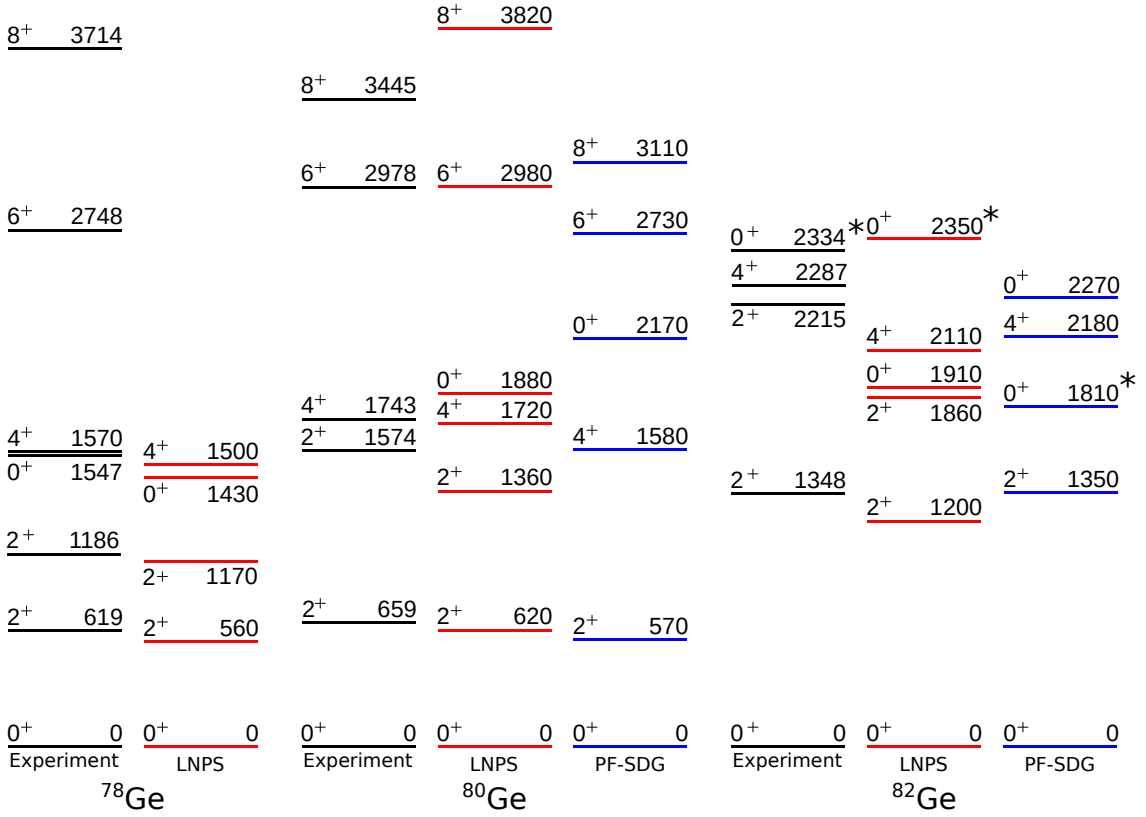

Figure 4.19: Theoretical calculations of the excited state in the ^{78,80,82}Ge isotopic chain. The experimental levels (black) are shown compared to the calculated states. The calculations are done with the LNPS (red) and the PF-SDG (blue) interactions. The intruder states are labelled by (*). Reprinted with permission from [93] by the American Physical Society.

The experimental results, having sufficient statistics and well-characterized detection limits, supported by the large-scale shell model calculations do not support the findings

of the ALTO collaboration. Given the capabilities and the power of the GRIFFIN spectrometer, this is indicative that this 639-keV 0_2^+ state does not exist and thus there is no low-energy shape coexistence in ^{80}Ge.

4.10 Future work - the search for shape coexistence in ^{80}Ge

This work probed shape coexistence in the ^{80}Ge nucleus, through the β-decay of ^{80}Ga, and while no evidence of the purported 639-keV 0^+ state was found, there is still much work that can be done in order to locate the theoretically suggested state near 2 MeV. The systematics of the region, as shown in Figure 4.12, suggest a state at this energy. The large scale shell model calculations in Figure 4.19 also indicate the presence of this 0_2^+ near $\sim$2 MeV, presenting a very compelling case to search for this state.

The limitation of this β-decay study in locating this 0^+ level lies in the β-decay selection rules; a β-transition between the $3(^-)$ isomer in ^{80}Ga to a 0^+ in ^{80}Ge would be a third forbidden transition, making it extremely unlikely to occur. Complimentary experiments such as the transfer reaction ^{79}Ge(d,p)^{80}Ge, where ^{79}Ge is bombarded by deuterons (at low energy) transferring one neutron to make ^{80}Ge, would not suffer from these selection rule restrictions. A similar reaction could be done in inverse kinematics, through bombardment of ^{78}Ge nuclei onto a tritium target, ^{78}Ge(t,p)^{80}Ge. These types of experiments could also yield further information about the character of these states and may firmly assign spins and parities to the existing and newly observed states.

There is clearly work that must still be done to better understand the nuclei in the region of ^{78}Ni, since it is potentially a portal to the fifth island of inversion.

Chapter 5

Conclusions & Future Directions

Tireless study in the field of fundamental nuclear science has led to great advances in the theoretical description of the nucleus, as well as the development of sophisticated spectroscopy tools with which to study the nucleus, one of the smallest building blocks of the universe.

The GRIFFIN spectrometer, built to study excited nuclei through decay spectroscopy is one such tool, that can be used to probe nuclear structure. The power of the GRIFFIN spectrometer lies not only in its suite of detectors, but also in its modularity, making it possible to study different decay modes, while being sensitive to weak transitions and spanning a wide energy range.

The use of this spectrometer lead to the observation of key nuclear structure data in the vicinity of two doubly-magic nuclei: $^{132}_{50}\mathrm{Sn}_{82}$ and $^{78}_{28}\mathrm{Ni}_{50}$, which will pave the way for further advances in nuclear theory.

In the case of the ^{129}Sn nucleus, the level scheme was greatly expanded with new transitions observed, populated by the ground state and isomers of ^{129}In. Most notably, the β decay of the $(29/2^+)$ ^{129m3}In high-spin isomer ($t_{1/2}$ = 0.110(15) s) was observed for the first time in this experiment. This lead to the calculation of a new β-branching ratio for this isomer. Furthermore, the half-lives of the ground state and the first two isomers were confirmed, and $\log ft$ values were used to tentatively assign spins to new states as well as to constrain previously suggested spins. These new findings will prove useful to the theoretical description of the region near doubly-magic ^{132}Sn. Future work must include the study of more neutron rich indium and tin species, particularly pushing towards the neutron drip line to study structure effects, as well as other exotic process such as β-delayed two neutron emission, predicted as a decay mode for ^{135}In. The Advanced Rare IsotopE Laboratory (ARIEL) facility, which will produce beams through photofission, will provide neutron-rich isotope beams, including ^{136,137}Sn, with experiments already in the works.

The ^{80}Ge data revealed over 100 transitions and 50 excited states, observed for the first time in this study. Previously observed but unplaced transitions were assigned to existing and newly observed states; $\log ft$ values were calculated for all known and newly observed

states, which gave guidance in tentative spin assignments. The most interesting insight gained through this experiment was the nonobservation of a previously assigned 0_2^+ excited state at 639 keV in ^{80}Ge. Through extensive spectroscopic studies, the presence of this state was brought into question. The characteristic peak in the conversion electron spectrum was missing, and the apparent coincidence between this peak and a higher lying γ-ray transition at 1764 keV was nowhere to be found — the 1764-keV peak is due to a multiplet, but no trace of a coincidence with a 628-keV conversion electron was found. These nonobservations, coupled with studies that were undertaken by theoretician collaborators lead to the conclusion that this 0_2^+ state at 639 keV did not in fact exist. This has massive implications for shape coexistence in the region: this nucleus no longer exhibited the signature of low-energy shape coexistence, leading to the question of whether the phenomenon is observed in the region around doubly-magic ^{78}Ni. Based on systematic arguments and theoretical calculations, the 0_2^+ state should appear near 2 MeV. This state was not observed in this work, likely due to the β-decay selection rules, which would make the direct transition between the $3(^-)$ isomer in ^{80}Ga into a potential 0_2^+ state in ^{80}Ge a third forbidden transition. Further study is required and will likely involve the use of other, complimentary, population mechanisms such as transfer reactions. Further work also involves the study of ^{82,84}Ge, which would, in turn, reveal more information about shape coexistence in the region.

Both studies were able to elucidate key features and structural information on isotopes in two different regions of magicity. These data will aid the further development of the theory, since any valid nuclear model must be able to reproduce excited states of not only magic nuclei and nuclei in their vicinity, but also other nuclei in the chart.

The new ARIEL facility [95] that is to come online at TRIUMF will expand the capabilities of the laboratory. Photofission is known to produce species in the neutron-rich side of the chart of nuclides, meaning that the facility will have access to a series of isotopes closer to the neutron drip line. Studies in these regions will aid not only fundamental nuclear structure, but also nuclear astrophysics, allowing experimenters a better handle on nucleosynthesis processes such as the rapid neutron capture (r-process). Other facilities around the world also provide complimentary production and study mechanisms. RIKEN (Institute of Physical and Chemical Research) in Japan and FRIB (Facility for Rare Isotope Beams) in the USA produce isotopes through the fragmentation technique, which does not suffer from losses related to the chemistry of the isotope in question. This, coupled with the various spectrometers present at these facilities can produce contemporary information to validate existing data and to expand the knowledge base.

Improvements to available beams and also to the GRIFFIN spectrometer could lead to further discoveries in these regions. Several different ancillary detectors are currently in the development stage and, when coupled to GRIFFIN, will yield further information and expand the power of the array. The Ancillary Detector for Rare-Isotope Event Selection (ARIES) [96], which will serve as an upgrade to SCEPTAR and ZDS, will provide better

β-detection efficiency ($> 90\%$) as well as increased timing efficiency for $\beta-\gamma-\gamma$ coincidence measurements. The Detector Array for Energy Measurements of Neutrons (DAEMON) [97] will provide energy information on the neutrons observed through the use of plastic scintillators and will prove useful in β-delayed neutron emission studies. The Regina Cube for Multiple Particles (RCMP) [98], comprised of a series of double sided silicon strip detectors, will provide an additional tag for α particles and protons, allowing for the studies of decay modes such as β-delayed two proton emission.

The theoretical work in both the ^{132}Sn [99] and ^{78}Ni [88] regions is ongoing, with the exploration of several different nucleon interactions and nuclear cores. The field is expanding rapidly, aided by the increasing capabilities of computer clusters, which can handle the exponential growth of parameters and inputs required by the models. As more experimental data become available, the models will become more precise and better at predicting properties of hitherto unobserved nuclei, in the hopes that a fully descriptive nuclear theory can be eventually formed.

The nuclear landscape is vast and everchanging; with newfound knowledge of the structure of these two nuclei, the promise of a cohesive nuclear theory is just a bit closer.

Bibliography

[1] P. Bizony. *Atom*. Icon Books Ltd., 2007.

[2] E. Rutherford. The scattering of α and β particles by matter and the structure of the atom. *The London, Edinburgh, and Dublin Philosophical Magazine and Journal of Science*, 21(125):669–688, 1911.

[3] J. Chadwick. The existence of a neutron. *Proceedings of the Royal Society A*, 136:692–708, 1932.

[4] F. H. Garcia. *Calculation of rates for radioactive isotope beam production at TRIUMF*. MSc thesis, Simon Fraser University, 2016.

[5] J. Erler et al. The limits of the nuclear landscape. *Nature*, 486:509–512, Jun. 2012.

[6] N. Bohr. Rydberg's discovery of the spectral laws, 1954. C.W.K. Gleerup.

[7] St. John Nepomucene. Rydberg: The Man and the Constant. *Historical Studies in the Physical Sciences*, 6:127–145, Jan. 1960.

[8] G. Choppin, J.-O. Liljenzin, J. Rydberg, and C. Ekberg. *Radiochemistry and Nuclear Chemistry*. Butterworth Heinemann, 4th edition, 2013.

[9] W. Pauli. The connection between spin and statistics. *Phys. Rev.*, 58:716–722, Oct. 1940.

[10] K.S. Krane. *Introductory Nuclear Physics*. John Wiley & Sons, 1988.

[11] K Vogt, T Hartmann, and A Zilges. Simple parametrization of single- and two-nucleon separation energies in terms of the neutron to proton ratio N/Z. *Phys. Lett. B*, 517(3):255–260, 2001.

[12] D. J. Griffiths and D. F. Schroeter. *Introduction to Quantum Mechanics*. Cambridge University Press, 3rd edition, 2018.

[13] B. A. Brown. Lecture notes in nuclear structure physics, 2005.

[14] Roger D. Woods and David S. Saxon. Diffuse surface optical model for nucleon-nuclei scattering. *Phys. Rev.*, 95:577–578, Jul. 1954.

[15] M. G. Mayer. On closed shells in nuclei. ii. *Phys. Rev.*, 75:1969–1970, Jun. 1949.

[16] M. G. Mayer. Nuclear configurations in the spin-orbit coupling model. i. empirical evidence. *Phys. Rev.*, 78:16–21, Apr. 1950.

[17] O. Haxel, J. H. D. Jensen, and H. E. Suess. On the "magic numbers" in nuclear structure. *Phys. Rev.*, 75:1766–1766, Jun. 1949.

[18] K. Heyde. *Basic Ideas and Concepts in Nuclear Physics.* Institute of Physics Publishing, Cornwall, 3rd edition, 2004.

[19] G. Friedlander, J. W. Kennedy, E. S. Macias, and J. M. Miller. *Nuclear and Radiochemistry.* John Wiley & Sons Inc, 1981.

[20] A. Kamal. *Nuclear Physics.* Springer, 2014.

[21] C. A. Bertulani. *Nuclear Physics in a Nutshell.* Princeton University Press, 2007.

[22] W. Loveland, D. J. Morrissey, and G. T. Seaborg. *Modern Nuclear Chemistry.* Wiley & Sons, 2006.

[23] D.H. Wilkinson and B.E.F. Macefield. A parametrization of the phase space factor for allowed β-decay. *Nuclear Physics A*, 232(1):58–92, 1974.

[24] D. H. Wilkinson, A. Gallmann, and D. E. Alburger. Super-allowed fermi β decay: Half-lives of ^{14}O and ^{38}K^{m}. *Phys. Rev. C*, 18:401–407, Jul. 1978.

[25] J. Kramp et al. Nuclear two-photon decay in $0^+ \rightarrow 0^+$ transitions. *Nuclear Physics A*, 474(2):412–450, 1987.

[26] R. A. Dunlap. *An Introduction to the Physics of Nuclei and Particles.* Brooks Cole, 2003.

[27] J. M. Blatt and V. F. Weisskopf. *Theoretical Nuclear Physics.* Springer, 1952.

[28] V. F. Weisskopf. Radiative transition probabilities in nuclei. *Phys. Rev.*, 83:1073–1073, Sept. 1951.

[29] F. H. Garcia et al. Spectroscopy of neutron-rich ^{80}Ge using the griffin spectrometer. *Phys. Rev. C*, To be submitted.

[30] A. Einstein. Über einen die erzeugung und verwandlung des lichtes betreffenden heuristischen gesichtspunkt. *Annalen der Physik*, 322(6):132–148.

[31] A. H. Compton. A quantum theory of the scattering of x-rays by light elements. *Phys. Rev.*, 21:483–502, May 1923.

[32] G. F. Knoll. *Radiation Detection and Measurement.* John Wiley & Sons, 2000.

[33] R. D. Evans. *The Atomic Nucleus.* Krieger Publishing, 1955.

[34] T.A. Domingo. *Time-resolved gamma-ray spectroscopy with the GEARS detector: applications in environmental radionuclide monitory and neutron activation analysis.* MSc thesis, Simon Fraser University, 2017.

[35] J. Dilling, R. Krücken, and G. Ball. ISAC overview. *Hyperfine Interact.*, 225:1, 2014.

[36] P. Van Duppen. Isotope separation on line and post acceleration. In *The Euroschool Lectures on Physics with Exotic Beams Vol II.* Springer, 2006.

[37] P. G. Bricault, F. Ames, M. Dombsky, P. Kunz, and J. Lassen. Rare isotope beams at ISAC – target & ion source systems. In J. Dilling, R. Krücken, and L. Merminga, editors, *ISAC and ARIEL: The TRIUMF Radioactive Beam Facilities and the Scientific Program*. Springer, 2013.

[38] S. Raeder, H. Heggen, J. Lassen, F. Ames, D. Bishop, P. Bricault, P. Kunz, Mjøs, and Teigelhöfer. *Rev. Sci. Instrum.*, 85:033309, Mar. 2014.

[39] P. Bricault et al. Rare isotopes beam at isac – target & ion source systems. In J. Dilling, R. Krücken, and L. Merminga, editors, *ISAC and ARIEL: The TRIUMF Radioactive Beam Facilities and the Scientific Program*. Springer, 2013.

[40] C. E. Svensson and A. B. Garnsworthy. The GRIFFIN spectrometer. *Hyperfine Interact*, 225:127–132, 2014.

[41] A. B. Garnsworthy et al. The GRIFFIN data acquisition system. *Nucl. Instrum. Meth. Phys. Res. A*, 85:85–104, 2017.

[42] A. B. Garnsworthy et al. The GRIFFIN Facility for Decay-Spectroscopy Studies at TRIUMF-ISAC. *Nucl. Instrum. Meth. Phys. Res. A*, 918:9–29, Feb. 2019.

[43] U. Rizwan et al. Characteristics of GRIFFIN high-purity germanium clover detectors. *Nucl. Instrum. Meth. Phys. Res. A*, 820:126–131, 2016.

[44] K. Raymond. Private Communication.

[45] P. E. Garrett et al. The TRIUMF nuclear structure program and TIGRESS. *Nucl. Instrum. Meth. Phys. Res. B*, 261:1084–1088, 2007.

[46] GRIFFIN Collaboration, GRIFFIN Efficiency Calculator. `https://griffincollaboration.github.io/efficiencyCalculator/`. 2015.

[47] P. E. Garrett. DESCANT - the deuterated scintillator array for neutron tagging. *Hyperfine Interact.*, 225:137, 2014.

[48] R. Dunlop. *β and β-delayed neutron decay of the $N \approx 82$ nuclei $^{128-130}$Cd and ^{131}In studied with the Gamma-Ray Infrastructure for Fundamental Investigations of Nuclei (GRIFFIN)*. PhD thesis, University of Guelph, 2019.

[49] R. Coleman. *Beta decay of Neutron-Rich $^{52}_{19}K_{33}$*. MSc thesis, University of Guelph, 2019.

[50] J. L. Pore. *The investigation of the β^- decay of ^{46}K: Detailed Spectroscopy of the low-lying structure of ^{46}Ca with the GRIFFIN spectrometer*. PhD thesis, Simon Fraser University, 2016.

[51] N. Bernier. *Decay Spectroscopy of Neutron-Rick Cadmium Around N=82 Shell Closure*. PhD thesis, University of British Columbia, 2018.

[52] L. Spanier, K. Aleklett, B. Ekström, and B. Fogelberg. The Q_β values of the heavy Cd and In isotopes. *Nuc. Phys. A*, 474(3):359 –372, 1987.

[53] K. Aleklett, E. Lund, and G. Rudstam. Total β -decay energies and masses of strongly neutron-rich indium isotopes ranging from ^{120}In to ^{129}In. *Phys. Rev. C*, 18(1):462 – 475, 1978.

[54] L.-E De Geer and G. B. Holm. Energy levels of ^{127,129,131}Sn populated in the β^- decay of ^{127,129,131}In. *Phys. Rev. C*, 22(5):2163 – 2177, 1980.

[55] H. Gausemel et al. Decay of ^{127}In and ^{129}In. *Phys. Rev. C*, 69:054307, 2004.

[56] J. Genevey et al. High spin isomers in ^{129}Sn and ^{130}Sb. *Phys. Rev. C*, 65:034322, 2002.

[57] R. L. Lozeva et al. New sub-μs isomers in ^{125,127,129}Sn and isomer systematics of $^{124-130}$Sn. *Phys. Rev. C*, 77:064313, 2008.

[58] P. Armbruster et al. The recoil separator Lohengrin: Performance and special features for experiments. *Nuclear Instruments and Methods*, 139:213–222, 1976.

[59] H. Geissel et al. The GSI projectile fragment separator (FRS): a versatile magnetic system for relativistic heavy ions. *Nucl. Instrum. Meth. Phys. Res. B*, 70(1):286–297, 1992.

[60] J. Timar, Z. Elekes, and B. Singh. *Nuc. Data Sheets*, 121(143), 2014.

[61] *Update of X Ray and Gamma Ray Decay Data Standards for Detector Calibration and Other Applications*. Non-serial Publications. IAEA, Vienna, 2007.

[62] H. Junde, H. Su, and Y. Dong. Nuclear Data Sheets for A = 56. *Nucl. Data Sheets*, 112(6):1513–1645, Jun. 2011.

[63] F. H. Garcia et al. Spectroscopic studies of neutron-rich ^{129}In and its β-decay daughter, ^{129}Sn, using the GRIFFIN spectrometer. *Phys. Rev. C*, 103:024310, 2021.

[64] T. Kibédi, T. W. Burrows, M. B. Trzhaskovskaya, P. M. Davidson, and C. W. Nestor Jr. Evaluation of theoretical conversion coefficients using BrIcc. *Nucl. Instrum Meth. Phys. Res. A*, 589(2):202–229, May 2008.

[65] NIST National Institute of Standards and Technology. National Nuclear Data Center Interactive Chart of Nuclides., 2016.

[66] M. Emeric and A. Sonzogni. LOGFT. National Nuclear Data Center, Brookhaven National Laboratory.

[67] M.R. Mumpower, R. Surman, G.C. McLaughlin, and A. Aprahamian. The impact of individual nuclear properties on r-process nucleosynthesis. *Prog. Part. Nucl. Phys.*, 86:86–126, 2016.

[68] P. Hoff. The population of excited states in residual nuclei via delayed neutrons. *Nuclear Physics A*, 359(1):9–35, 1981.

[69] P. Hoff and B. Fogelberg. Properties of strongly neutron-rich isotopes of germanium and arsenic. *Nuclear Physics A*, 368(2):210–236, Sept. 1981.

[70] J.A. Winger et al. Decay of ^{80}Zn: Implications for shell structure and r-process nucleosynthesis. *Phys. Rev. C*, 36:758–764, 1987.

[71] A. Makishima et al. $(\nu g_{9/2}^{-2})_{8^+}$ isomers ^{82}Se$_{48}$ and ^{80}Ge$_{48}$ populated by deep-inelastic collisions. *Phys. Rev. C*, 59:R2331–R2333, 1999.

[72] H. Iwasaki et al. Persistence of the $N = 50$ shell closure in the neutron-rich isotope ^{80}Ge. *Phys. Rev. C*, 78:021304, Aug. 2008.

[73] E. Padilla-Rodal et al. $B(E2) \uparrow$ measurements for radioactive neutron-rich Ge isotopes: Reaching the $N = 50$ closed shell. *Phys. Rev. Lett.*, 94:122501, Mar. 2005.

[74] B. Cheal et al. Discovery of a long-lived low-lying isomeric state in ^{80}Ga. *Phys. Rev. C*, 82:051302(R), 2010.

[75] D. Verney et al. Structure of ^{80}Ge revealed by the β decay of isomeric states in ^{80}Ga: Triaxiality in the vicinity of ^{78}Ni. *Phys. Rev. C*, 87(5):054307, May 2013.

[76] F. Azaiez, S. Essabaa, F. Ibrahim, and D. Verney. The ALTO facility in Orsay. *Nuc. Phys. News*, 23:10 – 5, 2013.

[77] A. Gottardo et al. First Evidence of Shape Coexistence in the ^{78}Ni Region: Intruder 0_2^+ State in ^{80}Ge. *Phys. Rev. Lett.*, 116(18):182501, 2016.

[78] A. M. Forney. *Nuclear Structure studies of ^{78,80}Ge and adjacent nuclei.* PhD thesis, University of Maryland, 2018.

[79] B. Singh. Nuclear Data Sheets for A=80. *Nucl. Data Sheets*, 105(2):223–418, Jun. 2005.

[80] K. Heyde and J. L. Wood. Shape coexistence in atomic nuclei. *Rev. Mod. Phys.*, 83:1467–1521, Oct.–Nov. 2011.

[81] A. Poves. Shape coexistence in nuclei. *J. Phys. G: Nucl. Part. Phys.*, 43:2, 2016.

[82] A. N. Andreyev et al. A triplet of differently shaped spin-zero states in the atomic nucleus ^{186}Pb. *Nature*, 405:430–433, May 2000.

[83] Y. Tsunoda et al. Novel shape evolution in exotic Ni isotopes and configuration-dependent shell structure. *Phys. Rev. C*, 89:031301, Mar. 2014.

[84] Z. Y. Xu et al. β-decay half-lives of ^{76,77}Co, ^{79,80}Ni, and ^{81}Cu: Experimental indication of a doubly magic ^{78}Ni. *Phys. Rev. Lett.*, 113:032505, Jul. 2014.

[85] A. Welker et al. Binding energy of ^{79}Cu: Probing the structure of the doubly magic ^{78}Ni from only one proton away. *Phys. Rev. Lett.*, 119:192502, Nov. 2017.

[86] R. Taniuchi et al. ^{78}Ni revealed as a doubly magic stronghold against nuclear deformation. *Nature*, 569:53–58, May 2019.

[87] C. Santamaria et al. Extension of the N= 40 island of inversion towards $N = 50$: Spectroscopy of ^{66}Cr, ^{70,72}Fe. *Phys. Rev. Lett.*, 115:192501, Nov. 2015.

[88] F. Nowacki, A. Poves, E. Caurier, and B. Bounthong. Shape Coexistence in ^{78}Ni as the Portal to the Fifth Island of Inversion. *Phys. Rev. Lett.*, 117(27):272501, Dec. 2016.

[89] B. H. Wildenthal and W. Chung. Collapse of the conventional shell-model ordering in the very-neutron-rich isotopes of na and mg. *Phys. Rev. C*, 22:2260–2262, Nov. 1980.

[90] E. K. Warburton, J. A. Becker, and B. A. Brown. Mass systematics for A=29–44 nuclei: The deformed A∼32 region. *Phys. Rev. C*, 41:1147–1166, Mar. 1990.

[91] T. Otsuka et al. Evolution of shell structure in exotic nuclei. *Rev. Mod. Phys.*, 92:015002, Mar. 2020.

[92] Brookhaven National Laboratory National Nuclear Data Center. NuDat (nuclear structure and decay data).

[93] F. H. Garcia et al. Absence of low-energy shape coexistence in ^{80}Ge: the nonobservation of a proposed excited 0_2^+ level at 639 kev. *Phys. Rev. Lett.*, 125:172501, 2020.

[94] S. M. Lenzi, F. Nowacki, A. Poves, and K. Sieja. Island of inversion around ^{64}Cr. *Phys. Rev. C*, 82(5):054301, Nov. 2010.

[95] J. Dilling, R. Krücken, and L. Merminga. ARIEL overview. In J. Dilling, R. Krücken, and L. Merminga, editors, *ISAC and ARIEL: The TRIUMF Radioactive Beam Facilities and the Scientific Program*. Springer, 2013.

[96] V. Vedia. ARIES detector. Joint GRIFFIN and TIGRESS Collaboration Meeting, 2021.

[97] H. Bidaman. Simulating the Detector Array for Energy Measurements of Neutrons (DAEMON) for the GRIFFIN decay station. Joint GRIFFIN and TIGRESS Collaboration Meeting, 2021.

[98] K. Kapoor. Regina Cube for Multiple Particles (RCMP): Mechanical Design. Joint GRIFFIN and TIGRESS Collaboration Meeting, 2021.

[99] K. Whitmore et al. β decay of ^{132}In and spectroscopy of ^{132}Sn and ^{131}Sb with the GRIFFIN spectrometer. *Phys. Rev. C*, 102:024327, Aug. 2020.

[100] M. Deutsch. Angular correlations in nuclear reactions. *Reports on Progress in Physics*, 14(1):196–226, Jan. 1951.

[101] A. MacLean. *Gamma-gamma Angular Correlation Measurements with GRIFFIN*. MSc thesis, University of Guelph, 2016.

[102] A. E. Litherland and A. J. Ferguson. Gamma-ray angular correlations from aligned nuclei produced by nuclear reactions. *Canadian Journal of Physics*, 39(6):788–824, 1961.

[103] H. Frauenfelder. Angular correlation of nuclear radiation. *Annual Review of Nuclear Science*, 2(1):129–162, 1953.

[104] H. J. Rose and D. M. Brink. Angular distributions of gamma rays in terms of phase-defined reduced matrix elements. *Rev. Mod. Phys.*, 39:306–347, Apr. 1967.

[105] J. K. Smith, A. D. MacLean, W. Ashfield, A. Chester, A. B. Garnsworthy, and C. E. Svensson. Gamma–gamma angular correlation analysis techniques with the griffin spectrometer. *Nucl. Instrum. Meth. Phys. Res. A*, 922:47–63, Apr. 2019.

[106] K. Ortner et al. Collective 2p-2h intruder states in ^{118}Sn studied via β decay of ^{118}In using the GRIFFIN spectrometer at TRIUMF. *Phys. Rev. C*, 102:024323, Aug. 2020.

[107] J. K. Smith et al. Spectroscopic study of ^{47}Ca from the β^- decay of ^{47}K. *Phys. Rev. C*, 102:054314, Nov. 2020.

Appendix A

Beta-decay of ^{129}In - publication

Garcia, F. H. and Andreoiu, C. and Ball, G. C. and Bernier, N. and Bidaman, H. and Bildstein, V. and Bowry, M. and Cross, D. S. and Dunlop, M. R. and Dunlop, R. and Garnsworthy, A. B. and Garrett, P. E. and Henderson, J. and Measures, J. and Olaizola, B. and Ortner, K. and Park, J. and Petrache, C. M. and Pore, J. L. and Raymond, K. and Smith, J. K. and Southall, D. and Svensson, C. E. and Ticu, M. and Turko, J. and Whitmore, K. and Zidar, T., ***Spectroscopic studies of neutron-rich ^{129}In and its β-decay daughter, ^{129}Sn, using the GRIFFIN Spectrometer***, *Physical Review C*, 103, 2, 024310 (2021).

Available from APS: http://dx.doi.org/10.1103/PhysRevC.103.024310

Spectroscopic studies of neutron-rich ^{129}In and its β-decay daughter, ^{129}Sn, using the GRIFFIN spectrometer

F. H. Garcia,[1,*] C. Andreoiu,[1] G. C. Ball,[2] N. Bernier,[2,3,†] H. Bidaman,[4] V. Bildstein,[4] M. Bowry,[2,‡] D. S. Cross,[1] M. R. Dunlop,[4] R. Dunlop,[4] A. B. Garnsworthy,[2] P. E. Garrett,[4] J. Henderson,[2,§] J. Measures,[2,5] B. Olaizola,[2,‖] K. Ortner,[1] J. Park,[2,3,¶] C. M. Petrache,[6] J. L. Pore,[1,#] K. Raymond,[1] J. K. Smith,[2,**] D. Southall,[2,††] C. E. Svensson,[4] M. Ticu,[1] J. Turko,[4] K. Whitmore,[1] and T. Zidar[4]
(GRIFFIN Collaboration)
[1]*Department of Chemistry, Simon Fraser University, Burnaby, British Columbia, Canada V5A 1S6*
[2]*TRIUMF, 4004 Wesbrook Mall, Vancouver, British Columbia, Canada V6T 2A3*
[3]*Department of Physics and Astronomy, University of British Columbia, Vancouver, British Columbia, Canada V6T 1Z4*
[4]*Department of Physics, University of Guelph, Guelph, Ontario, Canada N1G 2W1*
[5]*University of Surrey, Guildford GU2 7XH, United Kingdom*
[6]*Centre de Sciences Nucléaire et Sciences de la Matière, CNRS/IN2P3, Université Paris-Saclay, Orsay, France*

(Received 13 March 2020; revised 18 December 2020; accepted 13 January 2021; published 8 February 2021)

The β decay of neutron-rich ^{129}In into ^{129}Sn was studied using the GRIFFIN spectrometer at the ISAC facility at TRIUMF. The study observed the half-lives of the ground state and each of the β-decaying isomers. The level scheme of ^{129}Sn has been expanded with thirty-one new γ-ray transitions and nine new excited levels, leading to a reevaluation of the β branching ratios and level spin assignments. The observation of the β decay of the $(29/2^+)$ 1911-keV isomeric state in ^{129}In is reported for the first time, with a branching ratio of 2.0(5)%.

DOI: 10.1103/PhysRevC.103.024310

I. INTRODUCTION

The region around the doubly magic $^{132}_{50}$Sn$_{82}$ nucleus is replete with critical information required for nuclear structure models and astrophysical applications [1,2]. This isotope region is a key input to the nuclear shell model and the theoretical frameworks required to establish a working predictive and descriptive model of nuclei, and as a result it has been the focus of a series of theoretical studies [3–5].

In nuclear astrophysics there is also a need for information on this region due to the importance of the $A = 130$ elemental abundance peak [6,7]. The rapid neutron-capture process (r process) is responsible for the generation of isotopes heavier than iron in stellar environments [8,9] and is shown to have key waiting points at the magic shell closures in the vicinity of the tin isotopes [10,11].

The ^{129}Sn nucleus, three neutrons removed from the $N = 82$ shell closure, is important for studying the effects of single-neutron excitations and other shell effects, as evinced by the sixty years of study it has undergone. Several production mechanisms have been used in order to study ^{129}In, and its β^- daughter ^{129}Sn, including fission [12], β^- decay [13–17], βn decay [18,19], and internal transition decay [20,21]. Although the information on the transitions and energy levels in this daughter nucleus is plentiful, there are virtually no definitive spin or parity assignments for the levels above the $3/2^+$ ground state, the $11/2^-$ 35-keV isomer and the $(1/2)^+$ 315-keV excited state.

To study and increase the available information on this key nucleus, ^{129}Sn, high-efficiency γ-ray spectroscopy and coincidence techniques were used to uncover new transitions, new decay patterns, and new levels, providing more input information for state-of-the-art theoretical models.

II. EXPERIMENT

The Isotope Separator and Accelerator (ISAC) facility of TRIUMF [22] employs the isotope separation online (ISOL) technique to produce radioactive isotope beams [23]. Isotopes are generated by bombarding a uranium carbide (UC_x) target with a 9.8 μA beam of 480 MeV protons, provided by the main 520-MeV cyclotron [24]. The relevant isotopes are selectively ionized for extraction using the Ion-Guide Laser

*fatimag@sfu.ca
†Present address: Department of Physics, University of the Western Cape, P/B X17, Bellvill, ZA-7535, South Africa.
‡Present address: School of Computing, Engineering and Physical Sciences, University of the West of Scotland, Paisley PA1 2BE, United Kingdom.
§Present address: Department of Physics, University of Surrey, Surrey, GU2 7XH, United Kingdom.
‖Present address: ISOLDE, CERN, 1211 Geneva, 23 Switzerland.
¶Present address: Department of Physics, Lund University, 22100 Lund, Sweden.
#Present address: Lawrence Berkeley National Laboratory, Berkeley, California 94720, USA.
**Present Address: Department of Physics, Pierce College, Puyallup, Washington 98374, USA.
††Present address: Department of Physics, University of Chicago, Chicago, IL 60637, USA.

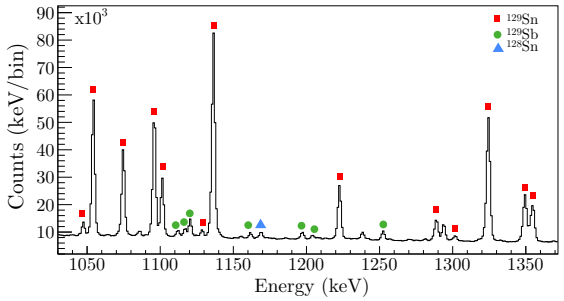

FIG. 1. β-gated γ-ray spectrum, in addback mode, showing various known transitions in ^{129}Sn (red squares). Transitions in ^{129}Sb (β decay daughter of ^{129}Sn; green circles) and ^{128}Sn (βn daughter of ^{129}In; blue triangles) are also observed.

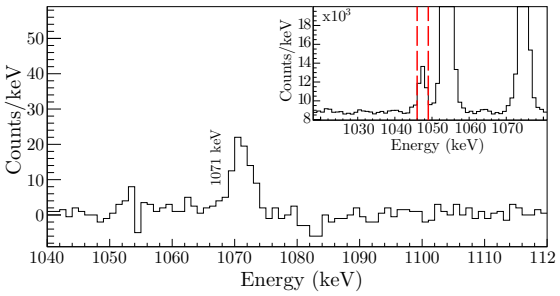

FIG. 2. A γ-ray spectrum, in addback mode, showing evidence for the 1071-keV γ ray, depopulating the 2118-keV state, in coincidence with the 1047-keV γ ray, depopulating the 1047-keV state of ^{129}Sn. The 1071-keV transition lies on the shoulder of a much more intense transition at 1075-keV, necessitating gating from below to obtain its relative intensity. The inset shows the gate on 1047 keV used to produce the spectrum.

Ion Source (IGLIS) [25], in order to reduce any isobaric contamination. The ionized species are then passed through the high-resolution mass spectrometer ($M/\delta M \approx 2000$) [26] in order to produce an isotopically clean beam. Once extracted, the desired ^{129}In radioactive isotope beam is transported to the experimental station. The β^- decay of the ^{129}In isotope to ^{129}Sn was observed using the Gamma-Ray Infrastructure for Fundamental Investigations of Nuclei (GRIFFIN) [27–29].

The GRIFFIN array is a state-of-the-art, high-resolution γ-ray spectrometer equipped with sixteen high-purity germanium (HPGe) clover detectors for the identification of γ rays [30]. Each of the sixteen HPGe clover detectors contains four crystals, making a total of 64 crystals that can detect γ rays, allowing for analyses to be carried out in single crystal or addback modes [28,30]. For this experiment, the Scintillating Electron-Positron Tagging Array (SCEPTAR) [28] was placed at the center of GRIFFIN in order to provide tagging for β particles. A cycling mylar tape station, the focus of which is at the center of SCEPTAR, provides a continuous implantation spot and aids in the removal of contaminants. An implantation cycle can be set to optimize observation of the decay of interest. During the course of this experiment, a mix of the β^- decaying isomers of ^{129}In were implanted at a rate of ≈5000 particles per second, with a beam composition of approximately 41% in the $9/2^+$ ground state, $^{129}\text{In}^{\text{g.s.}}$, 54% in the $(1/2^-)$ 459-keV $^{129}\text{In}^{m1}$ isomer, 3% in the $(23/2^-)$ 1630-keV $^{129}\text{In}^{m2}$ isomer, and 1% in the $(29/2^+)$ 1911-keV $^{129}\text{In}^{m3}$ isomer, neglecting the uncertainty in the ground-state branch of the $(1/2^-)$ isomer.

The GRIFFIN array was arranged in its high-efficiency configuration, where the HPGe clover detectors were positioned 11 cm away from the implantation spot [28]. A 20 mm Delrin shield was put in place around SCEPTAR to minimize Bremsstrahlung radiation from high-energy β^- particles. The experimental campaign for ^{129}In consisted of running the tape system in consecutive 21.5-s cycles, with 1.5 s for tape move, 5 s for background collection, 10 s for isotope implantation and 5 s for isotope decay. The total run duration was 2.75 hours, for a total of 460 cycles with 6.29×10^7 addback singles events, and 1.81×10^7 coincidence events collected during the runtime. The combination of GRIFFIN and SCEPTAR allowed for the correlated observation of γ rays in coincidence with the emitted β particles, in a 500-ns coincidence window, in order to tag on the specific ^{129}In decays. Furthermore, γ-γ coincidences with a 500-ns coincidence window were used for the verification of transitions and decay patterns through the excited levels of the ^{129}Sn daughter.

The energy and efficiency calibrations for GRIFFIN were done using a series of standard sources of ^{56}Co, ^{60}Co, ^{133}Ba, ^{152}Eu, allowing for a calibration to be made in the range between 81 keV and 3.6 MeV. Coincidence summing corrections were done by constructing a γ-γ matrix with detectors positioned at 180° of each other to correct for real coincidence summing, a methodology established for GRIFFIN in Ref. [29]. Transitions were also verified to be real transitions rather than sum or escape peaks.

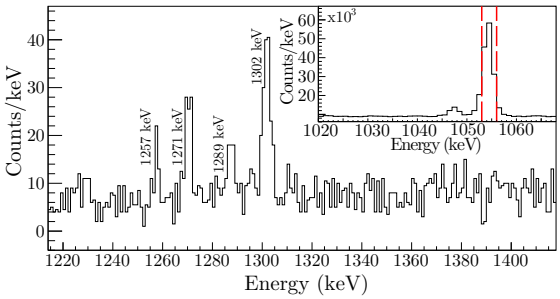

FIG. 3. A γ-ray spectrum, in addback mode, showing evidence for the 1271-keV γ ray, depopulating the new state at 2326-keV, in coincidence with the 1054-keV γ ray, depopulating the 1054-keV state in ^{129}Sn. Although weak, this transition is visible in the ungated γ-ray spectrum, but it is much more clear in the 1054-keV coincidence spectrum. This coincidence also confirms its placement in the level scheme. The transition at 1257 keV is also newly observed, while those at 1289 and 1302 keV are known in ^{129}Sn. The inset shows the gate on 1054 keV used to produce the spectrum.

TABLE I. Energy levels and transitions observed in ^{129}Sn, following the β^- decay of ^{129}In. All intensities are normalized to the most intense transition at 2118 keV, from the $(7/2^+)$ 2118-keV state to the $3/2^+$ ground state. The values calculated in this experiment are compared with those present in the Evaluated Nuclear Structure Data File search (ENSDF) database of the National Nuclear Data Center (NNDC). The level spins and parities are adopted from Ref. [31], unless otherwise stated.

This work							ENSDF
E level (keV)	E_γ (keV)	J_i^π	J_f^π	E_f (keV)	Relative I_γ	BR_γ	BR_γ
0		$3/2^+$					
35.2(2)		$11/2^-$					
315.1(2)	315.4(2)	$(1/2^+)$	$3/2^+$	0	0.611(5)	100	100
763.7(1)	728.5(2)	$(9/2^-)$	$11/2^-$	35.2(2)	0.163(2)	100	100
769.1(1)	769.3(2)	$(5/2^+)$	$3/2^+$	0	0.297(3)	100	100
1043.9(1)	280.4(2)[a]	$(7/2^-)$	$(9/2^-)$	763.7(1)	0.0068(8)	3.6(5)	4.3(6)
	1008.5(2)	$(7/2^-)$	$11/2^-$	35.2(2)	0.186(2)	100(1)	100
1047.0(2)	278.0(2)[a]	$(7/2^+)$	$(5/2^+)$	769.1(1)	0.0080(10)	95(7)	68(16)
	1047.4(2)	$(7/2^+)$	$3/2^+$	0	0.0086(4)	100(5)	100(8)
1054.3(2)	285.2(2)	$(7/2^+)$	$(5/2^+)$	769.1(1)	0.036(2)	34(1)	33(2)
	1054.4(2)	$(7/2^+)$	$3/2^+$	0	0.1050(10)	100.0(5)	100(7)
1171.5(3)	1136.4(2)	$(15/2^-)$	$11/2^-$	35.2(2)	0.1698(14)	100	100(7)
1222.4(2)	175.5(4)	$(3/2^+)$	$(7/2^+)$	1047.0(2)	0.0025(6)	5(1)	2.2(13)
	907.3(2)	$(3/2^+)$	$(1/2^+)$	315.1(2)	0.0394(7)	86(1)	74(5)
	1222.6(2)	$(3/2^+)$	$3/2^+$	0	0.0461(5)	100.0(9)	100(7)
1288.6(2)	519.5(7)	$(3/2^+)$	$(5/2^+)$	769.1(1)	0.007(3)	32(14)	36(6)[b]
	973.6(2)	$(3/2^+)$	$(1/2^+)$	315.1(2)	0.0193(9)	88(4)	80(5)[b]
	1288.8(2)	$(3/2^+)$	$3/2^+$	0	0.0220(4)	100(2)	100(6)[b]
1359.5(3)	1324.4(2)	$(13/2^-)$	$11/2^-$	35.2(2)	0.1306(13)	100	100
1455.2(2)	1455.0(2)	$(5/2^+)$	$3/2^+$	0	0.0306(9)	100	100
1534.4(2)	480.2(2)	$(7/2^-, 9/2^+)$	$(7/2^+)$	1054.3(2)	0.0137(11)	100(8)	100(9)
	765.0(3)	$(7/2^-, 9/2^+)$	$(5/2^+)$	769.1(1)	0.0037(11)	27(8)	69(6)
	1499.1(2)	$(7/2^-, 9/2^+)$	$11/2^-$	35.2(2)	0.0114(7)	84(5)	99(7)
1607.3(3)	553.1(3)	$(7/2 - 11/2)$[c]	$(7/2^+)$	1054.3(2)	0.0037(6)	58(9)	
	843.4(3)	$(7/2 - 11/2)$[c]	$(7/2^+)$	763.7(1)	0.0064(5)	100(7)	
1613.6(3)	1613.4(2)	$(7/2^+)$[d]	$3/2^+$	0	0.0359(5)	100	100(6)
1688.3(3)	919.0(3)	$(7/2^-, 9/2^+)$[c]	$(5/2^+)$	769.1(1)	0.0027(2)	100(9)	
	1653.0(3)	$(7/2^-, 9/2^+)$[c]	$11/2^-$	35.2(2)	0.0025(3)	92(12)	
1701.0(2)	657.3(2)	$(7/2^-)$	$(7/2^-)$	1043.9(1)	0.0043(3)	45(4)	75(6)[b]
	932.0(2)	$(7/2^-)$	$(5/2^+)$	769.1(1)	0.0094(4)	100(4)	100(9)[b]
	937.4(2)	$(7/2^-)$	$(9/2^-)$	763.7(1)	0.0075(5)	79(6)	95(9)[b]
	1665.6(3)	$(7/2^-)$	$11/2^-$	35.2(2)	0.0027(7)	28(8)	
1741.9(3)	382.4(2)	$(15/2^+)$	$(13/2^-)$	1359.5(3)	0.1235(12)	77.2(6)	75(4)
	570.4(2)	$(15/2^+)$	$(15/2^-)$	1171.5(3)	0.160(2)	100.0(7)	100(6)
1853.3(2)	318.0(6)	$(7/2, 9/2)$	$(7/2^-, 9/2^+)$	1534.4(2)	0.0073(3)	48(2)	32(4)
	799.4(2)	$(7/2, 9/2)$	$(7/2^+)$	1054.3(2)	0.0153(9)	100(6)	100(8)
	806.3(4)	$(7/2, 9/2)$	$(7/2^+)$	1047.0(2)	0.0016(4)	11(3)	
	1085.7(6)	$(7/2, 9/2)$	$(5/2^+)$	769.1(1)	0.0046(3)	30(2)	
1865.1(1)	330.9(3)	$(7/2^+)$	$(7/2^-, 9/2^+)$	1534.4(2)	0.0060(14)	0.7(2)	0.66(5)
	411.2(6)	$(7/2^+)$	$(5/2^+)$	1455.2(2)	0.0083(5)	1.03(6)	0.34(4)
	576.1(3)	$(7/2^+)$	$(3/2^+)$	1288.6(2)	0.0009(2)	0.11(3)	0.39(3)
	821.4(2)	$(7/2^+)$	$(7/2^-)$	1043.9(1)	0.0173(5)	2.14(5)	2.22(1)
	1095.9(2)[a]	$(7/2^+)$	$(5/2^+)$	769.1(1)	0.081(5)	9.9(6)	8.5(11)
	1101.4(2)	$(7/2^+)$	$(9/2^-)$	763.7(1)	0.0435(7)	5.36(7)	5.7(4)
	1830.6(3)	$(7/2^+)$	$11/2^-$	35.2(2)	0.0039(5)	0.48(6)	0.32(7)
	1864.8(2)	$(7/2^+)$	$3/2^+$	0	0.812(7)	100.0(6)	100(7)
1906.2(2)	1906.2(2)	$(7/2)$	$3/2^+$	0	0.0093(4)	100	100
2023.6(4)	969.2(3)	$(7/2 - 11/2)$[c]	$(7/2^+)$	1054.3(2)	0.0123(7)	100	
2118.3(1)	212.2(3)	$(7/2^+)$	$(7/2)$	1906.2(2)	0.0045(6)	0.45(6)	0.64(5)
	253.1(3)	$(7/2^+)$	$(7/2^+)$	1865.1(1)	0.0057(4)	0.57(4)	0.08(2)
	265.5(3)	$(7/2^+)$	$(7/2, 9/2)$	1853.3(2)	0.0036(4)	0.36(4)	0.35(5)
	583.6(2)	$(7/2^+)$	$(7/2^-, 9/2^+)$	1534.4(2)	0.0144(7)	1.44(7)	
	662.9(2)	$(7/2^+)$	$(5/2^+)$	1455.2(2)	0.0125(3)	1.25(3)	1.22(8)

TABLE I. *(Continued.)*

This work							ENSDF
E level (keV)	E_γ (keV)	J_i^π	J_f^π	E_f (keV)	Relative I_γ	BR_γ	BR_γ
	829.9(2)	$(7/2^+)$	$(3/2^+)$	1288.6(2)	0.0048(3)	0.48(3)	0.6(10)
	1071.0(2)[a]	$(7/2^+)$	$(7/2^+)$	1047.0(2)	0.0006(1)	0.06(1)	0.2(10)
	1074.7(2)	$(7/2^+)$	$(7/2^-)$	1043.9(1)	0.0666(7)	6.66(7)	6.1(4)
	1349.5(2)	$(7/2^+)$	$(5/2^+)$	769.1(1)	0.0511(8)	5.11(8)	4.6(3)
	1354.7(2)	$(7/2^+)$	$(9/2^-)$	763.7(1)	0.0417(11)	4.2(1)	2.9(3)
	2083.0(3)	$(7/2^+)$	$11/2^-$	35.2(2)	0.0033(4)	0.33(4)	0.42(4)
	2118.3(2)	$(7/2^+)$	$3/2^+$	0	1	100.0(6)	100(7)
2277(1)	474.0(2)	(21/2)	$(23/2)^+$	1803(1)	0.0220(5)	100(2)	100(8)
	514.8(3)	(21/2)	$(19/2)^+$	1762(1)	0.0081(6)	37(6)	30(3)
2326.1(4)	1270.5(6)	$(7/2, 9/2^+)$[c]	$(7/2^+)$	1054.3(2)	0.0012(3)	82(21)	
	1558.1(4)	$(7/2, 9/2^+)$[c]	$(5/2^+)$	769.1(1)	0.0015(3)	100(18)	
2406(1)	604.4(5)	$(23/2^-)$	$(23/2^+)$	1803(1)	0.0090(4)	100	100
2552(1)	145.5(3)[a]	$(27/2^-)$	$(23/2^-)$	2406(1)	0.0011(2)	100	100
2568.0(3)	2252.9(3)	$(1/2, 3/2)$[c]	$(1/2)^+$	315.1(2)	0.0009(3)	93(30)	
	2568.0(3)	$(1/2, 3/2)$[c]	$3/2^+$	0	0.0010(6)	100(56)	
2606.2(2)	1150.9(3)	$(1/2, 3/2)$[c]	$(5/2^+)$	1455.2(2)	0.0002(2)	6(4)	
	1384.2(3)	$(1/2, 3/2)$[c]	$(3/2^+)$	1222.4(2)	0.0035(4)	90(11)	
	2290.5(3)	$(1/2, 3/2)$[c]	$(1/2)^+$	315.1(2)	0.0013(2)	33(6)	
	2606.9(4)	$(1/2, 3/2)$[c]	$3/2^+$	0	0.0039(4)	100(9)	
2791.0(3)	1736.6(3)	$(7/2, 9/2^+)$	$(7/2^+)$	1054.3(2)	0.0018(3)	22(3)	36(24)
	2021.9(2)	$(7/2, 9/2^+)$	$(5/2^+)$	769.1(1)	0.0082(3)	100(3)	100(7)
2836.0(2)	718.0(3)	$(7/2^+, 9/2^+)$	$(7/2^+)$	2118.3(1)	0.0026(5)	5(1)	
	1301.8(2)	$(7/2^+, 9/2^+)$	$(7/2^-, 9/2^+)$	1534.4(2)	0.0058(8)	12(2)	10.2(8)
	1781.4(2)	$(7/2^+, 9/2^+)$	$(7/2^+)$	1054.3(2)	0.0490(6)	100(1)	100(7)
	1791.4(3)	$(7/2^+, 9/2^+)$	$(7/2^-)$	1043.9(1)	0.0031(4)	6.3(7)	7.2(7)
	2066.5(2)	$(7/2^+, 9/2^+)$	$(5/2^+)$	769.1(1)	0.0299(6)	61(1)	57(4)
	2072.9(3)	$(7/2^+, 9/2^+)$	$(9/2^-)$	763.7(1)	0.0003(1)	0.6(2)	3.5(9)
2981.9(2)	863.8(4)	$(7/2^+)$	$(7/2^+)$	2118.3(1)	0.0007(3)	3(1)	
	1128.7(2)	$(7/2^+)$	(7/2, 9/2)	1853.3(2)	0.0036(8)	18(4)	
	1927.6(3)	$(7/2^+)$	$(7/2^-)$	1054.3(2)	0.0015(3)	8(1)	
	2212.6(2)	$(7/2^+)$	$(5/2^+)$	769.1(1)	0.0201(5)	100(2)	100(6)
	2980.7(7)	$(7/2^+)$	$3/2^+$	0	0.0009(2)	4.5(8)	9.2(18)
3079.3(3)	2035.6(3)	$(3/2^-)$	$(7/2^-)$	1043.9(1)	0.0045(7)	79(11)	90(9)
	2764.0(2)	$(3/2^-)$	$(1/2)^+$	315.1(2)	0.0057(3)	100(5)	100(8)
3140.3(2)	1526.1(3)	$(7/2^+)$	$(7/2^+)$	1613.6(3)	0.0020(5)	17(4)	
	2094.0(3)	$(7/2^+)$	$(7/2^+)$	1047.0(2)	0.0041(4)	34(3)	
	2371.1(3)[a]	$(7/2^+)$	$(5/2^+)$	769.1(1)	0.0045(3)	37(3)	16.2(18)
	2376.4(3)	$(7/2^+)$	$(9/2^-)$	763.7(1)	0.0025(6)	20(5)	30(3)
	3140.1(2)	$(7/2^+)$	$3/2^+$	0	0.0123(3)	100(2)	100(8)
3393.9(4)	3078.7(3)	(1/2, 3/2)	$(1/2)^+$	315.1(2)	0.0077(3)	100	100
3446.7(4)	2683.0(3)	$(7/2 - 11/2)$[c]	$(9/2^-)$	763.7(1)	0.0005(2)	100	
3581.8(3)	1257.0(6)	$(7/2, 9/2^+)$[c]	(7/2, 9/2)	2326.1(4)	0.0013(2)	90(17)	
	2527.1(3)	$(7/2, 9/2^+)$[c]	$(7/2^+)$	1054.3(2)	0.0013(3)	93(23)	
	2812.7(8)	$(7/2, 9/2^+)$[c]	$(5/2^+)$	769.1(1)	0.0014(4)	100(25)	
	2818.4(5)	$(7/2, 9/2^+)$[c]	$(9/2^-)$	763.7(1)	0.0010(4)	69(27)	
3590.4(1)	1889.5(2)	$(3/2^-)$	$(7/2^-)$	1701.0(2)	0.0106(5)	23(1)	23(2)
	1977.0(2)	$(3/2^-)$	$(7/2^+)$	1613.6(3)	0.0113(5)	24(1)	21(2)
	2301.7(2)	$(3/2^-)$	$(3/2^+)$	1288.6(2)	0.0178(3)	38.0(5)	30(2)
	2367.9(2)	$(3/2^-)$	$(3/2^+)$	1222.4(2)	0.0292(4)	62.3(7)	51(4)
	2546.2(2)	$(3/2^-)$	$(7/2^-)$	1043.9(1)	0.0469(5)	100(1)	100(7)
	3276.0(2)	$(3/2^-)$	$(1/2)^+$	315.1(2)	0.0440(6)	94(1)	63(4)
	3589.7(3)	$(3/2^-)$	$3/2^+$	0	0.0058(5)	12(1)	12.6(11)
3993(1)	1586.3(3)[a]	$(21/2^-)$	$(23/2^-)$	2406(1)	0.011(6)	7.2(1)	
	1715.9(2)	$(21/2^-)$	(21/2)	2277(1)	0.0286(7)	17.6(4)	16.4(14)
	2189.8(2)	$(21/2^-)$	$(23/2^+)$	1803(1)	0.162(2)	100.0(7)	100(7)
	2230.8(2)	$(21/2^-)$	$(19/2^+)$	1762(1)	0.0577(9)	35.5(5)	41(2)

TABLE I. *(Continued.)*

This work							ENSDF
E level (keV)	E_γ (keV)	J_i^π	J_f^π	E_f (keV)	Relative I_γ	BR_γ	BR_γ
4136.6(3)	2847.8(2)	(1/2, 3/2)[c]	$(3/2^+)$	1288.6(2)	0.0026(1)	100(3)	
	2915.5(5)	(1/2, 3/2)[c]	$(3/2^+)$	1222.4(2)	0.0019(3)	73(12)	

[a]Intensity calculated from coincidences.
[b]Based on ENSDF information: Weighted average between ^{129}In$^{g.s.}$ and ^{129}In^{m1}.
[c]Spin assignment for new levels, based on β and γ decay systematics.
[d]Revised spin assignment for known levels, based on β and γ decay systematics.

III. RESULTS

A. Transitions and levels in ^{129}Sn

The Q_β value for the ^{129}In β decay to ^{129}Sn is 7.769(19) MeV and the neutron separation energy S_n for ^{129}Sn is 5.316(26) MeV [31]. Gamma-ray transitions were investigated up to the neutron separation energy. From the analysis of this data set, all but two of the transitions currently reported for the ^{129}Sn nucleus were observed [31]. There were also 31 newly observed transitions and 9 newly observed excited states in the ^{129}Sn nucleus, never observed through the β^- decay of its ^{129}In parent or otherwise. Figure 1 shows a portion of the β-gated γ-ray spectrum observed in this work; transitions in the ^{129}Sn of interest, along with transitions in the β granddaughter ^{129}Sb and in the ^{129}In βn daughter ^{128}Sn are identified. Figures 2 and 3 demonstrate the mechanism used to establish new transitions. Figure 2 shows the gating from below method used to determine several intensities, in this case that of the 1071-keV transition. The intensity of this transition required gating from below on the 1047-keV transition, while Fig. 3 shows the γ-ray spectrum resulting from a gate placed on the 1054-keV transition, where coincident transitions at 1257, 1271, and 1302 keV were observed.

Table I summarizes the energy levels observed in this work, along with the transitions from each level, the final state, the relative intensity with respect to the highest intensity 2118-keV γ ray, and the γ-ray branching ratio. The table also compares the branching ratios for each of the known γ rays appearing in the evaluation by Timar, Elekes, and Singh [31]. With the exception of seven γ rays at 146, 278, 280, 1071, 1096, 1586, and 2371 keV, all transition intensities were obtained from the addback singles spectrum. The seven γ rays mentioned required directly gating from below in order to fit their energy and intensity values, as demonstrated in Fig. 2. The other new transitions were observed in the γ-ray spectrum and their placement confirmed through coincidence gating, as in shown in Fig. 3. Although most of the branching ratios observed in the course of this work are in good agreement with the work of Gausemel *et al.* [17], there are some notable discrepancies. These are attributed to major differences in the conditions of the two experiments. The work by Gausemel *et al.* utilized three germanium detectors, while the present work made use of all 16 HPGe clover detectors available to the GRIFFIN array, allowing for more efficient coincidence detection. Furthermore, some of the transitions were observed with branching ratios down to 10^{-4}, pushing the limits of the detection mechanisms available to the previous experiment. The β decay of the $(29/2^+)$ 1911-keV isomer in ^{129}In to the $(27/2^-)$ 2552-keV state in ^{129}Sn was observed for the first time. This 2552-keV state was previously observed in the fission study done by Lozeva *et al.* [21]. The transitions from the isomeric states at 1762 and 1803 keV to lower-lying states in the level scheme, 19.7 and 41.0 keV, respectively, were not observed. However, transitions feeding into these states were present in the data, confirming the placement of the levels, within uncertainty.

B. Decay of the $9/2^+$ ^{129}In ground state

1. Half-life of ^{129}In$^{g.s.}$

Plotting the intensity of a γ ray as a function of cycle time allows for the measurement of isotope half-life; a spectrum can be generated and fit with a characteristic decay formula, from which the half-life can then be extracted. To improve statistics, background-corrected timing gates on 39 γ rays—shown in Table II—associated with the decay of the ^{129}In ground state into ^{129}Sn were summed and the counts as a function of cycle time fit using a standard exponential decay, as seen in Fig. 4. The fit returned a half-life of $t_{1/2} = 0.60(1)$ s, in agreement with $t_{1/2} = 0.611(5)$ s quoted in the evaluation by Timar, Elekes, and Singh [31]. A chop analysis, which involved a change in the width of the timing window for the fit, was conducted to check for any rate-dependent effects on the half-life; no discernible effects were observed. The weighted average value between the evaluated half-life of 0.611(5) s and the observed half-live of 0.60(1) s is calculated to be 0.609(4) s, where the uncertainty has been increased by $(\chi^2)^{1/2}$.

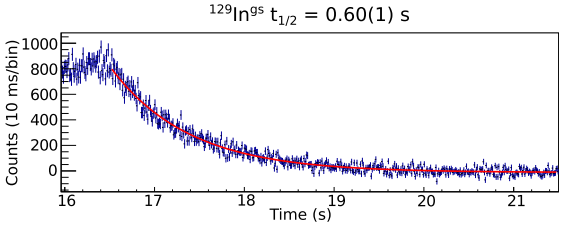

FIG. 4. A spectrum of total counts as a function of cycle time, representing 39 transitions associated with the ^{129}In ground-state decay into states in ^{129}Sn. The fit, seen in red, returned a value of $t_{1/2} = 0.60(1)$ s. The reduced χ^2 for this fit is 1.3.

TABLE II. Transitions used to build the half-life plot shown in Fig. 4. These were identified as transitions from states populated by the ground state of ^{129}In.

Transition (keV)
212.2(3)
253.1(3)
265.5(3)
278.0(2)
285.2(2)
318.0(6)
330.9(3)
411.2(6)
480.2(2)
576.1(3)
662.9(2)
765.0(3)
799.4(2)
821.4(2)
829.9(2)
1054.4(2)
1074.7(2)
1095.9(2)
1101.4(2)
1301.8(2)
1349.5(2)
1354.7(2)
1499.1(2)
1613.4(2)
1736.6(3)
1781.4(2)
1791.4(3)
1830.6(3)
1864.8(2)
1906.2(2)
2021.9(2)
2066.5(2)
2072.9(3)
2083.0(3)
2118.3(2)
2212.6(2)
2376.4(3)
2980.7(7)
3140.1(2)

2. β-feeding and log ft values

Several new transitions and new levels from the β decay of the ground state of ^{129}In into excited states of ^{129}Sn were observed. Figure 5 shows the γ rays observed in ^{129}Sn due to this decay. Newly observed transitions and levels are colored (red), along with their proposed spin assignments.

Table III lists the states that are populated by the ground state along with the β-feeding intensities and the log *ft* values calculated in this work, together with a comparison to the work of Gausemel *et al.* [17]. The electron conversion coefficients for low-energy γ rays are taken into account when doing these calculations, using the BrIcc utility available through the NNDC [32]. The data observed by Gausemel *et al.* showed direct β feeding to the 35-keV isomeric state on the order of $<10\%$. The β-feeding values obtained in the present work are normalized to reflect 100% feeding to excited states.

TABLE III. The β-feeding intensities and log *ft* values for states in ^{129}Sn, observed through the β decay of the $(9/2^+)$ ^{129}In$^{g.s.}$ state and calculated with the weighted average half-life of 0.609(4) s. Columns denoted by Ref. [17] contain values established in the work of Gausemel *et al.* The β-feeding values have been normalized to reflect 100% feeding of excited states.

	I_β (%)		log *ft*	
E_x (keV)	This work	Ref. [17]	This work	Ref. [17]
763.7(1)	2.03(8)	2.1(4)	6.43(2)	6.4(1)
1043.9(1)	1.95(8)	2.0(4)	6.36(2)	6.4(1)
1047.0(2)	0.30(4)	0.35(6)	7.17(6)	7.1(1)
1054.3(2)	1.62(10)	2.1(3)	6.44(3)	6.33(7)
1534.4(2)	0.60(9)	0.46(6)	6.73(7)	6.85(6)
1607.3(3)	0.14(2)		7.33(7)	
1613.6(3)	0.88(3)		6.54(2)	
1688.2(3)	0.20(2)		7.15(4)	
1701.0(2)	0.52(5)	0.24(2)	6.74(5)	7.08(4)
1853.3(2)	0.85(5)	0.76(6)	6.47(3)	6.53(4)
1865.1(1)	37.6(3)	36(2)	4.83(1)	4.85(3)
1906.2(2)	0.18(3)	0.13(3)	7.13(8)	7.3(1)
2023.6(4)	0.48(3)		6.67(3)	
2118.3(1)	46.9(3)	49(3)	4.64(1)	4.63(3)
2326.1(4)	0.06(2)		7.49(14)	
2791.0(3)	0.39(15)	0.47(9)	6.48(2)	6.4(1)
2836.0(2)	3.53(5)	3.36(15)	5.51(1)	5.54(2)
2981.9(2)	1.01(4)	0.74(5)	5.99(2)	6.14(3)
3140.3(2)	0.99(4)	0.67(4)	5.94(2)	6.11(3)
3446.7(4)	0.020(9)		7.5(2)	
3581.8(3)	0.19(3)		6.46(7)	

Spin assignments for the newly observed levels are proposed based on the β-decay selection rules and γ-ray systematics. The newly observed states at 1607, 2024, and 3447 keV are tentatively assigned spins between (7/2) and (11/2), because they are observed to decay to states with proposed spins between 7/2 and 9/2, while decays to states with spins of 3/2 or lower were not observed.

The new state at 1688 keV decays to the $11/2^-$35-keV and $(5/2^+)$ 769-keV levels such that the spin and parity of this state can be restricted to $(7/2^-, 9/2^+)$. The new states at 2326 and 3582 keV are observed to decay to states with tentative spins between $(5/2^+)$ and $9/2^-$, such that their spins can be restricted to $(7/2, 9/2^+)$. The log *ft* values calculated between the $(9/2^+)$ ^{129}In$^{g.s.}$ and the above-mentioned states, shown in Table III, are all consistent with the allowed or first-forbidden decays implied by the proposed spin assignments.

Previous work using γ-ray information [17,31] assigned a spin of between (1/2) and $(7/2^+)$ for the 1614-keV level, with no detectable β-feeding from the $(1/2^-)$ ^{129}In^{m1} parent. Gausemel *et al.* observed a transition at 1977 keV, from the $(3/2^-)$ 3590-keV state to the 1614-keV state, which was observed in the present work and is shown in Fig. 6. A new transition at 1526 keV was also observed from the $(7/2^+)$ state at 3140 keV, casting doubt on the possibility of a 1/2

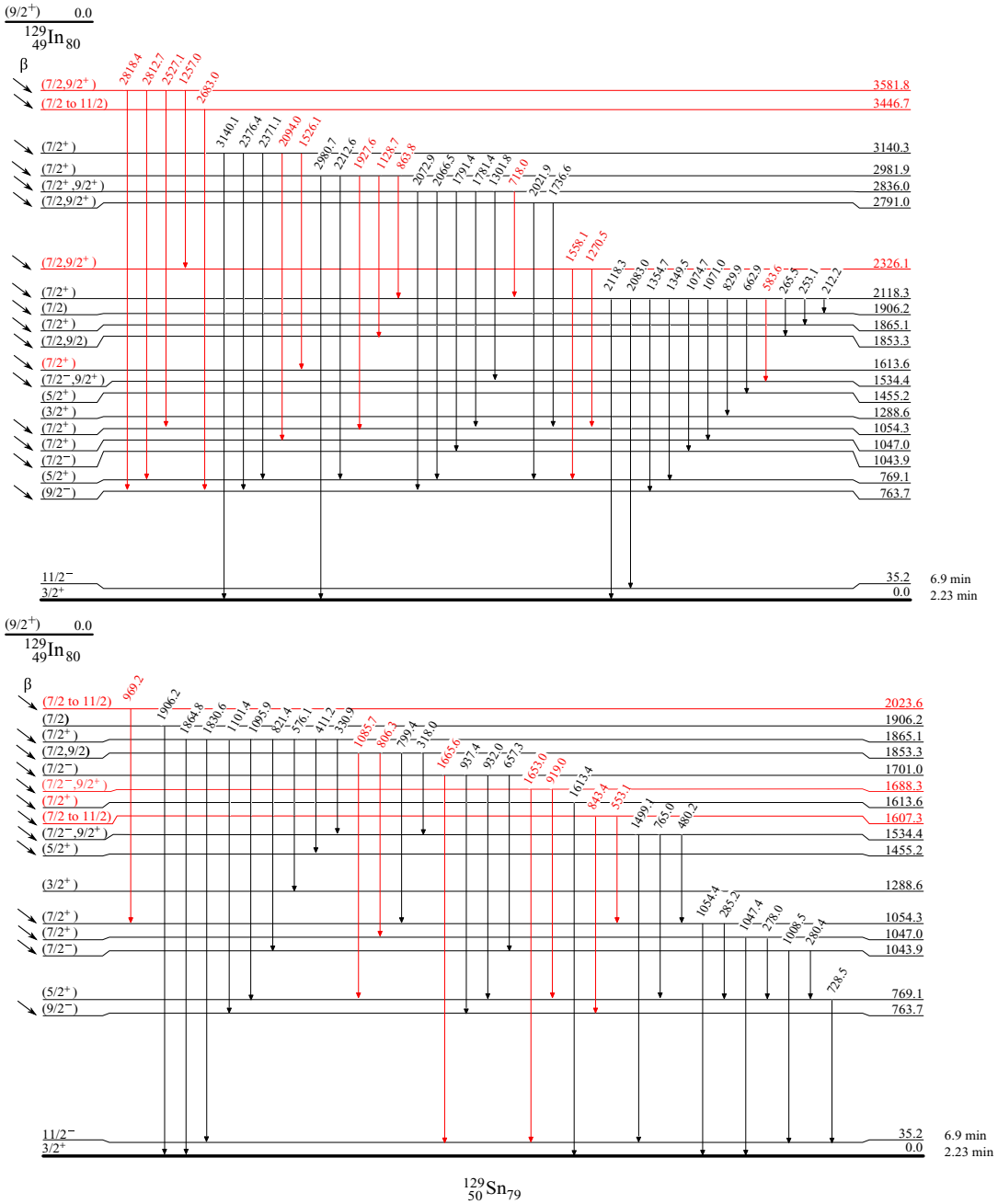

FIG. 5. The level scheme of ^{129}Sn, populated through the β decay of the ground state of ^{129}In, showing the high-lying states (top) and the low-lying states (bottom). The color (red) represents new transitions and levels found in this work. For the case of the 1614-keV state, the colored $(7/2^+)$ spin indicates a new spin assignment to a previously observed level. The half-lives of the ground state and the ^{129}Sn^{m1} 35-keV isomer are 2.23(4) min and 6.9(1) min, respectively, as given by Timar, Elekes, and Singh [31]. Information about γ-ray intensity and their uncertainties can be found in Table I.

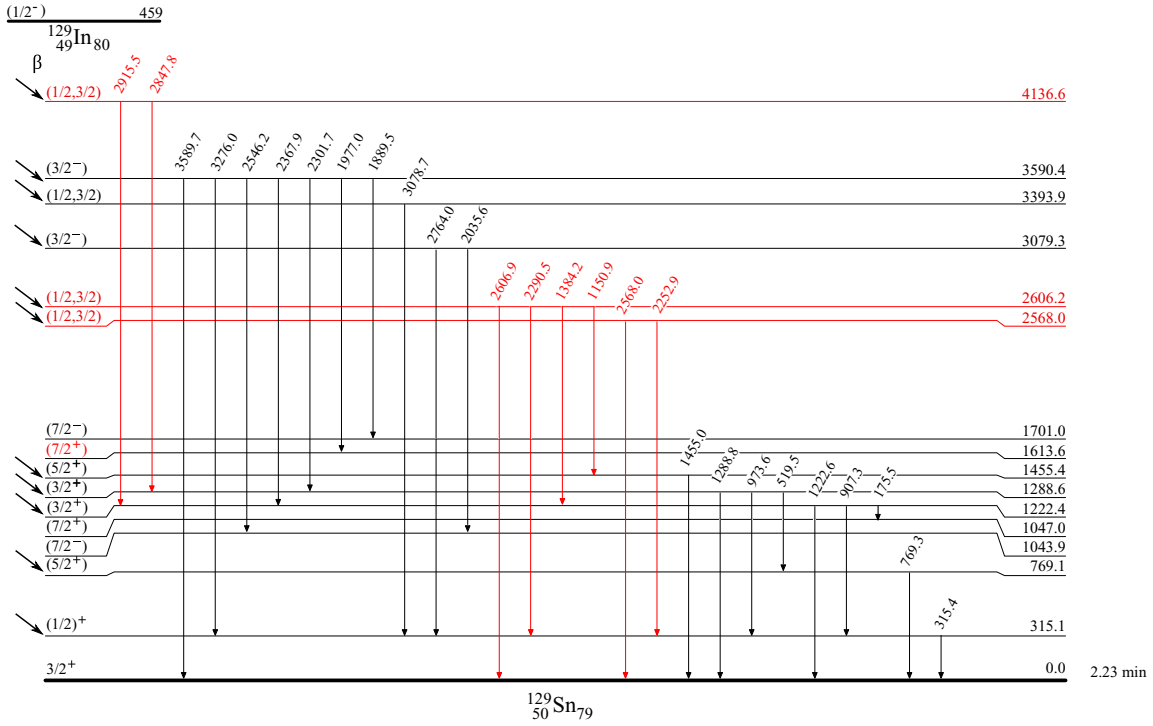

FIG. 6. The level scheme of ^{129}Sn, populated through the β-decay of the $(1/2^-)$ 459-keV isomer of ^{129}In. The color (red) represents new transitions and levels found in this work. The half-life of the ^{129}Sn ground state is 2.23(4) min, as given by Timar, Elekes, and Singh [31]. Information about γ-ray intensity and their uncertainties can be found in Table I.

spin. Furthermore, the 1614-keV level is observed to have a direct β-feeding component, equivalent to double the intensity of the 1977-keV transition from the 3590-keV state observed both by Gausemel *et al.* and in this work, indicating that the 1614-keV level is most likely fed by the $(9/2^+)$ ^{129}In$^{g.s.}$ and has a spin of $(7/2^+)$. This spin assignment is corroborated by the 6.54(2) log *ft* value shown in Table III, which is consistent with an allowed transition.

C. Decay of $(1/2^-)$ ^{129}In^{m1}

1. *Half-life of* ^{129}In^{m1}

The twelve γ-ray transitions used to generate the half-life spectrum shown in Fig. 7 are listed in Table IV. The fit to the data returned a half-life of $t_{1/2} = 1.16(1)$ s. A chop analysis was carried out and no systematic effects were observed. The present result is a factor of three more precise than the value 1.23(3) s quoted in the evaluation by Timar, Elekes, and Singh [31]. The weighted average of these two values is 1.17(2) s, with its uncertainty increased by $(\chi^2)^{1/2}$.

2. *β feeding and log ft values*

The ^{129}In^{m1} isomer was observed to decay to known states in ^{129}Sn, as well as to three newly observed states. Figure 6 shows the γ rays observed in this decay; the spins of the three new levels populated in ^{129}Sn were determined from β-feeding and γ-ray systematics. Table V summarizes the β-feeding intensities and the log *ft* values obtained in the present work using the weighted half-life of 1.17(2) s, compared with the results of Gausemel *et al.* [17] who also observed a 77(15)% direct β feeding to the $3/2^+$ ground state in ^{129}Sn; the present β-feeding intensities have been scaled to represent the remaining 23% of observed β feeding to excited states.

The new states at 2568 and 2606 keV are observed to decay to the $(1/2)^+$315-keV state; therefore they are likely to have a spin of either 1/2 or 3/2 and be fed by the $(1/2^-)$ ^{129}In^{m1}. The

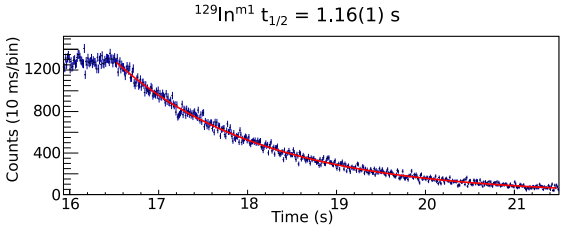

FIG. 7. A spectrum of total counts as a function of cycle time, representing twelve transitions associated with the decay of ^{129}In^{m1} into states in ^{129}Sn. The fit, seen in red, returned a value of $t_{1/2} = 1.16(1)$ s. The reduced χ^2 for this fit is 1.2.

TABLE IV. Transitions used to build the half-life plot shown in Fig. 7. These were identified as transitions from states populated by the $^{129}In^{m1}$ isomer.

Transition (keV)
175.5(4)
315.4(2)
907.3(2)
1222.6(2)
1889.5(2)
2035.6(3)
2367.9(2)
2546.2(2)
2764.0(2)
3078.7(3)
3276.0(2)
3589.7(3)

4137-keV state decays to the 1289- and 1222-keV states, both of which have tentative spin assignments of $(3/2^+)$, indicating that this state is likely to have a $1/2$ or $3/2$ spin. The log *ft* values for these states, shown in Table V, are consistent with either the allowed or first-forbidden transitions expected from the $(1/2^-)$ $^{129}In^{m1}$ to the respective states in ^{129}Sn.

The excess feeding into the $(5/2^+)$ states at 769 and 1455 keV has been attributed to direct β feeding from the $(1/2^-)$ $^{129}In^{m1}$ to these states, rather than to unobserved transitions feeding these levels from higher levels populated by either the β decay of the $(9/2^+)$ $^{129}In^{g.s.}$ or the $(1/2^-)$ $^{129}In^{m1}$. The log *ft* values for the 769- and 1455-keV states, calculated with feeding from $^{129}In^{m1}$, are 9.31(9) and 9.55(5), respectively, consistent with unique first-forbidden transitions, supporting the spin assignments for these states, given as $(5/2^+)$.

TABLE V. The β-feeding intensities and log *ft* values, calculated, for states in ^{129}Sn, observed through the β decay of the $(1/2^-)$ $^{129}In^{m1}$ isomer and calculated with the weighted average half-life of 1.17(2) s. The values calculated in this work are compared with the values calculated by Gausemel *et al.* [17].

	I_β (%)		log *ft*	
E_x (keV)	This work	Ref. [17]	This work	Ref. [17]
315.1(2)	14.3(2)	15.1(13)	6.10(1)	6.10(4)
769.1(1)[a]	0.9(2)		9.31(9)	
1222.4(2)	1.52(4)	1.56(14)	6.83(2)	6.85(4)
1288.6(2)	0.63(9)	0.58(7)	7.20(7)	7.26(6)
1455.2(2)[a]	0.28(3)		9.55(5)	
2568.0(3)	0.06(2)		7.86(15)	
2606.2(2)	0.25(2)		7.19(4)	
3079.3(3)	0.29(2)	0.42(3)	6.96(4)	6.82(4)
3393.9(4)	0.219(8)	0.22(2)	6.96(2)	6.98(5)
3590.4(1)	4.70(6)	5.10(17)	5.55(1)	5.54(2)
4136.6(3)	0.127(9)		6.88(4)	

[a]Unique first forbidden.

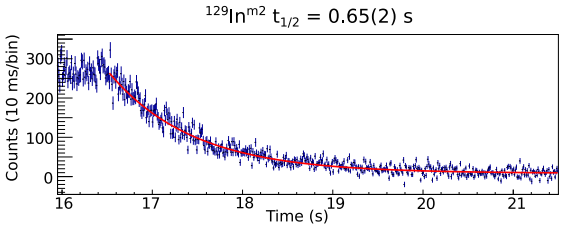

FIG. 8. A spectrum of total counts as a function of cycle time, representing four transitions associated with $^{129}In^{m2}$ decay into states in ^{129}Sn. The fit, seen in red, returned a value of $t_{1/2} = 0.65(1)$ s. The reduced χ^2 for this fit is 2.2.

D. Decay of $(23/2^-)$ $^{129}In^{m2}$

1. *Half-life of* $^{129}In^{m2}$

Only four viable γ-ray transitions, at 382, 515, 2190, and 2231 keV, could be used in the half-life fit of the $^{129}In^{m2}$ isomer. The spectrum and the fit are show in Fig. 8. The adopted value for the half-life of the $(23/2^-)$ $^{129}In^{m2}$ is $t_{1/2} = 0.65(2)$ s. This result, which includes a systematic uncertainty associated with the chop analysis, has an error of a factor of five times smaller than the established value, quoted by Timar, Elekes, and Singh [31] as $t_{1/2} = 0.67(10)$ s. The weighted average between the half-life in the evaluation and the half-life observed in this work is 0.65(2) s, with the uncertainty increased by $(\chi^2)^{1/2}$.

2. *β feeding and log ft values*

The level scheme associated with the β decay of the $^{129}In^{m2}$ is shown in Fig. 9. Table VI shows the β-feeding intensities and log *ft* values obtained in this work, along with a comparison to those observed by Gausemel *et al.* [17]. One new transition was observed in the present work. The branching ratios measured for the decay of the 3993-keV $(21/2^-)$ level to the 1762-, 1803-, and 2277-keV levels and for the decay of the 2277-keV level to the 1762- and 1803-keV levels are in reasonable agreement with previous data [17], as seen in Table I. However, the β-feeding intensity of the 2277-keV level is nearly a factor of ten smaller than the value previously observed.

Direct β feeding to the 1803-keV level was estimated based on the intensities of the γ rays populating this state and the γ-

TABLE VI. The β-feeding intensities and log *ft* values, calculated for states in ^{129}Sn, observed through the β decay of the $(23/2^-)$ $^{129}In^{m2}$ isomer and calculated with the weighted average half-life of 0.65(2) s. The values are calculated in this work are compared with those calculated by Gausemel *et al.* [17].

	I_β (%)		log *ft*	
E_x (keV)	This work	Ref. [17]	This work	Ref. [17]
1803(1)	10(4)	14(4)	5.92(18)	5.8(2)
2277(1)	0.5(3)	8.0(12)	7.1(3)	5.9(1)
3993(1)	89(4)	75(4)	4.31(2)	4.4(1)

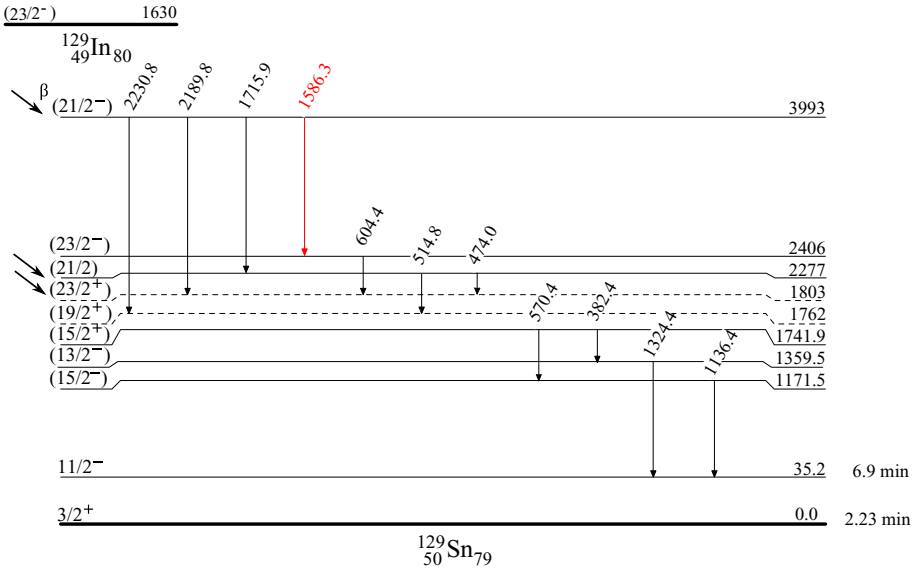

FIG. 9. The level scheme of ^{129}Sn, populated through the β decay of the $(23/2^-)$ ^{129}In. The color (red) represents new transitions and levels found in this work. The half-life of the ^{129}Sn ground state is 2.23(4) min, as given by Timar, Elekes, and Singh [31]. Information about γ-ray intensity and their uncertainties can be found in Table I. The dashed lines presented two known states, at 1762 and 1803 keV, whose energies can only be inferred in this work from feeding from above.

ray intensities depopulating states below, connected through two transitions, a 41.0(2)-keV transition from the 1803-keV state to the 1762-keV state, and a 19.7(10)-keV transition from the 1762-keV state to the 1742-keV state. A direct β feeding of 10(4)% to the 1803-keV state was observed, consistent with the previously reported value of 14(4)% β-feeding intensity observed previously [17]. Table VI also summarizes the β-feeding intensities and the log *ft* values for the 2277- and 3993-keV states.

E. Decay of $(29/2^+)$ ^{129}In^{m3}

Above the 1630-keV isomer in ^{129}In, there is another isomer at 1911 keV with spin $(29/2^+)$. This state has been shown to decay through a 281-keV internal transition to the 1630-keV ^{129}In^{m2} isomer. This transition lies very close in energy to two known transitions in the ^{129}Sn nucleus, at 278.0(2) and 280.4(2) keV, which depopulate the 1047- and 1044-keV states, respectively, as seen in Fig. 5.

The total relative intensity obtained in the addback singles γ-ray spectrum was 0.0805(4) for the triplet centered around 280 keV. This was inconsistent with the measured intensity of either the 278- and 280-keV transitions, observed in previous studies [17], and therefore the intensities of the transitions were measured by gating from below, on the 769-keV transition depopulating the 769-keV state for the transition at 278 keV, and the 728-keV transition that depopulates the 764-keV state for the 280-keV transition.

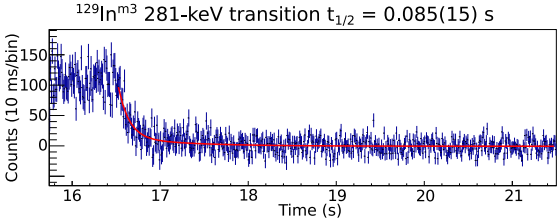

FIG. 10. A spectrum of total counts as a function of cycle time for the 281-keV transition. The fit, in red, returned a value of $t_{1/2} =$ 0.085(15) s, which is in good agreement with the half-life of the 1911-keV ^{129}In^{m3}, quoted at 0.110(15) s [31]. The fit returned a reduced χ^2 of 1.1. The fit included a component associated with the β decay of the ^{129}In$^{g.s.}$ since the energy of the 281-keV internal transition in ^{129}In is unresolved from two transitions in ^{129}Sn at 278 and 280 keV (see text for details).

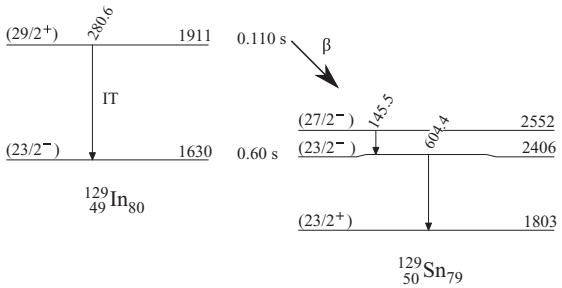

FIG. 11. Partial level scheme showing the decay of the $(29/2^+)$ 1911-keV ^{129}In^{m3} isomer into the $(27/2^-)$ 2552-keV state in ^{129}Sn. The intensity of the 146-keV transition was obtained in coincidence with the 604-keV transition.

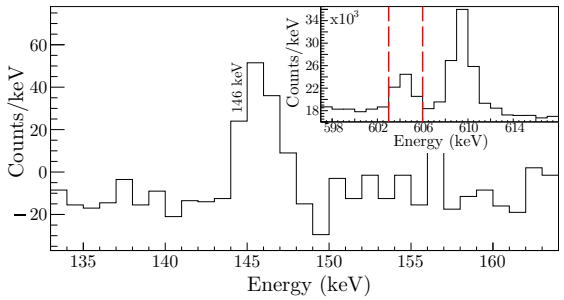

FIG. 12. A spectrum showing the 146-keV transition in the 604-keV gate. Note the red lines in the inset denote the placement of the gate.

The relative intensity of the 278-keV transition was found to be 0.0080(10), consistent with previous measurements of both γ-ray intensity and the β feeding of the 1047-keV state. Similarly, the relative intensity of the 280-keV transition in ^{129}Sn was measured to be 0.0068(8), in agreement with the previously measured γ-ray intensity and β feeding to the 1044-keV state. The remaining intensity at 281 keV, amounting to 0.0657(11), must then be due to the internal transition of ^{129}In^{m3}.

To confirm this assignment, a spectrum of total counts as a function of time, gated on the 281-keV transition was produced in the same manner as described in Secs. III B 1, III C 1, and III D 1. The fit, shown in Fig. 10, returned a half-life of 0.085(15) s, in good agreement with the 0.110(15) s half-life of the 1911-keV ^{129}In^{m3} state [31] and much shorter than the half-lives of the other β-decaying states in ^{129}In. This confirms that the presence of the excess intensity at 280 keV was due to the internal transition from ^{129}In^{m3} to ^{129}In^{m2}.

If this 1911-keV ^{129}In^{m3} isomer were to populate states in ^{129}Sn through β decay, these would have to be very high spin states. One such candidate is the 2552-keV state, with a proposed spin of $(27/2^-)$. Lozeva *et al.* [21] observed a 146-keV transition from this state to the $(23/2^-)$ 2406-keV state, having populated states in ^{129}Sn through ^{238}U fission and ^{136}Xe fragmentation experiments. The present work observed the 146-keV transition in coincidence with the 604-keV transition from the 2406-keV state to the $(23/2^+)$ 1803-keV state, also observed by Lozeva *et al.* and shown in Fig. 11. Figure 12 shows the coincidence spectrum, produced by gating on the 604-keV transition. This gate clearly shows the presence of the coincidence with the 146-keV γ ray.

An intensity balance calculation of the 2552-keV state implies β feeding, since there is no known higher-lying state in ^{129}In that could potentially populate this state. This feeding would amount to the portion represented by the intensity of the 146-keV transition, with respect to the sum of the intensities of the 146- and the 281-keV transitions, corrected for internal conversion.

Comparing the β feeding of the 2552-keV state and the 281-keV internal transition yielded a β branching ratio of 2.0(5)%. The log *ft* value for the β decay of the $(29/2^+)$ 1911-keV isomer in ^{129}In to the $(27/2^-)$ 2552-keV state in ^{129}Sn is then 5.68(12), consistent with a first-forbidden transition from the $(29/2^+)$ ^{129}In^{m3} state to the $(27/2^-)$ state in ^{129}Sn. This log *ft* value is calculated with a half-life of 0.10(1) s, the weighted average of the present result with the literature value. The log *ft* value in this transition is comparable to the 5.8 observed by Gausemel *et al.* between the $(23/2-)$ 1630-keV isomer in ^{129}In to the $(23/2^+)$ 1803-keV state ^{129}Sn, which is expected given the nearly pure $\pi(g_{9/2}^{-1}) \rightarrow \nu(h_{11/2}^{-1})$ β transition [17]. This is the first time the 1911-keV isomer in ^{129}In has been observed to β decay to excited states of ^{129}Sn. Figure 11 shows the partial level schemes of the states in both ^{129}In and ^{129}Sn involved in this decay.

IV. CONCLUSION

The present work reports new information observed through the β decay of ^{129}In to ^{129}Sn. The half-lives of the ground state and isomeric states in ^{129}In have been confirmed, with the uncertainty in the half-life value of the ^{129}In^{m2} isomer improved. The level scheme of ^{129}Sn has been greatly expanded, with nine new excited states and thirty-one new γ-ray transitions. Furthermore, this work observed, for the first time, the β decay of the $(29/2^+)$ 1911-keV ^{129}In^{m3} state. More work is needed, in particular in the determination of the spins and parities of the states above the ground state, the 35-keV isomer and the 315-keV first-excited state of ^{129}Sn. This work provides more rigid constraints on the spins of a number of the excited states, but further studies are needed in order to properly assign these values. This new information on these two nuclei, lying close to doubly magic $^{132}_{50}$Sn$_{82}$, provides important constraints and will guide future theoretical models in this region.

ACKNOWLEDGMENTS

The authors would like to thank the GRSI collaboration at TRIUMF for their aid during the course of this work. This work was supported, in part, by the Natural Sciences and Engineering Research Council of Canada (NSERC). Phase I of the GRIFFIN spectrometer was funded by the Canadian Foundation of Innovation (CFI), TRIUMF, and the University of Guelph. TRIUMF receives funding from the Canadian Federal Government via a contribution agreement with the National Research Council Canada (NRC). C.E.S. acknowledges support from the Canada Research Chairs program.

[1] P. Cottle, Nature (London) **465**, 430 (2010).
[2] D. Bazin, Nature (London) **486**, 330 (2012).
[3] F. Andreozzi *et al.*, Phys. Rev. C **56**, R16(R) (1997).
[4] T. Otsuka, R. Fujimoto, Y. Utsuno, B.A. Brown, M. Honma, and T. Mizusaki, Phys. Rev. Lett. **87**, 082502 (2001).

[5] T. Otsuka, T. Suzuki, R. Fujimoto, H. Grawe, and Y. Akaishi, Phys. Rev. Lett. **95**, 232502 (2005).
[6] J. Beun *et al.*, J. Phys. G **36**, 025201 (2009).
[7] R. Surman, J. Beun, G. C. McLaughlin, and W. R. Hix, Phys. Rev. C **79**, 045809 (2009).
[8] E. M. Burbidge, G. R. Burbidge, W. A. Fowler, and F. Hoyle, Rev. Mod. Phys. **29**, 547 (1957).
[9] A. G. W. Cameron, Publ. Astron. Soc. Pac. **69**, 201 (1957).
[10] A. G. W. Cameron, J. J. Cowan, and J. W. Truran, Astrophys. Space Sci. **91**, 235 (1983).
[11] M. R. Mumpower *et al.*, Prog. Part. Nucl. Phys. **86**, 86 (2016).
[12] J. A. Pinston, C. Foin, J. Genevey, R. Beraud, E. Chabanat, H. Faust, S. Oberstedt, and B. Weiss, Phys. Rev. C **61**, 024312 (2000).
[13] K. Aleklett, E. Lund, and G. Rudstam, Phys. Rev. C **18**, 462 (1978).
[14] L.-E. De Geer and G. B. Holm, Phys. Rev. C **22**, 2163 (1980).
[15] L. Spanier, K. Aleklett, B. Ekström, and B. Fogelberg, Nucl. Phys. A **474**, 359 (1987).
[16] H. Huck, M. L. Pérez, and J. J. Rossi, Phys. Rev. C **26**, 621 (1982).
[17] H. Gausemel, B. Fogelberg, T. Engeland, M. Hjorth-Jensen, P. Hoff, H. Mach, K.A. Mezilev, and J. P. Omtvedt, Phys. Rev. C **69**, 054307 (2004).
[18] R. Warner and P. Reeder, Radiat. Eff. **94**, 27 (1986).
[19] G. Rudstam, K. Aleklett, and L. Sihver, At. Data Nucl. Data Tables **53**, 1 (1993).
[20] J. Genevey, J. A. Pinston, C. Foin, M. Rejmund, H. Faust, and B. Weiss, Phys. Rev. C **65**, 034322 (2002).
[21] R. L. Lozeva *et al.*, Phys. Rev. C **77**, 064313 (2008).
[22] J. Dilling, R. Krücken, and G. Ball, Hyperfine Interact. **225**, 1 (2014).
[23] P. Van Duppen, in *The Euroschool Lectures on Physics with Exotic Beams* (Springer, Berlin, 2006), Vol. II.
[24] I. Bylinskii and M. K. Craddock, in *ISAC and ARIEL: The TRIUMF Radioactive Beam Facilities and the Scientific Program*, edited by J. Dilling, R. Krücken, and L. Merminga (Springer, Dordrecht, 2013).
[25] S. Raeder *et al.*, Rev. Sci. Instrum. **85**, 033309 (2014).
[26] P. Bricault *et al.*, in *ISAC and ARIEL: The TRIUMF Radioactive Beam Facilities and the Scientific Program*, edited by J. Dilling, R. Krücken, and L. Merminga (Springer, Dordrecht, 2013).
[27] C. E. Svensson and A. B. Garnsworthy, Hyperfine Interact. **225**, 127 (2014).
[28] A. B. Garnsworthy *et al.*, Nucl. Instrum. Methods Phys. Res., Sect. A **853**, 85 (2017).
[29] A. B. Garnsworthy *et al.*, Nucl. Instrum. Methods Phys. Res., Sect. A **918**, 9 (2019).
[30] U. Rizwan *et al.*, Nucl. Instrum. Methods Phys. Res., Sect. A **820**, 126 (2016).
[31] J. Timar, Z. Elekes, and B. Singh, Nucl. Data Sheets **121**, 143 (2014).
[32] T. Kibédi *et al.*, Nucl. Instrum. Methods Phys. Res., Sect. A **589**, 202 (2008).

Appendix B

Nonobservation of low-energy shape coexistence in ^{80}Ge - publication

Garcia, F. H. and Andreoiu, C. and Ball, G. C. and Bell, A. and Garnsworthy, A. B. and Nowacki, F. and Petrache, C. M. and Poves, A. and Whitmore, K. and Ali, F. A. and Bernier, N. and Bhattacharjee, S. S. and Bowry, M. and Coleman, R. J. and Dillmann, I. and Djianto, I. and Forney, A. M. and Gascoine, M. and Hackman, G. and Leach, K. G. and Murphy, A. N. and Natzke, C. R. and Olaizola, B. and Ortner, K. and Peters, E. E. and Rajabali, M. M. and Raymond, K. and Svensson, C. E. and Umashankar, R. and Williams, J. and Yates, D., ***Absence of Low-Energy Shape Coexistence in ^{80}Ge: The Nonobservation of Proposed 0_2^+ at 639 keV***, *Physical Review Letters*, 125, 17, 172501 (2020).

Available from APS: http://dx.doi.org/10.1103/PhysRevLett.125.172501

Absence of Low-Energy Shape Coexistence in ^{80}Ge: The Nonobservation of a Proposed Excited 0_2^+ Level at 639 keV

F. H. Garcia,[1,*] C. Andreoiu,[1] G. C. Ball,[2] A. Bell,[1] A. B. Garnsworthy,[2] F. Nowacki,[3,4] C. M. Petrache,[5] A. Poves,[6] K. Whitmore,[1] F. A. Ali,[7,8] N. Bernier,[2,9,†] S. S. Bhattacharjee,[2,‡] M. Bowry,[2] R. J. Coleman,[10] I. Dillmann,[2,11] I. Djanto,[1] A. M. Forney,[12] M. Gascoine,[1] G. Hackman,[2] K. G. Leach,[13] A. N. Murphy,[2] C. R. Natzke,[14,13] B. Olaizola,[14] K. Ortner,[1] E. E. Peters,[15] M. M. Rajabali,[16] K. Raymond,[1] C. E. Svensson,[10] R. Umashankar,[14] J. Williams,[1,§] and D. Yates[14,9]

[1]*Department of Chemistry, Simon Fraser University, Burnaby, British Columbia V5A 1S6, Canada*
[2]*TRIUMF, 4004 Wesbrook Mall, Vancouver, British Columbia V6T 2A3, Canada*
[3]*Université de Strasbourg, IPHC, 23 rue du Loess 67037 Strasbourg, France*
[4]*CNRS, UMR7178, 67037 Strasbourg, France*
[5]*Université Paris-Saclay, CNRS/IN2P3, IJCLab, 91405 Orsay, France*
[6]*Departamento de Física Teórica and IFTUAM/CSIC, Universidad Autónoma de Madrid, 28049 Madrid, Spain*
[7]*Department of Physics, University of Guelph, Guelph, Ontario, N1G 2W1, Canada*
[8]*Department of Physics, College of Education, University of Sulaimani, P.O. Box 334, Sulaimani, Kurdistan Region, Iraq*
[9]*Department of Physics and Astronomy, University of British Columbia, Vancouver, British Columbia V6T 1Z4, Canada*
[10]*Department of Physics, University of Guelph, Guelph, Ontario N1G 2W1, Canada*
[11]*Department of Physics and Astronomy, University of Victoria, Victoria, British Columbia V8P 5C2, Canada*
[12]*Department of Chemistry and Biochemistry, University of Maryland College Park, College Park, Maryland 20742, USA*
[13]*Department of Physics, Colorado School of Mines, Golden, Colorado 80401, USA*
[14]*TRIUMF, 4004 Wesbrook Mall, Vancouver, British Columbia, V6T 2A3, Canada*
[15]*Department of Chemistry, University of Kentucky, Lexington, Kentucky 40506-0055, USA*
[16]*Department of Physics, Tennessee Technological University, Cookeville, Tennessee 38505, USA*

(Received 19 June 2020; revised 19 August 2020; accepted 18 September 2020; published 23 October 2020)

The ^{80}Ge structure was investigated in a high-statistics β-decay experiment of ^{80}Ga using the GRIFFIN spectrometer at TRIUMF-ISAC through γ, β-e, e-γ, and γ-γ spectroscopy. No evidence was found for the recently reported 0_2^+ 639-keV level suggested as evidence for low-energy shape coexistence in ^{80}Ge. Large-scale shell model calculations performed in ^{78,80,82}Ge place the 0_2^+ level in ^{80}Ge at 2 MeV. The new experimental evidence combined with shell model predictions indicate that low-energy shape coexistence is not present in ^{80}Ge.

DOI: 10.1103/PhysRevLett.125.172501

Shape coexistence is ubiquitous across the chart of nuclides [1–4], but found mainly in the vicinity of shell and subshell closures. It manifests as the appearance of two or more quantum states of different intrinsic shapes located within a narrow energy range. A key signature of shape coexistence in even-even nuclei is the presence of low-lying excited 0^+ states above the 0^+ ground state. In most cases, these 0^+ states are connected by strong electric monopole transitions ($E0$), indicating significant mixing between different nuclear shapes with large differences in deformation. The microscopic origin of these 0^+ states is particle-hole excitations across a shell or subshell gap. The significant energy required to promote a pair of nucleons is offset by a large gain in correlation energy from the residual proton-neutron interaction [4]. Shape coexistence at the neutron-rich $Z = 28$, $N = 50$ doubly magic shell closure has been experimentally investigated in a spectroscopic study of ^{78}Ni via in-beam γ-ray spectroscopy [5]. The high-energy 2_1^+ excited state and a low-lying second 2_2^+ state separated by 0.31 MeV suggest that shape coexistence is present in ^{78}Ni [5].

A number of state-of-the-art theoretical calculations using modern approaches have been performed for the $N = 50$ region including doubly magic ^{78}Ni. These include *ab initio* approaches and the beyond-mean-field random-phase approximation [5] as well as large-scale shell-model calculations [6] employing various phenomenological shell-model interactions. These calculations are in agreement with the experimental data now available for ^{78}Ni, showing that the doubly magic nature is preserved, and a well-deformed prolate band is present at low excitation energy, representing a dramatic example of shape coexistence far from the valley of stability. Additionally, the phenomenological shell-model calculations predict a rapid transition from spherical ground states in the Ni isotopes up to ^{78}Ni and deformed ground states for more neutron-rich isotopes [5].

The structural evolution of the Ge and Se nuclei from $N = 34$–62 has been studied within the interacting boson model (IBM) [7]. In general, the IBM calculations agree with the trends in the experimental excitation energies for low-lying 0^+, 2^+, and 4^+ levels, including shape coexistence observed near $N = 40$, an increase in the excitation energies at $N = 50$, and also predict the onset of shape coexistence beyond $N = 52$.

New experimental results for ^{80}Ge, located two neutrons below the $N = 50$ shell closure, were recently reported from a study performed at the ALTO facility using the β decay of ^{80}Ga to perform β-delayed electron-conversion spectroscopy [8]. A conversion electron peak at 628 keV was reported and attributed to the decay of a 0_2^+ state at 639 keV in ^{80}Ge, located just below the first excited 2^+ state at 659 keV.

A comparison of the experimental energies of the 0_2^+ states in the $N = 48$ isotones with phenomenological estimates from mass data was used to show lowering of the 0_2^+ states at $Z = 32$ due to the pairing, monopole, and quadrupole terms of the interactions. Based on this analysis, the proposed 0_2^+ state in ^{80}Ge was interpreted as a $\nu(2p-2h)$ excitation across the $N = 50$ shell gap [8]: evidence of shape coexistence in ^{80}Ge.

In the present work, confirmation of the existence of the 0_2^+ state and shape coexistence in ^{80}Ge was sought. States in ^{80}Ge were studied via β decay of ^{80}Ga using conversion-electron and γ-ray spectroscopy. No experimental evidence for the previously proposed 0_2^+ 639-keV level was found. Large-scale shell model calculations support this finding, and suggest that the 0_2^+ level may be located near 2 MeV. These also agree with the theoretical trend found in the IBM [7], but contradict the recent IBM-2 calculations [9].

The experiment was conducted at the Isotope Separator and Accelerator (ISAC) facility [10] at TRIUMF, where radioactive beams are produced via the isotope separation on-line method. A 9.8 μA beam of protons was accelerated to 480 MeV by the main cyclotron and impinged onto a thick UC_x target, inducing spallation, fragmentation, and fission reactions. The Ga atoms of interest that did not diffuse from the production target were ionized using the ion-guide laser ion source [11] which also strongly suppressed the surface ionized ^{80}Rb isobaric contamination. An $A = 80$ beam at 30 keV was selected by a high-resolution mass separator and sent to the experimental area. The resulting beam composition was ~22% ^{80}Ga and 78% ^{80}Rb.

The 2×10^4 pps ^{80}Ga beam was delivered to the Gamma-Ray Infrastructure For Fundamental Investigation of Nuclei (GRIFFIN) [12–15] and implanted onto a Mylar tape system at the center of the GRIFFIN spectrometer. GRIFFIN is an array of up to 16 BGO compton-suppressed high-purity germanium (HPGe) clover detectors used for γ-ray detection and operated using a digital data acquisition system [14] in a triggerless mode. Only 15 HPGe clovers were used in the present work. GRIFFIN was operated in its optimal peak-to-total configuration [15] with the HPGe detectors located 14.5 cm from the beam implantation point, with an efficiency of 7% at 1332 keV in clover addback mode.

Electrons produced by internal conversion were detected using the Pentagonal Array of Conversion Electron Spectrometers (PACES) [15]. The array consists of five lithium-drifted silicon detectors, cooled with liquid nitrogen. The centers of the PACES detectors were located 3.15 cm from the implantation point, with an array efficiency ~2%. A single plastic scintillator, with an efficiency of ~40%, was positioned behind the implantation location at zero degrees to the beam axis for the tagging of β particles [15]. A 10 mm thick Delrin absorber was placed around the vacuum chamber to prevent high-energy β particles from reaching the surrounding HPGe detectors and limit bremsstrahlung [15].

Tape cycles were chosen to maximize the implantation time and total decays of ^{80g,m}Ga [$T_{1/2,gs} = 1.9(1)$ s, $T_{1/2,m} = 1.3(2)$ s] while reducing the activity from the subsequent decay of ^{80}Ge ($T_{1/2} = 29.5$ s) as well as the decay of the ^{80}Rb contaminant ($T_{1/2} = 33.4$ s). A typical cycle consisted of tape movement for 1.5 s, background measurement for 1.0 s, beam implantation for 15 s, and beam decay for 10 s. After each cycle, the implantation point on the tape was moved into a lead-shielded box outside of the spectrometer to reduce the background. Coincident hits from HPGe crystals within the same clover detector recorded within a 250 ns time window were combined into a single event to construct addback γ-ray events.

The efficiency of GRIFFIN was determined for the 81-keV to 3.2-MeV energy region using standard sources of ^{133}Ba, ^{152}Eu, ^{56}Co, and ^{60}Co. Summing corrections for γ-ray intensities were made by using a 180° γ-γ coincidence matrix as described in Ref. [15].

The ^{80}Ge level scheme was constructed by setting gates on the time-random background-subtracted γ-γ addback matrix. The comprehensive structure and spectroscopic information for ^{80}Ge, including γ-ray intensities, branching ratios, angular correlations, β-decay lifetime and fast γ-ray lifetime measurements will be discussed in a forthcoming paper [16]. All γ rays and levels presented in Ref. [17] were observed in the current work, confirming the presence of both the 6^- ground state and 3^- isomer in ^{80}Ga.

A portion of the γ-ray spectrum is shown in Fig. 1. Previously, Verney *et al.* [17], using a beam of ^{80}Ga produced by the photo-fission of UC_x, observed an increase in the relative intensity of γ rays from low-lying states in ^{80}Ge associated with the 6^- ground state decay of ^{80}Ga and a corresponding decrease in the relative intensity of the γ rays associated with the 3^- isomer decay, when compared with those obtained from a ^{80}Ga beam produced by the

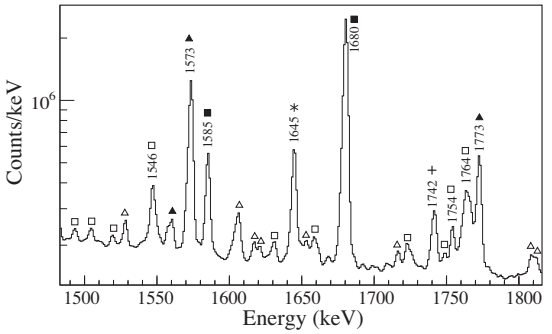

FIG. 1. The γ-ray spectrum in the energy range from 1500–1800 keV. The labels represent the following: the solid (open) squares are known (new) transitions from levels fed by the 6^- ground state of ^{80}Ga; the solid (open) triangles are known (new) transitions from levels fed by the 3^- isomer in ^{80}Ga, the asterisk ($*$) is a transition in ^{80}Se, the cross ($+$) is the sum peak between the strong 659.1- and 1083.4-keV transitions.

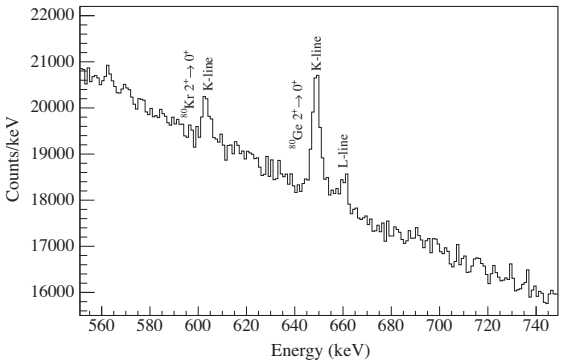

FIG. 2. β-gated electron spectrum obtained following the β-decay of ^{80}Ga showing the $2_1^+ \rightarrow 0_1^+$ K line at 648 keV and L line at 658 keV in ^{80}Ge. The peak at 601 keV corresponds to the $2_1^+ \rightarrow 0_1^+$ K line in ^{80}Kr from the decay of ^{80}Rb present in the beam. There is no evidence for the peak at 628 keV as reported by Gottardo *et al.* [8].

thermal neutron fission of ^{235}U studied by Hoff and Fogelberg [18]. In the present Letter, similar but larger differences were observed, indicating that the 3^- isomer content is different in all three cases. This difference can be used to estimate the 3^- isomer content of the beam in the present work. Specifically, the 2^+ 1573-keV state can only be directly fed by the 3^- isomer, and the 8^+ 3445-keV state is directly fed only by the 6^- ground state. Comparing the β-feeding intensities of these two states, determined from relative γ-ray intensities, with the previous work results in an increase of 1.55(6) and a decrease of 0.66(3) for the 3445- and 1573-keV levels, respectively. This corresponds to a 3^- isomeric content of 41(3)% in the present work and 62(4)% in the ^{80}Ga beam produced by thermal neutron fission [18] and ENSDF [19]. From a comparison of β-feeding intensities for all levels observed in both experiments, calculated from the relative γ-ray intensities and assuming no β feeding to the ground state of ^{80}Ge, 13 levels were clearly identified as being fed by the 3^- isomer; representing 46(2)% of the total β-feeding intensity in the present work and 62(5)% in Refs. [18,19] (see Ref. [16]). Relative γ-ray intensities were not reported by Verney *et al.* [17]; however, from the data shown in Fig. 2 of Ref. [17], it is estimated that the 3^- isomer content in the ^{80}Ga beam produced by photofission is ~52%.

A portion of the β-gated electron spectrum is shown in Fig. 2. The strong K line from the $2_1^+ \rightarrow 0_1^+$ transition in ^{80}Ge is clearly visible at 648 keV, along with the L line at 658 keV. The K line from the $2_1^+ \rightarrow 0_1^+$ decay in ^{80}Kr, populated by the β decay of ^{80}Rb, is also visible at 601 keV. The ratio of the intensity of these two K electron lines agrees with the value predicted from the ratio of the measured intensities of the corresponding γ rays, corrected for internal conversion [20]. No other significant features were observed in the rest of the spectrum outside the energy range shown in Fig. 2. There is no evidence for a peak near 628 keV where the $0_2^+ \rightarrow 0_1^+$ $E0$ transition in ^{80}Ge was previously reported [8].

Since 96% of all β decays from the 3^- isomer and 6^- ground state of ^{80}Ga emit a 659-keV γ ray, the intensity of the 648-keV K electron line in Fig. 2 is proportional to the total ^{80}Ga β decays observed in the present experiment. Integrating the region centered around 628 keV and comparing the intensity of a hypothetical $E0$ transition to the intensity of the 648-keV K line, corrected for the 41% 3^- isomeric content of the beam and for internal conversion [20], yields a 2σ limit of <0.02 per 100 decays of the 3^- isomer in ^{80}Ga. By analogy, from the data presented in Fig. 2 of Ref. [8] for a ^{80}Ga 3^- isomeric component of 52%, the intensity of the observed 628-keV electron peak is estimated to be ~0.08(2) per 100 decays, a factor of four times the 2σ upper limit and comparable to the intensity of the 601-keV ^{80}Kr K line observed in the present experiment. While there is no explanation for this discrepancy, it must be noted that the slope of the background in the β-gated electron spectrum shown in Fig. 2 of Gottardo *et al.* [8] has an unusual shape that is not typical of Si(Li) detectors used in direct view of a β-decay source with a high Q value emitting one or more γ rays per decay [21].

The 1764-keV γ ray that was assigned by Gottardo *et al.* [8] to decay from a 2403-keV 2^+ state in ^{80}Ge to the proposed 639-keV 0_2^+ level can be seen in the γ-ray spectrum in Fig. 1. The peak at 1742 keV has been identified as the sum peak of the intense 659- and 1083-keV transitions, and not from ^{80}As as suggested in Ref. [17]. An unresolved peak at 1768 keV representing the summing of the 659- and 1109-keV transitions is also present in this spectrum, with an intensity of 40% of the 1742-keV peak.

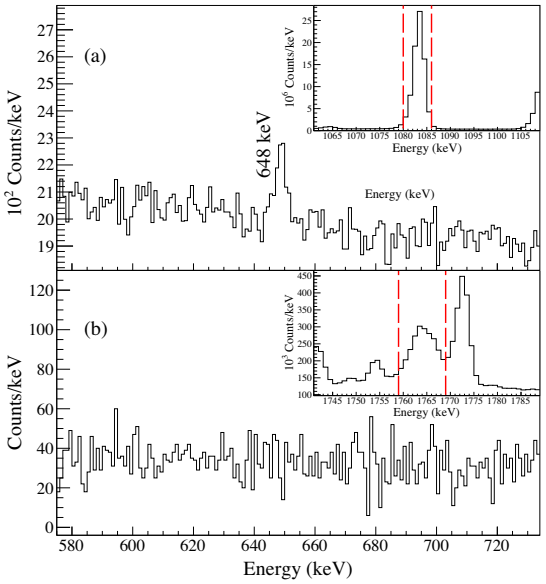

FIG. 3. Background-corrected electron spectra, obtained from a γ-electron matrix by placing (a) a gate on the 1083-keV transition, showing only the 648-keV K line corresponding to the 659-keV transition, and (b) a gate on the wide γ-ray peak in the 1764 keV region showing the absence of an electron line at 628 keV. The insets show the locations of the γ-ray gates.

Gates were placed on the γ-ray peaks in the e-γ matrix to look for a 1764-keV γ-ray transition in coincidence with a 628-keV electron peak. A gate placed on the $4_1^+ \rightarrow 2_1^+$ 1083-keV γ-ray generated the coincidence electron spectrum shown in Fig. 3(a) which shows the K line at 648 keV associated with the 659-keV $2_1^+ \rightarrow 0_1^+$ transition in ^{80}Ge. Comparing the converted intensity of the 648-keV electron line in the 1083-keV γ-gated electron spectrum, with the intensity of the γ-singles 1083-keV transition, yields an e-γ coincidence efficiency of 1.6(2)%. A wide gate on the region around 1764 keV produced the spectrum shown in Fig. 3(b); no peak near 628 keV is present in this electron spectrum. The 2σ limit for an $E0$ transition at 628 keV, determined from this spectrum, corresponds to <0.2% of the intensity of this broad γ-ray peak and is equivalent to a 1764-keV transition intensity from the proposed level at 2403 keV in ^{80}Ge [8] of <0.01 per 100 decays of the 3^- isomer in ^{80}Ga. Furthermore, the ratio of the 2σ intensity limit for the 1764-keV transition to the intensity of the 1773-keV transition from the decay of the 3515-keV level in ^{80}Ge, fed by the 3^- isomer [16,17] is <0.003, compared with the value of 0.3 reported by Gottardo *et al.* [8].

The unresolved γ rays in the 1764-keV region seen in Fig. 1 were further investigated by examining the $\gamma - \gamma$ coincidence relationships. By placing narrow gates in the 1764-keV region, distinct coincident spectra were observed, which were used to expand the ^{80}Ge level scheme as shown in Fig. 4. Four new transitions were observed at 1760.6, 1764.0, 1764.5, and 1766.5 keV, all with intensities well below 1%, relative to the 659-keV $2_1^+ \rightarrow 0_1^+$ transition. No evidence for the 2403-keV (2+) level or the 1764-keV transition from this state was found, as reported by Gottardo *et al.* [8].

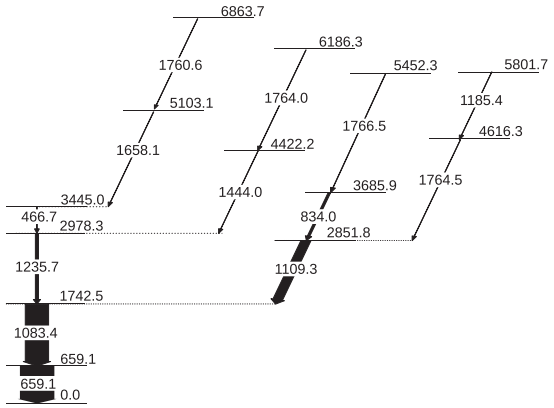

FIG. 4. Partial level scheme of ^{80}Ge showing the placement of four new transitions that make up the wide peak around 1764 keV. The widths of the arrows are proportional to the relative intensities of the γ-ray transitions.

Large-scale shell-model calculations with configuration interactions have been carried out to explore the nuclear structure around $N = 50$ above ^{78}Ni. Two valence spaces were considered. The first valence space, LNPS, is based on a ^{48}Ca core and encompasses the full pf shell for the protons and the pf-shell orbits above the $0f_{7/2}$ plus the $0g_{9/2}$ and $1d_{5/2}$ orbitals for the neutrons. The effective interaction is the current version of the original LNPS [22], which incorporates some minor changes which do not affect the predictions near $N = 40$ and improved the behavior towards $N = 50$. The second is the PF-SDG space, based on a ^{60}Ca core and consisting of the $p = 3$ major oscillator shell (pf) for the protons and the $p = 4$ major oscillator shell (sdg) for the neutrons. The PF-SDG interaction used in this work is the one described in Ref. [6]. In addition to ^{80}Ge, calculations have been performed for the neighboring isotopes ^{78}Ge and ^{80}Ge, where excited 0_2^+ states have been observed.

For the specific case of ^{82}Ge, both interactions predict a 0^+ intruder state near 2 MeV, but the deformation extracted from the restricted valance space is small. This prediction agrees with the observed 0_2^+ state at 2334 keV in ^{82}Ge that has been attributed to a deformed rotational band in ^{82}Ge resulting from $2p - 2h$ excitations across the $N = 50$ closed shell [23]. All of the other 0^+ states predicted by both interactions for ^{78,80,82}Ge arise from the recoupling of different valence particles. Additional intruder states likely exist at higher excitation energies but tracking them is computationally demanding and beyond the scope of this study.

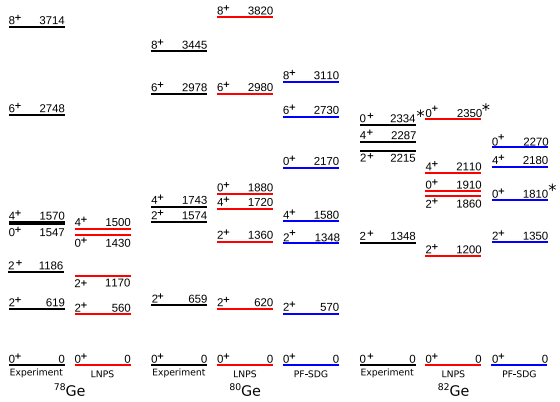

FIG. 5. Comparison of experimental (black) and calculated nuclear levels in ^{78,80,82}Ge using the LNPS (red) and PF-SDG (blue) interactions. The asterisks (*) identify intruderlike structures.

The results of these calculations can be seen in Fig. 5. For each of the ^{78,80,82}Ge isotopes, the energies of the low-lying positive-parity states are shown along with the calculated values. In all cases, the energies of the 2_1^+ and 4_1^+ levels are well reproduced. The calculation with the LNPS valence space also reproduces the 2_2^+ levels. In both ^{78}Ge and ^{82}Ge, the 0_2^+ levels are known to exist above 1.5 MeV, and the calculations predict these energies very well. In the case of ^{80}Ge, the calculations predict the 0_2^+ state to be at a relatively high excitation energy near 2 MeV. Whether the 0_2^+ state is observed near 2 MeV in the present work must wait for a more complete analysis of all the very weak γ-ray transitions observed in this high-statistics dataset [16].

In conclusion, the β decay of ^{80}Ga to ^{80}Ge has been studied using the GRIFFIN spectrometer at TRIUMF-ISAC. The ^{80}Ge nucleus has been investigated via γ-ray and conversion-electron spectroscopy. No evidence for an excited 0_2^+ state located below the 2_1^+ state at 659 keV is found in this experiment, despite detailed investigations using multiple β-electron, γ-electron, and γ-γ coincidences. Additionally, driven by these experimental results, large-scale shell-model calculations that reproduced well the excited 0_2^+ states in ^{78,82}Ge and other low-lying levels in $^{78-82}$Ge, cannot replicate the 0_2^+ state suggested at 639 keV in ^{80}Ge; the calculations instead predict the first excited 0^+ state at 2 MeV. We conclude that the 0_2^+ level at 639-keV excitation energy reported by Gottardo *et al.* [8] does not, in fact, exist in ^{80}Ge and that this isotope does not exhibit low-energy shape coexistence.

We would like to thank the operations and beam delivery staff at TRIUMF for providing the ^{80}Ge radioactive beam. This work was supported in part by the Natural Sciences and Engineering Research Council of Canada. The GRIFFIN infrastructure has been funded jointly by the Canada Foundation for Innovation, the University of Guelph, TRIUMF, the British Columbia Knowledge Development Fund, and the Ontario Ministry of Research and Innovation. TRIUMF receives federal funding via a contribution agreement through the National Research Council Canada. This work was funded in part by the U.S. Department of Energy, Office of Science under Grant No. DE-SC0017649. This material is based upon work supported in part by the U.S. National Science Foundation under Grant No. PHY-1913028. C. E. S. acknowledges support from the Canada Research Chairs program. A. P. acknowledges the support of the Ministerio de Ciencia, Inovación y Universidades (Spain), Severo Ochoa Programme No. SEV-2016-0597 and Grant No. PGC-2018-94583. C. A. acknowledges the fruitful discussions with D. Verney on the spectroscopy of Ge isotopes.

*Corresponding author.
fatimag@sfu.ca
†Present address: Department of Physics, University of the Western Cape, P/B X17, Bellville, ZA-7535 South Africa.
‡Present address: School of Computing, Engineering and Physical Sciences, University of the West of Scotland, Paisley PA1 2BE, United Kingdom.
§Present address: TRIUMF, 4004 Wesbrook Mall, Vancouver, British Columbia V6T 2A3, Canada.

[1] H. Morinaga, Phys. Rev. **101**, 254 (1956).
[2] K. Heyde and J. L. Wood, Rev. Mod. Phys. **83**, 1467 (2011).
[3] P. E. Garrett, J. Phys. G **43**, 084002 (2016).
[4] J. L. Wood, J. Phys. Conf. Ser. **403**, 012011 (2012).
[5] R. Taniuchi *et al.*, Nature (London) **569**, 53 (2019).
[6] F. Nowacki, A. Poves, E. Caurier, and B. Bounthong, Phys. Rev. Lett. **117**, 272501 (2016).
[7] K. Nomura, R. Rodríguez-Guzmán, and L. M. Robledo, Phys. Rev. C **95**, 064310 (2017).
[8] A. Gottardo, D. Verney, C. Delafosse, F. Ibrahim, B. Roussière *et al.*, Phys. Rev. Lett. **116**, 182501 (2016).
[9] D.-L. Zhang and C.-F. Mu, Chin. Phys. C **42**, 034101 (2018).
[10] J. Dilling, R. Krücken, and G. C. Ball, Hyperfine Interact. **225**, 1 (2014).
[11] S. Raeder, H. Heggen, J. Lassen, F. Ames, D. Bishop, P. Bricault, P. Kunz, A. Mjøs, and A. Teigelhöfer, Rev. Sci. Instrum. **85**, 033309 (2014).
[12] C. E. Svensson and A. B. Garnsworthy, Hyperfine Interact. **225**, 127 (2014).
[13] U. Rizwan *et al.*, Nucl. Instrum. Methods Phys. Res., Sect. A **820**, 126 (2016).
[14] A. B. Garnsworthy *et al.*, Nucl. Instrum. Methods Phys. Res., Sect. A **853**, 85 (2017).
[15] A. B. Garnsworthy *et al.*, Nucl. Instrum. Methods Phys. Res., Sect. A **918**, 9 (2019).
[16] F. H. Garcia *et al.* (to be published).

[17] D. Verney, B. Tastet, K. Kolos, F. Le Blanc, F. Ibrahim *et al.*, Phys. Rev. C **87**, 054307 (2013).
[18] P. Hoff and B. Fogelberg, Nucl. Phys. **A368**, 210 (1981).
[19] B. Singh, Nucl. Data Sheets **105**, 223 (2005).
[20] T. Kibédi, T. W. Burrows, M. B. Trzhaskovskaya, P. M. Davidson, and C. W. Nestor, Nucl. Instrum. Methods Phys. Res., Sect. A **589**, 202 (2008).
[21] K. Siegbahn, *Alpha- Beta- and Gamma-Ray Spectroscopy*, edited by K. Siegbahn (North-Holland, Amsterdam, 1965).
[22] S. M. Lenzi, F. Nowacki, A. Poves, and K. Sieja, Phys. Rev. C **82**, 054301 (2010).
[23] J. K. Hwang, J. H. Hamilton, A. V. Ramayya, N. T. Brewer, Y. X. Luo, J. O. Rasmussen, and S. J. Zhu, Phys. Rev. C **84**, 024305 (2011).

Appendix C

Angular Correlations

A γ-ray cascade, composed of two transitions can be used to determined the spin of a nuclear state. This is done by measurement of angular correlations.

Analogous to the Zeeman effect [100], in the presence of a magnetic field, the m-states associated with the level spin J can be split, the degeneracy lifted, and an anisotropic distribution observed, with the possible values of m_J given as: $-J \leq m_J \leq J$.

However, in the absence of such a field, the m-states are equally populated and the distribution will be isotropic, thereby obscuring all information about the spin of the states involved in the cascade. A schematic of a cascade between an initial state $J_i = 1$ and a final state $J_f = 0$ is shown in Figure C.1. The J_i state has three possible m-states as shown, each with an associated anisotropic distribution.

The emission probability for $m_J = 0$ will vary as $\sin^2\theta$ (blue), while the $m_J = \pm 1$ will vary as $\frac{1}{2}(1+\cos^2\theta)$ (red), where θ is an angle defined with respect to the z-axis used to measure the angular momentum components. If all states are equally populated, these distributions add and the total will appear isotropic (purple). An unequal population of the m-states is thus necessary in order to obtain information about the spins of the states involved.

The probability distribution $W(\theta)$ is then a function of the m-states and the population of the initial state, $p(m_i)$,

$$W(\theta) = \sum_{m_i} p(m_i) W_{m_i \to m_f}(\theta). \tag{C.1}$$

If the population of the m-states is even, then the distribution will be of the form [10],

$$W(\theta) \propto \frac{1}{3}\Big[\frac{1}{2}(1+\cos^2\theta)\Big] + \frac{1}{3}\Big[(\sin^2\theta)\Big] + \frac{1}{3}\Big[\frac{1}{2}(1+\cos^2\theta)\Big] \propto 1. \tag{C.2}$$

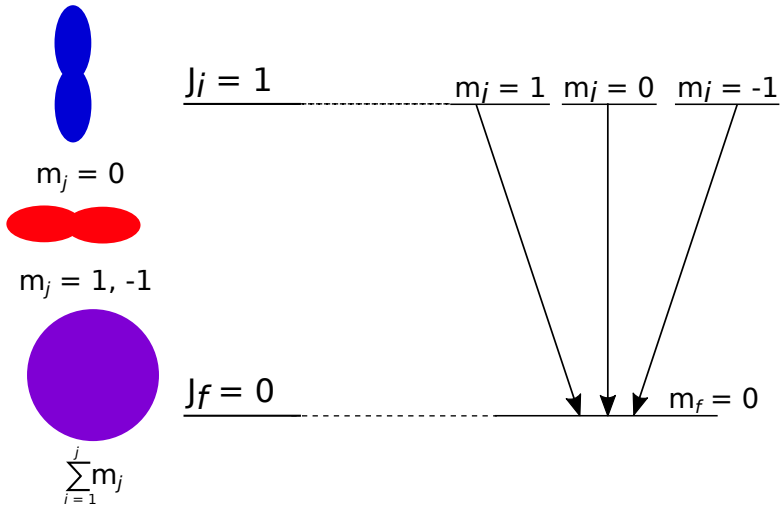

Figure C.1: A schematic view of a γ-ray decay between an initial state $J_i = 1$ and a final state $J_f = 0$. This transition has three different potential pathways, through the three states of $J_i = 1$, $m = 0, \pm 1$. The angular distributions for each of these states, shown in blue and red, are anisotropic, but when the m-states are all populated equally, the observed distribution will be isotropic, shown in purple. Adapted from Ref. [101].

Angular correlations are a method that can be used to produce an unequal population of the m-states, by observing a $\gamma - \gamma$ coincidence and obtaining information about the intermediate state [10], without the need for an external magnetic field. An example of the simplest dipole-dipole case is shown in Figure C.2, where a γ-ray cascade occurs between states with spins 0, 1 and 0, respectively, $(0 \rightarrow 1 \rightarrow 0)$.

The two γ-rays are detected in two separate detectors, with an angle, θ, between them. By fixing the z-axis as the emission axis of γ_1, information can be gathered about the spin of the intermediate state.

Given that the photon must carry at least one unit of angular momentum, a transition between $J_0 = 0$ and the $m_i = 0$ of $J_i = 0$ cannot occur, as depicted in Figure C.2, meaning that this state cannot be populated and therefore the $\sin^2\theta$ term will not contribute to the distribution. This would then reduce Equation C.2 to,

$$W(\theta) \propto (1 + \cos^2\theta). \tag{C.3}$$

This uneven population will generate an anisotropic distribution, thereby providing information on the spin of the state in question. Higher order multipole transitions will produce increasingly complex decay schemes. A more general version of Equation C.1 is given by,

$$W(\theta) = \sum_{k=0,k=even}^{2L} a_k P_k(\cos\theta), \tag{C.4}$$

where a_k are coefficients that depend upon the spin of the states involved in the cascade and the angular momenta and mixing ratios (δ) of each γ-ray in the cascade; $P_k(\cos\theta)$ are the Legendre Polynomials. The sum involves only even values of k, conserving parity, and extends to one term higher than the multipole order of the γ-ray.

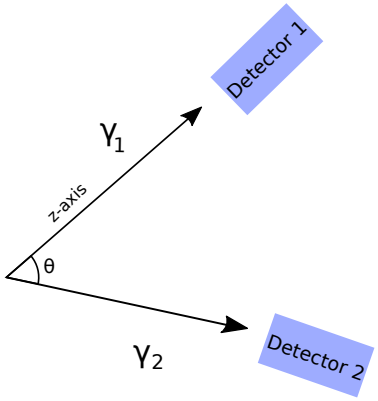

(a) Schematic of γ-ray cascade detection. The transitions, γ_1 and γ_2, are emitted by a source and detected in two different detectors, with an opening angle of θ between them.

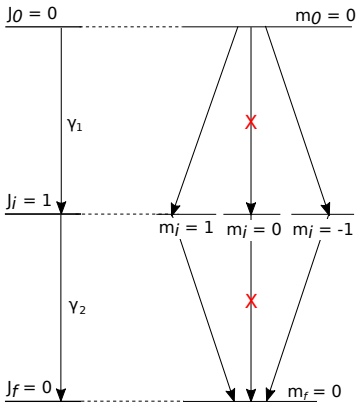

(b) Level scheme depicting a $0 \rightarrow 1 \rightarrow 0$ transition. The possible values of m_j, given the spins involved, indicate several possible pathways the decay can take, through each of the states. The (red) "X" denotes that the pathway through $m_i = 0$ is not a possible route given the γ-decay selection rules.

Figure C.2: A schematic angular correlation measurement. Given the detection shown in (a) and fixing the z-axis along the emission of γ_1, a correlation can be extracted, based on the m-states available in the decay, shown in (b). Adapted from Refs. [101, 50].

Detailed formalism on angular correlations can be found in the work of Litherland and Ferguson [102], who describe the theoretical framework and experimental results showing the efficacy of the method. Further treatments can be found in Ref. [103, 104].

The large number of detectors available in GRIFFIN provides an excellent tool to perform angular correlation analysis. The angular correlation methodology developed for GRIFFIN can be found in Ref. [105], and successful applications of this method can be found in Refs. [50, 99, 106, 107].